UNIVERSITÀ DEGLI STUDI DI PADOVA

Sede Amministrativa: Università degli Studi di Padova

Dipartimento di Astronomia

DOTTORATO DI RICERCA IN: Astronomia
CICLO: XX

Hierarchical Clustering: Structure Formation in the Universe

Coordinatore: Prof. Giampaolo Piotto
Supervisori: Prof. Giuseppe Tormen
Prof. Ravi K. Sheth

Dottorando: Carlo Giocoli

DATA CONSEGNA TESI
31 Gennaio 2008

a tutte le persone con le quali ho condiviso
i fantastici momenti della mia vita: grazie

to the beatiful and sweet things that change the life

Carlo Giocoli
e-mail: *carlo.giocoli@unipd.it*
web: *http://www.astro.unipd.it/cosmo/carlo*

January 29, 2008

Contents

List of Figures

List of Tables

ABSTRACT

In order to understand galaxy formation models it is necessary to have a reasonably clear idea of dark matter clustering. This because, in the standard cosmological scenario, galaxies are thought to reside in larger dark matter haloes, extending beyond the galaxy observable radius. Haloes form as consequence of gravitational instability of dark matter density perturbations, and collapse at a density about two hundred times that of the surrounding environment. Clustering happens at all masses at any time.

Until now no direct observations of the existence of these dark matter haloes have been done; however, their presence may be indirectly tested by their gravitational influence. For example, galaxies in groups have a velocity dispersion much higher than that caused only by visible matter. Astronomers thus assumed the existence of large amounts of dark matter, an hypothesis later found consistent with other independent observations like gravitational lensing, galaxy clustering on very large scales and anisotropies in the cosmic microwave background radiation.

In particle physics, supersymmetry predicts the existence of a particle named neutralino (Jungman *et al.*, 1996; Bertone *et al.*, 2005), today regarded as the most likely candidate for the dark matter. This particle is heavy and slow-moving (mass ≈ 100 Gev), so that dark matter density fluctuations can collapse for any mass larger than $10^{-6}\,M_\odot$ (Hofmann *et al.*, 2001; Green *et al.*, 2004, 2005). This places a mass cut-off on the smallest dark matter haloes that can collapse. Neutralino can also annihilate with its anti-particle, generating γ-ray photons (Bergström, 2000; Bertone *et al.*, 2005), with annihilation rates growing as the square of the density. Due to this process, it is expected that future γ-ray telescopes (like GLAST, Morselli (1997)) should be able to detect some excess in the γ-ray background signal from the center of the Milky-Way halo and from its satellites. This would be the first time of an in-”direct” detection of dark matter.

In this PhD dissertation we study the evolution of dark matter haloes, using two complementary approaches: numerical simulations and analytical modeling (through the extended Press & Schechter formalism). The work is organized as follows. In the first three chapters we describe and review some properties of

the early universe and the theory underlying models of dark matter clustering. We discuss how density perturbations evolve and form dark matter haloes inside which baryons can shock and cool, eventually form stars and galaxies. We also show how the number density of haloes can be estimated at any redshift using the excursion set approach, both for the spherical and ellipsoidal collapse models. These model mass functions are compared with those from numerical simulations in Chapter 4. We show that the ellipsoidal collapse model (Sheth *et al.*, 2001; Sheth and Tormen, 2002) perfectly reproduces the global mass function in N-Body simulations, while, on the other hand, the spherical collapse model (Press and Schechter, 1974; Lacey and Cole, 1993; Bond *et al.*, 1991) overpredicts the aboundace of small masses and underpredicts that of large ones.

Dark matter clustering is hierarchical, i.e. small systems collapse first (at higher redshift), and subsequently merge together forming larger haloes. In this scenario, if we define a formation time as the earliest redshift when an halo assembles half of its present-day mass, small haloes form first and large ones form later. The top of the hierarchical pyramid is occupied by galaxy clusters, which represent the largest virialized structures in the universe.

Another important quantity describing dark matter clustering is any conditional mass function. One example is the probability that an halo observed at redshift z_1, will be part of a larger halo at $z_0 < z_1$. This distribution is also called progenitor mass function; theoretical predictions and N-Body simulations are compared at the end of Chapter 4. There we show that, also in this case, the ellipsoidal collapse prediction well reproduces the distribution found in numerical simulations at most redshifts.

In Chapter 5 we will discuss how it is possible to estimate the formation time distribution from the conditional mass function, and present a new formula, based on the ellipsoidal collapse, that better fits the formation redshift distribution measured in N-Body simulations.

The progenitors accreted along the merging history tree of a halo can survive today in their host system, and constitute the so-called substructure population (Ghigna *et al.*, 1998; Tormen *et al.*, 2004; Gao *et al.*, 2004; De Lucia *et al.*, 2004; van den Bosch *et al.*, 2005). In Chapter 6 we discuss how it is possible to analytically estimate this population using the conditional mass function, assuming no tidal stripping and merging among substructures. By extrapolating the power spectrum of density perturbations down to the typical neutralino Jeans mass, we estimate the substructure population in a Milky-Way size halo, both for a spherical and ellipsoidal collapse model. Modeling the neutralino annihilation rate, we then estimate the γ-ray emission from this population and its detectability with a GLAST-like telescope.

In Chapter 7 we study the growth of the main progenitor halo, and the mass it accretes along its merging history tree using numerical simulations. The mass function of accreted haloes, called “unevolved subhalo mass function”, turns out to be independent of the final host halo mass, both before and after its formation redshift. The accreted haloes, called satellites, are then followed snapshot

by snapshot in order to compute their mass loss rate. This allow us to interpret the present-day subhalo population in term of the mass loss from the accreted satellites. Since smaller hosts form earlier than larger ones, the former will accrete satellites at earlier times; these satellites will therefore spend a longer time inside the host halo and lose a larger fraction of their initial mass. This translates the (mass-independent) unevolved subhalo population in a present-day subhalo distribution that depends on the host halo mass: at fixed subhalo-to-host halo mass: m_{sb}/M_0, more massive hosts contain more subhaloes than smaller hosts do.

Subhaloes defined in this way may contain other subhaloes within themselves (Diemand *et al.*, 2007b; Li and Helmi, 2007), which were accreted when they were still isolated systems. In Chapter 8 we show how subhaloes within subhaloes can be identified following all branches of the merging history tree of an host halo. We also compare our definition of substructures with that of other authors (Gao *et al.*, 2004), finding very good agreement.

In the last chapter of this dissertation, we show how the merging history tree of a halo can be followed using Monte Carlo realizations. The partition code, on which the tree is based, is very fast, time step independent, and provides results in excellent agreement with the spherical collapse conditional mass function down to any required mass resolution (Sheth and Lemson, 1999). The tree has been run following the main branch and resolving all satellites down to the typical neutralino Jeans mass, in order to study the Milky-Way subhalo population.

SOMMARIO

Al fine di comprendere i modelli di formazione delle galassie, è necessario avere le idee chiare circa il clustering della materia oscura. Questo perchè, il modello cosmologico standard prevede che le galassie risiedano in aloni di materia oscura che si estendono ben oltre il loro raggio osservabile. Gli aloni si formano come conseguenza di instabilitá gravitazionale del campo di fluttuazioni di densitá della materia oscura, e collassano quando queste raggiungono una densitá di almeno duecento volte quella dell'ambiente circostante. Il clustering avviene su tutte le masse e a tutti i tempi.

Fino ad oggi la materia oscura non é mai stata osservata direttamente; tuttavia, la sua presenza viene indirettamente avvertita attraverso la sua influenza gravitazionale. Per esempio, le galassie, che risiedono in gruppi, hanno una dispersione di velocitá molto più elevata di quella dovuta alla sola materia visibile. Gli astronomi hanno perciò ipotizzato l'esistenza di una grande quantità di materia oscura, successivamente consistente con altre indipendenti osservazioni come il lensing gravitazionale, il clustering delle galassie su grande scale e le anisotropie del fondo cosmico delle microonde.

Nel campo della fisica delle particelle, la teoria supersimmetrica predice l'esistenza di una particella chiamata neutralino (Jungman *et al.*, 1996; Bertone *et al.*, 2005), questa viene vista oggi come il candidato più probabile a comporre la materia oscura. Questa particella è pesante (massa $\approx$ 100 GeV) ed ha una bassa velocitá tipica; queste proprietà fanno si che solo le fluttuazioni di materia oscura maggiori di $10^{-6}\,M_\odot$ (Hofmann *et al.*, 2001; Green *et al.*, 2004, 2005) possano collassare, ponendo un cut-off in massa per il più piccolo alone che può formarsi nell'universo. Il neutralino, annichilendo con la sua antiparticela, genera fotoni con frequenze tipiche nei raggi γ (Bergström, 2000; Bertone *et al.*, 2005). Il tasso di annichilazione risulta proporzionale alla radice quadrata della densità. Questo processo causerebbe un eccesso del fondo di fotoni γ in corrispondenza del centro della Via Lattea e dei suoi satelliti, che ci si aspetta di poter osservare con i prossimi telescopi-γ, come ad esempio GLAST (Morselli, 1997). Questa sarebbe la prima in-"diretta" osservazione della materia oscura.

In questo lavoro di tesi studiamo l'evoluzione degli aloni di materia oscura usando due approcci complementari: simulazioni numeriche e modelli analitici (usando il formalismo esteso di Press & Schechter). La tesi è organizzata come di seguito. Nei primi tre capitoli descriviamo e rivediamo alcune proprietà dell'universo primordiale, e la teoria del clustering della materia oscura. Discutiamo come evolvono le perturbazioni di densità e come si formano gli aloni di materia oscura in cui i barioni possono subire shock e raffreddarsi, ed eventualmente formare stelle e galassie. Mostriamo anche come si può stimare la densità numerica degli aloni ad ogni redshift usando l'approccio dell'excursion set, sia per il modello del collasso sferico che per quello ellissoidale. Nel Capitolo 4, queste funzioni di massa teoriche vengono confrontate con i risultati di simulazioni numeriche. In questo capitolo si mostra che il modello del collasso ellissoidale (Sheth *et al.*, 2001; Sheth and Tormen, 2002) riproduce perfettamente la funzione di massa globale delle simulazioni, metre, d'altra parte, il collasso sferico (Press and Schechter, 1974; Lacey and Cole, 1993) sovrapredice l'abbondanza degli aloni di piccola massa e sottopredice quella dei sistemi grandi.

Il clustering della materia oscura è gerarchico, cioé gli aloni piccoli collassano prima, ad alto redshift, e successivamente si uniscono formando quelli più grandi. In questo scenario, definendo redshift di formazione come il redshift più alto al quale un alone assembla metà della sua massa al tempo presente, gli aloni piccoli si formano prima di quelli grandi. Il posto più alto di questa piramide gerarchica è occupata degli ammassi di galassie, che rappresentano le più grandi strutture virializzate dell'universo.

Un'altra importante quantità che descrive il clustering della materia oscura è la funzione di massa condizionale. Un esempio è rappresentato dalla probabilità che ha un alone, osservato a redshift z_1, di far parte di un alone più grande a $z_0 < z_1$. Questa distribuzione è anche chiamata funzione di massa dei progenitori; la predizione teorica e le simulazioni N-Body vengo confrontate alla fine del Capitolo 4, dove si mostra che, anche in questo caso, il collasso ellissoidale è ingrado di riprodurre molto bene le simulazioni numeriche a diversi redshifts.

Nel capitolo 5 mostriamo come è possibile stimare la distribuzione dei tempi di formazione dalla funzione di massa condizionale, e presentiamo una nuova formula, basata sul collasso ellissoidale che meglio fitta la distribuzione dei redshifts di formazione misurata nelle simulazioni N-Body.

I progenitori eccresciuti lungo il merging history tree di un alone possono sopravvivere oggi nel sistama ospite, constituendo la cosiddetta popolazione delle sottostrutture (Ghigna *et al.*, 1998; Tormen *et al.*, 2004; Gao *et al.*, 2004; De Lucia *et al.*, 2004; van den Bosch *et al.*, 2005). Nel capitolo 6 discutiamo come è possibile stimare analiticamente questa popolazione usando la funzione di massa condizionale, non assumendo, per semplicità, tidal stripping e merging tra le sottostrutture. Interpolando lo spettro delle perturbazioni di densità fino alla tipica massa di Jeans del neutralino, stimiamo la popolazione delle sottostrutture in un alone di dimensione della Via Lattea, sia per il collasso sferico che per quello ellissoidale. Modellando il tesso di annichilazione dei neutralini, misuriamo l'emissione γ da questa poplazione e la sua possibilità di essere osservata con un telescopio come GLAST.

Nel Capitolo 7 studiamo la crescita del progenitore principale e la massa che esso accresce lungo il merging history tree, usando simulazioni numeriche. La funzione di massa degli aloni accresciuti, chiamata “funzione di massa dei subaloni non evoluta”, risulta essere indipendente dalla massa dell’alone ospite, anche prima e dopo la sua formazione. Gli aloni accresciuti, chiamati satelliti, vegono poi seguiti snapshot per snapshot al fine di stimare il loro tasso di perdita di massa. Questo ci permette quindi di interpretare la popolazione presente di subaloni in termini della massa persa dai satelliti accresiuti. Giacché i piccoli aloni ospiti si formano prima di quelli grandi, i primi accresceranno satelliti a epoche più remote; questi satelliti spendendo un lungo tempo nell’alone ospite perderanno una frazione maggiore della loro massa iniziale. Questo traduce la funzione di massa non evoluta dei subaloni (indipendente dalla massa) in una distribuzione di subaloni al tempo presente che dipende dalla massa dell’alone ospite: a rapporto di massa subalone/massa alone ospite fissato: m_{sb}/M_0, aloni più massicci contengono più sottostrutture di quelli piccoli.

I subaloni come defїnti sopra tuttavia possono contenere altri subaloni al loro interno (Diemand *et al.*, 2007b; Li and Helmi, 2007), accresiuti quando erano ancora sistemi isolati. Nel Capitolo 8 mostriamo come i subaloni nei subaloni posso essere identificati seguendo tutti i rami del merger tree di un alone ospite. Paragonando, poi, la nostra definizione di sottostrutture con quella di altri autori (Gao *et al.*, 2004), troviamo un buon accordo.

Nall’ultimo capitolo di questa tesi, mostriamo come sviluppare un merger tree di un alone usando delle realizzazioni Monte Carlo. Il codice di partizione, su cui il tree è basato, risulta essere molto veloce e indipendente dal time-step, generando risultati in eccellente accordo con la funzione di massa condizionale del collasso sferico fino a qualsivoglia risoluzione in massa (Sheth and Lemson, 1999). Il tree è stato generato seguendo il ramo principale e risolvendo tutti i satelliti fino alla tipica massa di Jeans del neutralino, allo scopo di studiare la popolazione dei subaloni della Via Lattea.

INTRODUCTION

The attempts to understand the origin of the universe and formation of cosmic structures by applying the laws of physics lead to difficulties which have no parallel in the study of systems on more moderate scales - atoms, molecules and solids. The universe is one, and is evolving in time. Different epochs in its history are unique and have occurred only once. Within this framework, the standard rules of science, like repeatability, statistical stability and predictability, cannot be applied to study the entire universe. Considering that the speed of light is finite we can observe the universe, at the same time, in different fase of its evolution: the more distant we watch, the younger are the cosmic structures that we can see. This peculiarity suggest cosmologists that starting from the present configuration of the universe and using the laws of physics it is possible to reproduce its past and predict its future.

Progress in this direction is limited by the fact that our knowledge of the physical processes at energy scales above 100 GeV lacks direct experiments. Despite this, current observations of the cosmic microwave background radiation, high redshift supernovae and large scale structures suggest that nearly 95% of the matter in the universe is of a type which never seen in the laboratories, most of which exerts negative pressure.

The standard paradigm of cosmic structure formation is based on the idea that at sufficiently early times the universe was very homogeneous, isotropic and fairly featureless (Cosmological Principle) - except for small fluctuation in the stress-energy tensor. The Cosmological Principle has a very important role in the cosmological scenario of structures formation; above all it is a good approximation to the universe at early times and on large scales today, and helps us building up theoretical models with a small number of free parameters. Homogeneity is the property of being identical everywhere in space, while isotropy is the property of looking the same in every direction.

Starting from this, the results will depend only on a small number of parameters, describing: the composition of the universe, its current expansion rate and the initial spectrum of density perturbations. Varying these allows to construct a set of evolutionary models for the universe which can then be compared with observations in order to estimate the value for the parameters.

In this PhD dissertation we follow two main approaches in the study of cosmic structure formation: the extended Press & Schechter theory and numerical N-Body simulations. Using these tools we construct merger tree of dark matter haloes in order to compute and describe their formation and creation times. We study also the conditional and unconditional mass function of virialized haloes and discuss theoretical models able to describe these.

Some of progenitor haloes accreted by the main trunk of the tree can survive at the present-time in the host halo constituting the so called subhalo population. We study the subhalo mass function, both in extendend Press & Schechter formalim and in numerical simulations, discussing how it depends on host halo mass and on environment.

The Universe:
from Smooth to Clumpy

CHAPTER

1

Cosmological Background

1.1 Robertson-Walker Metric & Friedmann's Equations

Starting from the idea of the Cosmological Principle it is possible to construct models of the Universe in which this principle holds. Consider the Universe as a continuous fluid and assign to each fluid element three spatial coordinates $x^\alpha (\alpha = 1,2,3)$. Any point in space-time can be labeled by the coordinates x^α, corresponding to the fluid element which is passing through the point, and a time parameter which we take to be the proper time t measured by a clock moving with the fluid element. The coordinates x^α are called comoving coordinates. The geometrical properties of space-time are described by a metric, and the most general space-time metric describing a universe in which the Cosmological Principle is obeyed has the form:

$$\mathrm{d}s^2 = (c\mathrm{d}t)^2 - a(t)^2 \left[\frac{\mathrm{d}r^2}{1-kr^2} + r^2\left(\mathrm{d}\theta^2 + \sin^2\theta \mathrm{d}\phi^2\right)\right], \tag{1.1}$$

where (r,θ,ϕ) are the spherical comoving coordinates, t is the proper time, $a(t)$ is the *cosmic scale factor* or *expansion factor* and k is *curvature parameter*, a constant which can be rescaled to take the value 1, 0 or -1. This metric is called *Robertson-Walker Metric*.

Considering a uniform and isotropic distribution of matter, it is possible to define a *universal time*, such that at any instant the three-dimensional spatial metric is

$$\mathrm{d}l^2 = \gamma_{\alpha\beta}\mathrm{d}x^\alpha \mathrm{d}x^\beta \qquad (\alpha,\beta = 1,2,3), \tag{1.2}$$

so that the space-time metric can be written as:

$$\mathrm{d}s^2 = (c\mathrm{d}t)^2 - \mathrm{d}l^2 = (c\mathrm{d}t)^2 - \gamma_{\alpha\beta}\mathrm{d}x^\alpha \mathrm{d}x^\beta. \tag{1.3}$$

For three-dimensional flat, positively curved and negatively curved spaces one has, respectively:

$$\mathrm{d}l^2 = a^2\left(\mathrm{d}r^2 + r^2\mathrm{d}\Omega^2\right); \tag{1.4}$$

$$\mathrm{d}l^2 = a^2\left(\mathrm{d}\chi^2 + \sin^2\chi\mathrm{d}\Omega^2\right) = a^2\left(\frac{\mathrm{d}r^2}{1-r^2} + r^2\mathrm{d}\Omega^2\right); \tag{1.5}$$

$$\mathrm{d}l^2 = a^2\left(\mathrm{d}\chi^2 + \sinh^2\chi\mathrm{d}\Omega^2\right) = a^2\left(\frac{\mathrm{d}r^2}{1+r^2} + r^2\mathrm{d}\Omega^2\right), \tag{1.6}$$

where $\mathrm{d}\Omega^2 = \mathrm{d}\theta^2 + \sin^2\theta\mathrm{d}\phi^2$; $0 \leqslant \chi \leqslant \pi$ in (1.5) and $0 \leqslant \chi \leqslant \infty$ in (1.6). The values of $k = 1, 0, -1$ in equation (1.1) correspond to an hypersphere, the Euclidean space and a space of constant negative curvature, respectively.

The only force of nature effective on large scales is gravity, so the most important part of a physical description of the Universe is a theory of gravity. The best candidate to describe the universe and its time evolution as whole is given by Einstein's equations[1]:

$$R_{ij} - \frac{1}{2}g_{ij}R = \frac{8\pi G}{c^4}T_{ij} \qquad (i, j = 0, 1, 2, 3), \tag{1.7}$$

where R_{ij} and R are the *Ricci tensor* and *scalar*, respectively, T_{ij} is the *energy-momentum tensor* and g_{ij} is the *metric tensor*. These equations relate the geometrical properties of space-time with the energy-momentum tensor describing the content of the universe. In particular, for a homogeneous and isotropic perfect fluid with rest-mass energy density ρc^2 and pressure p, the solutions of Einstein's equations ($\Lambda = 0$) are Friedmann's equations:

$$\ddot{a} = -\frac{4}{3}\pi G\left(\rho + 3\frac{p}{c^2}\right)a, \tag{1.8}$$

$$\dot{a}^2 + kc^2 = \frac{8}{3}\pi G\rho a^2, \tag{1.9}$$

where the dots represent the derivative respect to cosmological proper time t.

Defining the *critical density* as:

$$\rho_c = \frac{3}{8\pi G}\left(\frac{\dot{a}}{a}\right)^2, \tag{1.10}$$

from equation (1.9) it is possible to write the space curvature as:

$$\frac{k}{a^2} = \frac{1}{c^2}\left(\frac{\dot{a}}{a^2}\right)^2\left(\frac{\rho}{\rho_c} - 1\right). \tag{1.11}$$

From this equation we see that:

- space is positively curved ($k = 1$, open universe) if $\Omega(t) \equiv \dfrac{\rho}{\rho_c} > 1$, where $\Omega(t)$ is called *density parameter*;

---

[1] Initially Einstein's equations did not include the cosmological constant, Λ, which was added later to allow for a static universe.

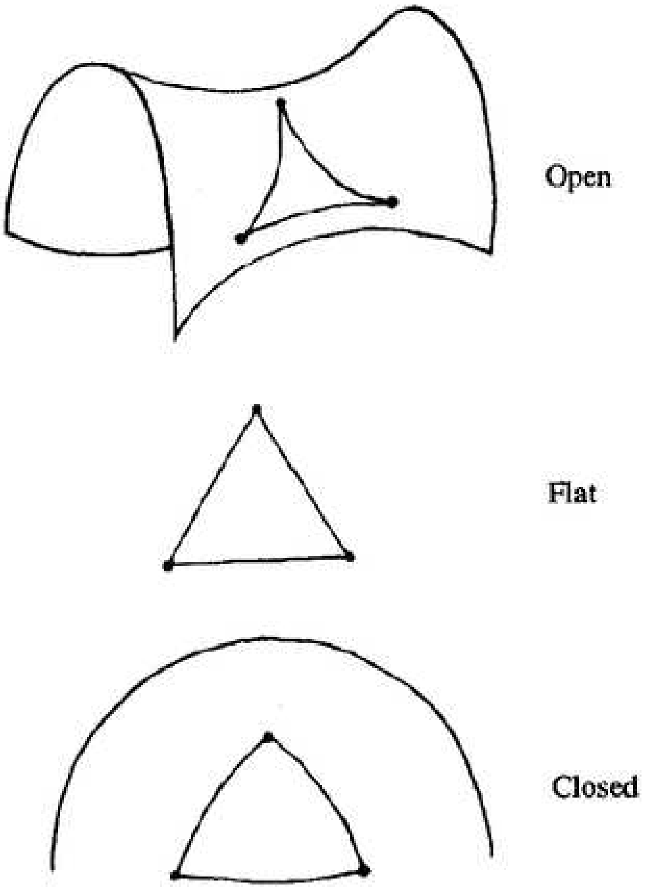

Figure 1.1: Examples of curved spaces in two dimensions. From top to bottom we show a property of the curved space: the sum of the internal angles of a triangle. This sum is less than 180^o if space has negative curvature (open universe), it is equal to 180^o if space is Euclidean (flat universe) and is bigger than 180^o if space has positive curvature (closed universe).

- space is Euclidean ($k = 0$, flat universe) if $\Omega(t) = 1$;
- space is negatively curved ($k = -1$, open universe) if $\Omega(t) < 1$.

In Figure 1.1 we show three examples of curved spaces in two dimensions. The triangle drawn in each case has sum of internal angles less, equal or more than 180^o for an open, flat or close universe. Space curvature can be measured by two further properties: (i) global versus local parallelism and (ii) the parallel transport of a vector. (i) Two locally parallel lines will also be globally parallel in a flat space, while they will converge or diverge in a positively or negatively curved space. (ii) Take a vector and transport it along a closed path, while keeping it parallel to its initial direction. In a flat space, the transported vector will coincide with the initial one, while in a positively or negatively curved space the two vectors will differ in direction by an amount depending on the curvature.

It is important to remember that the *density parameter* receives contributions from all matter and energy components in the universe: baryons, dark matter, radiation, neutrinos, etc. The ratio $H_0 = (\dot{a}/a)_0$ - called Hubble constant - is the rate of expansion of the universe at the present-time.

If a particular kind of energy density is described by an equation of state of the form $p = w\rho c^2$, where ρ is the pressure and w is a constant, then the condition for adiabatic expansion $\mathrm{d}(\rho a^3) = -\rho \mathrm{d}a^3$, can be integrated to give:

$$\frac{\rho}{\rho_0} = \left(\frac{a}{a_0}\right)^{-3(1+w)} . \tag{1.12}$$

1.2 Content of the Universe

Our knowledge of the observed universe have greatly improved over the last few years, especially thanks to studies of cosmic microwave background (CMB) anisotropies and to observations of high redshift objects. A concise summary of the main findings is the following:

1. matter-energy in the universe give $\Omega_0 = \sum_i \Omega_i \simeq 0.98 - 1.08$. This value can be derived from the angular anisotropy spectrum of the cosmic microwave background radiation (Netterfield *et al.*, 2002; Smoot *et al.*, 1992; Bennett *et al.*, 1996, 2003; Spergel *et al.*, 2003, 2007). These observations favor a flat universe: $k = 0$.

2. CMB anisotropies, large scale structures observations and studies of galactic dynamics (Abell, 1958; White and Rees, 1978; Abell *et al.*, 1989; Dressler, 1980; Navarro *et al.*, 1996; Davis *et al.*, 1985) suggest that the universe is populated by a non-luminous component of matter - called Dark Matter - made of weakly interacting particles which cluster at all scales above some critical mass, which is negligible for most cosmological applications. Such dark matter has non relativistic velocity at all epochs of interest, and contributes to the energy budget of the universe for about $\Omega_{DM} \simeq 0.20 - 0.35$. Its equation of state has $w_{DM} = 0$, giving $\rho_{DM}(t) \propto a^{-3}$.

3. Observations of primordial deuterium produced during the big bang nucleosynthesis, as well as CMB anisotropies, indicate that the total density of baryons is about $\Omega_b \simeq (0.024 \pm 0.0012)h^{-2}$ (Applegate *et al.*, 1987; Songaila *et al.*, 1994; Copi *et al.*, 1995) - where h is the Hubble constant in term of $100\,\mathrm{km}\, s^{-1}\mathrm{Mpc}^{-1}$. This, combined with the previous item, tells that most of the matter in the universe is non-baryonic.

4. Combining the previous points together one sees that $\Omega_0 - \Omega_{DM} - \Omega_b \simeq 0.7$, so there must be one more component to the energy density of the universe contributing about 70% of the critical density. Here again CMB observations, combined with high redshift supernovae, suggest that the missing component has an equation of state with negative pressure. The simplest

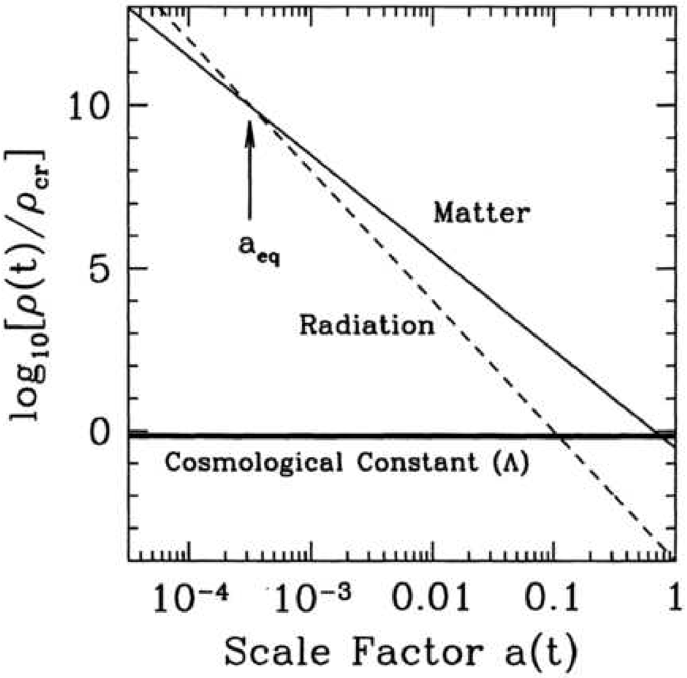

Figure 1.2: Energy density versus scale factor for different energy components of a flat universe. Shown are non-relativistic matter, radiation, and a cosmological constant in units of the critical density today. Even though matter and cosmological constant dominate today, at early times the radiation density was the largest.

and more accepted choice for the Dark Energy is the *cosmological constant*, a fluid with equation of state $p_{DE} = -\rho_{DE}$ ($w_{DE} = -1$), which gives $\rho_{DE} =$ *constant*.

5. The universe also contains radiation, contributing by $\Omega_R h^2 = 2.56 \times 10^{-5}$ today, most of which comes from the CMB. Its equation of state is $p_R = (1/3)\rho_R$, implying $\rho_R \propto a^{-4}$. Since for thermal radiation $\rho_R \propto T^4$, it follows that $T \propto a^{-1}$. While this component is negligible today, it was dominant at very high redshifts, when the universe was younger, smaller and hotter.

For a flat ΛCDM universe with $\Omega_0 = \Omega_b + \Omega_{DM} + \Omega_R + \Omega_{DE} \approx \Omega_m + \Omega_\Lambda$, using the Friedmann's equations and the energy density conservation in an expanding universe we can identify three distinct phases in the evolution of the universe. At high redshift the universe is radiation-dominated and $a(t) \propto t^{1/2}$, $T \propto t^{-1/2}$. Since radiation density decreases faster than matter density, at some later time t_{eq} the two densities are comparable, and for $t > t_{eq}$ matter will dominate the expansion, giving $a \propto t^{2/3}$. Finally, at some even later times Dark Energy, whose density is constant in time, will dominate over the rest, forcing the universe to expand in an accelerated way. For a concordance universe with $\Omega_{DE} \approx 0.7$, the accelerated phase starts at $z_{DE} \approx 0.67$.

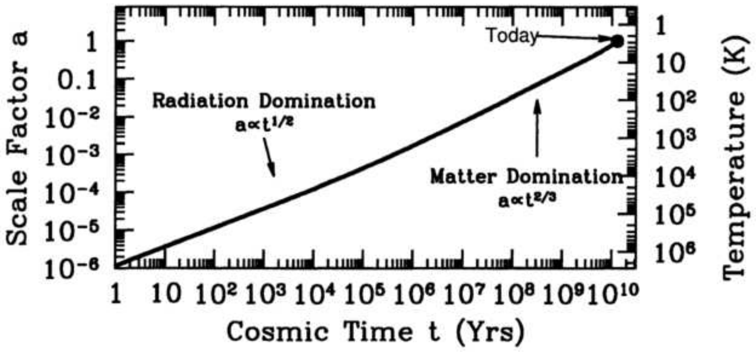

Figure 1.3: Evolution of the scale factor of the universe with cosmic time. When the universe was very young, radiation was the dominant component, and the scale factor increased as $t^{1/2}$. At later times, when matter come to dominate, this dependence switched to $t^{2/3}$. The vertical axis shows the corresponding temperature, today approximately equal to 3 K.

1.3 Cosmological Constant: the ΛCDM Universe

When Einstein first proposed his equations, the universe was thought to be static. The only way to allow for a static solution in Friedmann's equation is to add a *cosmological constant* term Λg_{ij} on the left hand-side of Einstein's equations (1.7), an addition that does not change their covariant character. Einstein's static solution results by assuming a closed universe ($\Omega > 1$) which is prevented from recollapsing by some non-gravitational force provided by a positive Λ.

Nowadays the cosmological constant is interpreted differently, by placing it instead on the right hand-side of Einstein's equations: this corresponds to modifying the *energy-momentum tensor* into:

$$\tilde{T}_{ij} = T_{ij} + \frac{\Lambda c^4}{8\pi G} g_{ij} = -\tilde{p} g_{ij} + (\tilde{p} + \tilde{\rho} c^2) U_i U_j \,, \tag{1.13}$$

where the effective pressure $\tilde{p}$ and density $\tilde{\rho}$ are related to the corresponding quantities for a perfect fluid by

$$\tilde{p} = p - \frac{\Lambda c^4}{8\pi G}, \quad \tilde{\rho} = \rho + \frac{\Lambda c^2}{8\pi G}, \tag{1.14}$$

Einstein's equations (and so Friedmann's ones) become:

$$\begin{aligned} R_{ij} - \frac{1}{2} g_{ij} R &= \frac{8\pi G}{c^4} \tilde{T}_{ij} \,, \\ \ddot{a} &= -\frac{4\pi}{3} G \left(\tilde{\rho} + 3 \frac{\tilde{p}}{c^2} \right) a \,, \\ \dot{a}^2 + k c^2 &= \frac{8\pi G}{3} \tilde{\rho} a^2 \,. \end{aligned}$$

From equation (1.14) we can see that $|\Lambda|^{1/2}$ has the dimensions of a length.

Today the cosmological constant is interpreted in terms of Dark Energy (DE), an unknown source of energy contributing by 70% to the *critical density* of the universe.

1.4 Evolution of Density Parameter and Hubble Constant

The recent CMB experiments, large scale structures observations and high redshift supernovae surveys, combined together, place stringent constraints on the values of many cosmological parameters. Our universe is well described by a flat spatial metric, is dominated by a cosmological constant and is seeded with an approximately scale-invariant primordial spectrum of Gaussian density fluctuation. The best fit parameters from the WMAP 3-year data release (Spergel *et al.*, 2007) give: $\Omega_m = 0.24$, $\Omega_\Lambda = 0.76$, $\Omega_b = 0.042$, $h = H_0/100\,\mathrm{km}s^{-1}\mathrm{Mpc}^{-1} = 0.73$, $n = 0.95$ - spectral index of the matter power spectrum at inflation - and $\sigma_8 = 0.75$ - the root-mean-square amplitude of mass fluctuations in a sphere of radius $8\,h/\mathrm{Mpc}$. According to this basic model, the cosmological constant is unclustered.

In this cosmology, according to Friedmann's equations, the expansion parameter H evolve in terms of redshift $z = 1/a(t) - 1$ as:

$$H(z) = \frac{1}{a}\frac{\mathrm{d}a}{\mathrm{d}t} = H_0\left[\Omega_m(1+z)^3 + \Omega_\Lambda\right]^{1/2}, \tag{1.15}$$

which gives for the density parameters of the matter and cosmological constant:

$$\begin{aligned} \Omega_\Lambda(z) &= \frac{\Omega_\Lambda}{\Omega_\Lambda + \Omega_m(1+z)^3}, & (1.16) \\ \Omega_m(z) &= \frac{\Omega_m(1+z)^3}{\Omega_\Lambda + \Omega_m(1+z)^3}, & (1.17) \end{aligned}$$

where H_0, Ω_Λ and Ω_m refer to the present-day quantities. The age of the universe today is:

$$t_0 = \int_0^\infty \frac{\mathrm{d}\zeta}{(1+\zeta)H(\zeta)} = \frac{2}{3H_0\sqrt{\Omega_\Lambda}}\ln\left[\frac{\sqrt{\Omega_\Lambda}+1}{\sqrt{\Omega_m}}\right] \approx 13.7\,\mathrm{Gyr}. \tag{1.18}$$

Consider now the situation of an observer located in the origin of a reference frame within an expanding universe. This will receive informations from any point of the space able to send him a light "message". However the photons have to reach the observer in a finite time compared to the age of the universe. The set of points that can communicate with O in this way must be inside a sphere, centered upon the origin, with proper radius

$$R_H(t) = a(t)\int_0^t \frac{c\mathrm{d}t'}{a(t')}, \tag{1.19}$$

From small time t the integral diverges because $a(t)$ goes to zero, in this case the observer can receive informations from the whole universe. When t grow, the integral assume a finite value and O can reach informations only from points that are inside a sphere with finite radius called *particles horizon.*

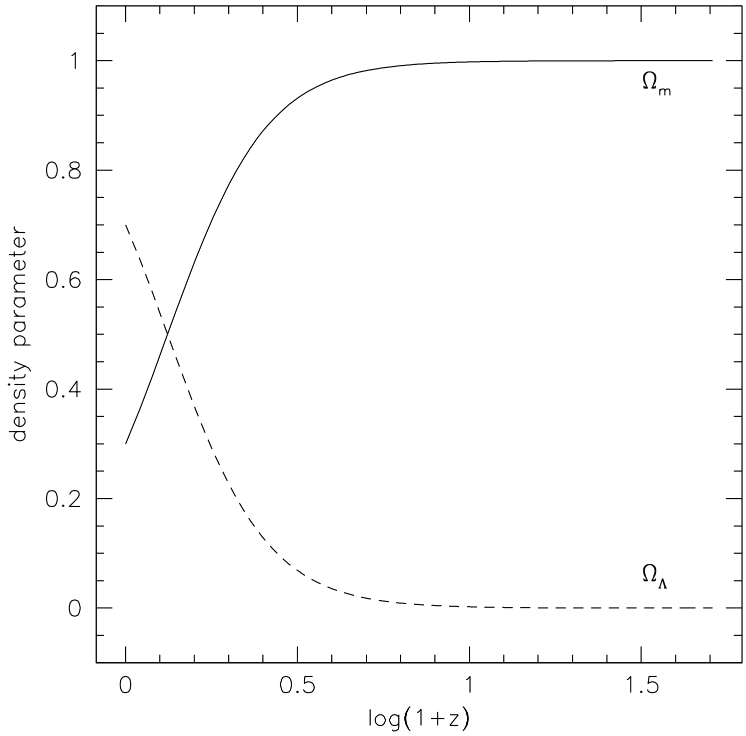

Figure 1.4: Evolution of the density parameters for cosmological constant and matter in term of redshift as in the equations (1.16) and (1.17).

1.5 Recombination and Decoupling

Since in the past the universe was denser and hotter, there have been times when the time-scale of scattering between matter and radiation was lower that the expansion time. In this phase photons and matter scattered together maintaining equilibrium conditions.

Before the universe cooled to temperatures of order 1 eV photons were tightly coupled to electrons via Compton scattering, electrons and protons via Coulomb forces. One could naively think that at this energy neutral hydrogen (with binding energy $\epsilon_0 = 13.6\,\mathrm{eV}$) could start to form. However, the high photon-to-baryon ratio forced any new hydrogen atom to instantaneously re-ionize. In other words, even when the mean temperature of the universe is smaller than the hydrogen binding energy, the exponential tail of the black-body radiation still contains enough photons to keep the universe ionized.

In order to understand the evolution of the different components of the universe at early time, let define three different, but physically closely related, moments. The *recombination* epoch when the baryons component goes from being totally ionized to neutral ($n_{ions} = n_{n,atoms}$). The *decoupling* time when the rate at which the photons scatter from electrons becomes smaller than the Hubble time: the universe becomes transparent and the radiation is free to move inside it. The *last scattering* when the photons underwent their last scattering from electrons.

To avoid complications for the following calculations, let us assume that the epoch of *recombination* the baryon component is entirely made by hydrogen: neutral (H) or ionized (proton - p). The neutrality of the universe tell that the number density of free electron n_e has to be equal to that of free protons n_p, the equilibrium is guarantee be the reaction

$$e^- + p \leftrightarrows \mathrm{H} + \gamma\,.$$

At equilibrium the fraction of free electrons, in term of the temperature is given by the Saha equation:

$$\frac{X_e^2}{1-X_e} = \frac{1}{n_e+n_p}\left[\left(\frac{m_e k_B T}{2\pi\hbar^2}\right)^{3/2} e^{-[m_e+m_p-m_\mathrm{H}]c^2/(k_B T)}\right], \tag{1.20}$$

where $\epsilon_0 = (m_e+m_p-m_\mathrm{H})c^2$ and $X_e = X \equiv n_e/n_b = n_p/n_b$ where n_b is the baryon density. Solving this quadratic equation, considering positive root, and defining the moment of recombination when $X = 1/2$ we have

$$kT_{rec} = 0.323\,\mathrm{eV},$$

and so $T_{rec} = 3740$ K at redshift $z_{rec} = 1370$.

When a reaction is in statistical equilibrium at temperature T the number density n_x of particles with mass m_x is given by the Maxwell-Boltzmann's equation. To estimate the evolution of the ionized fraction we need to integrate this equation, which gives:

$$\frac{\mathrm{d}X_e}{\mathrm{d}t} = \left\{(1-X_e)\beta - X_e n_b \alpha^{(2)}\right\}, \tag{1.21}$$

where β is the ionization rate and $\alpha^{(2)}$ the recombination rate at states higher than the ground one.

Since the number density of free electrons drops rapidly during the *recombination*, the *decoupling* comes soon after it. The rate of photons scattering, when the hydrogen is partially ionized, is given by:

$$\Gamma(z) = n_e(z)\sigma_e c = X(z)(1+z)^3 n_{b,0}\sigma_e c\,. \tag{1.22}$$

using the redshift evolution of the cosmological parameters in ΛCDM universe, the value of free electron fraction after the recombination and setting the rate of photon scattering equal the Hubble constant $z_{dec} = 1130$. At redshift lower that this the temperature of intergalactic gas fall adiabatically faster than that of the radiation.

After this time the baryon matter become free to move through the radiation field to form the first generation of gravitationally bound systems. The decoupled photons can still be observed today as a uniform and homogeneous blackbody that embed the whole universe: CMB, Cosmic Microwave Background radiation.

A particle specie decouple with the other particles, or in particular with the photons, if the their scattering time scale is higher than the expansion time. In the early phase of the universe, not only the baryons, but also dark matter particles were coupled with the radiation field, through the reaction of annihilation with anti-dark matter particles. This produce two high energy photons still in equilibrium with the radiation field. As temperature drop below dark matter particle rest frame energy, photons and dark matter particles decouple, and the latter *freeze-out*.

If these particles have kept scattering with the radiation, their abundance would have been reduced at the present-day under non-observability limits, in the whole universe, because of the appearance of of the typical Boltzmann suppression factor $\exp\left\{-m_X c^2/(k_B T)\right\}$ in the equation that describe their number density evolution.

Let define a_{XD} the time at which the dark matter specie X decouple with the remaining matter and radiation. The dark matter particle X with mass m_X will become non-relativistic when the temperature of the universe is equal to its rest frame energy:

$$kT \approx m_X c^2 . \tag{1.23}$$

Considering that T is a decreasing monotonic function of the time, the more massive is the particle mass the sooner it will become non-relativistic.

Hence the contribution of these particles to the Ω_{DM} is determined by two parameters: the mass m_X and the temperature at which the particles X decouples, which fixes the number of surviving particles. Different analysis and studies about galaxy clustering and large scale structures prefer a dark matter that is non-relativistic: so that decouple from the radiation and remaining matter when its mean velocity is less than c: CDM particles. The most accepted candidate for this kind of matter is neutralino that has a mass approximately equal to 100 GeV (Mori *et al.*, 1993; Berezinsky *et al.*, 1996; Baer and Brhlik, 1998).

In the pure cold dark matter model, almost all of energy density Ω_{DM} is provided by CDM particles alone. However, some researchers claim that this model of only CDM can not correctly reproduce the power spectrum of density perturbation at all scales. However it is clear that CDM was needed anyway in order to obtain a successful scheme for large-scale structure formation. These considerations together gave origin to a model of flat universe realized with the total energy density mostly provided by two different matter components, CDM and HDM in a convenient fraction: $\Omega_{DE} = \Omega_{HDM} + \Omega_{CDM}$. These models, which have been called mixed DM, succeeded in fitting the entire power spectrum quite well. The problem now is that a little amount of HDM has a dramatic effect on CDM particles, because their free-streaming, to wash out any inhomogeneities in their spatial distribution which will become galaxies. Therefore their presence slows the growth rates of the density inhomogeneities which will lead to galaxies. For this reason this model with HDM has been rejected.

Another route which has been followed in the attempt to go beyond the pure CDM proposal is the possibility of having some form of warm DM (Avila-Reese *et al.*, 2001; Viel *et al.*, 2005). As will be underlined in the next chapters, this model has been considered also by different researcher to reduce the power of the matter power spectrum on small scales and so the number of substructures in simulated dark matter haloes (Colín *et al.*, 2000; Götz and Sommer-Larsen, 2002). From this side the debate is still opened.

CHAPTER

2

Structure Formation: Growth of Density Perturbations

After hydrogen *recombination*, neutral atoms start to form, and baryons become dynamically decoupled from radiation. As we shall see, dark matter density perturbations can grow already after the *equivalence* epoch z_{eq}, so that at *recombination* there exist dark matter fluctuations of order $\simeq 10^{-3}$ times the mean density. From now on, baryons are free to follow the gravitational pull of these dark matter linear perturbations. The amplitude of these fluctuations at all scales is an important constraint for galaxy-formation models, because it determines the times when cosmic structures will collapse and form, giving rise to various observational patterns like filaments, sheets and voids on different scales (Shen *et al.*, 2006; Hahn *et al.*, 2007).

2.1 Density perturbations in a Static Universe

Let us begin our study of density perturbation with the toy model of Newtonian perturbations in a static universe. This universe can be represented by a perfect fluid characterized by random fluctuations in density, velocity, pressure, entropy and gravitational potential around some mean values. The evolution of these fluctuations is calculated by considering the contrasting influence of self-gravity and random fluid velocities. Large enough overdense regions are gravitationally amplified and eventually grow into cosmic structures, depleting adjacent regions.

The time evolution of density, velocity, pressure, entropy and gravitational potential of a given volume element of a perfect fluid is described by the following equations:

1. *Continuity equation*:

$$\frac{\mathrm{d}\rho}{\mathrm{d}t} = -\rho\vec{\nabla}\cdot\vec{v}\,. \tag{2.1}$$

2. *Euler's equation*:

$$\frac{\mathrm{d}\vec{v}}{\mathrm{d}t} = -\frac{1}{\rho}\vec{\nabla}p - \vec{\nabla}\Phi\,. \tag{2.2}$$

3. *Poisson's equation*:
$$\nabla^2\Phi = 4\pi G\rho\,. \tag{2.3}$$

4. *Equation of state*:
$$p = p(\rho, S) = p(\rho)\,, \tag{2.4}$$
where the third equality holds for adiabatic systems: $\mathrm{d}S/\mathrm{d}t = 0$.

This system of equations admits a simple unperturbed solution of a *static, homogeneous* and *isotropic* universe: $\rho(t) = \bar{\rho}$, $\vec{v}(t) = 0$, $p(t) = \bar{p}$, $\phi(t) = \bar{\phi}$.

Let us define the local density $\rho(\vec{r}, t)$ at spatial coordinate $\vec{r}$ at some cosmic time t. The fractional departure at $\vec{r}$ from the spatial mean density $\bar{\rho}(t)$ is represented by the dimensionless *density contrast*:

$$\delta(\vec{r}, t) = \frac{\rho(\vec{r}, t) - \bar{\rho}(t)}{\bar{\rho}(t)}\,, \tag{2.5}$$

in linear approximation holds $\delta(\vec{r}, t) \ll 1$. Let us perturb the fields around the static solutions considering:

$$\begin{aligned}
\rho(\vec{r}, t) &= \bar{\rho}(t) + \delta\rho(\vec{r}, t)\,,\\
p(\vec{r}, t) &= \bar{p}(t) + \delta p(\vec{r}, t)\,,\\
\vec{v}(\vec{r}, t) &= \delta\vec{v}(\vec{r}, t)\,,\\
\phi(\vec{r}, t) &= \bar{\phi}(t) + \delta\phi(\vec{r}, t)\,.
\end{aligned}$$

Substituting these in the fluid equations, replacing pressure for density using the state equation, and subtracting the unperturbed solutions we obtain:

$$\begin{cases}
\dfrac{\partial\delta\rho}{\partial t} = -\bar{\rho}\vec{\nabla}\delta\vec{c}\\[2ex]
\dfrac{\partial\delta\vec{v}}{\delta t} = -\dfrac{v_s^2}{\bar{\rho}}\vec{\nabla}\delta\rho - \vec{\nabla}\delta\phi\\[2ex]
\nabla^2\delta\phi = 4\pi G\delta\rho.
\end{cases} \tag{2.6}$$

This system of equations admits plane wave solutions of type:

$$f(\vec{r}, t) = f_k \exp(i\vec{k}\cdot\vec{r} + i\omega t)\,. \tag{2.7}$$

where $k = 2\pi/\lambda$ is the wave number and f_k the amplitude. The (2.6) is in real space a system of linear differential equations in the variables $\delta(\vec{r}, t)$, $\delta\vec{v}(\vec{r}, t)$ and $\delta\Phi$.

Performing a Fourier decomposition, in the linear regime, ensures that waves of different frequencies evolve independently on each other, and so can be treated separately. A general perturbation is so given by a sum of plane waves of all frequencies, appropriately weighted.

It can be shown that the system of differential equations becomes in Fourier space a system of algebraic equations. The variables will be ω and k. Performing some algebraic calculations, these, in Fourier space, gives the following *dispersion relation*:

$$\omega^2 = k^2 v_s^2 + 4\pi G\bar{\rho}\,, \tag{2.8}$$

where v_s is the sound velocity in the fluid defined by

$$v_s = \sqrt{\left.\frac{\partial p}{\partial \rho}\right|_S}\,. \tag{2.9}$$

The value of k for which $\omega^2 = 0$ define the Jeans wave length $\lambda_J \equiv 2\pi/k_J$:

$$\begin{aligned} k_J &= \sqrt{\frac{4\pi G\bar{\rho}}{v_s^2}}\,, \\ \lambda_J &= v_s\sqrt{\frac{\pi}{G\bar{\rho}}}\,, \end{aligned} \tag{2.10}$$

which allow us to write ω as:

$$\omega^2 = k^2 v_s^2 \left[1 - \left(\frac{\lambda}{\lambda_J}\right)^2\right]. \tag{2.11}$$

Depending on the wave length value we can discriminate two cases:

- for $\lambda < \lambda_J$, ω is real and equal to:

  $$\omega = \pm k v_s \sqrt{1 - \left(\frac{\lambda}{\lambda_J}\right)^2}\,,$$

  and the density perturbation $\delta\rho$ is a couple of plane wave with fase velocity c_s:

  $$c_s = \pm v_s \sqrt{1 - \left(\frac{\lambda}{\lambda_J}\right)^2}\,, \tag{2.12}$$

  from the equation we see that when $\lambda \to 0$ the wave becomes a pure sonar wave, when if $\lambda \to \lambda_J$ the wave is *stationary*;

- for $\lambda > \lambda_J$, ω is imaginary and equal to:

  $$\omega = \pm i \sqrt{4\pi G\bar{\rho}\left[1 - \left(\frac{\lambda}{\lambda_J}\right)^2\right]}\,,$$

  in this case the wave is *stationary* and can be written as:

  $$\delta\rho(\vec{r}, t) = \delta\rho_k \mathrm{e}^{\pm|\omega|t}\, \mathrm{e}^{i\vec{k}\cdot\vec{r}}\,. \tag{2.13}$$

This last case described is called *gravitational instability*: a stationary wave with an amplitude that increase (or decrease) with time in an exponential way. The characteristic time of the instability is defined by

$$\tau = \frac{1}{\omega} = 1/\sqrt{4\pi G\bar{\rho}\left[1-\left(\frac{\lambda}{\lambda_J}\right)^2\right]}\,, \tag{2.14}$$

that for $\lambda \gg \lambda_J$ approach to the free-fall time. For $\lambda \to \lambda_J$, for the balance between pressure and gravity, $\tau \to +\infty$.

2.2 Density perturbations in an Expanding Universe

In principle, the evolution of density perturbations at all epochs and scales in an expanding universe requires solving the full set of Einstein's equations for a mixture of perturbed perfect fluids. However, we can still use the far simpler Newtonian approach if we restrict our attention to matter fluctuations, at epochs when the universe is matter dominated and at scales smaller than the particle horizon.

Let us define $\vec{r}$ and $\vec{x}$ as the physical and comoving coordinates in an expanding universe, respectively. If a represents the scale factor, then $\vec{r} = a\vec{x}$. The physical velocity is:

$$\vec{u} = \frac{\mathrm{d}\vec{r}}{\mathrm{d}t} = \dot{a}\vec{x} + a\dot{\vec{x}} = H\vec{r} + \vec{v}\,. \tag{2.15}$$

We see that this velocity is naturally split in two terms:

- $H\vec{r}$: *Hubble term* or *recession* velocity, due to the expansion of the universe;
- $\vec{v}$: *peculiar* velocity, due to the gravitational attraction of the surrounding matter.

In the comoving reference frame the *Hubble term* is by definition zero.

For a matter-dominated expanding universe the system of equations (2.6), written in the comoving reference frame, becomes:

$$\frac{\partial\delta}{\partial t} + \frac{\bar{\rho}}{a}\vec{\nabla}\vec{v} + 3H\delta = 0\,, \tag{2.16}$$

$$\frac{\partial}{\partial t}\vec{v} + H\vec{v} = -\frac{v_s^2}{a}\vec{\nabla}\delta - \frac{1}{a}\vec{\nabla}\phi\,, \tag{2.17}$$

$$\frac{1}{a^2}\nabla^2\phi = 4\pi G\bar{\rho}\delta\,. \tag{2.18}$$

These equations in Fourier space become respectively:

$$\dot{\delta}_k + \frac{i\vec{k}\vec{v}_k}{a} = 0\,, \tag{2.19}$$

$$\dot{\vec{v}}_k + \frac{\dot{a}}{a}\dot{\vec{v}}_k = -\frac{i\vec{k}}{a}(v_s^2\delta_k + \phi_k)\,, \tag{2.20}$$

$$\phi_k = -\frac{4\pi G\bar{\rho}\delta_k a^2}{k^2}\,. \tag{2.21}$$

Before we continue, notice that the velocity field $\vec{v}_k$ can be split in two components: $\vec{v}_{||}$ and $\vec{v}_{\perp}$, the first parallel to the wavevector $\vec{k}$ (longitudinal or irrotational term) and the second perpendicular to $\vec{k}$ (with null divergence). The component of Euler's equation perpendicular to $\vec{k}$ gives immediately $\vec{v}_{\perp} \propto a^{-1}$. This tells us that vorticity motions are decoupled from δ and decay. Combining together equations (2.19), (2.21) and the longitudinal part of (2.20) we obtain our final equation:

$$\ddot{\delta}_k + 2\frac{\dot{a}}{a}\dot{\delta}_k + \delta_k \left[\frac{k^2 v_s^2}{a^2} - 4\pi G\bar{\rho}\right] = 0. \tag{2.22}$$

In order to solve this second-order differential equation we need to explicitly write the time dependence of $a(t)$ and $\bar{\rho}(t)$.

Evolution of perturbations after the matter-radiation *equivalence*

Let us first consider the case of a closed matter universe after the *equivalence*. The evolution of scale factor and background density is given, respectively, by the following equations:

$$\bar{\rho} = \frac{1}{6G\pi t^2}, \tag{2.23}$$

$$a(t) = a_0 \left[\frac{3H_0 t}{2}\right]^{2/3}. \tag{2.24}$$

Substituting these in equation (2.22) and looking for solutions of type $\delta_k(t) \propto t^{\alpha}$ we obtain the following dispersion equation:

$$3\alpha^2 + \alpha + 2\left(\frac{k^2 v_s^2}{4\pi G\bar{\rho}} - 1\right) = 0. \tag{2.25}$$

As done in the previous section, we can define the Jeans scale by setting the discriminant of the equation to zero, that is:

$$k_J(t) = \frac{5}{v_s}\sqrt{\frac{\pi G\bar{\rho}}{6}}, \quad \text{and} \quad \lambda_J(t) \equiv \frac{1}{k_J(t)}. \tag{2.26}$$

For $\lambda < \lambda_J$ the solutions are imaginaries and correspond to progressive acoustic waves. For $\lambda > \lambda_J$ the solutions are real:

$$\delta_{\pm}(\vec{x}, t) = \delta_k(t)_{\pm} \exp(i\vec{k}\cdot\vec{r}) \propto \exp(i\vec{k}\cdot\vec{r})\, t^{\left[\frac{-1\pm 5\sqrt{1-(\lambda_J/\lambda)^2}}{6}\right]}. \tag{2.27}$$

In particular, when $\lambda \gg \lambda_J$ we obtain:

$$\delta_{\pm}(\vec{x}, t) \propto \exp(i\vec{k}\cdot\vec{r})\, t^{\frac{-1\pm 5}{6}}. \tag{2.28}$$

Notice that one solution is decaying with time, while the other, more interesting for us, is growing. The growing solution is the one relevant for structure formation:

$$\delta_{+}(\vec{x}, t) \propto t^{2/3} \propto a. \tag{2.29}$$

The above solution holds for Einstein-de Sitter universes. Solutions for matter-dominated universes of any geometry can be obtained by the following method. If we restrict our study to scales much larger than the Jeans scale, we can use the Hubble parameter $H(t)$ to study the evolution of density perturbations. From Friedmann's equations, and considering that $\dot{\bar{\rho}} = -3H\bar{\rho}$, we have:

$$\ddot{H} + 2H\dot{H} - 4\pi G\bar{\rho}H = 0\,. \tag{2.30}$$

A comparison of this equation with (2.22), show that the Hubble parameter evolves as density perturbations, that is $H(t) \propto \delta_k(t)$. However, since $H(t)$ decreases in all cases except for exponential expansion, the Hubble constant must behave as the decaying solution: $H(t) \propto \delta_-(t)$. We can find the growing solution by using the following property of differential equations: considering the two linearly independent solutions δ_- and δ_+ of equation (2.30, the following relation holds:

$$\delta_-\dot{\delta}_+ - \delta_+\dot{\delta}_- \propto \frac{1}{a^2}\,, \tag{2.31}$$

The growing solution will thus be given by:

$$\delta_+(t) = H(t)\int \frac{\mathrm{d}t}{a^2H^2(t)}\,; \tag{2.32}$$

changing variable from time t to redshift z, and substituting the time evolution of the Hubble parameter, we get:

$$\delta_+(z) = \frac{(1+z)\sqrt{1+\Omega_m z}}{(H_0a_0)^2}\int_z^\infty \frac{\mathrm{d}z}{(1+z)^2(1+\Omega_m z)^{3/2}}\,, \tag{2.33}$$

where Ω_m is the present-day matter density parameter. In Table 2.1 we summarize the solution of this equation for flat, open and close universes.

$\Omega_m = 1$	$t^{2/3}$
$\Omega_m < 1$	$1 + \frac{3}{x} + \frac{3\sqrt{1+x}}{x^{3/2}}\ln[\sqrt{1+x} - \sqrt{x}]$
$\Omega_m > 1$	$-1 + \frac{3}{x} - \frac{3\sqrt{1+x}}{x^{3/2}}[\arctan(\theta) - \eta]$

Table 2.1: Evolution of the density perturbation δ_+ in term of redshift for a matter dominated universe and the three different geometries. $x = |\Omega(z)^{-1} - 1|$, $\theta = \sqrt{x/(1-x)}$, while $\eta = 0$ for $0 < \theta < \pi$ and $\eta = \pi$ for $\pi < \theta < 2\pi$.

Evolution of perturbations before the *equivalence*

Let us first consider the case of a radiation-dominated universe. As we have shown in the previous chapter, this is a good approximation for our universe at $t < t_{eq}$. General Relativity calculations show that equation (2.22) becomes, for a relativistic fluid:

$$\ddot{\delta}_k + 2\frac{\dot{a}}{a}\dot{\delta}_k + \frac{\delta_k}{3}\left(\frac{k^2c^2}{a^2} - 32\pi G\bar{\rho}\right) = 0\,, \tag{2.34}$$

where we took $v_s = c/\sqrt{3}$ for the sound velocity. As in the previous section, we need to explicitly write the time evolution of $a(t)$ and $\bar{\rho}(t)$:

$$\begin{aligned} \bar{\rho}(t) &= \frac{3}{32\pi G t^2} & (2.35)\\ a(t) &\propto t^{1/2}. & (2.36) \end{aligned}$$

Substituting these in equation (2.34) we can write:

$$\ddot{\delta}_k + \frac{\dot{\delta}_k}{t} + \delta_k\left(\frac{k^2c^2}{3} - \frac{1}{t^2}\right) = 0\,. \tag{2.37}$$

This equation admits power-law solutions: $\delta \propto t^{\alpha}$; by replacing these in equation (2.34) and defining $\lambda_J = 2\pi v_s t = 2ct\frac{\pi}{\sqrt{3}}$, we obtain a dispersion equation whose solutions have discriminant

$$\alpha^2 = 1 - \left(\frac{\lambda_J}{\lambda}\right)^2.$$

Gravitational instability requires $\alpha^2 > 0$. However, for $t < t_{eq}$, the particle horizon $R_H(t) = 2ct$, so it turns out that $\lambda_J > R_H$: in a radiation-dominated universe the Jeans scale for radiation perturbations is larger than the particle horizon. This means that there cannot be gravitational instability within the horizon. We can physically understand this result noticing that the sound velocity of photons is of the order of the speed of light: for the acoustic waves propagating with a such speed, pressure is extremely efficient in erasing density perturbations. Before the *equivalence*, the universe is well described by an unperturbed distribution of matter: $\delta = \langle\delta_R\rangle \approx= 0$ where sound waves propagate at speed $c\sqrt{3}$.

Let us now consider the Newtonian evolution of fluctuations for a component which is not dominant. The appropriate equation is similar to (2.22), where now the gravitational potential term takes into account all sources of gravity; on the other hand, the kinetic term will contain the sound velocity of the component X we want to study. The generalization of the previous evolution equation will therefore be:

$$\ddot{\delta}_{k,X} + 2\frac{\dot{a}}{a}\dot{\delta}_{k,X} + k^2v_s^2\delta_{k,X} - \sum_i A_i\bar{\rho}_i\delta_{k,i} = 0\,. \tag{2.38}$$

Let us specialize this equation to the evolution of dark matter fluctuations during the radiation era ($X = DM$). Above the Jeans scale we can neglect the pressure term; moreover, the results previously obtained for radiation tells us that $\langle\delta_R\rangle \approx 0$; finally, since baryons are coupled to radiation, $\langle\delta_B\rangle \approx 0$. Our equation thus reduces to:

$$\ddot{\delta}_{k,DM} + 2\frac{\dot{a}}{a}\dot{\delta}_{k,DM} - 4\pi G\bar{\rho}_{DM}\delta_{k,DM} = 0 \tag{2.39}$$

Using Friedmann's equations, we can rewrite this as:

$$\delta''_k + \frac{(2+3x)}{2x(1+x)}\delta'_k - \frac{3}{2x(1+x)}\delta_k = 0\,, \tag{2.40}$$

where $x = a/a_{eq}$ and $'$ indicates the derivative respect to this variable.

It is possible to show (Mezsaros, 1974) that this equation has a growing solution of the form:

$$\delta_{k,DM_+} = 1 + \frac{3}{2}x = 1 + \frac{3}{2}\frac{a}{a_{eq}}\,. \tag{2.41}$$

This shows that dark matter perturbations, from their entry in the cosmological horizon, will grow at most by a factor 5/2. This stagnation (or Mezsaros) effect is responsible for the shape of the spectrum of matter density fluctuations at small scales.

Evolution of baryonic perturbations after *decoupling*

We have seen that in the universe before *decoupling* no baryon perturbation can grow, and that the structure formation process is driven by dark matter density perturbations that start growing after the *equivalence*. From present-day observations we know that galaxies are systems composed by both dark matter and baryons. We study the evolution of the baryon perturbations by considering equation (2.38) at $t > t_{dec}$, with $X = b$ (for baryons):

$$\ddot{\delta}_{k,b} = +2\frac{\dot{a}}{a}\dot{\delta}_{k,b} - 4\pi G\rho_{k,DM} = 0\,, \tag{2.42}$$

where the gravitational potential term is dominated by dark matter fluctuations. Assuming for simplicity an Einstein-de Sitter universe (an excellent approximation at high redshifts), and proceeding as done before, we can arrive at the solution:

$$\delta_b(a) = \delta_{DM}\left(1 - \frac{a_{dec}}{a}\right)\,. \tag{2.43}$$

This shows that, after *decoupling*, baryon fluctuations undergo an accelerated growth due to the gravitational attraction of dark matter perturbations. For this reason, baryon perturbations soon become as large as the dark matter ones.

CHAPTER

3

Excursion Set Theory: Mass Function of Dark Matter Haloes

As discussed in the previous chapter, in the standard hierarchical cold dark matter (CDM) paradigm, galaxy formation begins with the gravitational collapse of dark matter overdense regions. Once their enclosed density will exceed some critical value they will collapse forming dark matter haloes as we will see in the following chapter. The average density of dark matter haloes out-weighs that of baryonic matter by roughly six to one. Bound in the potential wells of dark matter haloes, baryons proceed to cool, condense, and form galaxies (White and Rees, 1978). Understanding the fundamental properties and abundances of these dark matter haloes is the first, necessary step in understanding the properties of galaxies along the cosmic time.

3.1 Random Fields

Let consider the density fluctuation field $\delta(\vec{x})$:

$$\delta(\vec{x}) = \frac{\rho(\vec{x}) - \bar{\rho}}{\bar{\rho}}, \tag{3.1}$$

where we remember that $\bar{\rho}$ represent the mean mass density of the universe and $\vec{x}$ the comoving spatial coordinate. Statistically the density field $\delta(\vec{x})$ is stochastic, homogeneous and isotropic. This means that the joint probability distribution of the density contrast, in a given set of points of the space, is given by a multivariate Gaussian distribution. This has the property that the joint probability density of a finite number of points is invariant under translation, rotation and reflection[1]. The universe we observe is so a statistical realization of the stochastic density field $\delta(\vec{x})$. The Fourier transform of the density contrast is given by the following equation:

$$\delta(\vec{k}) = \int \mathrm{d}\vec{x}\, \delta(\vec{x})\, \mathrm{e}^{i\vec{k}\cdot\vec{x}}, \tag{3.2}$$

---

[1] The *ergodicity* of a Gaussian field also gives that the temporal mean of the field in a region, is equal to the spatial mean, at a given time, computed in different regions.

and the inverse transform by:

$$\delta(\vec{x}) = \frac{1}{(2\pi)^3}\int \mathrm{d}\vec{k}\,\delta(\vec{k})\,\mathrm{e}^{-i\vec{k}\cdot\vec{x}}. \tag{3.3}$$

It is interesting remember that $\delta(\vec{k})$ has dimensions of volume and that for a field with real variable $\delta(\vec{x})$: $\delta(-\vec{k}) = \delta^*(\vec{k})$. In terms of Fourier coefficients, it is possible to define the two-point correlation function $\xi(\vec{r}) \equiv \langle\delta(\vec{x})\delta(\vec{x}+\vec{r})\rangle$, where the average taken over all space gives:

$$\xi(\vec{r}) = \frac{1}{(2\pi)^6}\int \mathrm{d}k^3 \int \mathrm{d}k'^3 \langle\delta(\vec{k})\delta(\vec{k}')\rangle\,\mathrm{e}^{i\vec{k}\cdot(\vec{x}+\vec{r})}\mathrm{e}^{i\vec{k}'\cdot\vec{x}}, \tag{3.4}$$

and the Power Spectrum of density fluctuations will be:

$$P(k) = \frac{1}{(2\pi)^3\delta_D^{(3)}(\vec{k}-\vec{k}')}\langle\delta(\vec{k})\delta(\vec{k}')\rangle, \tag{3.5}$$

where $\delta_D^{(3)}$ represents the 3-dim Dirac Delta function. Substituting this definition in equation (3.4), and considering that the two-point function depends only on the amplitude $\vec{r}$, we can write:

$$\xi(r) = \frac{1}{(2\pi)^3}\int P(k)\mathrm{e}^{i\vec{k}\cdot\vec{r}}\mathrm{d}^3k, \tag{3.6}$$

which shows that the power spectrum of the density perturbation is the Fourier transform of the two-point correlation function, and that for the isotropy condition does not depends on the direction.

Considering the definition of the 3-dim Dirac Delta

$$\delta_D^{(3)}(0) = \frac{V_\infty}{(2\pi)^3}$$

where V_∞ represents the volume of a large cut-off scale $L \equiv V^{1/3}$, it follows that:

$$\langle|\delta(\vec{k})|^2\rangle = P(k)V_\infty, \tag{3.7}$$

from which we have that the power spectrum has dimensions of volume, while the correlation function $\langle\delta^2(\vec{x})\rangle$ is simply the mass variance of the considered region: $\sigma \equiv \langle\delta^2(\vec{x})\rangle$.

In the observable universe a quantity of physical interest is the density fluctuations field smoothed on a given scale:

$$\delta(\vec{x},R) \equiv \int \mathrm{d}^3x'\,W(|\vec{x}'-\vec{x}|,R)\delta(\vec{x}'), \tag{3.8}$$

where $W(x,R)$ represents the window function that weights the density field on a scale R. In Fourier space the smoothed field is the product between the Fourier transform of the density field and that of the window function $W(\vec{k}, R)$. The mass variance of a region of universe with mass M, with linear size R, is given by:

$$S(M) = \sigma_M^2 = \frac{1}{(2\pi)^3 V} \int \mathrm{d}^3 k \langle |\delta(k)|^2 \rangle W^2(k, R) \,. \tag{3.9}$$

From the previous equation we see that the definition of collapsed region and mass variance depend on the window function considered. The most common window functions used in literature are:

- **the top-hat in real space**

  $$W(x, R) = \frac{3}{4\pi R^3} \begin{cases} 1 & (x \leq R) \\ 0 & (x > R) \end{cases}$$

  the window volume is simply the volume of a sphere with radius R and the Fourier transform is given by

  $$W(k, R) = \frac{3[\sin(kR) - kR\cos(kR)]}{(kR)^3} \,,$$

  the sharp transition of the function in real space leads to power on all scale in Fourier space;

- **the top-hat in Fourier space**

  $$W(k, R) = \begin{cases} 1 & (k \leq R^{-1}) \\ 0 & (k > R^{-1}) \end{cases}$$

  and in the real space

  $$W(x, R) = \frac{1}{2\pi^2 R^3} \frac{3[\sin(xR^{-1}) - xR^{-1}\cos(xR^{-1})]}{(xR^{-1})^3} \,.$$

  Contrarily to the previous case, this function has the disadvantage to not have a well-defined volume in the real space;

- **the Gaussian window in real space**

  $$W(x, R) = \frac{1}{(2\pi)^{3/2} R^3} \mathrm{e}^{-x^2/2R^2} \tag{3.10}$$

  and in the Fourier space

  $$W(k, R) = \mathrm{e}^{-k^2 R^2/2} \,, \tag{3.11}$$

  from which we see that the volume of the Gaussian window function is equal to $V = (2\pi)^{3/2} R^3$.

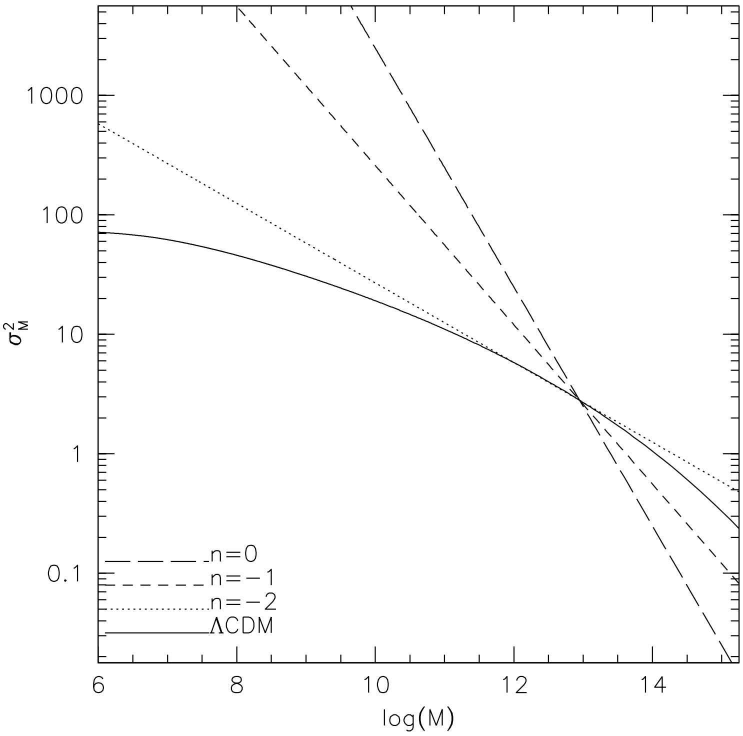

Figure 3.1: Mass variance of virialized regions in term of their mass. For the ΛCDM power spectrum the mass variance has been computed using a top-hat window function in the real space. The primordial power spectrum considered has a spectral index $n = 1$ and has been evolved with a transfer function computed using CMBFAST. For the scale free power spectrum $P(k) \sim k^n$ with $n = -2, -1, 0$ the mass variance has been normalized the have the same value of M^*.

The initial perturbed density field and its power spectrum evolve with the cosmic time because of the growth of the cosmological horizon. Larger R_H causally connect regions of universe on larger scale, on which the physical processes can take place. It is possible to show that for CDM cosmology, the power spectrum at some redshift z_{fin} can be written in term of the the initial one at z_{in} as follow:

$$P_{fin}(k) = k^n T^2(k) \left[\frac{D(z_{fin})}{D(z_{in})} \right]^2 , \tag{3.12}$$

where $D(z)$ is the linear growth factor of density perturbations and $T(k)$ is the transfer function defined as:

$$T(k) \equiv \frac{\delta(k, z_{fin})}{\delta(k, z_{in})} \frac{D(z_{in})}{D(z_{fin})} . \tag{3.13}$$

In Figure 3.1 we plot the mass variance versus the mass of virialized regions. The solid curve corresponds to a ΛCDM power spectrum where we considered a primordial power spectrum with $n = 1$. The transfer function has been calculated with CMBAST (Seljak and Zaldarriaga, 1996) for a flat ΛCDM universe with:

$\Omega_m = 0.3$, $\Omega_b h^2 = 0.0196$, $\sigma_8 = 0.9$ $\lambda = 0.7$ and $h = 0.7$. CMBFAST is a code for computing cosmic microwave background anisotropy, polarization and matter power spectra, it has been tested over a wide range of cosmological parameters and many publications are available in literature. In the figure we shown also the mass variance for tree scale free power spectrum $P(k) \sim k^n$ with $n = -2, -1, 0$. The correspondent mass variances have been normalized to have the same value of M^*, defined as $\sigma^2_{M^*} \equiv \delta^2_{sc}(0)$ where $\delta_{sc}(0)$ is the spherical collapse overdensity at the present time, $z = 0$, that will be introduced in the next section. The mass variance has been computed considering a top-hat window function in real space. The use of this function is related to the fact that we will define in numerical simulations (see the next chapter) dark matter haloes as spherical and overdense regions.

3.2 Mass Function of Dark Matter Haloes: The Spherical Collapse Model

In the previous chapter we have seen that in an expanding universe the dark matter density perturbations grow with cosmic time, depending on the geometry of the universe. As they become enough large they stop growing and collapse forming virialized regions that we will call dark matter haloes. The collapse of dark matter haloes can be elegantly and easily described considering a spherical model.

Let consider an initial region with comoving Lagrangian size R_0 and initial density δ_i, let suppose that the initial fluctuations are Gaussian distributed around the mean and that the root mean square is such that $|\delta_i| \ll 1$. The mass within the region R_0 is defined by:

$$M_0 = \frac{4}{3}\pi R_0^3 \bar{\rho}(1+\delta_i) \approx \frac{4}{3}\pi R_0^3 \bar{\rho}\,.$$

As the universe expand the Lagrangian dimension of the region changes. In the case of an Einstein-de Sitter universe, the evolution of the dimensions of the collapsing region can be easily calculated, and is expressed by the following parametric equation:

$$\begin{aligned} \frac{R(z)}{R_0} \equiv \frac{1}{(1+\delta(z))^{1/3}} &= \frac{(1+z)}{(5/3)|\delta_0|}\frac{(1-\cos\theta)}{2}\,, \\ \frac{1}{1+z} &= \left(\frac{3}{4}\right)^{2/3}\frac{(\theta-\sin\theta)^{2/3}}{(5/3)|\delta_0|} \\ \frac{R(z)}{R_0} &= \frac{2}{6^{2/3}}\frac{(1-\cos\theta)}{(\theta-\sin\theta)^{2/3}}\,, \end{aligned} \tag{3.14}$$

where δ_0 represents the initial overdensity extrapolated to the present time using linear theory.

Assuming spherical symmetry, from equation (3.14) we notice that the collapse of a region is characterized by tree different fases, these are:

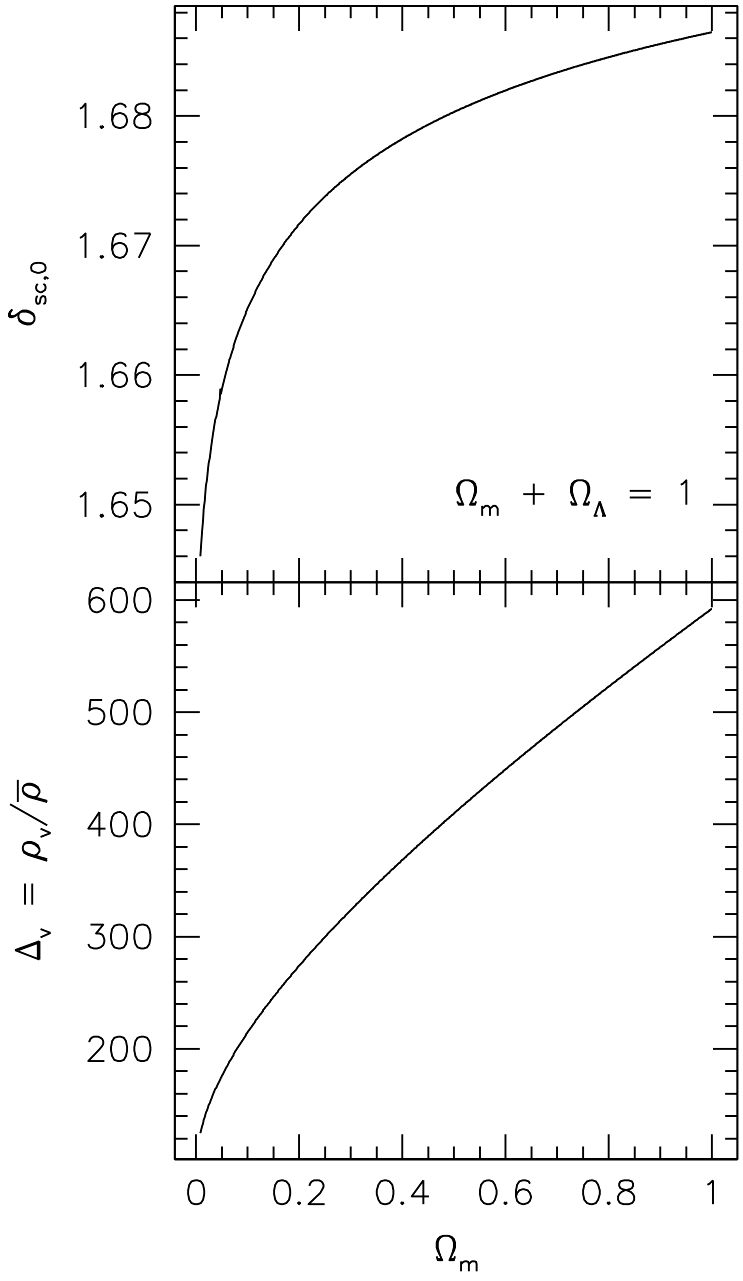

Figure 3.2: **Top**: initial critical spherical overdensity, linearly extrapolated to the present time in term of the matter density parameter. **Bottom**: virial overdensity versus matter density parameter for a flat ΛCDM universe (see Eke *et al.* (1996) for more details). In the bottom panel we notice that that for an closed universe with $\Omega_m = 0.3$ at the present time the virial overdensity is of the order of $324\,\bar{\rho}$.

- $\theta = 0$ at start,
- $\theta = \pi$ at turnaround,

- $\theta = 2\pi$ at collapse.

The equation (3.14) shows that at turnaround the average density within the region is about 5.55 times that of the background universe. We notice also that collapse formally we expect $R_c = 0$. However in practice the region does not collapse to a vanishingly small size. The virial density can be estimated assuming that at the virialization $R_v = R_{ta}/2$, so the object is eight times denser than it was at turnaround. Because the universe from turnaround to collapse expands of a factor $(1+z_{ta})/(1+z_c) = 2^{2/3}$, the virialized object is $\Delta_v = (9\pi^2/16) \times 8 \times 4 = 18\pi^2$ times the density of the background, in an Einstein-de Sitter universe.

From the equation (3.14) can also be estimated the overdensity that must have a region to collapse at redshift z, that is:

$$\frac{\delta_{sc}(z)}{(1+z)} = \frac{3}{5}\left(\frac{3\pi}{2}\right)^{2/3} . \tag{3.15}$$

The previous equations show a very important result for the spherical collapse model: the relation between the actual density δ and that provided by the linear theory $\delta_{sc,0}$ is the same for all R_0. This, because of the mass is proportional to R_0^3, implies that the critical overdensity for collapse δ_{sc} is the same for all objects, whatever their mass. Eke *et al.* (1996), performing the same calculations considering a flat ΛCDM universe, computed that the virial overdensity of virialized objects. The model shows that at the present time the virial overdensity of dark matter haloes is of the order of 324 times the mean background density (see Figure 3.2). In Figure 3.2 we show the behaviour of the spherical collapse overdensity and virial overdensity in term of the matter density parameter and closed universe from the model of Eke *et al.* (1996). We notice that when $\Omega_m = 0.3$, $\delta_{sc,0} = 1.676$.

The fraction of smoothed density perturbations, on a scale R, bigger than the critical value $\delta_{sc}(z)$ at a redshift z, gives the mass function of virialized dark matter haloes. The number of collapsed objects can be studied in the excursion set approach. In this, the density perturbation field can be represented by a sample of random walks in the plane ($s = \sigma_M^2, \delta$) that start from the origin of the reference frame. The mass fraction in virialized haloes will thus be represented by the trajectories that cross for the first time the critical overdensity $\delta_{sc}(z)$, when z is fixed, (see Bond *et al.* (1991)).

Excursion Set: Mass Function of Virialized Haloes

Let us now show how the virialized dark matter halo mass function can be estimated using the excursion set approach. As said, the density field is represented by Brownian walks in the plane (s, δ), starting from $(0, 0)$. In the left panel of Figure 3.3 we shown a sample of random walks.

The Brownian motion of a trajectory is mathematically described by the fol-

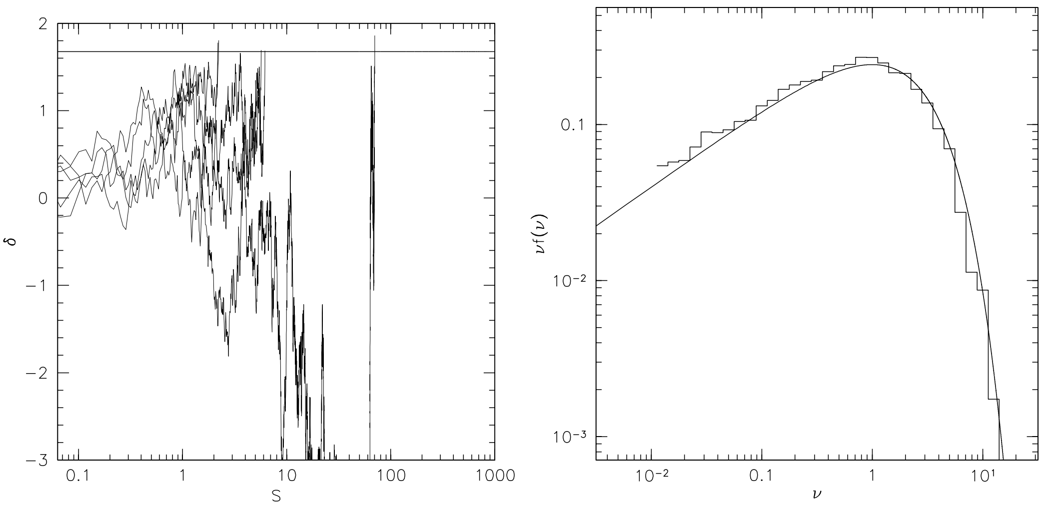

Figure 3.3: **Left**: unconditional random walks that up-cross a constant barrier, representing the spherical collapse overdensity at the present time. **Right**: distribution of the fraction of walks that up-cross the barrier. The histogram is a result of 10^4 random walks, the solid line is the mass function of collapsed object expressed in term of $\nu = \delta_{sc}^2/S$.

lowing diffusion equation:

$$\frac{\partial Q(s,\delta)}{\partial s} = \frac{1}{2}\frac{\partial^2 Q(s,\delta)}{\partial \delta^2}, \tag{3.16}$$

where $Q(s,\delta)$ represents the probability distribution that a trajectory in s has value δ. For Brownian walks the solution of the diffusion equation, and so compute what is the distribution in S for walks that have $\delta = \delta_{sc}$, is a Gaussian function of the form:

$$Q(S,\delta_{sc}) = \frac{1}{\sqrt{2\pi S}} \exp\left(-\frac{\delta_{sc}^2}{2S}\right). \tag{3.17}$$

This kind of approach proposes to re-formulate the Press and Schechter (1974) model using Brownian walks in the plane (s,δ) (Bond *et al.*, 1991): trajectories that, starting from the origin, up-cross for the first time $\delta = \delta_{sc}(z)$, at the abscissa S, correspond to virialized dark matter haloes of mass M, where S .

Computing the mass function means count, at a fixed cosmic time z, the fraction of trajectories that go over δ_{sc}. It is necessary to remember that given the power spectrum, s does not correspond only to a mass m, but also to a scale k. Fixing the redshift z, in a given $\tilde{s}$ we could have three different kinds of trajectories:

- (a) those that have crossed δ_{sc} and that are still over the barrier;
- (b) those that are under δ_{sc} but have crossed the barrier at $S < s_f$;
- (c) those that have been always under the barrier.

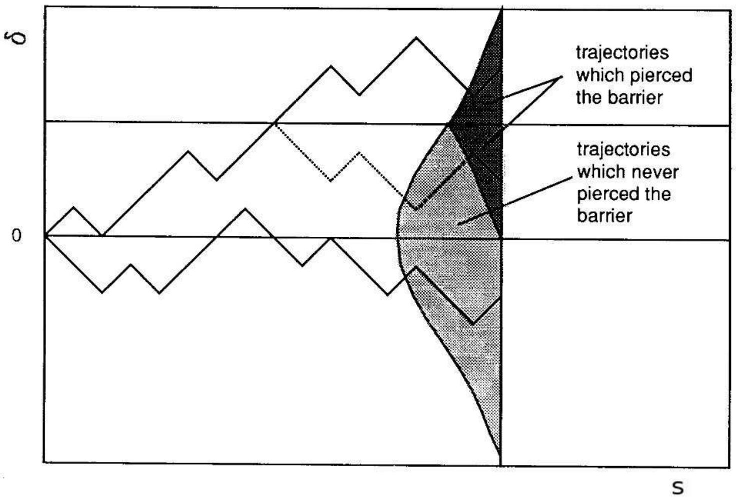

Figure 3.4: Random walks associated with the three probability (a), (b) and (c). See the main text for more details.

As first step, let compute the fraction of trajectories that are still under the barrier, case (c): to all trajectories that are under the barrier we have to subtract that oh kind (b). Considering that for a given walk of kind (b) there is another one, virtual-kind (reflecting barrier: Chandrasekhar (1943)), that starting from $(0, 2\delta_{sc})$ intersect the barrier at the same point (see Figure 3.4, for a schematic representation of the three kind of barriers), satisfying always the equation (3.16), the probability associated with walks (b)-kind is:

$$Q_b(\delta, s, \delta_{sc})\mathrm{d}\delta = \frac{1}{\sqrt{2\pi s}} \exp\left[-\frac{(\delta - 2\delta_{sc})^2}{2s}\right]\mathrm{d}\delta\,. \tag{3.18}$$

The probability for (c)-kind walks will so be:

$$\begin{aligned} Q_c(\delta, s, \delta_{sc})\mathrm{d}\delta &= [Q(\delta, s, \delta_{sc}) - Q_b(\delta, s, \delta_{sc})]\mathrm{d}\delta \\ &= \frac{1}{\sqrt{2\pi s}}\left\{\exp\left(-\frac{\delta^2}{2s}\right) - \exp\left[-\frac{(\delta - 2\delta_{sc})^2}{2s}\right]\right\}\mathrm{d}\delta\,. \end{aligned} \tag{3.19}$$

From this equation we can write the cumulative fraction of trajectories that have never crossed the barrier δ_{sc} as:

$$P_c(s, \delta_{sc}) = \int_{-\infty}^{\delta_{sc}} Q_c(\delta, s, \delta_{sc})\mathrm{d}\delta\,. \tag{3.20}$$

The complementary of this will represent the walks that have intersected the barrier (that cosmologically represents the fraction of elements in collapsed objects with mass variance less than s), that is

$$P_{a,b}(s, \delta) = 1 - P_c(s, \delta_{sc}) = P(< s)\,, \tag{3.21}$$

and the differential distribution:

$$p(s,\delta_{sc}) = \frac{\partial P(<s)}{\partial s} = -\frac{\partial}{\partial s}\int_{-\infty}^{\delta_{sc}} Q_c(\delta,s,\delta_{sc})\mathrm{d}\delta\,, \tag{3.22}$$

that, considering the diffusion equation (3.16) for (c)-kind trajectories, becomes

$$\begin{aligned} p(s,\delta_{sc}) &= -\frac{1}{2}\frac{\partial Q_c}{\partial \delta}\bigg|_{-\infty}^{\delta_{sc}} \\ &= \frac{\delta_{sc}}{\sqrt{2\pi}s^{3/2}}\exp\left(-\frac{\delta_{sc}^2}{2s}\right). \end{aligned} \tag{3.23}$$

In order to show the consistency of this argumentation we show on the right panel of Figure 3.3 the fraction of walks that cross the value $\delta_{sc,0}$. The distribution has been plotted in term of the rescaled variable $\nu = \delta_{sc}^2/s$, considering 10^4 random walk realizations. The solid line is the equation (3.23) expressed in term of power spectrum independent variable ν, that is:

$$\nu f(\nu) = \sqrt{\frac{\nu}{2\pi}}\exp\left(-\frac{\nu}{2}\right). \tag{3.24}$$

This equation has been formulated for the first time by Press and Schechter (1974) studying the formation of "self gravitating" masses and their evolution during the cosmic time in order to form galaxies and clusters of galaxies at the present time. The mass function can so be written in term of m as follow:

$$m^2\frac{n(m,z)}{\bar{\rho}} = \nu f(\nu)\frac{\mathrm{d}\ln(\nu)}{\mathrm{d}\ln(m)}\,. \tag{3.25}$$

3.3 The Ellipsoidal Collapse Model

4.3 The spherical collapse model allows to predict the shape and evolution of the mass function of dark matter haloes assuming the initial fluctuations small and Gaussian. However, as we will show in the next chapter, when this mass function is compared to the results of N-Body simulations it underpredicts the abundance of large mass virialized objects and overpredicts the small ones (Sheth *et al.*, 2001; Sheth and Tormen, 2002). Sheth *et al.* (2001) showed that these discrepancies can be interpreted considering that the dark matter haloes do not collapse spherically, depending on the surrounding tidal field and initial overdensity, ellipsoidally. In Gaussian random fields, the distribution of these quantities depends on the size of considered region. Since the mass of a region is related to its initial size, there is a relation between the density threshold value required for collapse and the mass of the final object (Sheth *et al.*, 2001). In excursion set approach the shape of the barrier that random walks have to cross in order to generate virialized object, is not constant but depends on mass. Let $B(s,\delta_{sc})$ a general shape for this kind of barrier where $s = s(m)$ and $\delta_{sc}(z)$. Inverting the relation between δ_{sc} and z, we see δ_{sc} can be used as time variable.

The gravitational collapse of homogeneous ellipsoids has been studied by Icke (1973); White and Silk (1979); Barrow and Silk (1981); Lemson (1993); Eisenstein and Loeb (1995). Sheth *et al.* (2001), considering the evolution of the initial shear field (Bond and Myers, 1996) and defining the virialization of a dark matter halo, in the ellipsoidal collapse model, when the third axis collapses. They determined the evolution of an ellipsoidal perturbation in term of the eigenvalues of the deformation tensor: the initial ellipticity e, prolateness p and the density contrast δ_{sc} (which, as we said, is interpreted as a time variable).

On average in a Gaussian field, $p = 0$, so the associated overdensity will depend on e and z: $B(e, z)$. Relating the ellipticity e to the mass m of the collapsing object, the shape of the barrier can be written as:

$$B(m,z) = \delta_{sc}(z)\left\{1+\beta\left[\frac{s(m)}{\delta_{sc}^2(z)}\right]^{\gamma}\right\}. \tag{3.26}$$

Notice that the power spectrum enters only in the relation between s and m, whereas the effects of cosmology enter in the relation between δ_{sc} and z.

The equation (3.26) is extremely useful because it allows one to include the effects of ellipsoidal collapse into the Bond *et al.* (1991) excursion set model in a straightforward manner. The distribution of first crossing of this barrier, by independent random walks, gives an estimate of the mass function of dark matter haloes associated with ellipsoidal collapse.

In order to compare dark matter halo mass function in N-Body simulations and that associated with the barrier in equation (3.26) it is necessary to introduce a calibration factor q that depends on how haloes are identified in numerical simulations. Thus, more generally the ellipsoidal collapse barrier can be written as:

$$B(s,\delta_{sc}) = \sqrt{q}\delta_{sc}\left[1+\beta\left(\frac{s}{q\delta_{sc}^2}\right)^{\gamma}\right], \tag{3.27}$$

where $\beta = 0.5$ and $\gamma = 0.7$ have been estimated studying the collapse of ellipsoids in numerical simulations by Sheth *et al.* (2001), while $q = 0.707$ is the normalization factor to the dark matter halo mass function of N-Body simulations. For general value of β and γ, the barrier 3.27 does not admit an exact solution. However Sheth and Tormen (2002), following the approach of Sheth (1998) that computed the probability of first crossing of a linear barrier, suggested an approximated equation for the probability of first crossing an ellipsoidal collapse barrier (eq. 3.27, which works rather well for a wide range of moving barrier shape $B(s, \delta_{sc})$, that is:

$$f_B(s,\delta_{sc})\mathrm{d}s = \frac{|T(s)|}{\sqrt{2\pi}s^{3/2}}\exp\left[-\frac{B^2(s,\delta_{sc})}{2s}\right]\mathrm{d}s, \tag{3.28}$$

where $T(s)$ denotes the sum of the first six terms in the Taylor series expansion of the barrier:

$$T(s) = \sum_{n=0}^{5}\frac{(-s)^n}{n!}\frac{\partial^n B(s,\delta_{sc})}{\partial s^n}. \tag{3.29}$$

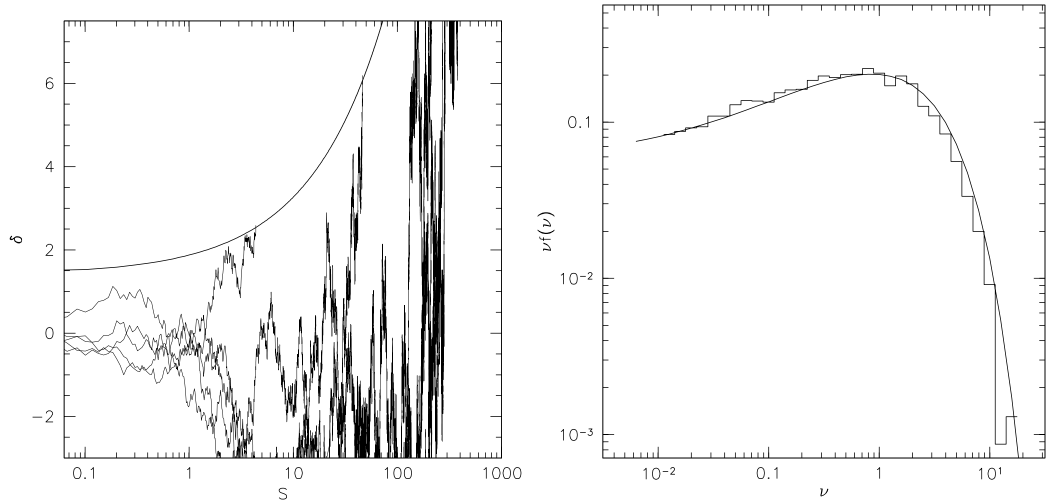

Figure 3.5: **Left**: unconditional random walks absorbed by the ellipsoidal collapse barrier (Sheth *et al.*, 2001) ($q = 0.707$, $\beta = 0.5$, $\gamma = 0.6$) with $\delta_{sc} = \delta_{sc}(z = 0)$. **Right**: fraction of walks that up-cross the ellipsoidal collapse barrier. The histogram is a result of 10^4 random walks realization, the solid line is the ellipsoidal collapse mass function expressed in term of $\nu = \delta_{sc}^2/S$ (eq. 3.28).

In Figure 3.5 we plot a sample of uncorrelated walks absorbed by the ellipsoidal barrier. On the left panel the histogram shows the fraction of walks that cross the barrier over a sample of 10^4 realizations. The solid line is the approximated solution to the ellipsoidal collapse barrier proposed by Sheth and Tormen (2002), in perfect agreement with the numerical realizations.

Square-root Barrier: Exact Solutions

As said, the probability of first crossing distribution a moving barrier for general β and γ does not admit exact solutions. However there is a particular case for which an exact solution can be computed, the square-root case:

$$B(s, \delta_{sc}) = \sqrt{q}\delta_{sc}\left(1 + \beta\frac{\sqrt{s}}{\sqrt{q}\delta_{sc}}\right). \tag{3.30}$$

For simplicity, we set $q = 1$ hereafter (it can always be reintroduced at the end), and by virtue of $\gamma = 1/2$, the coefficient of s^γ is z-independent:

$$B(s, z) = \delta_{sc}(z) + \beta\sqrt{s}. \tag{3.31}$$

The exact solution presented here was first envisaged by Breiman (1967) and then implemented by Mahmood and Rajesh (2005), for dark matter haloes.

To compute the solution of first crossing distribution, we need to solve $Q(\delta, S)$, that is the density of walks at (S, δ). We know that this quantity obeys the diffusion equation (eq. 3.16).

The problem to solve is to compute the distribution in walks that emanating from $(0,0)$ are later absorbed by $B(s,\delta_{sc})$ between S and $S+\mathrm{d}S$. By absorption we mean that $Q(S,\delta)$ obeys Dirichlet boundary conditions on the barrier:

$$Q(S,\delta=\delta_{sc}+\beta\sqrt{S})=0\,. \tag{3.32}$$

Since $Q(S,\delta)$ is a normalizable distribution, we expect it and its derivatives to go to zero at infinity. Finally, since when $S=0$ all walks are for certain at $\delta=0$ and nowhere else, the following boundary condition must hold:

$$Q(S=0,\delta)=\delta_D(\delta=0)\,. \tag{3.33}$$

Solving equation (3.16) subjected to the boundary conditions in (3.32) and (3.33) allow to compute the fraction of walks absorbed by the barrier:

$$f(S)\mathrm{d}S=-\mathrm{d}S\frac{\partial}{\partial S}\int_{-\infty}^{B(S)}Q(S,\delta)\mathrm{d}\delta\,. \tag{3.34}$$

When a problem involving diffusion and barriers is encountered, it's convenient to work in terms of the distance to the barrier, let us define $x=B(S)-\delta$ (shifted barrier case). In these coordinates, equation (3.34) becomes:

$$f(S)\mathrm{d}S=-\mathrm{d}S\frac{\partial}{\partial S}\int_{0}^{+\infty}Q(S,\delta)\mathrm{d}\delta\,, \tag{3.35}$$

while the diffusion equation:

$$\frac{\partial Q(S,x)}{\partial S}+\frac{\beta}{2\sqrt{S}}\frac{\partial Q(S,x)}{\partial x}=\frac{1}{2}\frac{\partial^2 Q(S,x)}{\partial x^2}\,. \tag{3.36}$$

The boundary condition on the barrier gives

$$Q(S,x=0)=0\,, \tag{3.37}$$

while at the origin:

$$Q(S=0,x)=\delta_D(x-\delta_{sc})\,. \tag{3.38}$$

$Q(S,x)$ and its derivatives are null at infinity here too.

Making some changes of variable, it is possible to show that the diffusion equation, considering a square-root barrier can be written as:

$$D''(\zeta)+\left(\lambda+\frac{1}{2}-\frac{\zeta^2}{4}\right)D(\zeta)=0\,. \tag{3.39}$$

This is the Webber differential equation, whose solutions are the parabolic cylinder functions $D_\lambda(\zeta)$. Two properties that will prove to be useful are:

- orthogonality:

$$\int_{-\beta}^{+\infty}D_\lambda(\zeta)D_{\lambda'}(\zeta)\mathrm{d}\zeta\equiv\delta_{\lambda\lambda'}I_\lambda(-\beta)\,, \tag{3.40}$$

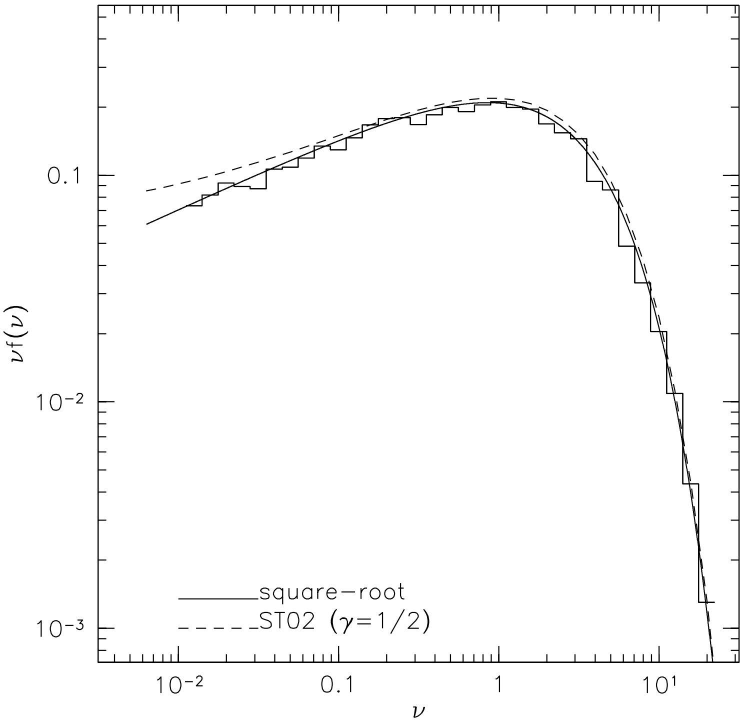

Figure 3.6: Unconditional probability of first crossing distribution of a square-root barrier. The histogram has been obtained generating 10^4 random walks and computing the mass variance s at which they cross the square-root barrier (eq. 3.30) for the first time. The solid line is the exact solution (eq. 3.44) while the dashed is the Sheth and Tormen (2002) equation using the parameter γ, β and q for the square-root case.

- asymptotic limit:

$$\lim_{\zeta\to\infty} D_\lambda(\zeta) = \zeta^\lambda e^{-\zeta^2/4}\left[1+O\left(\frac{1}{\zeta}\right)\right]. \tag{3.41}$$

The solution to the diffusion equation can be written as a sum of the eigenfunctions:

$$Q(S,\zeta) = \sum_{\{\lambda\}} A_\lambda \Theta_\lambda(S) D_\lambda(\zeta) e^{-\zeta^2/4}. \tag{3.42}$$

where the eigenvalues $\{\lambda\}$ and the A_λ coefficients are fixed by the boundary conditions.

The boundary condition on the barrier given by (3.37) fixes the eigenvalues:

$$D_\lambda(-\beta) = 0. \tag{3.43}$$

Using the properties of the parabolic cylinder function, the unconditional crossing distribution is given by

$$f_{sr}(s,\delta_{sc})\mathrm{d}s = \frac{e^{-\beta^2/4}}{2}\sum_{\{\lambda\}}\left(\frac{\delta_{sc}^2}{s}\right)^{\frac{\lambda}{2}} \frac{D'_\lambda(-\beta)}{I_\lambda(-\beta)}\frac{\mathrm{d}s}{s}, \tag{3.44}$$

where $D'_\lambda(\xi)$ is the derivative of the parabolic cylinder function and

$$I_\lambda(\xi) = \int_\xi^\infty D_\lambda^2(\zeta)\mathrm{d}\zeta\,.$$

It can be shown that this reduce to the constant barrier counterparts as β goes to zero. Mahmood and Rajesh (2005) comparing the this first crossing distribution with N-Body simulations found the best fit for the normalization factor $q \approx 0.55$. The three parameter to use in the equation (3.27) that define a square-root barrier normalized to N-Body mass function are so $\gamma = 1/2$, $\beta = 0.5$ and $q = 0.55$.

CHAPTER

4

Cosmological *N*-Body Simulations & Re-simulations

The non-linearity of the equations of the density perturbations require numerical calculations to follow their evolution during the cosmic time. In the last half century cosmologists, or more in general astrophysicists, have developed different computational technique to reproduce the evolution of the structures in the universe. Even that these techniques require a lot of computational resources, they are able to reproduce quite well the large scale structures and dynamic of the observed galaxies in the universe. Considering the universe as a fluid of uncollisional particles (dark matter) and evolving them with Newtonian gravity in an expanding metric, at the present time Springel *et al.* (2005) were able to perform the largest cosmological N-Body simulations containing over 10 billion particles on a cube of 500 Mpc/h on a side: Millennium Simulation.

Using the same approach in 2001 J. Stadel (Stadel, J. 2001, PhD thesis, U. Washington) performed a N-Body simulation of the Milky-Way halo. This simulation has been resimulated at much higher force and mass resolution by J. Diemand resolving the Milky-Way dark matter halo with 234 million particles (Diemand *et al.*, 2007a).

In this thesis we analyze two cosmological N-Body simulations and a sample of 17 resimulated galaxy clusters in order to study the dark matter halo conditional and unconditional mass function and substructures population, as we will discuss in the following chapters.

In this chapter we review some properties of N-Body simulations and will present the post-processing of the considered numerical simulations.

4.1 *N*-Body Methods

Following the evolution of a number of particles under the gravity is the main problem of the N-Body simulations. However it is important to take into account that the larger is the number of particles, the longer is the computational time need to compute forces and velocities. Reduce computational time without lose information of the particles is the main purpose in writing a N-Body code.

We will briefly describe some methods developed to compute force, position and velocity of each particle in the simulated region.

PP: Particle-Particle

The Particle-Particle method is the simplest. The method consists in accumulating forces by finding the force $\vec{F}_{ij}$ of particle j on particle i, using the Newton equation:

$$\vec{F}_{ij} = \frac{m_i m_j G}{d_{ij}^2} \vec{u}_{ij} ,$$

where $d_{ij} = r_{ij} + \epsilon$, with r_{ij} the distance between the two particles and ϵ the gravitational softening introduced to avoid an infinite force when r_{ij} goes to zero. The total gravitational force on particle i will be:

$$\vec{F}_i = \sum_{j \neq i}^{N} \frac{m_i m_j G}{(r_{ij} + \epsilon)^2} \vec{u}_{ij} . \tag{4.1}$$

Afterward it is necessary integrate the equations of motion and update the time counter. The procedure is after repeated at the next time-step.

This approach allow to compute the force accurately, however the computational time is very expensive and of the order of $O(N(N-1))$.

PM: Particle-Mesh

In this method the space containing N particles is represented by a cubic box with L on a side. On this it is defined a mesh for example with M knots, on which is spread the held mass M according to the equation:

$$\rho(x_{ijk}) = m_p M^3 \sum_{l}^{N} \Pi(\delta \vec{x}_l) , \tag{4.2}$$

where $\delta \vec{x}_l$ is the distance of the particle l from the grid point (i, j, k) and Π is an interpolation function. From the Poisson Equation it is possible to compute the force field and, interpolating the force on the grid, find forces on particles. Like the PP method, the forces have to be integrated to get particle positions and velocities. The procedure is thus repeated updating the time counter.

The main advantage of the PM methods is the speed. The number of computations is of order $O(N + N_g \log(N_g))$ where N_g is the number of grid points. The slowest step is in solving the potential equation, usually with the help of a Poisson solver, which often relies on a fast Fourier transform. Other numerical methods may be used to solve the potential (Poisson's) equation too, such as a finite element method or a finite volume method.

The PM method is basically unacceptable for studying close encounters between systems because the algorithm, in effect, treats particles as being fuzzy. This method is good for simulations where we want a "softening" of the inverse square law force. In general, the mesh spacing should be smaller than the wavelengths of importance in the physical system. Another disadvantage of using the mesh-based methods are that they have difficulties handling non-uniform particle distributions. This means that the PM methods offer limited resolution. To overcome this problem, some researchers have developed PM algorithms which employ meshes of finer griding in selected subregions of the system. These finer meshes permit a more accurate modeling of regions of higher density. If one wishes to further refine the grid due to large dynamical changes in the system, then one can apply moving grids or adaptive grids.

P3M: Particle-Particle/Particle-Mesh

The P3M method has been developed to solve the major shortcoming of the PM method: low resolution forces computed for particles near each other. This method supplements the inter-particle forces with a direct sum over pairs separated by less than about 3 times the grid spacing. The inter-particle forces are split into a rapidly-varying short-range part and a slowly-varying long-range part. The PP method is used to find the total short-range contribution to the force on each particle and the PM method is used to find the total slowly-varying force contributions.

In this method the computational time is of order $O(N+N_g)$. This allow to use P3M in cosmological simulations and also when forces can be readily split between short-range and long-range.

The disadvantage of the P3M algorithm is that it can be dominated by the direct summation part. A solution to this problem has been proposed by Couchman (1991) developing an Adaptive P3M algorithm allowing spatially adaptive mesh refinements in regions of high particles density.

TC: Tree-Code

In this method, called also hierarchical tree, the particles are assembled in groups in hierarchical structures (trees and cells). The first step is to build up the trees and compute the distance among the cells. The multiple moments are so computed for each group until the desired order.

Generally the force is estimated considering a concept as the P3M algorithm:

$$F = F_{\text{external}} + F_{\text{nearest neighbor}} + F_{\text{far field}}\,.$$

The gravitational force acting on a single particle is computed considering the hierarchical element with which it interacts. In detail for nearby particles the method used to compute the force is similar to the PP approach.

Tree Codes are gridless, have no preferred geometry and can incorporate either vacuum or periodic boundary conditions. In addition, they waste no time simulating regions devoid of matter. Hence, Tree-Codes are particularly effective for modeling collisions between galaxies. Forces on all particles are obtained with $O(N\log(N))$ operations. The down side is that tree codes require a large amount of auxiliary storage.

4.2 Numerical Simulations

In this section we will describe the numerical simulations used in this thesis. All runs assume ΛCDM universe and it has been followed only the evolution of the dark matter component.

GIF Simulations

These simulations have been performed by Kauffmann *et al.* (1999) in a joint project between astrophysicists from Germany and Israel. The runs were started at the Computer Centre of the Max-Planck Society in Garching (128 processors) and finished a the Edinburgh Parallel Computer Centre (256 processors).

The primary goal has been to study the structures formation in a cosmological context using semi-analytical galaxy formation models. However different other researches have been performed on these simulations: gravitational lensing by clusters (Bartelmann *et al.*, 1998) and studies about conditional and unconditional mass function of dark matter haloes (Sheth and Tormen, 1999, 2002).

The code used for GIF simulations is called HYDRA. This is a parallel adaptive particle-particle particle-mesh (AP3M) algorithm written by Couchman *et al.* (1995); Pearce and Couchman (1997).

The project is characterized by a set of four simulations with $N = 256^3$ particles and with different cosmological parameters (for more details see Kauffmann *et al.* (1999)). Among the whole sample we used only the ΛCDM run. This simulation has a box size of $141\,\mathrm{Mpc}/h$ ans an individual dark matter particle mass $m_p = 1.4 \times 10^{10}\,M_\odot/h$. The cosmological parameters adopted are: $\Omega_m = 0.3$, $\Omega_\Lambda = 0.7$, $h = 0.7$, $\sigma_8 = 0.9$, baryon fraction $f_b = 0.15$ and a gravitational softening (Plummer equivalent) $\epsilon = 30\,\mathrm{kpc}/h$. Figure 4.1 we show the dark matter particle distribution in four different redshifts for the ΛCDM GIF simulation. As we can see while at high redshift the dark matter distribution is smooth and the typical mass for collapse is small, at the present time the distribution is more clumpy and number of large mass halo bigger.

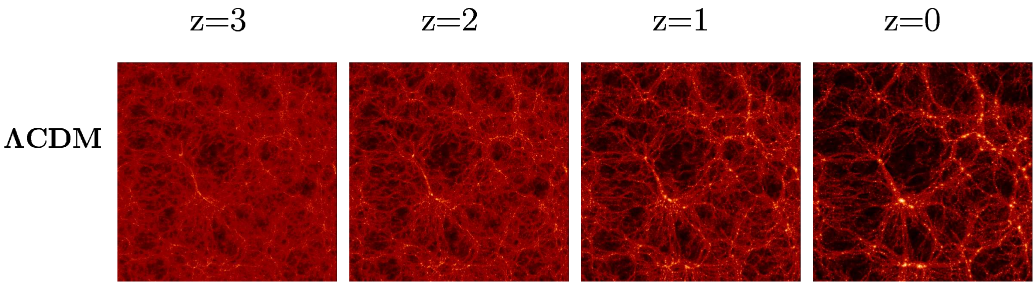

Figure 4.1: GIF simulation: dark matter distribution in the simulation box at four different redshifts.

GIF2 Simulation

The GIF2 is a cosmological simulation of a flat ΛCDM universe in a periodic cube of side 110 h^{-1}Mpc. The total number of particles considered is 400^3, with an individual mass of $m_p = 1.73 \times 10^9 \, M_\odot / h$. This is a factor of 8 better than the mass resolution of GIF simulation described in the previous section. This simulation has been performed and described for the first time by Gao *et al.* (2004).

The cosmological parameters adopted are: $\Omega_m = 0.3$, $\lambda = 0.7$, $\sigma_8 = 0.9$ and $h = 0.7$. The initial fluctuation power spectrum index has been chosen to be $n = 1$, and the transfer function has been produced using CMBFAST (Seljak and Zaldarriaga, 1996) for $\Omega_b h^2 = 0.0196$. The initial condition were produced by perturbing an initially uniform state represented by a "glass" distribution of particles. This particle distribution has been generated with the method developed by White (1993) which involves evolution from a Poisson distribution with the sign of Newton's constant changed when calculating peculiar gravitational forces. Fluctuations are imposed using the algorithm described in Efstathiou *et al.* (1985). Based on the Zel'Dovich (1970) approximation, a Gaussian random field has been set up by perturbing the particle positions and by assigning them velocities according to the growing mode solution of linear theory.

In order to save computational time, the simulation has been performed in two steps:

- from high redshift until $z = 2.2$ the simulation has been run with SHMEM (parallel version of HYDRA Couchman *et al.* (1995)). At these times the particle distributions are lightly clustered and thus the P3M-based gravity solver is quite efficient;

- from $z = 2.2$ to $z = 0$ the simulation has been completed with a tree-based parallel code, GADGET Springel *et al.* (2001), which has better performance in the heavily clustered regime.

However the two codes adopt different force-softening schemes, so it is necessary to match the force shape at the time of switch from one code the the other. Experimentation showed that $\epsilon_{\mathrm{HYDRA}} = 1.06 \epsilon_{\mathrm{GADGET}}$, produces an excellent match of two force laws. To take into account this difference from $z = 49$ to $z = 2.2$ the simulation has been performed with a gravitational softening $\epsilon = 7\,\mathrm{kpc}/h$ in comoving units, while from $z = 2.2$ to $z = 0$ $\epsilon = 6.604\,\mathrm{kpc}/h$ using GADGET.

The numerical data for GIF and GIF2 simulation are publicly available at: *http://www.mpa-garching.mpg.de/Virgo.*

Re-simulation of Galaxy Clusters

This sample is composed by 48 dark matter haloes, extracted from ten high-resolution N-body resimulations of 17 galaxy clusters. Halo masses are in the range $5.1 \times 10^{13} - 2.3 \times 10^{15} \, M_\odot / h$ at redshift $z = 0$; mass resolution is $1.3 \times 10^9 \, M_\odot / h$;

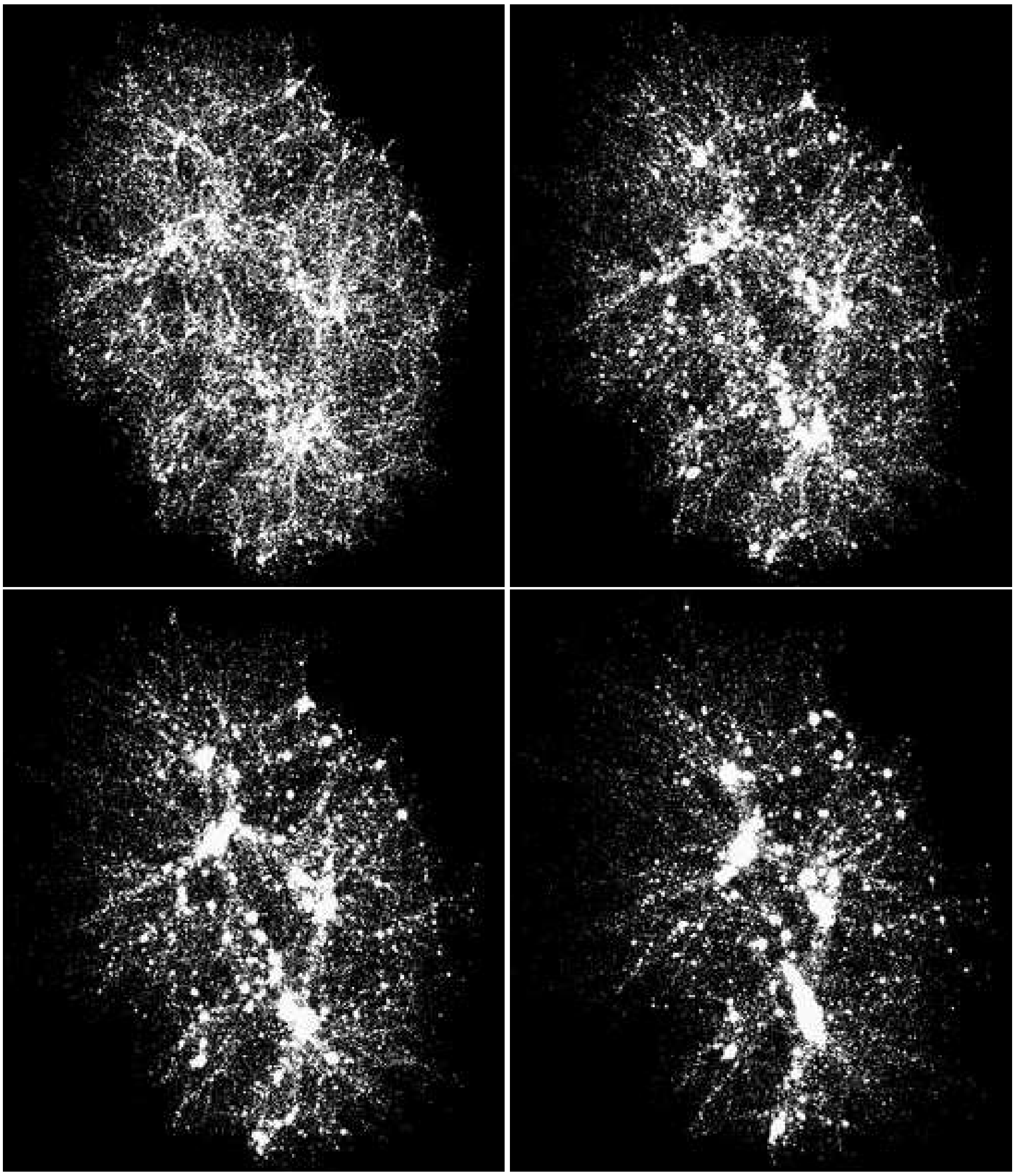

Figure 4.2: High resolution dark matter particles distribution in haloes at four different redshifts in a resimulated group of clusters (filament) ($z = 2$ **upper left**, $z = 1$ **upper right**, $z = 0.5$ **lower left** and $z = 0$ **lower right**. The high resolution region is resolved with five million of not-interacting particles in a region of 60 Mpc of a side.

the gravitational softening (Plummer equivalent) in each resimulation is $\epsilon = 5$ kpc/h.

The resimulated systems were extracted from a cosmological N-Body simulation containing 512^3 particles in a cube 479 Mpc/h on a side, assuming a flat ΛCDM model with $\Omega_0 = 0.3$, $h = 0.7$, $\sigma_8 = 0.9$ and $\Omega_b = 0.04$ (Yoshida *et al.*, 2001), in agreement with recent measurements of cosmic shear on large scale structure

(Van Waerbeke *et al.*, 2001; Refregier *et al.*, 2002). The lower value of σ_8, mass variance on a scale of 8 Mpc/h as best fit of the 3-year WMAP (Spergel *et al.*, 2007) data has the effect of delay the structures formation (Wang *et al.*, 2007).

simulation	n. of particles	particle mass $[M_\odot/h]$	box size $[\mathrm{Mpc}/h]$
GIF	256^3	1.40×10^{10}	141
GIF2	400^3	1.73×10^{9}	110
g1	4937886	1.30×10^{9}	61.73
g1542	328162	1.30×10^{9}	31.15
g3344	293209	1.30×10^{9}	29.51
g51	2219034	1.30×10^{9}	49.70
g6212	280343	1.30×10^{9}	28.41
g676	314518	1.30×10^{9}	31.30
g696 (filament)	16959053	1.30×10^{9}	91.47
g72	4379049	1.30×10^{9}	61.53
g8	5602561	1.30×10^{9}	61.81
g914	387014	1.30×10^{9}	35.10

Table 4.1: Summarized properties of cosmological N-Body simulations and resimulated galaxy clusters.

In order to resimulate the selected haloes with higher mass and force resolution, new initial conditions were generated using the Zoomed Initial Condition technique (ZIC, Tormen *et al.* (1997)): halo Lagrangian regions were populated with a larger number of less massive particles, and additional small-scale power was appropriately added. The new initial conditions were evolved using a non public version of GADGET2 (Springel, 2005) (TreePM algorithm) from redshift $z = 60$ to the present time. We will study these resimulations using 88 output times equally spaced between $z = 10$ and $z = 0$. In Table 4.1 we summarize the properties of the simulations.

4.3 Post-processing

Halo Finder and Universal Mass Function

We adopt the *spherical overdensity* (SO) (Lacey and Cole, 1994) criterion to identify haloes at each simulation output time (also called "‘snapshot"’). For each snapshot we estimate the local dark matter density at the position of each particle by calculating the distance to the tenth closest neighbour. We assign to each particle a local density $\rho_{i,\mathrm{DM}} \propto d^3_{i,10}$, sort particles in density and take as centre of the first halo the position of the densest particle. We then grow a sphere of matter around this centre, and stop when the mean density within the sphere first falls below the virial value appropriate for the cosmological model at that redshift. For the definition of virial density we adopted the model of Eke *et al.* (1996). As discussed in Section 3.2 the spherical collapse model for ΛCDM universe predict haloes at redshift $z = 0$ to be dense at least 324 times the back-

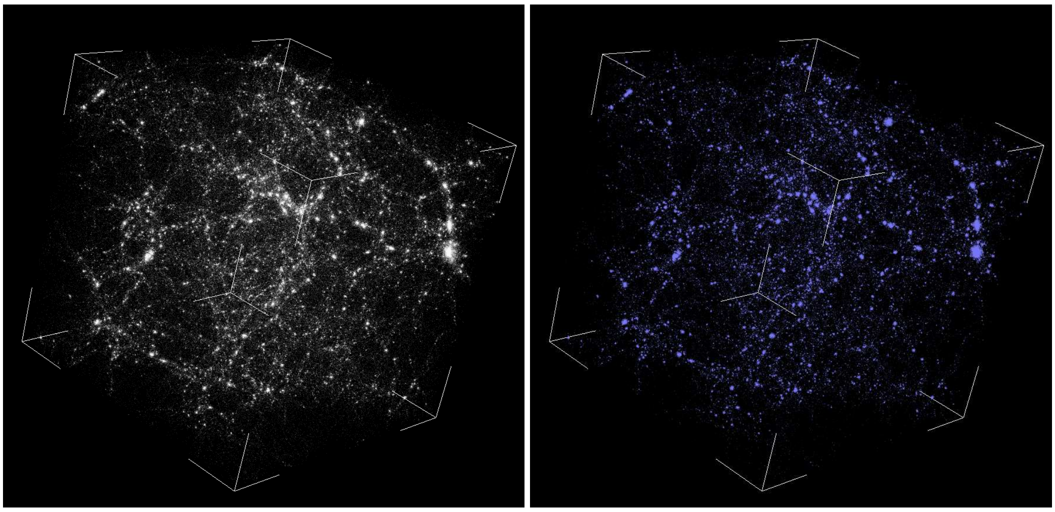

Figure 4.3: **Left**: particles distribution in GIF2 simulation at redshift $z = 0$. **Right**: corresponding particles in virialized haloes as identified with the SO criteria. The plots have been done using the publicly available code Visivo (*http://visivo.cineca.it*) (Becciani *et al.*, 2006).

ground density. At this point we assign all particles within the sphere to the newly formed halo, and remove them from the global list. We take the centre of

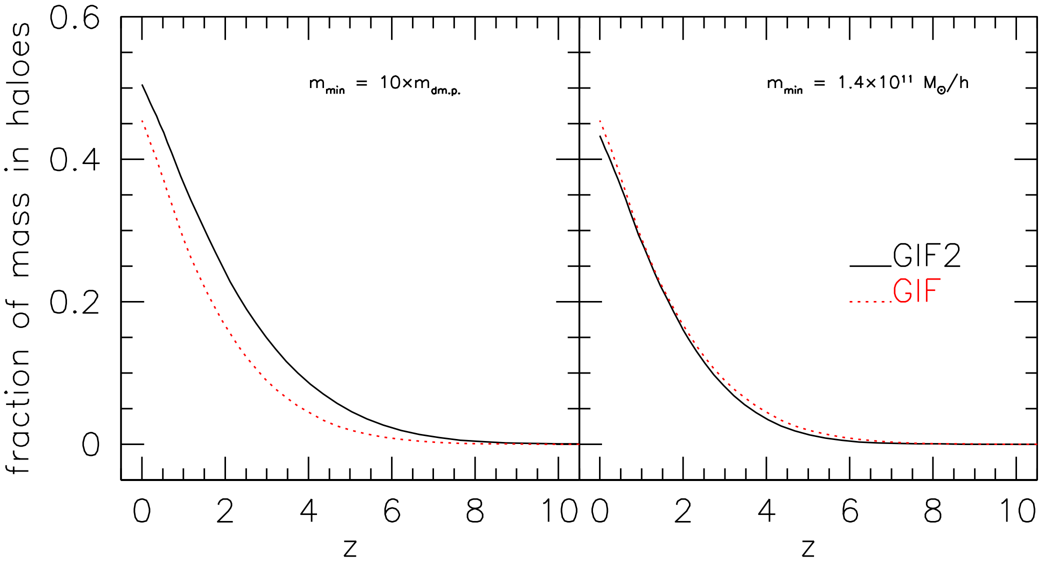

Figure 4.4: Mass fraction in dark matter haloes (SO), in the cosmological simulations GIF and GIF2, in term of redshift. **Left**: the minimum masses considered are haloes with at lest 10 particles. Taking into account that GIF2 has a mass resolution that is a factor of 10 smaller than GIF, this translate in a larger mass fraction in identified haloes. However when we cut the resolution at the GIF halo mass (**right**) the mass fraction in haloes in the two simulations match each other.

the next halo at the position of the densest particle among the remaining ones, and grow a second sphere. We continue in this manner until all particles are screened. we include in the haloes catalogue only groups with at least 10 particles within the virial radius; particles not ending up in any halo are considered as "‘field"’ or "‘dust"’ particles. In Figure 4.3 we show the particles distribution in GIF2 simulation at the present (left panel). The right panel of the figure show the corresponding dark matter particles distribution in virialized haloes identified with SO criterium. In Figure 4.4 we show the dark matter mass fraction, in GIF

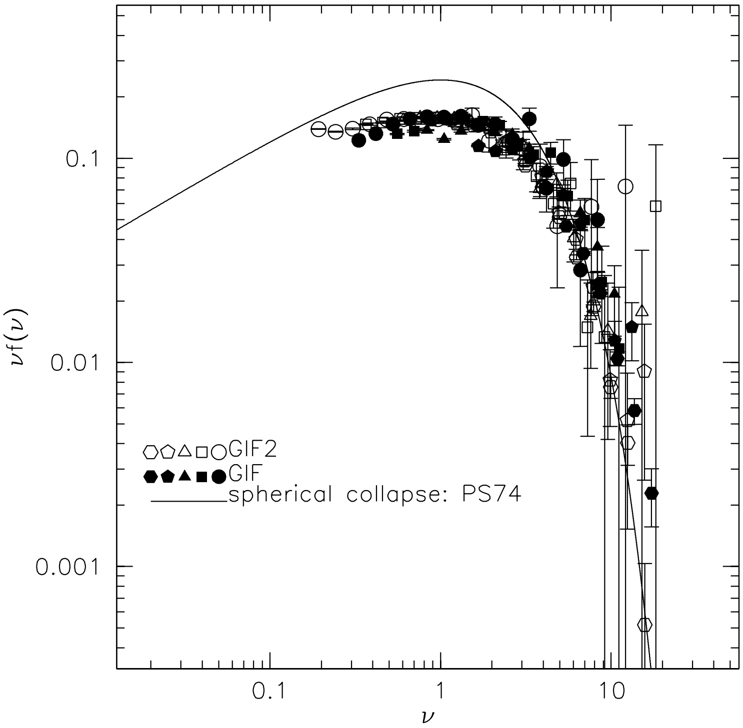

Figure 4.5: Mass function of dark matter haloes at five different redshifts in GIF (solid point type) and GIF2 (open point type) simulations. The different points type refer respectively to $z = 4$ (hexagons), $z = 2$ (pentagons), $z = 1$ (triangles), $z = 0.5$ (squares) and $z = 0$ (circles). The solid line shows the spherical collapse prediction for the mass function of collapsed dark matter haloes, equation (3.24.

and GIF2 simulations, in identified haloes in term of redshift. We see that the dark matter particles, with cosmic time, cluster forming larger and larger collapsed regions. On the left the the minimum halo mass considered correspond to the halo finder resolution, i.e. 10 particles. We see that GIF2 has a larger mass fraction in virialized haloes than GIF, because its mass resolution is a factor of 8 smaller. However cutting the resolution at the same mass (right panel) the two fraction in term of redshift match each other. In the figure we notice also that, at the present, roughly half of dark matter particles belong to virialized object more massive than $10^{11}\ M_{\odot}/h$.

The adopted definition of dark matter haloes, as individual groups of particles with enclosed density equal to the critical virial value, has been chosen to make a more direct comparison with the Press & Schechter and extended Press & Schechter theory of hierarchical clustering (Press and Schechter, 1974; Bond *et al.*, 1991; Lacey and Cole, 1993), as we will show in the next sections and chapters.

However other different definitions has been adopted in literature to define the edge of the haloes: 200 times the mean background or the critical density of the universe. We will show in Appendix A as it is possible to rescale the radius of the dark matter haloes, when identified as 200 times the critical or background density respect to the spherical collapse definition, making use of some interesting fitting functions.

In literature it has been proposed also another approach to identify haloes in numerical simulations. The method consist in linking together groups of particles with a distance less than b times the mean inter-particles separation. This not ensure haloes to be spherical overdense regions as in the case of spherical overdensity, and is called *friends-of-friends* (FOF) (Davis *et al.*, 1985). Haloes identified in this way result in groups of particles bounded by a surface of approximately constant density: $\rho/\bar{\rho} \approx 3/(2\pi b^3)$. The advantage of this algorithm is that it is faster than SO. Many authors using it (Frenk *et al.*, 1988; Efstathiou *et al.*, 1988) in N-Body simulations found good agreement with the theoretical prediction and SO method when $b = 0.2$. The FOF algorithm picks out most of the groups that can be identified by eye, however occasionally it can join together two or more distinct density centers that are linked by a tenuous bridge of particles. To solve this problem many authors, after identified groups with FOF technique, use a SO method to compute the virial overdensity assuming spherical symmetry.

In Figure 4.5 we show the mass function of dark matter haloes in GIF and GIF2 simulations at different redshifts. As previously described haloes have been identified with the SO algorithm at each simulation snapshot. The solid curve is the theoretical prediction of the mass function computed by Press and Schechter (1974); Lacey and Cole (1993) (eq. 3.24) expressed in term of the redshift independent variable ν. In the figure we notice that the spherical collapse model underpredicts the abundance of large masses and overpredicts that of the small ones respect to measurements in N-Body simulations.

Sheth and Tormen (1999) proposed for the first time a modification of the Press & Schechter global mass function. Their equation has been parametrized in term of ν in order to fit the halo mass function in GIF simulations, and is:

$$\nu f(\nu) = A\left(1 + \frac{1}{\nu'^p}\right)\left(\frac{\nu'}{2}\right)^{1/2} \frac{\mathrm{e}^{-\nu'/2}}{\sqrt{\pi}} \tag{4.3}$$

where $\nu' = a\nu$, with $a = 0.707$, $\nu = \delta_c^2/s$, $p = 0.3$ and $A \approx 0.322$ obtained normalizing the distribution. The original Press & Schechter formula can be obtained with $a = 1$, $p = 0$ and $A = 1/2$. The fit has been tested on different redshift halo catalogues of the SCDM, OCDM and ΛCDM runs of the GIF simulations.

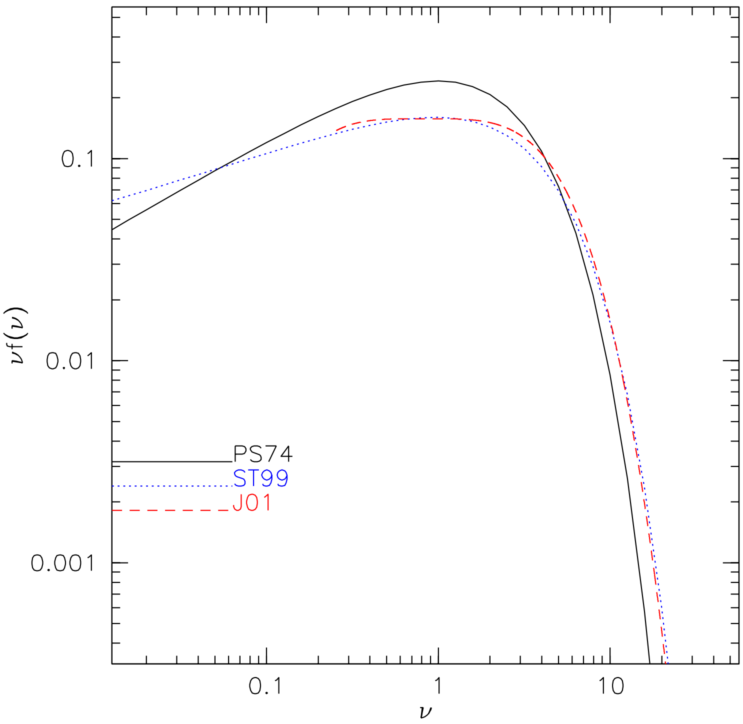

Figure 4.6: Unconditional mass function of dark matter haloes. The solid lines represents the Press & Schechter prediction for the dark matter haloes population (eq. 3.24), the dotted curve is the Sheth & Tormen generalization of the spherical collapse prediction (eq. 4.3), the dashed lines is the Jenkins et al. fit (eq. 4.4).

Another fitting function to the simulations data has been also proposed by Jenkins *et al.* (2001). They combined data from a number of N-body simulations and predicted the abundance of dark haloes in cold dark matter (CDM) universes over more than four orders of magnitude in mass. They showed that for a range of CDM cosmologies and for a suitable halo definition (both FOF and SO), the mass function in numerical simulations is almost independent of epoch, of cosmological parameters and of the initial power spectrum also when expressed in term of $\sigma = \sqrt{s}$. The proposed mass function has the following expression:

$$f(\sigma) = 0.315 \exp(-|\ln \sigma^{-1} + 0.61|^{3.8}), \tag{4.4}$$

over the range $-1.2 \leq \ln \sigma^{-1} \leq 1.05$.

These two formula proposed do not have any physical justifications in order to take into account discrepancies between PS formula and N-Body simulations, but are only fits to the numerical data. Sheth *et al.* (2001) analyzing the collapse of dark matter haloes in N-Body simulations showed that the discrepancy between theory and simulations can be reduced substantially if bound structures are assumed to form from an ellipsoidal, rather than a spherical, collapse. In the original, standard, spherical model, a region collapses if the initial density within it exceeds a threshold value, $\delta_{sc}(z)$. This value is independent of the initial size of the region, and since the mass of the collapsed object is related to its initial size, this means that $\delta_{sc}(z)$ is independent of final mass. As we showed in Section , in the ellipsoidal model, the collapse of a region depends on the surrounding shear field, as well as on its initial overdensity. These will require small haloes to be more strong to virialize. The mass function can be expressed considering the probability of first crossing a moving barrier equation (3.28) (Sheth and Tormen, 2002) or equation (3.44) (Mahmood and Rajesh, 2005) for the square-root case. As shown by Sheth and Tormen (2002) the approximated solution of the probability of first crossing a moving barrier (with $\gamma = 0.6$, $\beta = 0.5$ and $q = 0.707$) does a very good job in reproducing the N-Body simulation mass functions.

Merger Tree

We build the merging-history-tree for all haloes in simulations (or resimulations) using the halo catalogues at all snapshots, separated by redshift intervals $\mathrm{d}z_i$, as follow. Starting from an halo at $z = 0$, we define its progenitors at the previous output $z = \mathrm{d}z_1$, to be all haloes contributing with at least 50% of their particles to the initial system. Among them we call *main progenitor* (MPH) at $z = \mathrm{d}z_1$ the progenitor halo providing the largest mass contribution to the halo at $z = 0$. We repeat the procedure, starting now at $z = \mathrm{d}z_1$ and considering the progenitors at $z = \mathrm{d}z_1 + \mathrm{d}z_2$ of the $\mathrm{d}z_1$-*main progenitor* halo, and so on backward in redshift. In this merging-history-tree we term *satellites* all progenitors which, at any time, merge directly on the MPH, contributing with at least with 50% of their particles to the initial system at $z = 0$.

The hierarchical growth of the haloes can be followed considering also another definition for the main brunch: the most contributing progenitor to the present-day system. Instead of following the progenitors of an halo along adjoining snapshots, we considered at any redshift $z > 0$ all the halo that contribute at least with 50% of their particles to the present-day halo. Among them we call *most contributing progenitor* (MCH) (that correspond to the most massive one) the halo which donate the largest number of particles to the present-day system. When the MPH has a mass greater than half the initial halo mass, then it is guaranteed to be the most contributing progenitor. For lower masses, and so higher redshift, this is not the case and, in principle, the main trunk progenitor could be much less massive than the most contributing progenitor at any given epoch. Furthermore, the identity of the main branch can depend on the time resolution with which the tree is stored. However, if we generate Monte Carlo trees at the same time-steps as in the simulation, then the difference between Monte Carlo and N-body results for the main trunk progenitors is very similar to that for the most contributing progenitor. However in simulations the dynamical processes are not linear: in the mean the dark matter haloes grow hierarchically in time,

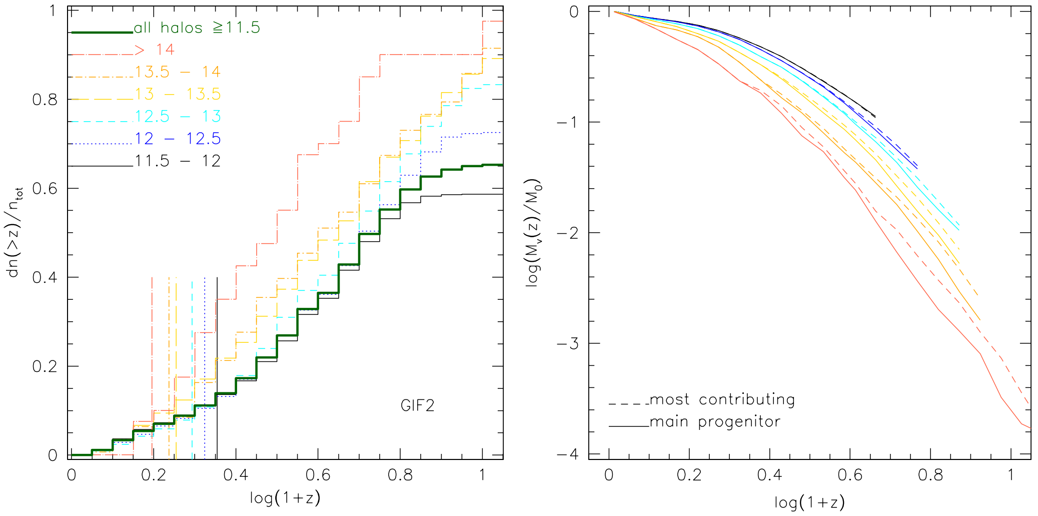

Figure 4.7: **Left**: cumulative distribution of the "*first jump*" between the *main progenitor* and the *most contributing* halo as defined by the two algorithms, see the main text for more details. The considered redshifts at which the two algorithm are compared refer to the GIF2 simulation snapshots. The various line types refer to different present-day halo masses. In the figure n_{tot} represents the total number of haloes in each considered bin. The six vertical lines are the average formation redshift, along the *main progenitor*, for each of the six mass bin considered. **Right**: median mass growth history of different present-day haloes. The color type is the same as in the left panel, solid and dashed curves refer to the two algorithm that define the main branch of the tree.

but in same cases can happen that a halo merge with a more massive one and after go out of this: in numerical simulations hierarchical growth is not guarantee for all systems. Following the growth along adjoining snapshots the mass of the MPH, at a given redshift $z > 0$, for example, could also become bigger that the final one Cole *et al.* (2008).

Other researchers however use different definitions to follow the merger tree of dark matter haloes. For example the Munich group (Springel *et al.*, 2005; Croton *et al.*, 2006; De Lucia *et al.*, 2006) use as their basic unit of the tree not the haloes but the substructures within haloes (that they identify with SUBFIND Springel *et al.* (2001)) linking them between time-steps. The Durham group (Bower *et al.*, 2006; Harker *et al.*, 2006), to the other hand, primarily link the haloes between time-steps and after make use of the substructure catalogue to track informations about prematurely e/or temporarily linked haloes (for example the cases in which the main progenitor of an halo do not grow between two time steps: $M_v(z_2) \geq M_v(z_1)$ with $z_2 > z_1$).

Let us define "*first jump*" as the earliest snapshot where the most contributing progenitor and the main progenitor halo definitions do not identify the same system along the tree. In the left panel of Figure 4.7 we plot the cumulative distribution of "*first jump*". The results are shown considering present day haloes in GIF2 simulation and binning them in six mass intervals (see the label of the figure). In Figure 4.7 is also shown the average formation redshift (vertical lines) Lacey and Cole (1993) for each mass bin, defined as the earliest redshift where the mass of the *main progenitor* halo become half of its present-day value. As we can see less than 10% of all the haloes in each bin has a *first jump* before the average formation redshift: the *main progenitor* is univocally defined for mass bigger than $1/2 \times M_0$. In the right panel of Figure 4.7 we show the median mass of the main progenitor and of the most contributing halo versus redshift. The color type are the same as in the left panel. We see that starting from the present until the formation the two definition agree, while the higher is the redshift the bigger is the median mass of the MCH respect to the MPH, as also found by Cole *et al.* (2008) using a mergertree based on halo catalogue in Millennium Simulation.

4.4 Conditional Mass Function

Present day dark matter haloes assemble hierarchically with time, so at each redshift $z > 0$ they are divided in a sample of progenitors. The progenitor mass function (called also conditional mass function) gives the mass function of haloes at a redshift z that will end up at redshift $z_0 = 0$ in an M_0-halo:

$$f(m,z|M_0,z_0)\mathrm{d}m = f(s,\delta_{sc,1}|S,\delta_{sc,0})\mathrm{d}s\,.$$

where s represents the corresponding mass variance of an m-halo, given by the equation (3.9) once the power spectrum is defined, $\delta_{sc,1}$ and $\delta_{sc,0}$ represent the spherical collapse overdensity corresponding respectively at redshift z and z_0. The mean number of progenitors at redshift z will thus be:

$$N(m,z|M_0,z_0)\mathrm{d}m = \frac{M_0}{m} f(s,\delta_{sc,1}|S,\delta_{sc,0})\mathrm{d}s\,. \tag{4.5}$$

The mathematical equation for the progenitor mass function can be estimated using the excursion set approach as done for the global mass function(called also unconditional) in the previous chapter. The fraction of m-progenitors at redshift z that will end up in an M_0-halo at the present time can be can be obtained considering the conditional probability of first crossing of barrier. In this case the Brownian and uncorrelated walks start from (S, δ_0) (see Bond *et al.* (1991); Lacey and Cole (1993); Sheth and Tormen (2002) for the theoretical discussion).

Remembering that in spherical collapse model, the barrier is independent of the mass, the conditional probability of first crossing can be easily obtained from equation (3.23) changing variables as following:

$$s \to (s - S)\,,$$
$$\delta_{sc} \to (\delta_{sc,1} - \delta_{sc,0})\,;$$

which gives:

$$f(s,\delta_{sc,1}|S,\delta_{sc,0})\mathrm{d}s = \frac{1}{\sqrt{2\pi}} \frac{(\delta_{sc,1} - \delta_{sc,0})}{(s-S)^{3/2}} \exp\left[\frac{(\delta_{sc,1} - \delta_{sc,0})^2}{2(s-S)}\right]\mathrm{d}s\,. \tag{4.6}$$

However, as discussed for the unconditional mass function, when the analytical spherical collapse prediction is compared to N-Body simulations the agreement is not satisfying. The mass function that better fits the numerical simulations is the ellipsoidal prediction. Sheth and Tormen (2002) showed that an approximate solution for the conditional probability of first crossing distribution of a moving barrier can be written as:

$$f_B(s,\delta_{sc,1}|S,\delta_{sc,0})\mathrm{d}s = \frac{|T(s|S)|}{\sqrt{2\pi(s-S)}}\exp\left\{-\frac{[B(s,\delta_{sc,1})-B(S,\delta_{sc,0})]^2}{2(s-S)}\right\}\frac{\mathrm{d}s}{s-S}, \quad (4.7)$$

with

$$T(s|S) = \sum_{n=0}^{5}\frac{(S-s)^n}{n!}\frac{\partial^n[B(s,\delta_{sc,1})-B(S,\delta_{sc,0})]}{\partial s^n}; \quad (4.8)$$

where $B(s,\delta)$ is given by equation (3.27). As we will see this equation reproduce simulation data better than the spherical collapse mass function.

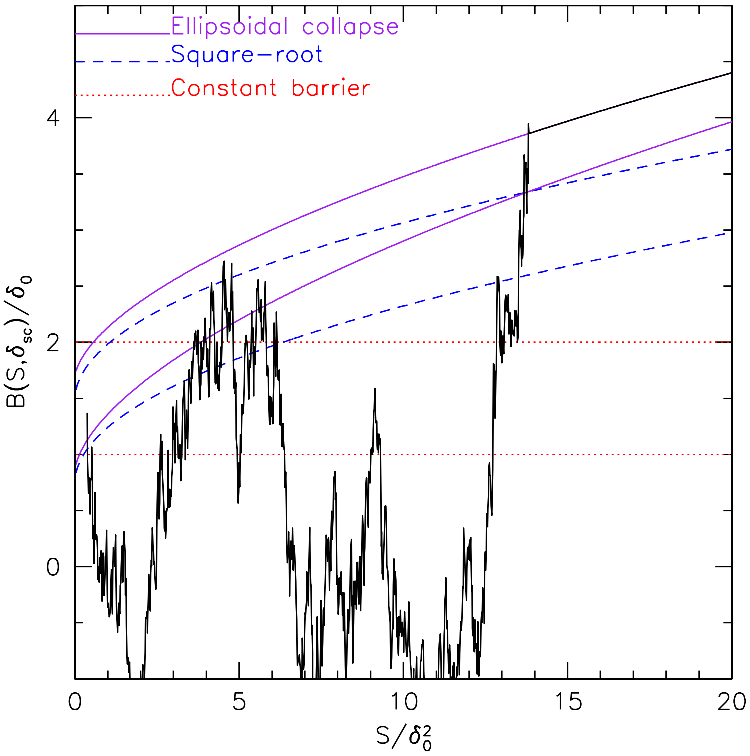

Figure 4.8: An example of a random walk and the three barrier shapes we consider hereafter. Here δ_0 refers to the critical value associated with spherical collapse overdensity at redshift z_0. The jagged line is a sample Brownian walk absorbed by the barrier associated with ellipsoidal collapse (solid curve). Short-dashed curves show the square-root barriers which we will also use to approximate the ellipsoidal collapse barrier, and horizontal dotted lines show the constant barrier associated with spherical collapse. The upper set of barriers are associated with collapse at an earlier time.

In the case of a square-root barrier, the conditional probability of first crossing has an exact solution too. This can be obtained performing the same calculations done in section 3.3 for the unconditional case. The conditional fraction of walks that cross a square-root barrier is thus given by:

$$f_{sr}(s,\delta_{sc,1}|S,\delta_{sc,0})\mathrm{d}s = \frac{1}{2}\exp\left[\frac{w_\beta^2-\beta^2}{4}\right]\sum_\lambda\left(\frac{S}{s}\right)^{\lambda/2} D_\lambda(w_\beta)\frac{D'_\lambda(-\beta)}{I_\lambda(-\beta)}\frac{\mathrm{d}s}{s}, \qquad (4.9)$$

where we have defined the following conventional variable:

$$w_\beta = \frac{\sqrt{q}(\delta_{sc,1}-\delta_{sc,0})}{\sqrt{S}} - \beta.$$

In Figure 4.8 we show a conditional walk absorbed by the ellipsoidal collapse barrier. In the figure are also shown the constant and the square-root barrier normalized to have the same initial overdensity for the S-halo.

Comparison with N-Body Simulations: Assembly History of Dark Matter Haloes

In this section we show some comparisons between the theoretical predictions of the conditional mass function (spherical, ellipsoidal and square-root barrier case) and the results of GIF2 N-Body simulation.

In the numerical simulation, the sample of present-day haloes is made by all systems with mass $M_0 > 10^{11.5} M_\odot/h$ (that correspond to virialized group with more or less at least 200 dark matter particles). From the sample we removed all haloes which main progenitor at any redshift exceed the present-day mass value, in order to neglect non conventional history-tree. The progenitors mass function at six different redshifts as been estimated for 5611 with $\log(M_0/h^-1M_\odot)$ in the range $11.5-12$, 2431 in the range $12-12.5$, 892 in the range $12.5-13$, 341 in the range $13-13.5$, 92 in the range $13.5-14$ and 29 in the range >14.

At each redshift z the progenitors have been defined to be all haloes that contribute at least with 50% of their particles to the final M_0-halo. It is interesting also take into account the fact that, in numerical simulations, not all the particles of each progenitor will end up in the final halo, and that the mass of the M_0-halo is made by some particles that came from haloes that contribute with less than 50% of their mass and by some particles that come from the field (see Figure 4.9 where we show a schematic representation of the progenitors of an halo).

In order to take into account these situations the virial mass of each progenitor halo m_i at redshift z has been normalized not by M_0 but $M_{0,z}$, that is:

$$M_{0,z} = \sum_i m_i + \sum_j f_j \tilde{m}_j + \text{field mass} \qquad (4.10)$$

where f_j is the contributing mass fraction from the haloes $\tilde{m}_j$ that give less then 50% of their particles to the initial mass M_0, and m_i are the progenitors.

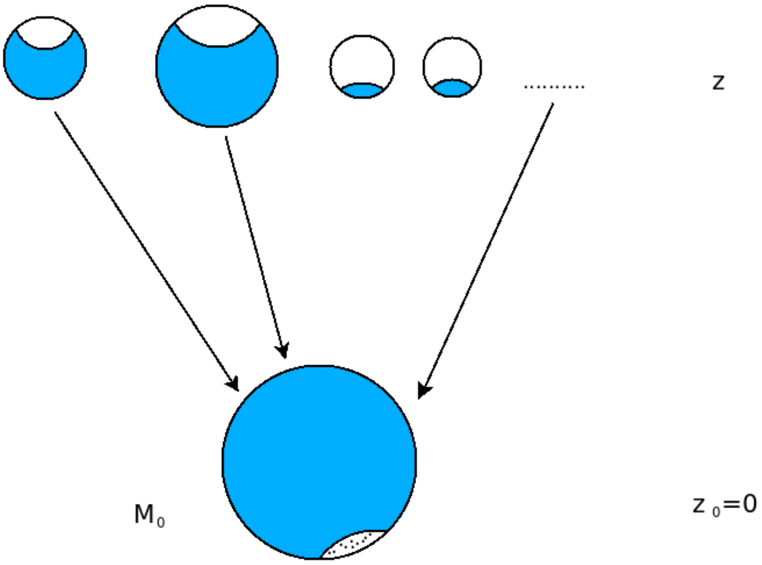

Figure 4.9: Schematic representation of progenitor haloes at redshift z of an M_0-halo. From the left, the first two represent haloes that contribute more than 50% of their mass to M_0. The other two instead represent haloes that give only a small fraction to M_0; the dots, on the right, symbolize the dust particles.

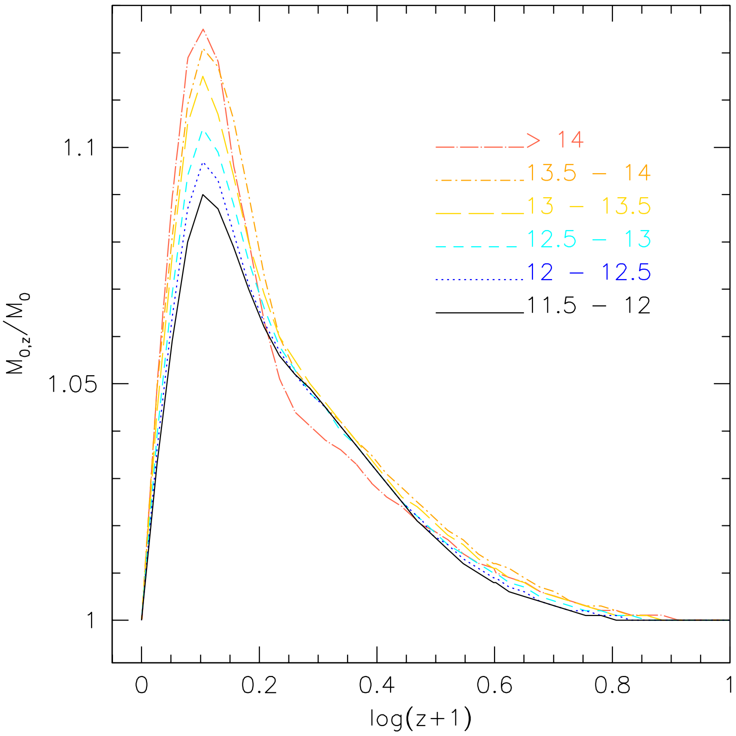

Figure 4.10: Total mass in progenitors and field that will end up in the final halo. The plot has been done considering the sample of present-day haloes as described in the text, and dividing them in six mass bin.

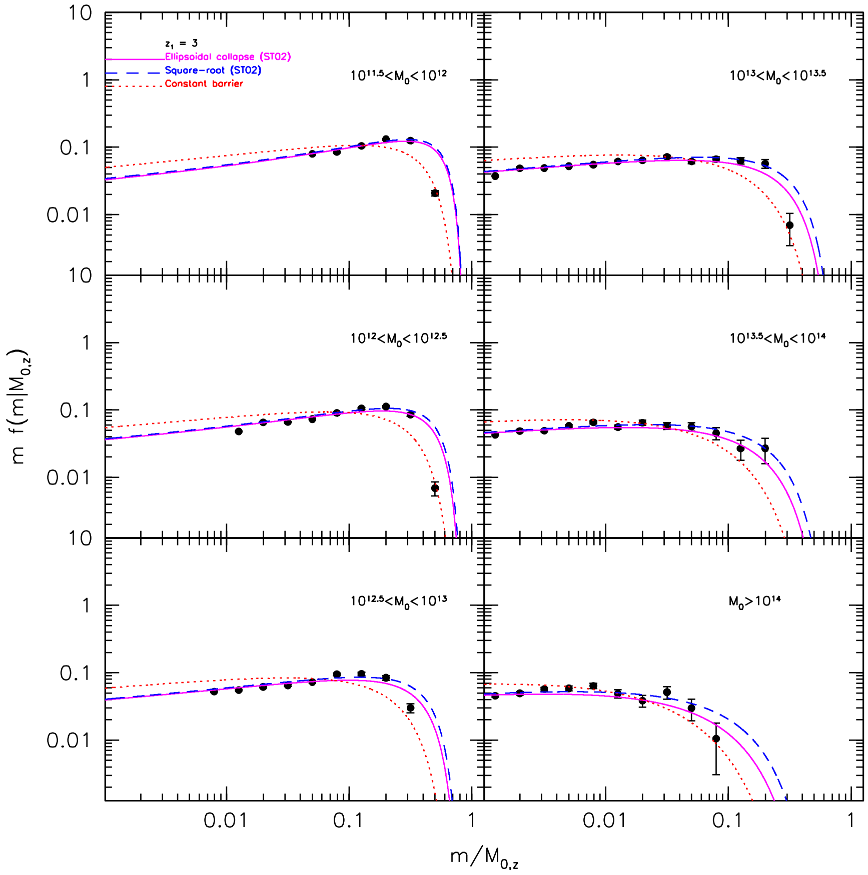

Figure 4.11: Conditional mass function at redshift $z_1 = 3$ of a sample of present day dark matter haloes in GIF2 simulation. The haloes has been divided in six mass bin as shown in the panels. The spherical and ellipsoidal collapse (Sheth and Tormen, 2002) prediction are shown for comparison. In the figure is also shown the square root conditional mass function ($\gamma = 1/2$, $\beta = 0.5$ and $q = 0.55$). Considering that the equation (4.9) involve the parabolic cylinder function, its derivative and primitive that are very difficult to compute, we use the Sheth and Tormen (2002) approximate solution with the appropriate value of the parameters that define the barrier (Mahmood and Rajesh, 2005).

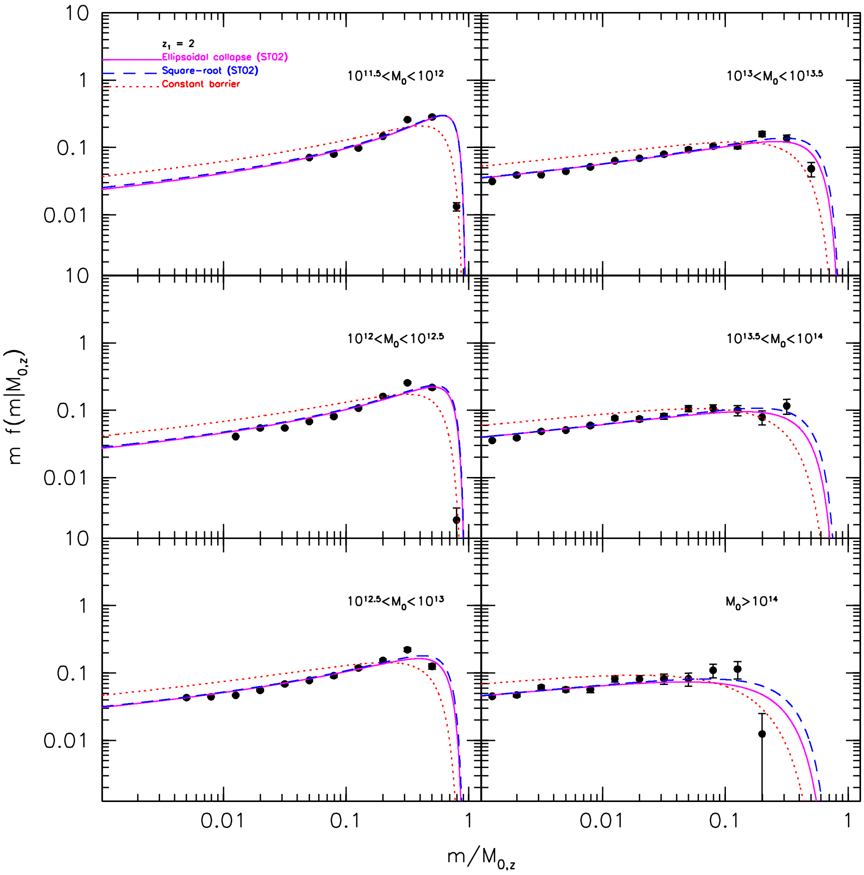

Figure 4.12: As in Figure 4.11 with $z_1 = 2$.

In Figure 4.10 we show the total mass in progenitors and field that will end up in a present-day halo. The haloes are those considered in the six different mass bins as described before. As shown by Tormen (1998) the progenitors halo mass fraction has a distribution that grow with the cosmic time with a peak around $z \approx 0.25$. In the figure we notice also that the value of the maximum increase with the final halo mass.

In the Figures 4.11, 4.12, 4.13, 4.14, 4.15, 4.16 and 4.17 we show the conditional mass function in GIF2 simulation considering different final redshifts. In each figure the various panels refer to different present day halo masses as described before. In figure we also show the theoretical prediction for the spherical (dotted line) (Lacey and Cole, 1993) and ellipsoidal (solid line) (Sheth and Tormen, 2002) collapse compared to GIF2 simulation. The dashed line represents the approximate solution (Sheth and Tormen (2002) equation) to the probability of first crossing distribution of a square-root barrier. We chose to use the approximate solution for the square root barrier because easier to plot considering that the exact solution involve the use of the parabolic cylinder function and its eigenvalues. As can be seen in figures at high redshifts the agreement between

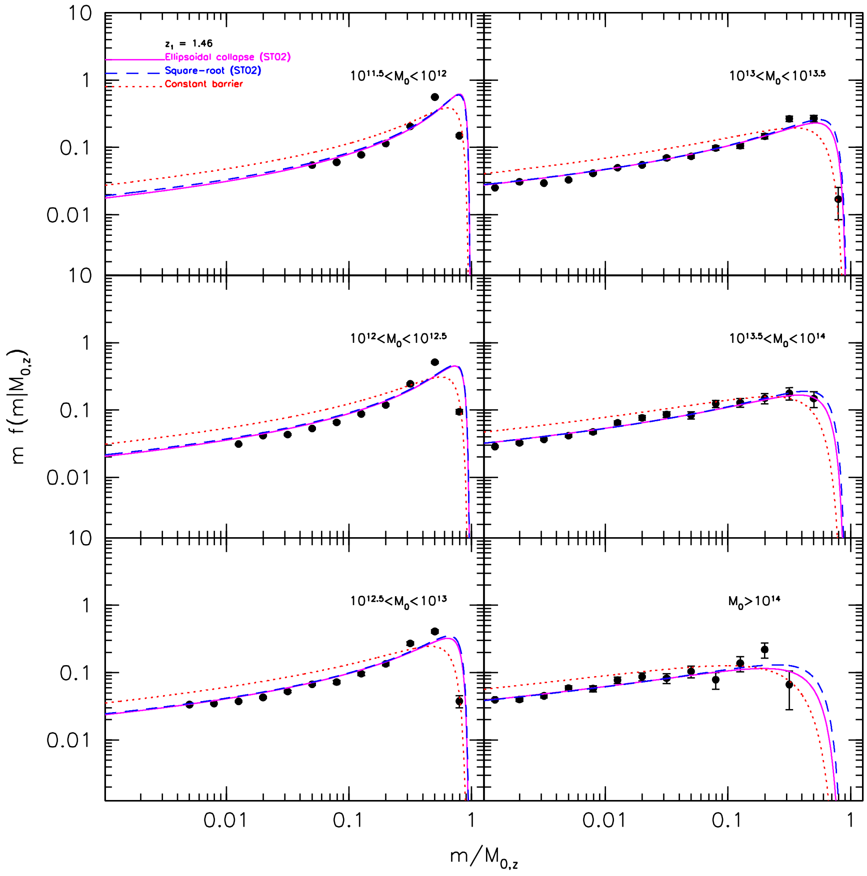

Figure 4.13: As in Figure 4.11 with $z_1 = 1.46$.

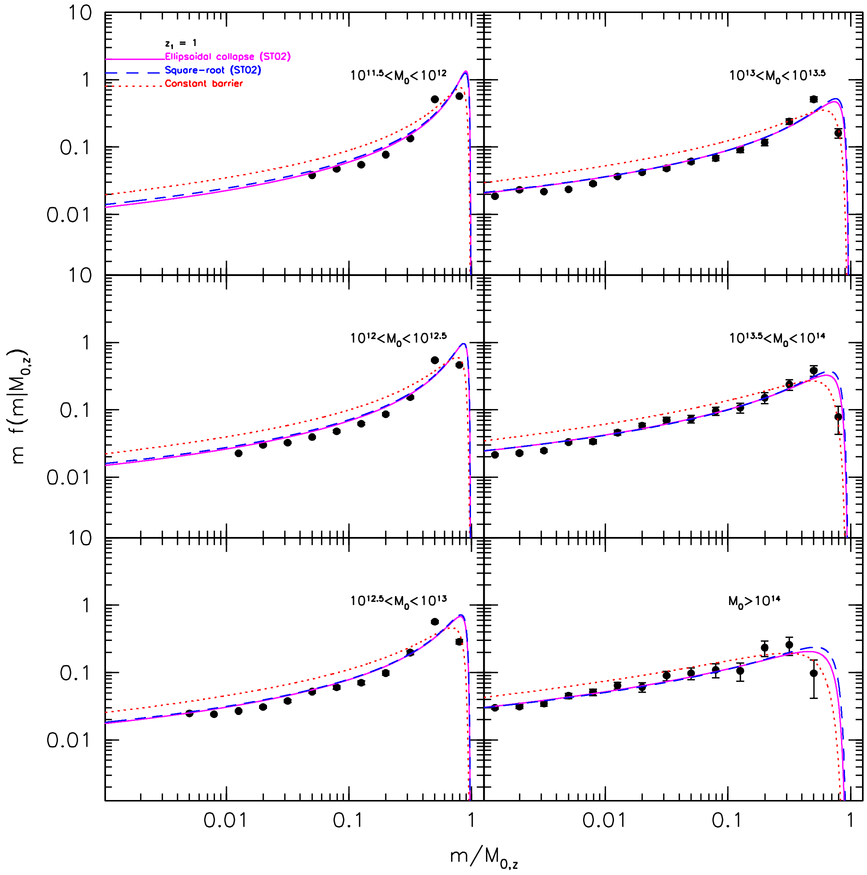

Figure 4.14: As in Figure 4.11 with $z_1 = 1$.

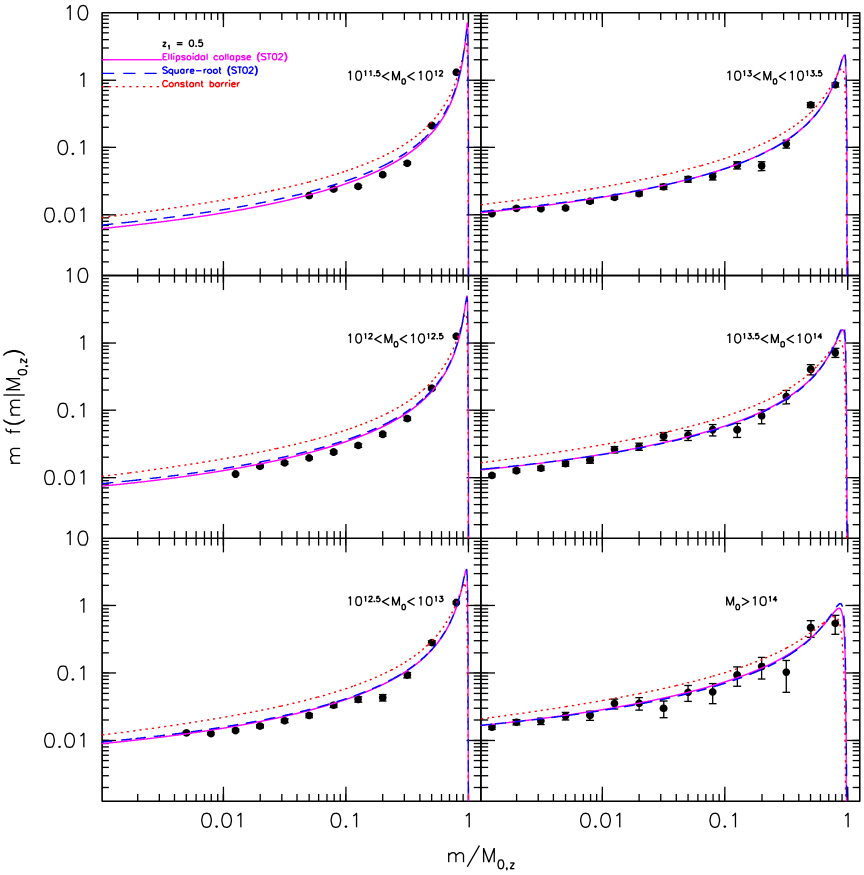

Figure 4.15: As in Figure 4.11 with $z_1 = 0.5$.

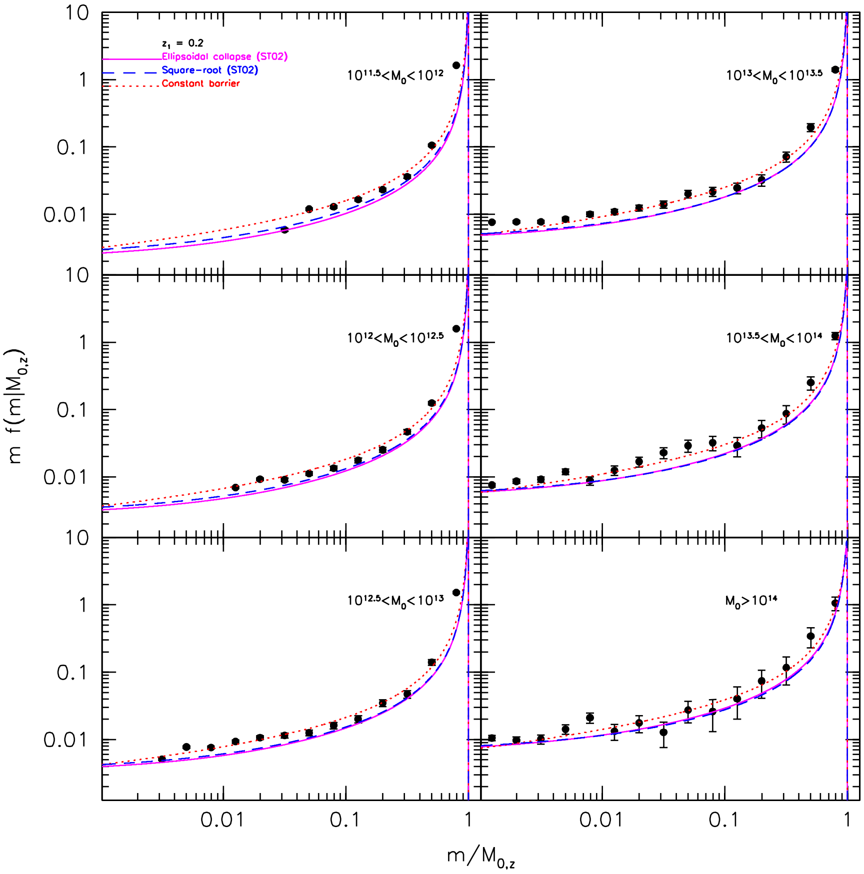

Figure 4.16: As in Figure 4.11 with $z_1 = 0.2$.

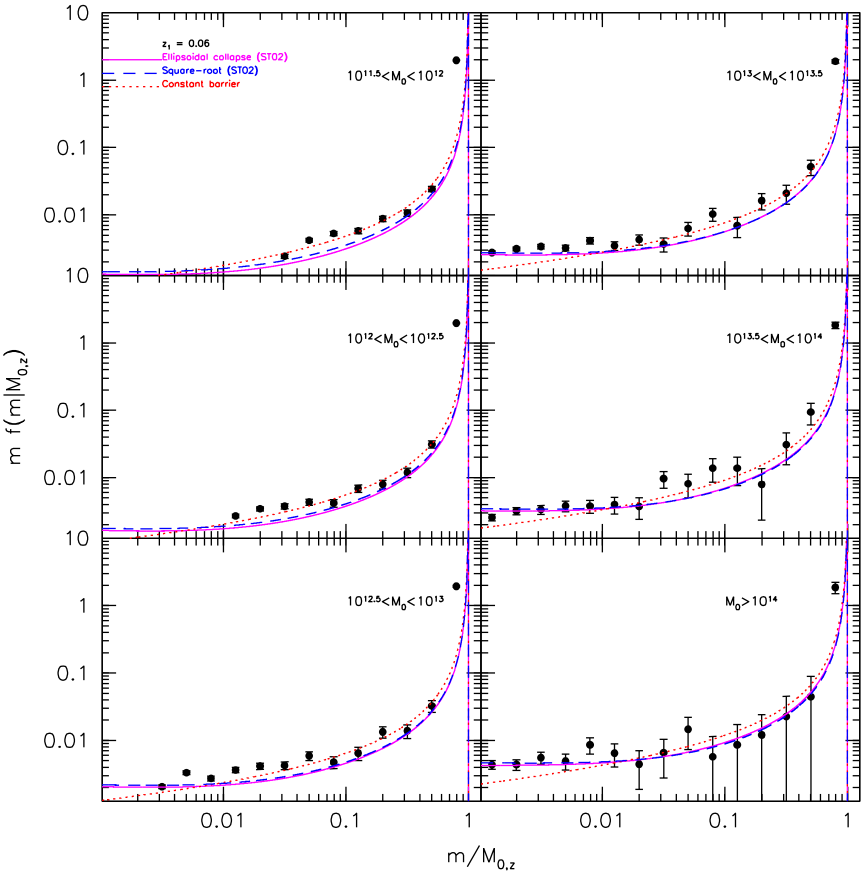

Figure 4.17: As in Figure 4.11 with $z_1 = 0.06$.

N-Body simulation and ellipsoidal collapse prediction is satisfying. However at large mass the scatter and the discrepancy is larger because of the few number of progenitors. At small redshift too the Sheth and Tormen (2002) conditional mass function describe the N-Body results quite well as can be seen in Figure 4.17 where progenitors in the lowest redshift before $z = 0$ have been considered.

CHAPTER

5

An Improved Model for the Formation Times of Dark Matter Haloes

Large samples of galaxy clusters selected in the optical (Miller *et al.*, 2005; McKay *et al.*, 2005) and other bands (ACT, SPT) will soon be available. These cluster catalogs will be used to constrain cosmological parameters. The tightness of such constraints depends on the accuracy with which the masses of the clusters can be determined from observed properties. These properties are expected to depend on the formation histories of the clusters. Models of cluster formation identify clusters with massive dark matter haloes, so understanding cluster formation requires an understanding of dark halo formation.

There is also some interest in using the distribution of galaxy velocity dispersions (Sheth *et al.*, 2003) to constrain cosmological parameters (Newman and Davis, 2002). The velocity dispersion of a galaxy is expected to be related to the concentration of the halo which surrounds it, and this concentration is expected to be influenced by the formation history of the halo (Tormen, 1998; Bullock *et al.*, 2001; Wechsler *et al.*, 2002). Hence, this program also benefits from understanding the formation histories of dark matter haloes.

In hierarchical models, the formation histories of dark matter haloes are expected to depend strongly on halo mass – massive haloes are expected to have formed more recently (Press and Schechter, 1974). But quantifying this tendency requires a more precise definition of what one means by the 'formation time'. Lacey and Cole (1993) provided a simple definition – it is the earliest time when a single progenitor halo contains half the final mass. For this definition, they showed how to estimate the distribution of halo formation times. Sheth and Tormen (2004) provide associated expressions for the joint distribution of formation time and the mass at formation. This estimate depends on the distribution of progenitor masses at earlier times, and Lacey & Cole used the assumption that haloes form from a spherical collapse to estimate this conditional mass function. However, a model based on ellipsoidal collapse provides a more accurate description of the abundances of dark haloes (Sheth *et al.*, 2001) and of their progenitors (Sheth and Tormen, 2002) (see also section 4.4 of the Chapter 4). Hence, one expects to find that the ellipsoidal collapse model also provides a better description of halo formation.

In the following section we reviews Lacey & Cole's argument and their definition of formation time.

Hereafter we will use z, t and δ_{sc} at the same way, referring to a time variable. It is also important to remember that while z and δ_{sc}, from the present-time, are increasing variable t is a decreasing one.

5.1 Distribution of Formation Times

Following Lacey and Cole (1993), we will define the formation time of a halo as the earliest time that at least half of its mass has been assembled into a single progenitor.

Relation to the Progenitor Mass Function

Consider an ensemble of haloes of mass M at time T, and let $N(m,t|M,T)$ denote the average number of progenitors of these haloes that have mass $m < M$ at time $t < T$. Since a halo can have at most one progenitor of mass $m > M/2$, the fraction of haloes which have a progenitor of mass $m > M/2$ at time t is

$$\int_{M/2}^{M} \mathrm{d}m\, N(m,t|M,T).$$

But, because they have a progenitor of mass $m > M/2$, these haloes are also the ones which formed at some $t_\mathrm{f} < t$. Hence,

$$P(<t_\mathrm{f}) = \int_0^{t_\mathrm{f}} \mathrm{d}t\, p(t|M,T) = \int_{M/2}^{M} \mathrm{d}m\, N(m,t_\mathrm{f}|M,T), \tag{5.1}$$

where $p(t|M,T)$ denotes the probability that a halo of mass M at T formed at time t. Differentiating with respect to t_f yields

$$\begin{aligned} p(t_\mathrm{f}|M,T) &= \frac{\mathrm{d}}{\mathrm{d}t_\mathrm{f}} \int_{M/2}^{M} \mathrm{d}m\, N(m,t_\mathrm{f}|M,T) && (5.2)\\ &= \int_{M/2}^{M} \mathrm{d}m\, \frac{\mathrm{d}N(m,t_\mathrm{f}|M,T)}{\mathrm{d}t_\mathrm{f}}. && (5.3) \end{aligned}$$

Evidently, the formation time distribution is closely related to the distribution of progenitor masses and its evolution. Different estimates of the progenitor mass function will result in different formation time distributions.

In what follows, we will estimate the distribution of halo formation times using equation (5.2) and analytically for a white-noise power spectrum, where $s(M) \propto 1/M$. Thinking along the lines of equation (5.3) instead shows how $p(t_\mathrm{f}|M,T)$ can be related to quantities which arise naturally in binary merger models of hierarchical clustering.

Spherical Collapse Dark Matter Haloes Formation Time

Lacey and Cole (1993) used the equation (4.6) to estimate $N(m,t|M,T)$, which was derived from a model in which haloes form from a spherical collapse (Gunn and Gott, 1972; Press and Schechter, 1974). Considering a white-noise power spectrum, $P(k) \sim k^n$ with $n = 0$, the number of progenitors halo can be written as:

$$N(m,t_{\rm f}|M,t)\mathrm{d}m = \frac{s}{S} f(s,\delta_{\rm f}|M,\delta_{sc,0})\mathrm{d}s\,, \tag{5.4}$$

where $\delta_{sc,0} = \delta_{sc}(T)$ and $\delta_{\rm f} = \delta_{sc}(t_{\rm f})$. The cumulative distribution of formation time, defining $\Delta\delta = (\delta_{\rm f} - \delta_{sc,0})$ can be written as:

$$P(<t_{\rm f}) = \frac{1}{\sqrt{2\pi}} \int_{2S}^{S} \frac{s}{S} \frac{\Delta\delta}{(s-S)^{3/2}} \exp\left[\frac{\Delta\delta^2}{2(s-S)}\right]\mathrm{d}s\,; \tag{5.5}$$

and computing the integral

$$\frac{1}{\sqrt{2\pi}S} \exp\left(-\frac{\Delta\delta^2}{2S}\right)\left\{2\sqrt{S}\Delta\delta - \exp\left(\frac{\Delta\delta^2}{2S}\right)\sqrt{2\pi}(S-\Delta\delta^2)\,\mathrm{erf}\left(\frac{\Delta\delta}{2S}\right)\right\}. \tag{5.6}$$

Defining

$$\omega = q\frac{\delta_{\rm f} - \delta_{sc,0}}{\sqrt{s(M/2) - s(M)}}\,, \tag{5.7}$$

where in the spherical collapse case $q = 1$, we can write [1]:

$$P(>\omega) = \sqrt{\frac{2}{\pi}}\,\omega\,\mathrm{e}^{-\omega^2/2} + (1-\omega^2)\,\mathrm{erfc}\left(\frac{\omega}{\sqrt{2}}\right). \tag{5.8}$$

and for the differential distribution of formation redshift, taking the derivative of the previous expression:

$$p(\omega) = 2\omega\,\mathrm{erfc}(\omega/\sqrt{2})\,. \tag{5.9}$$

Let us remember that here $\delta_{sc}(t) = \delta_{sc}(z)$ is the overdensity required for spherical collapse at z, and $s(M)$ is the variance in the linear fluctuation field when smoothed with a top-hat filter of scale $R = (3M/4\pi\bar{\rho})^{1/3}$, where $\bar{\rho}$ is the comoving density of the background. In hierarchical models, $s(M)$ is a monotonically decreasing function of mass M. In essence, ω is simply a scaled time variable: in an Einstein de-Sitter background cosmology $\omega \propto (z_{\rm f} - z_0)$, where the constant of proportionality depends on the final mass M.

Strictly speaking, this expression is valid for a white-noise power spectrum ($S(M) \propto M^{-1}$), but it has been found to provide a reasonable approximation for more general power spectra as well (see Figure 5.1 where has been plotted the formation redshift distribution for four scale-free power spectrum, from bottom to top at the peak $n = -2$, $n = -1$, $n = 0$ and $n = 1$). For the withe-noise distribution, the median value of ω is 0.974 considering the cumulative distribution as in the equation (5.8).

---

[1] Remember that $\mathrm{erf}(x) = 1 - \mathrm{erfc}(x)$.

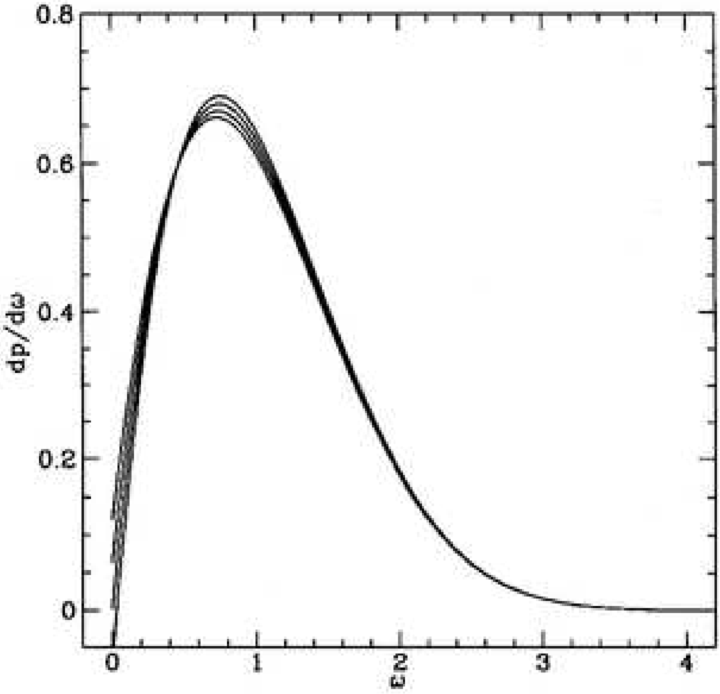

Figure 5.1: Spherical collapse formation redshift distribution for four different scale-free power spectrum. From bottom to top at the peak $n = -2$, $n = -1$, $n = 0$ and $n = 1$.

However, recent work has shown that the spherical collapse model predicts fewer massive haloes and more intermediate mass haloes than are seen in simulations of hierarchical gravitational clustering (Sheth and Tormen, 1999). Models in which haloes form from an ellipsoidal collapse may be more accurate (Sheth *et al.*, 2001). These models also provide a better description of the progenitor mass function (Sheth and Tormen, 2002).

In what follows, we will show the effects of substituting the ellipsoidal collapse based expressions for $N(m,t|M,T)$ in equation (5.1). We will also show that simply taking values of q smaller than one will make equation (5.8) a good fit to the formation redshift associated to the ellipsoidal collapse.

Progenitor Mass Functions in the Excursion Set Approach

We will use two approximations for the progenitor mass function. Both forms are derived from casting the ellipsoidal collapse model in the same language used for the spherical model – the excursion set formalism of Bond *et al.* (1991). In this formalism, as said in the previous chapters, halo abundances at a given time are associated with the first crossing distribution by Brownian motion random walks, of a barrier whose height decreases with time, and may in addition depend on how many steps the walk has taken. Hereafter we will use $\delta_{sc,0}$ and $\delta_{sc,1}$ to indicate the overdensity associated with the spherical collapse model respectively at redshift z_0 and z_1.

In the excursion set approach, the shape of the barrier, $B(S)$, depends on the collapse model. If the barrier is crossed on scale $S(M)$, then this indicates that the mass element on which the sphere is centered will be part of a collapsed object of mass M. Bond et al. used the fraction of walks which cross $B(S)$ at $S(M)$ as an estimate of the fraction of mass in haloes of mass M: the parent halo mass function. Similarly, the fraction $f(s|S)$ of walks which start from some scale $S(M)$ and height $B(S)$ and first cross the barrier $B(s)$ at some $s > S$, can be used to provide an estimate of the progenitor mass function of M haloes:

$$N(m|M)\,\mathrm{d}m = \left(\frac{M}{m}\right) f(s|S)\,\mathrm{d}s \tag{5.10}$$

(note that $m < M$ because $s > S$). Thus, in the excursion set approach, the shape of $N(m|M)$ depends on how the shape of the barrier changes with mass – it is in this way that the collapse model affects the parent halo and progenitor mass functions.

The barrier shape is particularly simple for the spherical model: $B = \delta_{sc}$ is the same constant for all values of S. For the ellipsoidal collapse we will refer to the equation (3.27) using the value of the parameters as determined by Sheth *et al.* (2001).

It is known that for general γ, exact analytic solutions to the first crossing distribution of a moving barrier are not available. For this reason, we have studied two analytic approximations which result from addressing the first crossing problem in two different ways. The first approach uses an analytic approximation to the first crossing distribution which Sheth and Tormen (2002) showed was reasonably accurate.

Our second approach is to substitute the ellipsoidal collapse barrier, as showed at the end of the previous chapter, for one which is similar, but for which an exact analytic expression for the first crossing distribution is available. Specifically, when $\gamma = 1/2$, then the barrier height increases with the square-root of S, and the first crossing distribution can be written as a sum of parabolic cylinder functions (Breiman 1966). In this approach, we approximate the progenitor mass function using an expression which would be exact for a square-root barrier, bearing in mind that the square-root barrier is an approximation to the ellipsoidal collapse dynamics. For this barrier shape, we set $\beta = 0.5$ and $q = 0.55$ since these choices result in parent halo and progenitor mass functions which best fit the simulations; Figure 4.8 illustrates the similarity of the barrier shapes. We have also shown in the Figure 4.11, 4.12, 4.13, 4.14, 4.15, 4.16 and 4.17 of the Chapter 4, that both these approximations provide substantially better descriptions of the simulations than does the expression which is based on spherical collapse. We will show that this is true also for the formation redshift distribution.

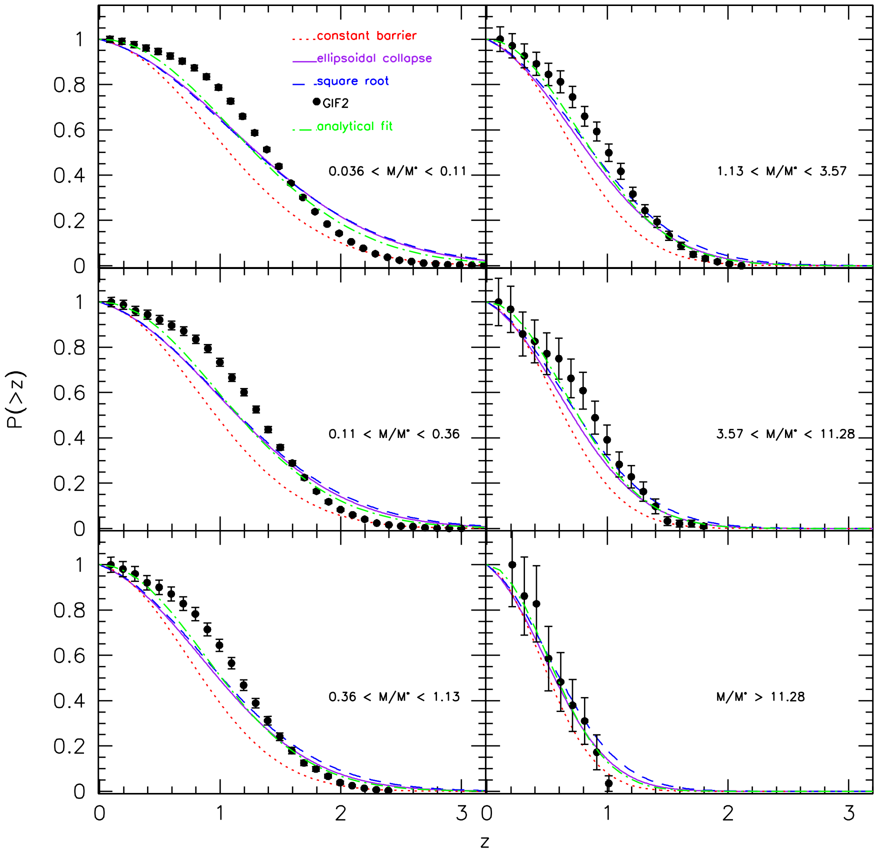

Figure 5.2: Cumulative distribution of dark halo formation times for haloes identified at $z = 0$. From top to bottom, panels show results for haloes with masses in the range $\log_{10} M/h^{-1}M_{\odot}$: 11.5 – 12, 12 – 12.5, 12.5 – 13, 13 – 13.5, 13.5 – 14 and > 14. Symbols show the measurements in GIF2; dotted curve shows the prediction associated the constant barrier spherical collapse model; dot-dashed curve shows the analytical fit equation (5.8) with $q = 0.707$. Short-dashed and solid curves show the predictions associated with the square-root and ellipsoidal collapse based models.

5.2 Comparison with N-Body Simulations

We use the data from GIF2 simulation to make a comparison with the analytical prediction of the formation redshift distribution. The simulation has been described in the section 4.2 of the Chapter 4 and we recall that the row data are publicly available at: *http://www.mpa-garching.mpg.de/Virgo*.

The GIF2 simulation followed the evolution of 400^3 particles in a periodic cube 110 h^{-1} Mpc on a side. At each simulation snapshot the haloes have been unidentified with the SO criteria and their story has been followed backward in time as described in the section 4.3 of the Chapter 4. The results presented here take into account all the haloes more massive than $10^{11.5}\,h^{-1}M_{\odot}$ (i.e., containing more than 180 particles) at $z = 0$ with the condition that their main progenitor at

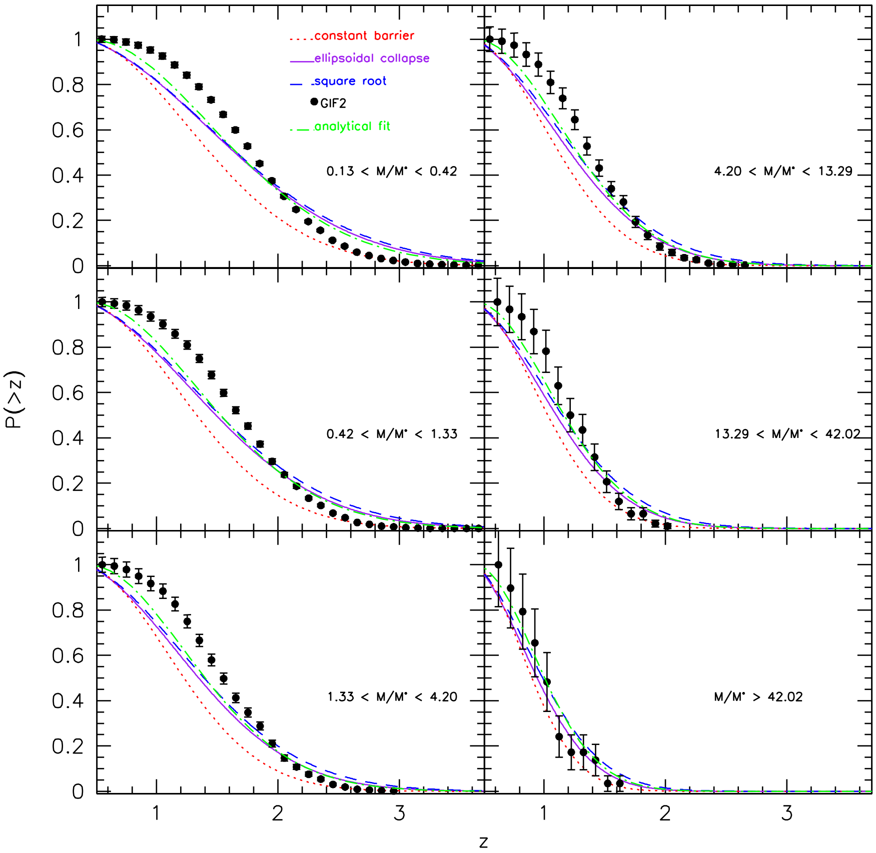

Figure 5.3: Same as previous figure, but now for haloes identified at $z = 0.5$. As before, the spherical model predicts lower formation redshifts than observed. Whereas the ellipsoidal collapse based expressions predict the median formation redshift reasonably well, they predict a broader range of redshifts than are observed.

any time $z > 0$ has to be smaller than the present-day mass.

Cumulative Distribution of Formation Times

Figure 5.2 shows the cumulative distribution of dark halo formation redshifts (i.e., equation 5.1) for haloes identified at $z = 0$. In general the analytical expressions obtained from the two different approximate solutions to the ellipsoidal collapse barrier problem – the Sheth and Tormen (2002) approximation for the first crossing distribution of the ellipsoidal collapse barrier, or the exact expression for the first crossing distribution of the square root barrier – are complicated. However, we have found that the predictions of the two ellipsoidal based models are quite well approximated by the expression for the spherical model with $n = 0$, equation (5.8), by simply changing the value of q.

Different panels show results for the mass bins described above. The points show measurements in the GIF2 simulation, and the four curves show the forma-

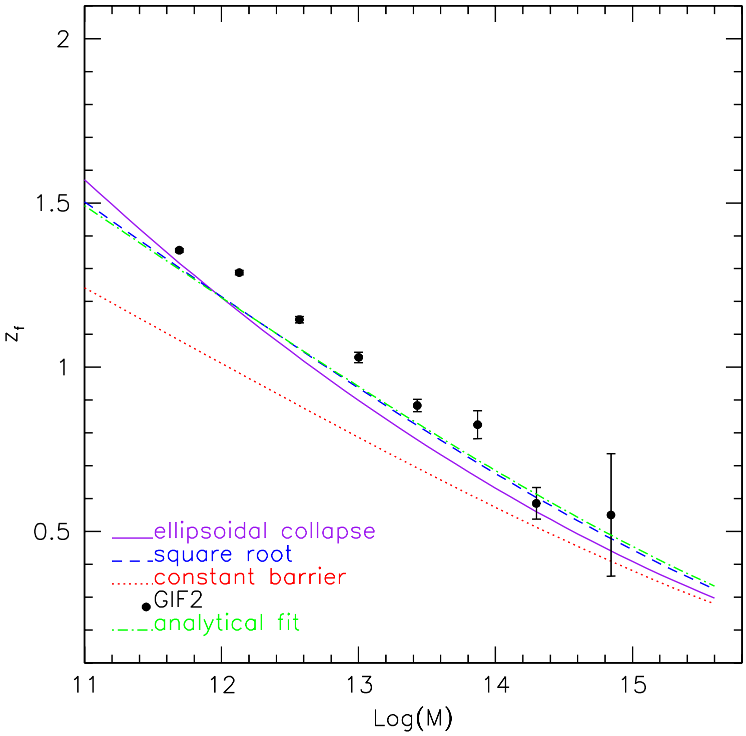

Figure 5.4: Median formation redshift for haloes identified at $z = 0$ as a function of halo mass. Points with (Poisson) error bars show our measurements in the GIF2 simulation. Smooth curves show the median formation times associated with three different models of halo formation: spherical collapse (dotted), ellipsoidal collapse (solid) and the square-root barrier approximation (short-dashed). Dot-dashed curve shows the prediction of equation (5.12) with $q = 0.707$.

tion time distributions associated with the ΛCDM spherical collapse (dotted), ellipsoidal collapse (solid), square-root barrier approximation (dashed) and with equation (5.8) using $q = 0.707$ (dot-dashed).

Again, the spherical collapse model severely underestimates the redshifts of halo formation. The two ellipsoidal collapse based estimates fare better, in the sense that they predict median formation redshifts which are closer to those seen in the simulation.

However, both ellipsoidal based estimates clearly predict a wider range of formation redshifts than is seen in the simulation – at fixed mass, the distribution of halo formation redshifts is narrower than predicted. This remains true for the formation time distribution of haloes identified at $z = 0.5$ shown in Figure 5.3.

Mass-Dependence of Median Formation Time

Figure 5.4 shows the median formation redshift of haloes identified at $z = 0$ as a function of halo mass. Points show our measurements in the GIF2 simulation. The simulation shows that massive haloes formed more recently: the median

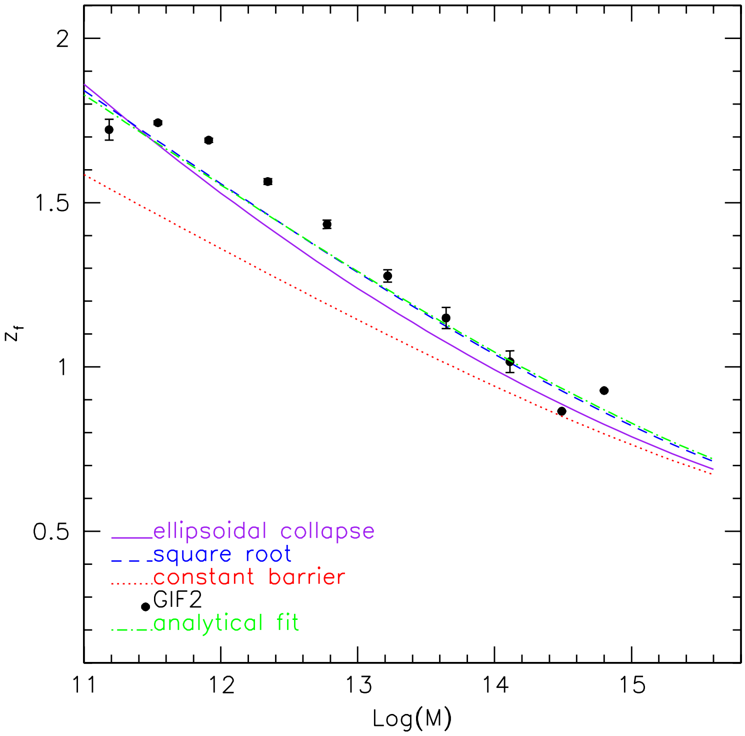

Figure 5.5: Same as previous Figure, but for haloes identified at $z = 0.5$ in the GIF2 simulation.

formation redshift decreases with halo mass.

Smooth curves show the formation time distributions associated with three different models of halo formation: ΛCDM spherical collapse (dotted), ellipsoidal collapse (solid) and the square-root approximation (short-dashed). In all cases, the model predictions for the median formation redshift were obtained by finding that $\bar{z}_f$ at which

$$\int_{M/2}^{M} \mathrm{d}m\, N(m, z_\mathrm{f}|M, z) = \frac{1}{2}. \tag{5.11}$$

The Figure shows that haloes less massive than $10^{14}h^{-1}M_\odot$ clearly form at higher redshifts than predicted by the spherical collapse model (dotted line). Both our estimates of the ellipsoidal collapse prediction are in substantially better agreement with the simulations. The prediction associated to equation (5.8) is given implicitly by inserting the median rescaled formation redshift $\bar{\omega} = 0.974$ into equation (5.7), providing:

$$\delta_{sc}(\bar{z}_\mathrm{f}|M, z_0) = \delta_{sc}(z_0) + \frac{0.974}{\sqrt{q}}\sqrt{S(M/2) - S(M)}. \tag{5.12}$$

The choice $q = 0.707$ is shown by the dot-dashed line in the Figures; setting $q = 0.6$ yields even better agreement with the simulations.

Fitting functions, accurate to a few percent, for $\delta_{sc}(z)$ and $S(m)$ are available in the literature. For instance,

$$\delta_{sc}(z) \approx D_+(z)\,\frac{3}{20}\,(12\pi)^{2/3}\,\Omega_m^{0.0055} \tag{5.13}$$

Navarro *et al.* (1997), where Ω_m is the ratio of the background to the critical density at z, and

$$D_+(z) = \frac{5}{2}\Omega_m\left[\Omega_m^{4/7} - \Omega_\Lambda + \left(1+\frac{1}{2}\Omega_m\right)\left(1+\frac{1}{70}\Omega_\Lambda\right)\right]^{-1} \tag{5.14}$$

Carroll *et al.* (1992), and, for a CDM power spectrum,

$$S(m) = A\left(1 + 2.208\bar{m}^p - 0.7668\bar{m}^{2p} + 0.7949\bar{m}^{3p}\right)^{-4/(9p)} \tag{5.15}$$

Taruya and Suto (2000), where A is the normalization factor of the linear theory power spectrum at $z = 0$ (so it depends on σ_8), $\bar{m} = m(h\Gamma)^2/10^{12}M_\odot$, where Γ is the parameter which describes the shape of the power spectrum (typically $\Gamma \approx \Omega h$), and $p = 0.0873$.

5.3 Discussion

Lacey and Cole (1993) defined the formation time of an object as the earliest time when at least half its mass was assembled into a single progenitor. We clarified the relation between this definition of formation time, and a quantity which arises in binary merger models of clustering (see Appendix B). We have shown that insertion of spherical collapse based expressions in Lacey & Cole's (1993) formalism for halo formation underestimates the redshifts of halo formation; this is consistent with previous work Lin *et al.* (2003). Ellipsoidal collapse based expressions are a marked improvement: although they result in formation redshift distributions which are broader than seen in simulations (Figures 5.2 and 5.3), they predict the median formation redshift quite well (Figure 5.4 and 5.5).

The fact that our predicted formation time distributions are broader than those seen in the simulation can be traced back to the fact that the low redshift progenitor mass functions from the excursion set approach are not in particularly good agreement with the simulations. This is similar to the findings of Sheth and Tormen (2002), who noted that some of the discrepancy was almost certainly due to the idealization that the steps in the excursion set walks are uncorrelated. Recent work has shown that there is some correlation between halo formation and environment (Sheth and Tormen, 2004; Gao *et al.*, 2005; Harker *et al.*, 2006; Wechsler *et al.*, 2006) – this almost certainly indicates that a model with uncorrelated steps will be unable to provide a better description of the simulations. Nevertheless, the fact that the median formation redshifts are quite well reproduced by our model does represent progress.

Although the exact expressions associated with our models are complicated, we was able to find a useful fitting formula for the median formation redshift, equation (5.12), which we hope will be useful in studies which relate the formation times of haloes to observable quantities.

Substructure Population in Dark Matter Haloes

CHAPTER

6

Analytical Approach to Subhalo Population in Dark Matter Haloes

The present-day description of the universe includes the presence of a large amount of cold dark matter (CDM) whose nature and distribution is unknown. This Dark Matter (DM) provides about 26% of the energy budget of the universe.

The amount and properties of CDM is well constrained by astrophysical observations such as the anisotropies in the Cosmic Microwave Background, large scale structure and distant type I A supernovae (Spergel *et al.*, 2003; Astier *et al.*, 2006; Tegmark *et al.*, 2006). On the other hand, two main open questions arise. The first concerns the particle physics nature of the CDM. Weakly interacting massive particles (WIMPs) are attractive candidates since their relic abundance can fit the observed one (Dimopoulos, 1990). Stable neutralinos in supersymmetric extensions of the standard model (SUSY) (Jungman *et al.*, 1996; Bertone *et al.*, 2005) or Kaluza-Klein particles (KKP) in theories with a TeV^{-1} size universal extra dimension (Appelquist *et al.*, 2001; Servant and Tait, 2003) are the most commonly studied particles. Since these particles have never been observed, there is a large uncertainty on the prediction of their effects which has to be taken into account. The other open question regards the distribution of DM inside the haloes. Numerical N-body simulations (Navarro *et al.*, 1997; Diemand *et al.*, 2004; Navarro *et al.*, 2004), whose scale resolution is about ~ 0.1kpc, allow solely an extrapolation of the very inner slope of the DM profile and do not take into account interactions with the baryons which fall in the DM potential well or the presence of inner cores (Berezinsky *et al.*, 2003) or the controverse effect of the presence of a black hole at the centre of the halo (Ullio *et al.*, 2001; Bertone and Merritt, 2005; Merritt *et al.*, 2002). Experimental data on DM distribution in the haloes of galaxies and clusters are not conclusive too (see, i.g., the discussion in Fornengo *et al.* (2004)). In the hierarchical formation scheme of the CDM scenario, large systems are the result of the merging and accretion of smaller haloes (subhaloes), whose dense central cores would survive the merging event and continue to orbit within the parent halo, as shown by high resolution N-body simulations (Moore *et al.*, 1999; Ghigna *et al.*, 2000; Blasi and Sheth, 2000). CDM models are characterized by an excess of power on small scales. The arising divergence of the linear density contrast at large wavenumbers has been proved to be damped by collisional processes and free streaming, respectively before and after kinetic decoupling, leading to exponential damping of the linear CDM density contrast and to the existence of a typical scale (Jeans scale) for the first haloes corresponding to a Jeans mass about $10^{-6}\,M_{\odot}$ (Hofmann *et al.*, 2001; Green *et al.*, 2004, 2005). Numerical simulations have indeed reproduced hierarchical clustering in CDM cosmologies with a mass resolution sufficient to resolve the Jeans mass (Diemand *et al.*, 2005) with particle mass $m_p = 1.2 \times 10^{-10}\,M_{\odot}$ and force resolution of $\epsilon = 0.01$ pc; however such a high resolution run could be evolved only to $z = 26$, in a very small spatial patch, and producing haloes of mass $[10^{-6}, 10^{-4}]\,M_{\odot}$.

Among the simulations evolved on larger scales and to redshift $z = 0$, present milestones are the Millennium Simulation (Springel *et al.*, 2005) and the Via Lactea Simulation (Diemand *et al.*, 2007a). The first is a cosmological N-Body run with over 10 billion particles in a cubic region 500 Mpc/h on a side (particle mass $m_p = 1.23 \times 10^9 M_{\odot}$; force resolution $\epsilon = 7$ kpc); the second was done to obtain a simulated Milky Way with the highest possible mass resolution (particle mass $m_p = 2.09 \times 10^3 M_{\odot}$; force resolution $\epsilon = 90$ pc). However a simulation with the mass and force resolution similar to that of (Diemand *et al.*, 2005), evolved to redshift zero over a region containing a mass comparable to that of our Galaxy would require about 10^{20} particles and a time resolution of a few years. Such requirements are way beyond the computational capabilities of present-day supercomputers: applying Moore's law and starting from present day state-of-the-art, a run like this could be performed in roughly 50 years from now.

A reasonable alternative is to study the clustering properties of Milky Way-like systems through an analytical approach. We use the fact that the probability that a halo of mass m at redshift z will be part of a larger halo of mass M at the present time is described by the progenitor conditional mass function $f(m, z|M, z_0 = 0)$, according to the so-called extended Press & Schechter theory. Using the progenitor mass function, we can calculate analytically, at redshift zero, the distribution of subhaloes in mass, formation epoch and rarity of the peak of the density field at the formation epoch. That is done for a Milky Way-size system, assuming both a spherical and an ellipsoidal collapse model.

Numerical simulations described in Diemand *et al.* (2005) show that the distribution of material originating from the earliest branches of the merger tree within the present day haloes depends on the σ-peaks of the primordial density fluctuation field it belonged to. We extend their numerical results by performing an analytical estimate of the density peaks distribution as a function of the halo mass traced back to the smallest scale haloes, thus avoiding the limitation imposed by numerical simulations. In this way we obtain a realistic estimate of the distribution and mass function of the whole population of subhaloes.

Such an analytical estimate can provide a powerful tool to take into account the effect of early high-density peaks in present day haloes.

This is particularly important in the framework of dark matter indirect detection, since a high σ-peak halo translates into a higher concentration and thus a higher value for the density squared which has to be integrated along the line of sight to obtain a prediction for particle fluxes coming from dark matter annihilation.

Given some model for the hierarchical formation of our Galaxy, and for the internal structure of subhaloes, DM may be in fact indirectly detected using annihilation rates predicted from particle physics (Bergström, 2000; Bertone *et al.*, 2005) through the observation of high density point-source or extended regions inside our Galaxy. If we restrict ourselves to γ-ray observations, these can be obtained using either atmospheric Cerenkov telescopes (Weekes *et al.*, 1997; Aharonian *et al.*, 1997; Baixeras, 2003) or satellite-borne detectors like GLAST (Morselli, 1997). The detectability of DM substructures with GLAST has been widely discussed in the literature (see, e.g. Pieri *et al.* (2007) and references therein). The small mass haloes have been found to give the main contribution to an unresolved γ-ray foreground arising from DM annihilation, while their detection as resolved objects has been proved to be very unlike. Indeed the unresolved subhalo foreground is prominent above the MW smooth foreground far from the Galactic Center, where the overall flux is still too low to be detected.

In this work we apply the analytical derivation of the subhalo population properties, such as the σ-peak distribution, on the indirect detection of γ-rays. We thus study the possibility that high σ-peak material could arise the foreground level above the detectability threshold of a GLAST-like large field of view satellite.

As in Pieri *et al.* (2007), we use different models for the virial concentration of subhaloes.

6.1 Extended Press & Schechter theory: from Progenitors to Subhaloes

In the hierarchical picture of galaxy formation, structures up to protogalactic scale grow as a consequence of repeated merging events. Smaller systems collapse at high redshifts, when the universe is denser, and subsequently assemble to form bigger and bigger haloes (Lacey and Cole, 1993). This merging history is often represented by the so called ”merger tree”.

Smaller systems accreted onto a larger halo along its merging-history-tree and still surviving at a later time are called ”substructures” or ”subhaloes” (Ghigna *et al.*, 1998; Tormen *et al.*, 2004; Gao *et al.*, 2004; De Lucia *et al.*, 2004; van den Bosch *et al.*, 2005). In what follows we will discuss an analytical approach to derive the mass function of subhaloes. We will use the simplifying assumption that no tidal stripping nor merging events among substructures happen. In this approach the mass of each subhalo remains constant in time, and equals the original virial mass (Eke *et al.*, 1996) of the progenitor halo at the considered redshift. A similar study was carried out by Sheth (2003), who calculated the subhalo mass function using the creation rate of the progenitors of a present day dark matter halo; our approach is different: we derive the subhalo mass function from the entire population of progenitors (as shown by eq. 6.3), in order to allow a direct comparison with the N-Body results of Diemand *et al.* (2005).

Conditional Mass Function

Let us consider a halo with virial mass M at some final redshift z_0. According to the hierarchical picture of galaxy formation, going backward in time the halo will be splitted in smaller and smaller systems, called ”progenitors”. Mass conservation tells us that the sum of all masses of progenitor haloes at any given redshift equals the mass of the halo at z_0. Let us define the conditional mass function $f(m,z|M,z_0)\mathrm{d}m$ as the fraction of mass belonging to haloes with mass between m and $m+\mathrm{d}m$ at redshift z, which are progenitors of a halo of mass M (a M-halo) at a later redshift z_0.

Assuming the spherical collapse model (Press and Schechter, 1974), we can express m and z as a function of the new variables s and δ_{sc} and write the conditional mass function, as in equation 4.6, that is:

$$f(s,\delta_{sc}|S,\delta_{sc,0})\mathrm{d}s = \frac{\delta_{sc}-\delta_{sc,0}}{\sqrt{2\pi(s-S)}}\exp\left\{-\frac{(\delta_{sc}-\delta_{sc,0})^2}{2(s-S)}\right\}\frac{\mathrm{d}s}{s-S}, \tag{6.1}$$

where $s=\sigma^2(m)$ is the square of the mass variance of a m-halo, and δ_{sc} is the spherical collapse overdensity at redshift z. S and $\delta_{sc,0}$ are the mass variance of an M-halo and the spherical collapse overdensity at the present time, respectively. To compute the mass variance we have chosen a power spectrum with primordial spectral index $n=1$, and a transfer function obtained from CMBFAST (Seljak and Zaldarriaga, 1996) for a concordance ΛCDM universe (Ω_m, Ω_Λ, $h=0.3, 0.7, 0.7$) with $\sigma_8=0.772$, extended down to a mass $M=10^6 M_\odot/h$.

We have integrated this power spectrum using a top-hat filter in real space. To obtain the mass variance until the typical Jeans neutralino mass we linearly extrapolate the log(m)-s relation to $M=10^{-6}M_\odot/h$.

Over the last ten years N-Body simulations have shown that the collapse of dark matter haloes is actually not well described by an isolated spherical model; the influence of surrounding proto-haloes can be reproduced using an ellipsoidal model (Sheth *et al.*, 2001; Sheth and Tormen, 2002), as discussed also in Section 4.4.

In the excursion set approach, the progenitor mass function of a halo is described by the conditional probability of first upcrossing distribution. Such a probability is well fitted by a random walk in the plane (s, δ), starting from (S, $\delta_{sc,0}$) (Bond *et al.*, 1991). Assuming a moving barrier, as in equation (3.27) – with $q=0.707$, $\beta=0.5$ and $\gamma=0.6$ – an approximate solution for the diffusion equation is as follows:

$$\begin{aligned} f(s,\delta_{sc}|S,\delta_{sc,0})\mathrm{d}s &= \frac{|T(s,\delta_{sc}|S,\delta_{sc,0})|}{\sqrt{2\pi(s-S)}}\times \\ &\quad \exp\left\{-\frac{[B(s,\delta_{sc})-B(S,\delta_{sc,0})]^2}{2(s-S)}\right\}\frac{\mathrm{d}s}{s-S}, \end{aligned} \tag{6.2}$$

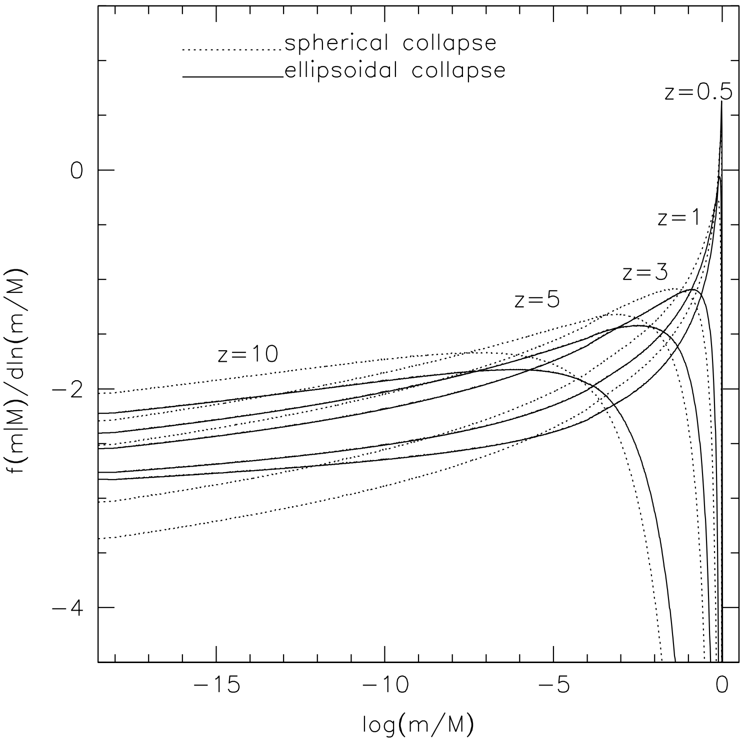

Figure 6.1: Ellipsoidal (solid curve) and spherical (dotted curve) conditional mass function computed for a present-day dark matter halo with mass $10^{12} M_{\odot}/h$ and for five different redshifts.

with $T(s|S)$:

$$T(s,\delta_{sc}|S,\delta_{sc,0}) = \sum_{n=0}^{5} \frac{(S-s)^n}{n!} \frac{\partial^n [B(s,\delta_{sc}) - B(S,\delta_{sc,0})]}{\partial s^n}.$$

In Figure 6.1 we show the conditional mass function at five different redshifts for a halo with present-day mass $M = 10^{12} M_{\odot}/h$, both for the spherical (dotted curves) and ellipsoidal (solid) collapse prediction. It can be observed that the halo is splitted in smaller and smaller progenitors at higher redshifts; discrepancies between the two models depend both on mass and on redshift.

Comparing the two prediction at fixed redshift, one can note that the spherical model predicts more progenitors at intermediate mass, and fewer at both very small and very large masses, compared to the ellipsoidal model (Sheth and Tormen, 2002). In other words, the two predictions cross each others in two points, although these crossings do not necessarily fall in the range of masses plotted in the figure.

A direct consequence of this is that massive progenitors exist at higher redshifts in the ellipsoidal collapse, and the distribution of formation redshifts (defined as the earliest epoch when a halo assembles half of its final mass in one system) is consequently shifted to earlier epochs (Giocoli *et al.*, 2007).

From $f(s,\delta_{sc}|S,\delta_{sc,0})\mathrm{d}s$ we can write the total number of progenitors at any given redshift as:

$$N(m,\delta_{sc}|M,\delta_{sc,0})\mathrm{d}m = \frac{M(S)}{m(s)} f(s,\delta_{sc}|S,\delta_{sc,0})\mathrm{d}s. \tag{6.3}$$

Considering a scale free power spectrum $P(k) \propto k^n$, the mass variance scales as $s(m) \propto m^{-(n+3)/3}$, and the number of progenitors can be explicitly written in terms of s:

$$N(m,\delta_{sc}|M,\delta_{sc,0})\mathrm{d}m = \left(\frac{s}{S}\right)^{(n+3)/3} f(s,\delta_{sc}|S,\delta_{sc,0})\mathrm{d}s. \tag{6.4}$$

Number of Progenitors

Integrating eq. (6.3) over mass we obtain the total number of progenitors in the given mass interval, as a function of redshifts:

$$\mathrm{d}N(z,\Delta m) = \int_{m_i}^{m_f} N(m,\delta_{sc}|M,\delta_{sc,0})\mathrm{d}m = \mathbb{N}(z)\Big|_{m_i}^{m_f}, \tag{6.5}$$

where m_i and m_f represent the bounds of the interval. For a white-noise power spectrum (scale free with $n = 0$) and a spherical collapse mass function, a primitive of this integral can be written as:

$$\begin{aligned} \mathbb{N}(z) \quad = \quad & \frac{1}{S\sqrt{2\pi}} \Bigg\{ \mathrm{e}^{-\dfrac{(\delta_{sc}-\delta_{sc,0})^2}{2(s-S)}} \\ & \Bigg[2\sqrt{s-S}(\delta_{sc}-\delta_{sc,0}) - \mathrm{e}^{\dfrac{(\delta_{sc}-\delta_{sc,0})^2}{2(s-S)}} \\ & \sqrt{2\pi}[S-(\delta_{sc}-\delta_{sc,0})^2]\mathrm{erf}\Big(\frac{\delta_{sc}-\delta_{sc,0}}{\sqrt{2(s-S)}}\Big)\Bigg]\Bigg\}. \end{aligned} \tag{6.6}$$

In Figure 6.2 we show the total number of progenitors in five different mass decades, for a halo with mass $M = 10^{12} M_{\odot}/h$ at z_0, as a function of redshifts. We have assumed a concordance ΛCDM power spectrum and have integrated eq. (6.3) numerically. The solid lines represent the prediction for the ellipsoidal collapse model while the solid ones refer to the ellipsoidal model. From top to bottom the curves represent the following mass bins: $[h\,10^{-6}, 10^{-5}]$, $[10^{-1}, 1]$, $[10^{2}, 10^{3}]$, $[10^{6}, 10^{7}]$ and $[10^{9}, 10^{10}]$, all but the first expressed in term of $M_{\odot}/h$.

It can be observed that the spherical collapse, for a fixed mass bin, underpredicts the number of haloes at high redshifts compared to the ellipsoidal model. We will see in the next sections that if we consider the variable $\nu(z,m) = \delta_{sc}(z)/\sigma(m)$, for any given mass this will result in the inequality $\nu_{ec}(m) > \nu_{sc}(m)$.

6.2 Unevolved Subhalo Mass Function

The progenitors mass function, integrated over δ_{sc}, gives the total number of progenitors of mass between m and $m + \mathrm{d}m$ that a halo of final mass M has had

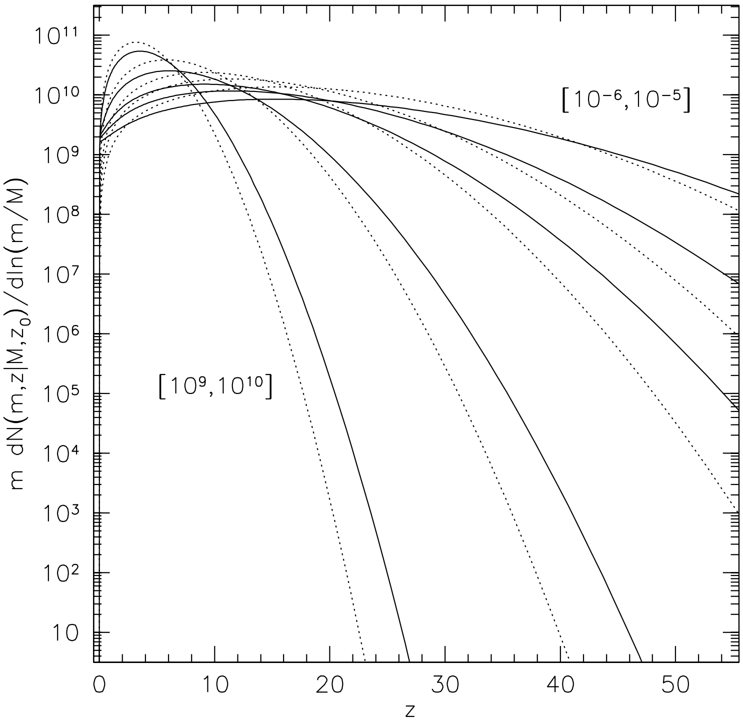

Figure 6.2: Total number of progenitors in a given mass bin, as a function of redshifts, for a present day halo with mass $M = 10^{12}\ M_{\odot}/h$. For each mass bin we show the prediction for spherical (dotted curves) and ellipsoidal (solid curves) collapse models.

at all times:

$$\frac{\mathrm{d}N(m)}{\mathrm{d}m} = \int_{\delta_{sc,0}}^{\infty} \frac{M}{m} f(s,\delta_{sc}|S,\delta_{sc,0})\mathrm{d}\delta_{sc}; \tag{6.7}$$

in the case of the spherical collapse this integral results in:

$$\frac{\mathrm{d}N(m)}{\mathrm{d}\ln(m)} = \frac{M}{\sqrt{2\pi}} \frac{|\mathrm{d}s/\mathrm{d}m|}{\sqrt{s-S}} \propto m^{-\alpha}, \tag{6.8}$$

with $\alpha \approx 1$ for a LCDM power spectrum. Since the same system may be a progenitor of the same final halo at more than one redshift, integrating the progenitor mass function overcounts the total number of progenitors. The result of this integration must then be properly re-normalized by imposing the constrain coming from (Diemand *et al.*, 2005) that roughly 10% of the total Milky Way mass ($M = 10^{12} M_{\odot}/h$) is in systems with mass ranging from 10^7 to $10^{10}\ M_{\odot}/h$:

$$\int_{10^{-5}}^{10^{-2}} \frac{m}{M} \mathrm{d}n = 0.1 \tag{6.9}$$

In Figure 6.3 we plot the differential mass distribution of subhaloes in a $10^{12}\ M_{\odot}/h$ (Milky Way-like) dark matter halo. The distribution has a power law behaviour

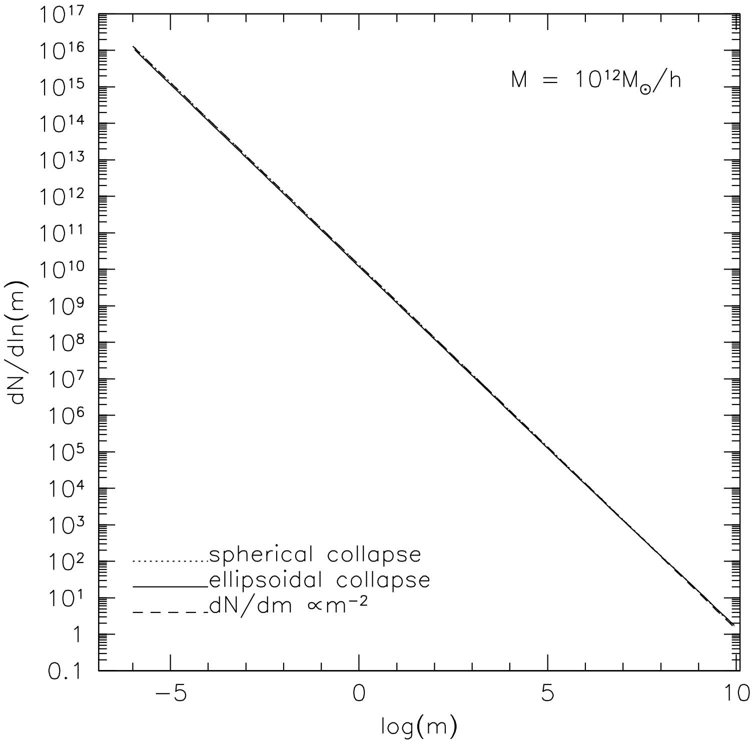

Figure 6.3: Differential distribution of subhaloes in a $10^{12}\ M_{\odot}/h$ dark matter halo. The distribution has a slope approximately equal to 1 and has been normalized considering that 10% of the total mass is in subhaloes with mass from 10^7 to $10^{10}\ M_{\odot}/h$.

approximately described by the relation:

$$\frac{\mathrm{d}N(m)}{\mathrm{d}m} = Am^{-\gamma}, \tag{6.10}$$

with $\gamma \approx 2$ for both the spherical and the ellipsoidal collapse model, respectively[1]. Once fixed the normalization factor, we find that the differential distribution of the subhaloes is independent on the mass of the progenitor halo, M, considering all the progenitors with mass from $10^{-6}\ M_{\odot}$ to $m/M = 0.01$.

Progenitor σ-peaks in the Host Halo

Using high resolution N-Body simulations, Diemand *et al.* (2005) studied the spatial distribution - at $z = 0$ - of matter belonging to high redshift progenitors of a given system. They found that this distribution mainly depends on the rareness of the density peak corresponding to the progenitor, expressed in terms of $\nu = \delta_{sc}/\sigma(M, z)$, and is largely independent on the particular value of z and M: matter from high ν progenitors ends up at smaller distances from the center of the final system.

---

[1] A least-squares fit on the points gives $\gamma_{\mathrm{sc}} = -1.9972 \pm 0.0001$ and $\gamma_{\mathrm{ec}} = -1.9937 \pm 0.0003$.

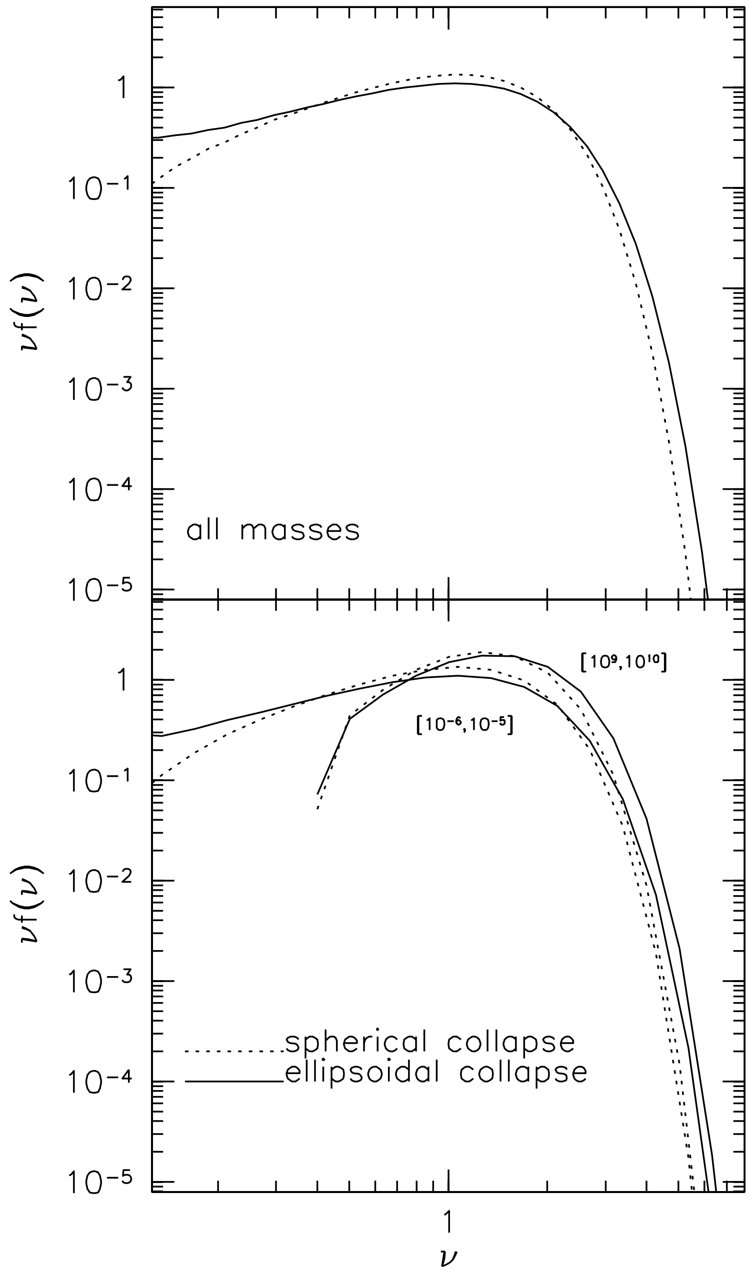

Figure 6.4: Progenitor mass function integrated over all redshifts. In the top panel we show the distribution for all the masses, while in the bottom panel we consider only progenitors in the first and last subhalo mass decades.

We can understand this in term of the revised secondary infall (Quinn and Zurek, 1988; Zaroubi *et al.*, 1996): the formation of haloes in N-Body simulations preserves ranking of particle binding energy, that is, particles in the cores of progenitor haloes will end up in the core of the final system. Equally, particles from progenitors accreted at earlier times, hence possessing more negative initial binding energies, will likely have a more negative final energy, and so be more centrally concentrated than average matter.

At fixed redshift (hence at fixed δ_{sc}), higher mass progenitors have a larger ν, are more self-bound than smaller mass ones, and thus end up closer to the center of the final system. Analogously, for a fixed progenitor mass, higher redshift progenitors have a larger δ_{sc}, hence a larger ν; since at higher redshift the universe is denser, they also are more self-bound than lower redshift siblings, and so end up closer to the center of final system.

In Figure 6.4 we plot the subhalo mass function in terms of ν. To compute the factor ν for each progenitor we integrated the total number of progenitors in a given mass bin (eq. 6.5), at all redshifts. In the top panel we consider all the progenitors at all redshifts, with mass in the full range $h10^{-6}$ to $10^{10}\ M_\odot/h$; in the bottom panel we show the similar distribution only for the smallest and larger decade of the progenitors mass.

6.3 γ-ray Flux from Galactic Substructures

Modeling the Galactic Halo and its Substructures

We model the distribution of DM in our Galaxy after Diemand *et al.* (2005).
For the smooth component of the Milky Way we use the best fit to the high resolution numerical experiments of Diemand *et al.* (2005):

$$\rho_\chi(r) = \frac{\rho_s}{\left(\frac{r}{r_s}\right)^\gamma \left[1+\left(\frac{r}{r_s}\right)^\alpha\right]^{(\beta-\gamma)/\alpha}} \tag{6.11}$$

with $(\gamma, \beta, \alpha) = (1.2, 3, 1)$. The scale radius r_s and density ρ_s, are constrained by the virial properties of the halo. Following Diemand *et al.* (2005) we adopt $r_s = 26$kpc, while ρ_s has to be normalized to the virial mass of the smooth DM halo. We include a physical cutoff $r_{cut} = 10^{-8}$kpc which represents the distance at which the self-annihilation rate equals the dynamical time of spike formation.

We shape the spatial distribution of subhaloes according to the fact that it traces the mass distribution of the parent halo from R_v down to a minimum radius $r_{min}(M)$ where tidal effects become important. We use eq. (6.11) together with the fact that the dependence from the initial conditions when the haloes accreted onto the present-day Milky Way halo is set through the parameter $\nu(M)$. We then use the parametrization obtained in Diemand *et al.* (2005):

$$r_s \longrightarrow r_\nu = f_\nu r_s$$

$$f_\nu = \exp(\nu/2)$$

$$\beta \longrightarrow \beta_\nu = 3 + 0.26\nu^{1.6} \tag{6.12}$$

This parametrization reflects the fact that material accreted in areas with high density fluctuations is more concentrated toward the centre of the galaxy, and has a steeper outer slope. We also use the mass function derived in Sec. 6.1 to model the number density of subhaloes per unit mass at a distance r from the GC, for a given $\nu(M)$:

$$\rho_{sh}(M,r,\nu) = \frac{AM^{-2}\theta(r - r_{min}(M))}{\left(\frac{r}{r_\nu(M)}\right)^\gamma \left[1 + \left(\frac{r}{r_\nu(M)}\right)^\alpha\right]^{(\beta_\nu-\gamma)/\alpha}}, \tag{6.13}$$

in units of $M_\odot^{-1}\text{kpc}^{-3}$. The mass dependence in r_ν depends reflects the mass dependence of the virial parameter $r_s = R_v/c_v$. The effect of tidal disruption is taken into account through the step function $\theta(r - r_{min}(M))$, where $r_{min}(M)$ is estimated following the Roche criterion. A is a normalization factor obtained by imposing that 10% of the MW mass is distributed in subhaloes with masses in the range $10^7 - 10^{10} M_\odot$ (Diemand *et al.*, 2005) as in Sec.6.1.

As a result about 50% of the Milky Way mass is contained within $\sim 2 \times 10^{16}$ subhaloes in the mass range $[10^{-6}, 10^{10}]M_\odot$. The solar neighborhood density is $\sim 280\text{pc}^{-3}$, mainly constituted by haloes with mass of $10^{-6}M_\odot$. The halo closest to the Earth is expected to be located $\sim 9.5 \times 10^{-2}$pc away.

The remaining 50% of the Milky Way mass is assumed to be smoothly distributed, and we use this half mass value to normalize ρ_s in eq. (6.11).

Few constraints exist on the density profile of each subhalo. Numerical simulations (Diemand *et al.*, 2005, 2006, 2007b) suggest they were formed with a NFW profile, which is described by eq. (6.11) with $(\gamma, \beta, \alpha) = (1, 3, 2)$. Even if subhaloes probably underwent tidal stripping and consequent mass loss after merging, their higher central density should prevent the inner regions from being affected. Pieri *et al.* (2007) explored different possibilities for the concentration parameter $c_v = R_v/r_s$, where R_v is defined as the radius at which the mean halo density is 200 times the critical density. Following their guidelines, we use two models for the concentration c_v: we assume that the inner structure of subhaloes is either fixed at the time they merge onto the parent halo (z-labeled model) or that it evolves with redshift until the present time (0 model). In model $\text{B}_{ref,0}$ the NFW concentration is computed at $z = 0$ according to Bullock *et al.* (2001) (hence the prefix B), and extrapolated to low masses. In model $\text{B}_{ref,z}$, the values of $c_v(M,z)$ are obtained from those at $z = 0$ using the evolutionary relation $c_v(M,z) = c_v(M,z=0)/(1+z)$, where the merging redshift z is determined by the knowledge of the value of ν assigned to each progenitor. Therefore, subhaloes are much denser in model $\text{B}_{ref,z}$than in model $\text{B}_{ref,0}$.

The values c_v thus found refer to progenitors formed from average density fluctuations ($\nu = 1\sigma$ peaks of the fluctuation density field). However, haloes with equal mass at redshift z_1 may have assembled at different previous epochs; specifically, if we call $z_i > z_1$ the redshift of mass assembly for progenitors observed at redshift z_1, the amplitude of the initial density fluctuations producing the progenitors is an increasing function of z_i. Therefore, their concentration $c(M,z)$ is also an increasing function of the peak amplitude ν. To account for this effect, we use the relation $c_v(M,\nu) = \nu(M) c_v(M,\nu=1)$, which has been tested against simulations by Diemand *et al.* (2005).

Modeling the γ-ray Flux from Dark Matter Annihilation

We model the photon flux from neutralino annihilation in the population of galactic subhaloes following Pieri *et al.* (2007). Given a direction of observation defined by the angle–of–view ψ from the Galactic Center, and a detector with angular resolution θ, the γ-ray flux can be parametrized as:

$$\frac{d\Phi_\gamma}{dE_\gamma}(E_\gamma,\psi,\theta) = \frac{d\Phi^{\mathrm{PP}}}{dE_\gamma}(E_\gamma) \times \Phi^{\mathrm{cosmo}}(\psi,\theta) \tag{6.14}$$

The particle physics dependence in eq. (6.14) is given by the annihilation spectrum and DM properties and is embedded in the term:

$$\frac{d\Phi^{\mathrm{PP}}}{dE_\gamma}(E_\gamma) = \frac{1}{4\pi}\frac{\sigma_{\mathrm{ann}} v}{2m_\chi^2} \cdot \sum_f \frac{dN_\gamma^f}{dE_\gamma} B_f. \tag{6.15}$$

m_χ is the DM particle mass, $\sigma_{\mathrm{ann}} v$ is the self–annihilation cross–section times the relative velocity of the two annihilating particles, and dN_γ^f/dE_γ is the differential photon spectrum for a given final state f with branching ratio B_f, which we take from Fornengo *et al.* (2004).

The line–of–sight integral defined as:

$$\begin{aligned}\Phi^{\mathrm{cosmo}}(\psi,\Delta\Omega) = \int_M dM \int_\nu d\nu \int\int_{\Delta\Omega} d\theta d\phi \int_{\mathrm{l.o.s}} d\lambda \int_c dc \\ [\rho_{sh}(M, R(R_\odot,\lambda,\psi,\theta,\phi),\nu) \times P(\nu(M)) \times P(c(M)) \times \\ \times \Phi^{\mathrm{cosmo}}_{halo}(M, r(\lambda,\lambda',\psi,\theta',\phi'),\nu,c) \times J(x,y,z|\lambda,\theta,\phi)]\end{aligned} \tag{6.16}$$

accounts for the influence of cosmology in the flux computation. $\Delta\Omega$ is the solid angle defined by the angular resolution of the instrument, $J(x,y,z|\lambda,\Delta\Omega)$ is the Jacobian determinant, $R = \sqrt{\lambda^2 + R_\odot{}^2 - 2\lambda R_\odot C}$, is the galactocentric distance and r is the radial distance inside the single subhalo. $R_\odot$ is the distance of the Sun from the galactic center and $C = \cos(\theta)\cos(\psi) - \cos(\phi)\sin(\theta)\sin(\psi)$. $P(\nu(M))$ is the probability distribution function for the peak rarity $\nu(M)$ calculated using the extended Press-Schechter formalism. $P(c(M))$ is the lognormal probability distribution for c centered on $c_v(M)$ as it is computed in our models. While $P(\nu(M)$ is determined by the merging history of each subhalo, $P(c(M))$ describes the scatter in concentration for haloes of equal mass (Bullock *et al.*, 2001; Neto *et al.*, 2007); therefore the two probabilities may be assumed independent. The single halo contribution to the total flux is given by

$$\Phi^{\mathrm{cosmo}}_{halo}(M,r,\nu,c) = \int\int_{\Delta\Omega} d\phi' d\theta' \int_{\mathrm{l.o.s}} d\lambda'$$

$$\left[\frac{\rho_\chi^2(M,r(\lambda,\lambda',\psi,\theta'\phi'),\nu,c)}{\lambda^2}J(x,y,z|\lambda',\theta'\phi')\right]. \qquad (6.17)$$

This equation is also used to derive the contribution of the smooth component of the MW itself.

Eq. (6.16) gives the average subhalo contribution to the Galactic annihilation flux within $\Delta\Omega$ along the direction ψ.

This contribution is shown in Fig. 6.5, together with the MW smooth halo component obtained with eq. (6.17), for the two models considered in this analysis, for $\Delta\Omega = 10^{-5}$sr, corresponding to an experimental angular resolution of 0.1°. The sum of the MW smooth and clumpy diffuse contributions is shown as well. We define this sum as our ”annihilation signal”, which will be multiplied by eq. (6.15) to obtain the predicted γ-ray diffuse flux from neutralino annihilation in our Galaxy. In the small box we show a zoom at small angles of the annihilation signal and we superimpose the signal obtained in Pieri *et al.* (2007) for two similar models (we refer to their paper for the detailed explanation of models). Our models give a higher flux at the Galactic Center, where the signal is dominated by the MW smooth contribution. This is due to the different MW profile adopted. Yet, we find one order of magnitude of enhancement at the GC in the subdominant subhalo contribution as well, due to the presence of $P(\nu(M))$ in our determination of flux. Since more concentrated haloes are closer to the GC in our approach, the enhancement is greater close to the GC: indeed, at the anticenter it goes down to a factor 2.

We have used the $P(\nu(M))$ for the ellipsoidal collapse in eq. (6.16). We have checked that using the corresponding probability function for the spherical collapse does not change the result on Φ^{cosmo}. This is due to the fact that the main difference between the two models resides at small values of ν. A small ν gives low concentration parameter and its contribution to eq. (6.17) is then depressed with respect to that of a haloes with a higher ν.

Normalization to EGRET Data

In order to make predictions on detectability, we impose the best value of Φ^{PP} compatible with the available experimental limits. As in Pieri *et al.* (2007), we first assume the optimistic model where $m_\chi = 40\ GeV$, $\sigma_{\rm ann} v = 3\times 10^{-26}\ cm^3\ s^{-1}$ and the branching ratio is 100% in $b\bar{b}$. We then integrate eq. (6.15) above 3 GeV. This choice of parameters gives a value of $\Phi^{PP} = 2.6\times 10^{-9}\mathrm{cm}^4\mathrm{kpc}^{-1}\mathrm{GeV}^{-2}\,\mathrm{sec}^{-1}\,\mathrm{sr}^{-1}$. We then compute the expected number of photons above 3 GeV in 1 year for a solid angle of 10^{-5}sr corresponding to the angular resolution of a GLAST-like satellite. The result for the $\mathrm{B}_{ref,0}$ (dashed curve) and $\mathrm{B}_{ref,z}$(dotted) models is shown in Fig. 6.6.

We compare the obtained number of events with the EGRET data for the dif-

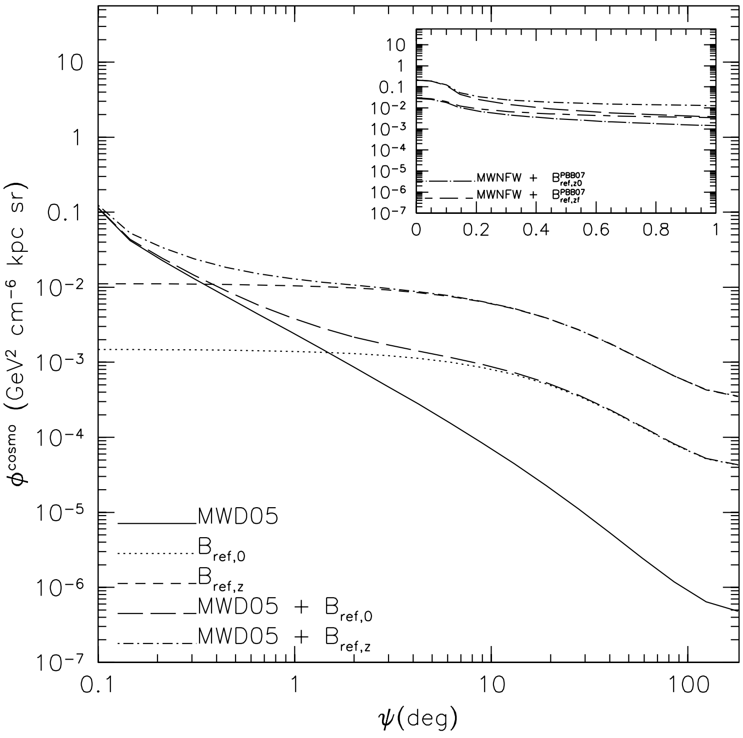

Figure 6.5: Subhalo contribution to the γ-ray flux for the two different models for the concentration parameters described in the text. MW smooth and clumpy contributions are shown separately, together with their sum. In the small box, zoomed at small angles from the Galactic Center only the sum is shown, and it is compared with the values obtained in Pieri *et al.* (2007).

fuse Galactic component parametrized according to Bergström *et al.* (1998)

$$\frac{d\phi^{\rm gal-\gamma}_{\rm diffuse}}{d\Omega dE} = N_0(l,b)\, 10^{-6}\, E_\gamma^{-2.7} \frac{\gamma}{\rm cm^2\, sec\, sr GeV}, \tag{6.18}$$

and with the diffuse extragalactic γ emission, as extrapolated from EGRET data at lower energies (Sreekumar *et al.*, 1998):

$$\frac{d\phi^{\rm extra-\gamma}_{\rm diffuse}}{d\Omega dE} = 1.38 \times 10^{-6} E^{-2.1} \frac{\gamma}{\rm cm^2\, sec\, sr GeV}. \tag{6.19}$$

The normalization factor N_0 in eq. (6.18) depends only on the interstellar matter distribution. The resulting number of photons above 3 GeV in 1 year for $\Delta\Omega = 10^{-5}$sr, computed along $l = 0$ where its value is minimum, is shown in Fig. 6.6 (solid curve).

We find an excess of annihilation signal photons toward the Galactic centre in both models. Yet, the angular resolution of EGRET corresponding to $\Delta\Omega = 10^{-3}$sr does not allow to reconstruct a spiky source as it is ours. We have checked that, if we compute the number of annihilation signal photons toward $\psi = 0$ smeared

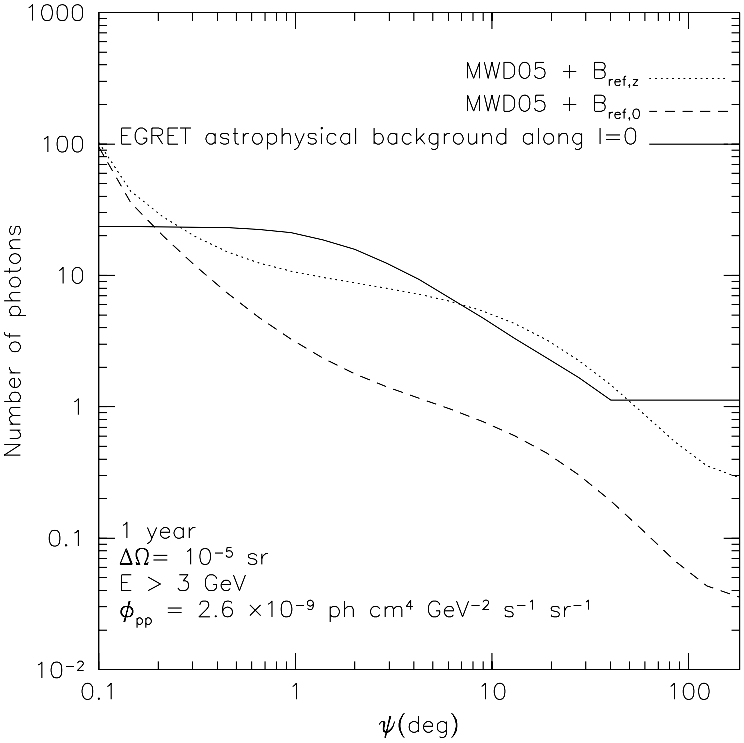

Figure 6.6: Number of photons above 3 GeV, in 1 year in a solid angle of 10^{-5}sr. The annihilation signal models $B_{ref,0}$ (dashed) and $B_{ref,z}$(dotted) are shown together with the EGRET diffuse expected Galactic and extragalactic background (solid), as a function of the angle of view ψ from the Galactic Center.

in a cone of view of 1°, it is below the number of EGRET detected photons for the same angular resolution.

Yet, the $B_{ref,z}$model exceeds the extragalactic diffuse measured background too, which is dominant above $\psi = 40°$. Since the extragalactic background is not due to any point source, we safely expect that it will scale with the solid angle. The number of annihilation signal photons produced in the $B_{ref,z}$model should then be less or at most comparable with the number of measured background photons. We make the optimistic assumption that the two numbers are comparable at $\psi = 40°$ where the discrepancy is larger, and we thus fix $\Phi^{PP}_{B_{ref,z}} = 2.0 \times 10^{-9}\mathrm{cm}^4\mathrm{kpc}^{-1}\mathrm{GeV}^{-2}\,\mathrm{sec}^{-1}\,\mathrm{sr}^{-1}$ for the $B_{ref,z}$model, correctly normalized to EGRET data, while we keep $\Phi^{PP}_{B_{ref,0}} = 2.6 \times 10^{-9}\mathrm{cm}^4\mathrm{kpc}^{-1}\mathrm{GeV}^{-2}\,\mathrm{sec}^{-1}\,\mathrm{sr}^{-1}$ for the $B_{ref,0}$ model.

6.4 Prospects for Detection

In this section we study the sensitivity of a GLAST-like apparatus for 1 year of effective data taking.

We define the experimental sensitivity σ as the ratio of the number n_γ of annihilation signal photons and the fluctuation of background events $n_{\rm bkg}$:

$$\begin{aligned}\sigma &\equiv \frac{n_\gamma}{\sqrt{n_{\rm bkg}}} \\ &= \sqrt{T_\delta}\epsilon_{\Delta\Omega}\frac{\int A^{\rm eff}_\gamma(E,\theta_i)[d\phi^{\rm signal}_\gamma/dEd\Omega]dEd\Omega}{\sqrt{\int\sum_{\rm bkg}A^{\rm eff}_{\rm bkg}(E,\theta_i)[d\phi_{bkg}/dEd\Omega]dEd\Omega}}\end{aligned} \tag{6.20}$$

where $T_\delta = 1$ year is the effective observation time and ϕ_{bkg} is the background flux given by eqs. 6.18 and 6.19, computed along $l = 0$, that we assume to be composed by astrophysical photons only. The quantity $\epsilon_{\Delta\Omega}$ is the fraction of signal events within the optimal solid angle $\Delta\Omega$ corresponding to the angular resolution of the instrument and it is optimistically set to 1. $A^{\rm eff}$ is the effective detection area defined as the detection efficiency times the geometrical detection area. We use $A^{\rm eff} = 10^4{\rm cm}^2$, independent from the energy E and the incidence angle θ_i. Finally we assume an angular resolution of 0.1° and an energy threshold of 3 GeV.

The resulting sensitivity curves as a function of the angle of view ψ are shown in Fig.6.7 for the $\mathrm{B}_{ref,0}$ (solid curve) and $\mathrm{B}_{ref,z}$(dotted) annihilation signal models. In the small box a zoom at GC is shown. An almost 2 σ around 10° is found for the $\mathrm{B}_{ref,z}$model. The same model would be detected at about 30 σ at the Galactic Centre. As far as the $\mathrm{B}_{ref,0}$ model is concerned, it would show up with $\sim 40\sigma$ effect toward the GC, that would rapidly fall down 1 σ after 0.5°. A 5 σ detection at the Galactic Center would be possible for both models with a value of Φ^{PP} even 6 times lower. In case of a striking excess detection along the GC, a milder excess a larger angles could be a hint for the discrimination about the models, though no discovery could be claimed.

Pieri *et al.* (2007) studied the detectability of resolved haloes which would shine above the Galactic foreground, finding in their best case scenario that only a tenth of large mass haloes would be detected, with a mass slope of -2 for the halo mass function.

Repeating their analysis is beyond the goal of this work. Yet we note that the effect of including the $P(\nu(M))$ factor in eq. (6.16) with respect to the concentration models in Pieri *et al.* (2007) leads to an enhancement of the Galactic foreground. We thus expect that including $P(\nu(M))$ will be compensated by the increased foreground and we do not expect a dramatic change in the number of detectable haloes.

As a further test, we have computed the sensitivity of a GLAST-like experiment for a $\mathrm{B}_{ref,z}$halo once Φ_{PP} has been normalized to the EGRET data. We chose the closer $M = 10^{-6}M_\odot$ halo, located at 9.5×10^{-2}pc from the sun. We chose $\nu = 2.4$ given from the probability of finding 1 halo with such a value in a 1 pc^3 sphere around the sun. We conservatively considered only the astrophysical background in eq. (6.21), while the annihilation signal foreground should be considered too. Even in these very optimistic hypothesis, we found that the

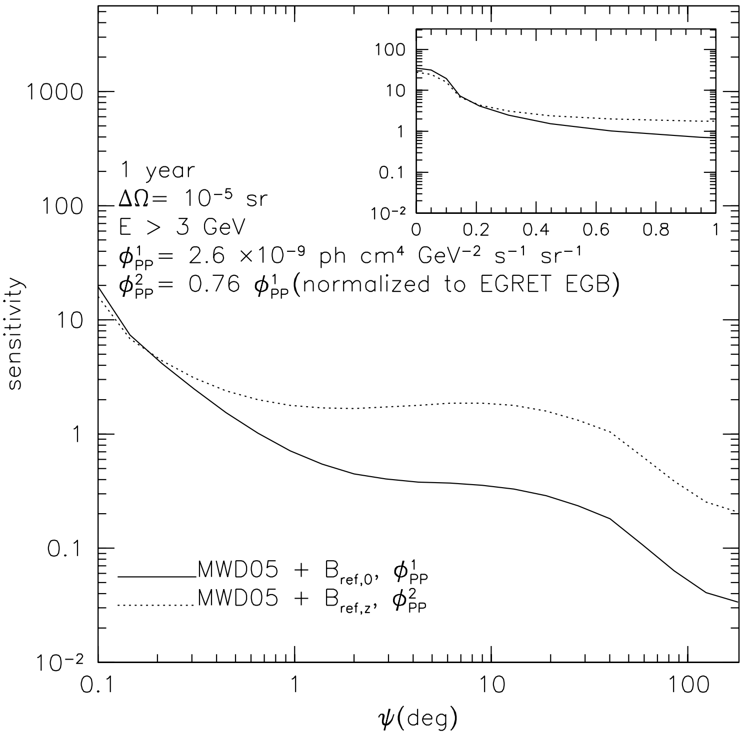

Figure 6.7: Sensitivity curves for a GLAST-like experiment, for the $\mathrm{B}_{ref,0}$ (solid) and the $\mathrm{B}_{ref,z}$(dotted) models described in the text. A zoom at small angles is provided in the superimposed frame.

source would produce a 5 σ effect only furtherly multiplying by a factor of 4 the concentration parameter. This could be achieved using the lognormal probability $P(c(M))$ but with a ridiculously small probability.
We conclude that the effect of introducing the $P(\nu(M))$ can only be observed in a global enhancement of the diffuse Galactic annihilation foreground.

6.5 Discussion

In this work we have, for the first time, derived an analytical description of the mass function and distribution of rareness of density peaks in the subhalo population of our Galaxy, applying the extended Press & Schechter formalism. To make the calculation possible, tidal interactions and close encounters between subhaloes have been neglected. Very small (micro solar mass) subhaloes are extremely concentrated, therefore, at least for them, our approximation is a reasonable one.

The obtained results are valid over the whole range of subhalo masses $[10^{-6}, 10^{10}]M_{\odot}$ and thus confirm and extend the results of the N-body simulations, whose resolution is still far too low in order to simulate coherently this mass range.

Making use of the results of Diemand *et al.* (2005) on the distribution of different σ-peak material inside our Galaxy, we have been able to shape and model the total expected annihilation γ-ray foreground, statistically taking into account the merging history of each progenitor.

We have used the best case particle physics scenario to derive predictions for the detectability of such a signal with a GLAST-like experiment. We have shown how both the merging history and the intrinsic properties of the halo formation can contribute to an enhancement of the expected flux, by arising the inner concentration of subhaloes. Yet the real concentration of the single subhalo today remains an open question. We use two models which result in very different inner densities inside the haloes. In the first model we assume that the inner shells of the subhaloes remain frozen at the moment they enter the parent halo and thus compute the concentration parameter at the merging epoch, as it is derived in our calculations. Alternatively we assume that the subhaloes continue to evolve with redshift, and thus compute the halo properties today. We use the Bullock *et al.* (2001) model for the concentration parameter at $z = 0$, extrapolated at low masses. We refer to Pieri *et al.* (2007) for the effect of using different models.

Our results on detectability show that a detection would be possible and impressive toward the GC for both models. This detection would be mainly due to the spike in the MW halo at the GC. Unfortunately, a reliable modeling of the astrophysical background coming from the GC and of the effect of the central Super Massive Black Hole on the inner DM density profile are still poorly known.

A 2-σ effect would show up as well, around ~ 10° from the GC, only for the $\mathrm{B}_{ref,z}$model. Though no discovery could be claimed for, this could be a significant hint for the existence of such a population of subhaloes, and it would be propulsive for successive studies with upcoming experimental technologies.

A final note on the methodology. In the present work we derived the final subhalo mass function starting from all progenitor haloes at any redshift. We did so in order to directly compare our analytical results to the results obtained by Diemand *et al.* (2005) using N-Body simulations. However, the subhalo population should indeed be derived starting from the population of ”satellite haloes” directly accreted by the proto-halo (also called main progenitor) at all previous times (Tormen, 1997), since only a fraction of progenitors at redshift z merge directly with the main halo progenitor. Unfortunately, the mass function of satellite haloes cannot be obtained analytically: it requires Monte Carlo simulations of the merging history tree of halo formation (Somerville and Kolatt, 1999; van den Bosch, 2002; van den Bosch *et al.*, 2005). We are currently working on this issue (Giocoli, Pieri, Sheth & Tormen, in prep.), and it will be interesting to compare the results obtained using the two methods.

CHAPTER

7

Subhaloes Mass Function and Average Mass-Loss Rate

Understanding structure formation is a fundamental topic in modern cosmology. In the current ΛCDM concordance cosmology, the matter density of the Universe is dominated by cold dark matter (CDM), whose gravitational evolution gives rise to a population of virialized dark matter haloes spanning a wide range of masses. Numerical simulations of structure formation in a CDM universe predict that these dark matter haloes contain a population of subhaloes, which are the remnants of haloes accreted by the host, and which are eroded by the combined effects of gravitational heating and tidal stripping in the potential well of the main halo. In previous simulations, haloes falling into clusters usually evaporated quickly, and the clusters exhibited little sign of substructures (Frenk *et al.*, 1996). In now appear that sufficient numerical force and mass resolution is enough to resolve this "overmerging" problem.

Understanding the evolution of the subhalo mass function, as function of cosmology, redshift, and host halo mass, is of paramount importance, with numerous applications. For one, subhaloes are believed to host satellite galaxies, which can thus be used as luminous tracers of the subhalo population. In particular, linking the observed abundances of satellite galaxies to the expected abundance of subhaloes, provides useful insights into the physics of galaxy formation (e.g., Moore *et al.*, 1999; Bullock *et al.*, 2000; Somerville, 2002; Kravtsov *et al.*, 2004; Vale and Ostriker, 2006). Studies along these lines indicate that galaxy formation becomes extremely inefficient in low mass haloes, and suggest that there may well be a large population of low mass subhaloes with no optical counterpart (e.g., Moore *et al.*, 1999; Stoehr *et al.*, 2002; Kravtsov *et al.*, 2004). In principle, though, these truly 'dark' subhaloes may potentially be detected via γ-ray emission due to dark matter annihilation in their central cores (Stoehr *et al.*, 2003; Bertone, 2006; Koushiappas, 2006; Pieri *et al.*, 2007; Diemand *et al.*, 2007a), or via their impact on the flux-ratio statistics of multiply-lensed quasars (e.g., Metcalf and Madau, 2001; Dalal and Kochanek, 2002). Alternatively, these techniques may be used to constrain the abundance of subhaloes, which in turn has implications for cosmological parameters and/or the nature of dark matter. The evolution of the subhalo mass function is also of importance for the survival probability of disk galaxies (e.g., Toth and Ostriker, 1992; Benson *et al.*, 2004; Stewart *et al.*, 2007) and even has implications for direct detection experiments of dark matter (e.g., Goerdt *et al.*, 2007) Finally, understanding the rate at which dark matter subhaloes loose mass has important implications for their dynamical friction times, and thus for the merger rates of galaxies (e.g., Benson *et al.*, 2002; Zentner and Bullock, 2003; Taylor and Babul, 2004).

Despite significant progress in the last years, there are still numerous issues that are insufficiently understood. What is the mass function of haloes accreted onto the main progenitor of a present day host halo? How do the orbits and masses of subhaloes evolve as they are subjected to dynamical friction, tidal forces and close encounters with other subhaloes? How does this depend on the properties of the host halo? In this work we address these questions using high-resolution numerical simulations. We trace back the evolution of self-bound substructures identified in present-day host haloes up to the point where they are first accreted by the main progenitor of the host halo. Using this method we are able to link the present-day population of subhaloes to the merging history of the host system. We will show that larger systems, forming at lower redshifts and so accreting their satellites more recently, contain at the end more subhaloes than smaller hosts (see also Gao *et al.*, 2004; van den Bosch *et al.*, 2005).

7.1 The Simulations

The simulation used for this work are two cosmological N-Body simulations GIF, GIF2 and a sample of resimulated Galaxy Clusters. These simulations have been described in the section 4.2 of the Chapter 4. At each simulation snapshot has been run the halo finder and all the groups with more than ten particles has been stored. From redshift $z = 0$ we also followed the growth of all dark matter haloes with $M_0 \geq 10^{11.5} M_{\odot}/h$ as described in section 4.3 of the same chapter. The GIF2 simulation has been performed by Gao *et al.* (2004). In their work they used a FOF algorithm, with a linking length $b = 0.2$ the mean interparticles separation. In Figure 7.1 we show the mass function of the haloes as identified at three different snapshot in the simulation. We are also plotting (with filled triangle) the data of the FOF mass function as obtained by Gao *et al.* (2004) at redshift $z = 0$. The solid line is the Press and Schechter (1974) prediction (eq. 3.24) at the three considered redshifts, while the dashed line is the Sheth and Tormen (1999) (eq. 4.3). To convert these distribution in term of the universal variable ν in a mass function we took into account that:

$$M^2 \frac{n(M,z)}{\bar{\rho}} = \nu f(\nu) \frac{\mathrm{d}\log(M)}{\mathrm{d}\log(\nu)} . \tag{7.1}$$

From the figure it is also interesting notice that at small masses the FOF algorithm link together more groups of particles than the SO. To solve this problem usually the people use to compute the density of each group of particles removing from the original list those that do not exceed for example the critical virial overdensity (at redshift $z = 0$ for a ΛCDM universe is $324\bar{\rho}$).

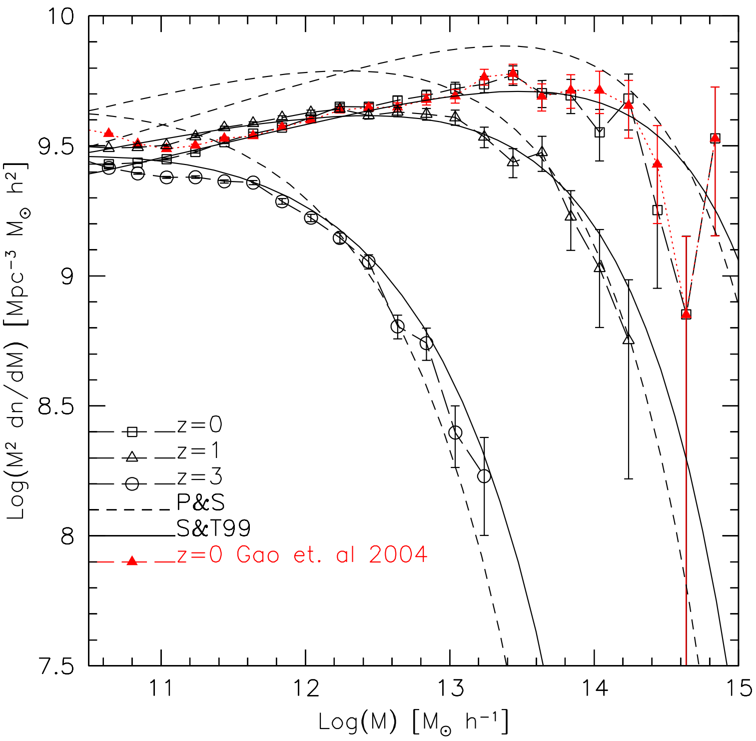

Figure 7.1: Mass function of identified dark matter haloes at three snapshots in GIF2 simulation. The open points refer to the mass function obtained using a SO algorithm while the filled triangle to the FOF method used by Gao *et al.* (2004)

	11.5-12	12-12.5	12.5-13	13-13.5	13.5-14	14-14.5	> 14.5
Resim.	-	-	-	-	21	17	10
GIF	-	-	2693	971	290	99	16
GIF2	8305	3349	1186	461	127	35	4

Table 7.1: Number of haloes considered in each logarithmic mass bin for the different simulations. For GIF & GIF2 we considered all the halo with more than 200 particles in their virial radius at redshift zero and whose main progenitor at any redshift has virial mass not exceeding the final value by more than ten percent. For the resimulated haloes we follow the merger tree and the satellites populations for all the haloes with more than 40000 at the present time.

In the following analysis we only consider haloes at redshift $z = 0$ whose main progenitor at any redshift has virial mass not exceeding the final value by more than ten percent. This eliminates pathological merging histories, involving encounters either unbound or still undergoing.
For all simulations we split the halo samples at $z = 0$ in mass bins of amplitude $d\log(M) = 0.5$, with a minimum mass roughly corresponding to 200 particles within the virial radius for GIF and GIF2, and to 40000 particles for the resimulations. The actual mass bins for each run are listed in Table 7.1.

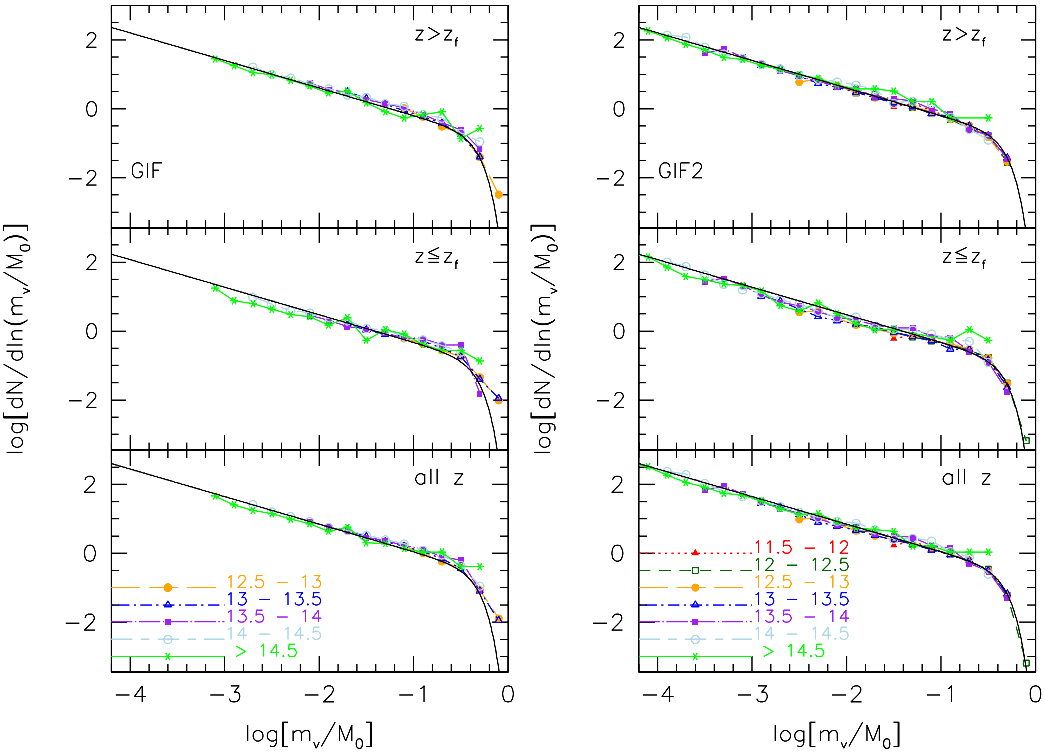

Figure 7.2: Mass functions of accreted satellites (unevolved subhalo mass functions). In the panels the various data points and line types refer to different present-day host halo masses. In the figures the the bounds of the mass bins are expressed in unit of $\log(M_\odot/h)$. The solid lines represent the fitting function to the distributions: equation (7.3) (see the main text for more details). Note that we only consider subhaloes that at $z = 0$ contribute at least 50% of their mass. This ensures that at $z = 0$ their center of mass lies within the virial radius of the host. **Top**: Unevolved subhalo mass function accreted before the formation redshift z_f of the host halo (defined as the earliest redshift when the mass of the main progenitor exceeds half the final mass). **Center**: Same as above, but only counting satellites accreted after z_f. **Bottom**: Same as above, but now counting satellites accreted at any redshift.

7.2 Merger Tree: Mass Accreted by the Main Branch

Starting from each halo at $z = 0$, we read its merging history tree backward in time and note down all its satellites, i.e. all haloes directly accreted by the main halo progenitor at any output time. In order to remove subhaloes that at $z = 0$ reside outside the host due to their elongated orbits (and so do not contribute to the subhalo population) we only consider satellites which donate at least at least 50% of their mass to the final halo. Let $n(m_v/M_0, z)$ be the number of satellites of virial mass m_v, accreted at redshift z by a host halo with mass M_0 at redshift zero. Integrating this expression over some redshift interval we obtain the total number of satellites of mass m_v accreted in that interval.

$$\mathrm{N}\left(\frac{m_v}{M_0}\right) = \int_{z_1}^{z_2} n\left(\frac{m_v}{M_0},\zeta\right) \mathrm{d}\zeta \tag{7.2}$$

which we will term *unevolved subhalo mass function.*

In Figure 7.2 we plot the unevolved subhalo mass function for different redshift intervals, as measured in the GIF (left) and GIF2 (right) simulations. The data points refer to different mass bins for the parent haloes at redshift $z = 0$. As stated above, we only considered satellites yielding at least 50% of their mass to the final ($z = 0$) host. In each panel we overplot the Schechter-like fitting formula:

$$\frac{\mathrm{dN}}{\mathrm{d}\ln(m_v/M_0)} = N_0 x^{-\alpha} \mathrm{e}^{-6.283\,x^3}, \quad x = \left|\frac{m_v}{\alpha M_0}\right| \tag{7.3}$$

with α and N_0 slope and normalization respectively; in all panels the slope is $\alpha = 0.8$, while the normalization is $N_0 = 0.21$ for satellites accreted at all redshifts.

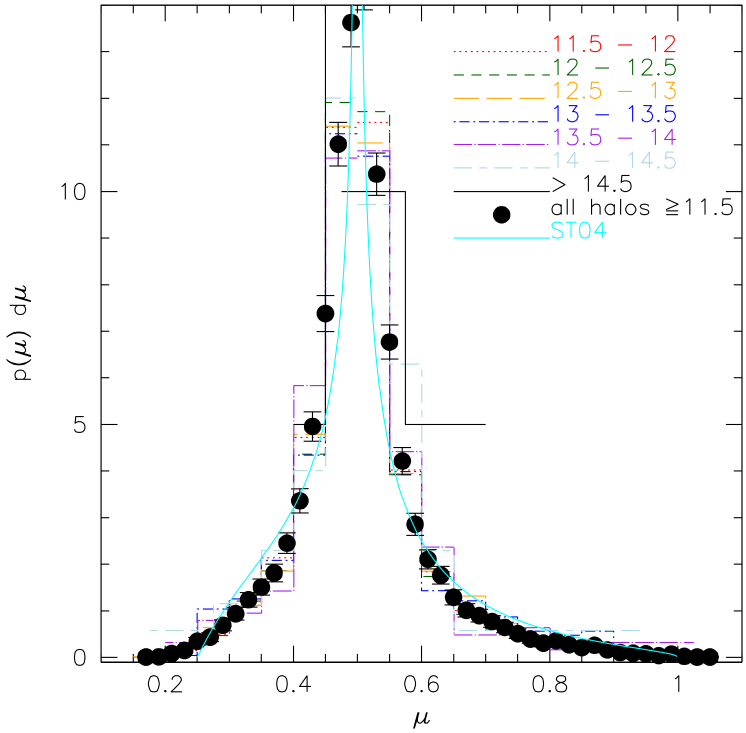

Figure 7.3: Formation mass distribution measured in GIF2 simulation for different final halo mass bins for $1/2 \le \mu \le 1$. The various line type histograms show the result of different final parent halo masses. Considering that the distribution does not depend on M_0, we plot all the halo more massive than $10^{11.5}\,M_\odot/h$ with filled circles. The corresponding error bars assume Poisson counts. For $\mu \le 1/2$ the mass distribution just before the formation is shown. See the main text for more details.

In order to compute the normalization of the distributions of the satellites mass function before and after the formation redshift z_f of the host halo (defined as the earliest redshift when the mass of the main progenitor exceeds half of the final halo mass) we need to compute the distribution of main progenitor mass at formation redshift.

If M_0 is the host halo mass at the present time, for the mass conservation, the sum of the mass of all progenitors at the previous snapshot (let us call z_1 the corresponding redshift) has to give:

$$\sum_i m_i(z_1) = M_0 \, . \tag{7.4}$$

If among $m_i(z_1)$ we define $M_0(z_1)$ the mass of the main progenitor at that redshift has also be true that:

$$M_0 = \sum_{i \neq 0} m(z_1) + M_0(z_1) = \sum_{i \neq 0} m(z_1) + \sum_j m_j(z_2) \, , \tag{7.5}$$

where $m_j(z_2)$ represent the progenitors of $M_0(z_1)$ at redshift $z_2 > z_1$, and $m_{j \neq 0}(z_1)$ the satellites accreted by M_0 at z_1. Following the equations of the mass conservation until the formation redshift we can so write:

$$M_0 = \sum_{i \neq 0} m_i(z_1) + \sum_{j \neq 0} m_j(z_2) + \sum_{k \neq 0} m_k(z_3) + ... + \mu M_0 \, , \tag{7.6}$$

where each term represents the mass in satellites accreted by the main branch at the corresponding redshift and μM_0 the mass of the host halo at the formation redshift z_f. If the mass at the formation were $M_0/2$ we would have half of the total mass accreted in satellites before z_f and half after. In reality, due to the finite size of accreted haloes, the average formation mass $M(z_f) = \mu M_0$ is slightly larger than $0.5 M_0$.

Sheth and Tormen (2004) show that, for the spherical collapse case and assuming a white noise power spectrum, the mass at formation has a distribution given by the equation:

$$p(\mu) \mathrm{d}\mu = \frac{2}{\pi} \sqrt{\frac{1-\mu}{2\mu - 1}} \frac{\mathrm{d}\mu}{\mu^2} \, . \tag{7.7}$$

with $1/2 \leq \mu \leq 1$. The mean value of the distribution will be:

$$\bar{\mu}_{ST04} = \int_{1/2}^{1} \mu \, p(\mu) \mathrm{d}\mu = 0.586 \pm 0.005 \, . \tag{7.8}$$

They argue that this distribution is slightly power spectrum dependent, however the agreement with the formation mass in the GIF numerical simulation is good. Here, combining haloes from GIF and GIF2, we find a mean formation mass $\bar{\mu}_{GIF+GIF2} M_0 = (0.572 \pm 0.001) M_0$, in excellent agreement with the prediction of Sheth and Tormen (2004). In Figure 7.3, for $\mu \geq 1/2$ we show the formation redshift mass distribution measured in GIF2 simulation for different final mass bins (histograms with different line type). The data points represent all considered haloes (Table 7.1) with mass bigger than $10^{11.5} \, M_\odot/h$ (error bars were estimated assuming Poisson counts), the solid line is the equation (7.7). From the figure it is possible to see that the formation redshift mass distribution is also independent on the final mass of the parent halo. In the figure, for $\mu \leq 1/2$ is shown the mass distribution just before the formation, the solid line represents the equation:

$$q(\mu)\mathrm{d}\mu = \frac{\mathrm{d}\mu/\mu^2}{\pi(1-\mu)}\left(\sqrt{\frac{\mu}{1-2\mu}} - \sqrt{1-2\mu}\right), \tag{7.9}$$

with $1/4 \leq \mu \leq 1/2$, see Sheth and Tormen (2004) for more details.

The normalizations of the *unevolved subhaloes mass function* accreted before $N_{0,b}$ and after $N_{0,a}$ the formation redshift are therefore:

$$N_{0,b} = \bar{\mu}N_0 = 0.572N_0\,, \tag{7.10}$$

$$N_{0,a} = (1-\bar{\mu})N_0 = 0.428N_0\,. \tag{7.11}$$

The fitting formula agrees very well with all data at all redshift, provided the correct normalization is used. This indicates that the shape of the unevolved subhalo mass function is indeed universal, as found by (van den Bosch *et al.*, 2005).

To further clarify this asymmetry in the mass accreted in satellites by the main halo progenitor before and after the formation redshift, let us define:

$$P(>z) = \frac{1}{N_{tot,0}}\int_{\infty}^{z}\mathrm{d}z\int_0^1 \mathrm{d}\frac{m_v}{M_0}N\left(\frac{m_v}{M_0},\zeta\right). \tag{7.12}$$

as the fraction of mass accreted by the main halo progenitor before redshift z in satellites of any mass. This in Figure 7.4 we plot the median and the quartiles error bar of the median cumulative distribution of the mass accreted by the main branch of different present day haloes in term of redshift and rescaled redshift (to the formation). This figure can be interpreted as complementary to the mass growth history of the main halo progenitor (van den Bosch, 2002; Wechsler *et al.*, 2002). Small haloes formed at higher redshift, accrete their satellites before that in the large ones (see left panel of Figure 7.4). From the right panel of the figure can be seen that when $z/z_f = 1$ the cumulative distributions of the mass accreted is bigger than 1/2, so most of the mass is accreted by the main branch before its formation (something like 57% of the total as shown before). From the same figure it is also interesting to note that the accretion in term of redshift after the formation, $z/z_f \leq 1$, is independent on the final halo mass (except for the most massive bin in GIF2 where we have only 4 haloes), while depends on it for $z/z_f > 1$.

Different Observation Redshifts z_0

In this section we will analyze the mass accreted by the main branch of the tree, and the formation mass distribution, following the haloes in GIF2 simulation from different initial redshifts: $z_0 = 0$ (repeated for comparison), $z_0 = 0.5$, $z_0 = 1$ and $z_0 = 2$. At each initial redshift (hereafter also observation redshift) we considered all the haloes bigger than $10^{11.5}\,M_\odot/h$ and divided them in 7 mass bins.

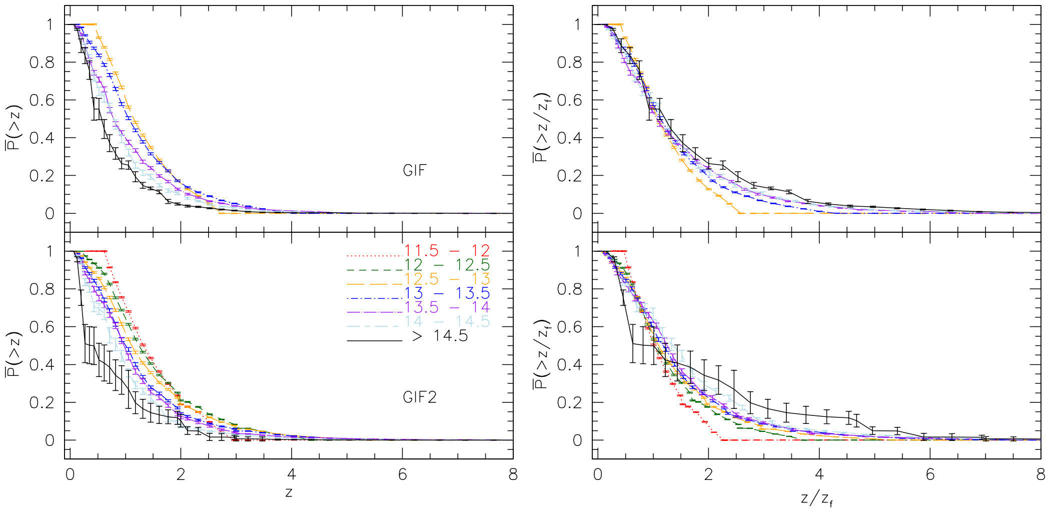

Figure 7.4: Cumulative distribution of the median mass fraction accreted in satellites by the main branch for different present day masses. In the **left** panel: the distribution is plotted in term of redshift, while in the **right** the redshift has been rescaled to the corresponding formation one. The error bars are the quartiles of the distributions.

We followed their tree along the main progenitor and considered only haloes whose main progenitor at any redshift has virial mass not exceeding the final value by more than ten percent (see Table 7.2 for the mass bins for each run).

	11.5-12	12-12.5	12.5-13	13-13.5	13.5-14	14-14.5	> 14.5
GIF2 ($z_0 = 0$)	8305	3349	1186	461	127	35	4
GIF2 ($z_0 = 0.5$)	9347	3544	1244	394	94	21	2
GIF2 ($z_0 = 1$)	9574	3455	1095	279	57	2	1
GIF2 ($z_0 = 2$)	8465	2461	593	98	5	2	0

Table 7.2: Number of haloes considered in each mass bins for different observation redshift z_0 in GIF2 simulations. In the sample we considered all the haloes that at z_0 have at least 200 particles.

In Figure 7.5 we show the mass accreted in satellites by the main branch of the tree at all redshifts. Each panel refers to different observation redshift considered from which we started to follow the tree of the haloes. The data points refer to different final parent halo masses at z_0, the solid line is the fitting function (eq. 7.3). From the figure we can argue that the haloes, independently on the considered redshift and mass, have a mass function accreted in satellites that is universal and well described by the fitting function proposed in the last section.

In the Figure 7.6 and 7.7 we show the mass function accreted in satellites on the main branch of the tree before and after the formation of the parent halo. Starting to follow the haloes from z_0, we define the formation time as the redshift at which for the first time the main progenitor become bigger than half of

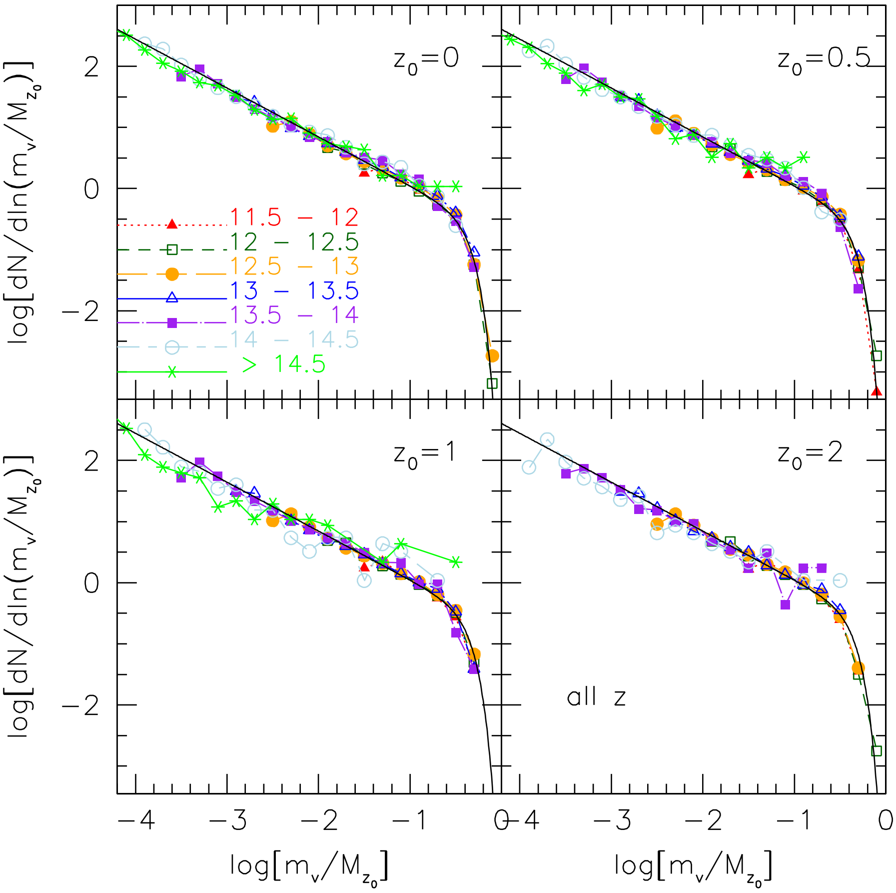

Figure 7.5: Mass accreted in satellites (*unevolved* Subhalo Mass Function) by the main branch of the tree at all redshifts. In each panel we show the results following the tree from different observation redshifts z_0 and parent halo masses (see Table 7.2 for more details). The solid lines represent the fitting function: equation (7.3).

its corresponding value at z_0. The solid lines in each panel of the figures are the equation (7.3) with the appropriate normalization factor $N_{0,a}$ (after) or $N_{0,b}$ (before the formation). The normalizations of the two distributions are expected, even for the halo observed from $z_0 > 0$, considering that the mass of the main progenitor at the formation is always well described by the Sheth and Tormen (2004) equation as can be seen in Figure 7.8.

7.3 Subhalo Mass Function

The evolved subhalo mass function at any redshift z is built from all the satellite haloes accreted on the main progenitors at all redshifts larger than z, and computing for each satellite the self-bound mass $m_{sb}(z)$. Operationally, we perform the following steps:

- given a satellite halo, we identify its merging redshift, z_m, defined as the

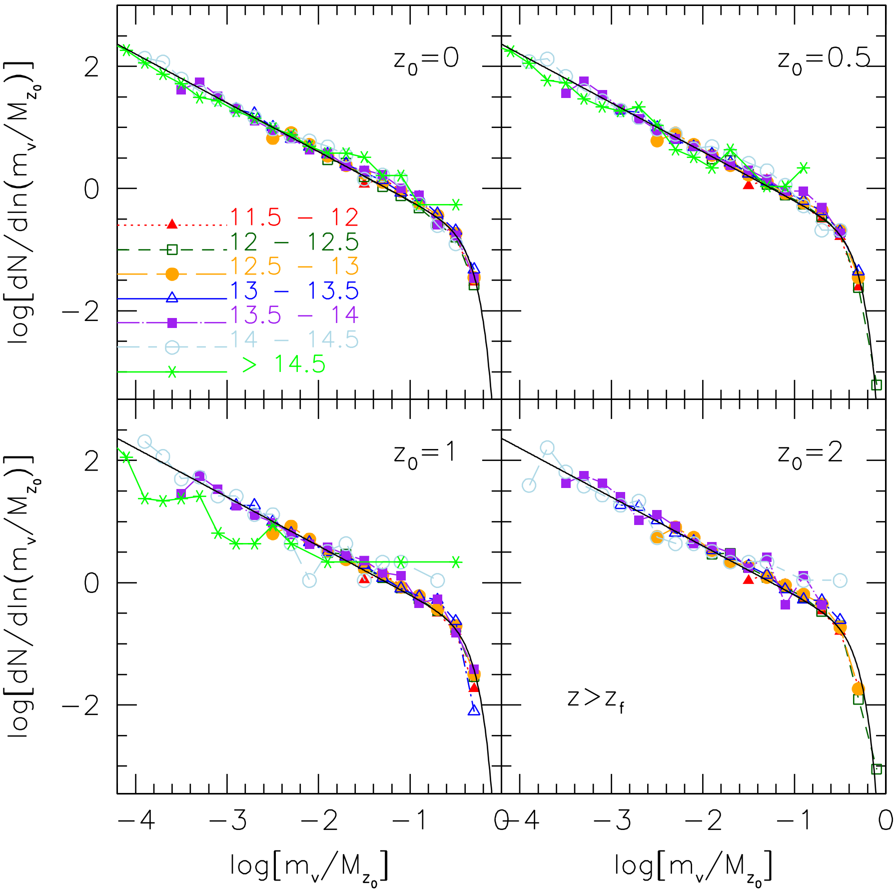

Figure 7.6: Mass accreted in satellites (as in Figure 7.5), before the formation redshift. The solid line in each panel is the equation (7.3) with the normalization factor equal to $N_{0,b}$.

latest redshift when the satellite was still an isolated halo, just before it was accreted by the main progenitor;

- we calculate the position of its center using the "moving center method"' (Tormen *et al.*, 1997), i.e. by repeated calculation of its center of mass using smaller and smaller radii to identify the subhalo densest core[1];
- we compute the subhalo tidal radius - as in Tormen *et al.* (1998);
- we evaluate the binding energy of each subhalo particle by summing its potential energy (calculated using all particles inside the tidal radius) and its kinetic energy (using its residual velocity with respect to the average value inside the tidal radius);
- we remove all particles with positive binding energy, and iterate the previous steps until the self-bound subhalo mass converges.

---

[1] In Appendix C we show the different tests done in developing the subhalo-finder code.

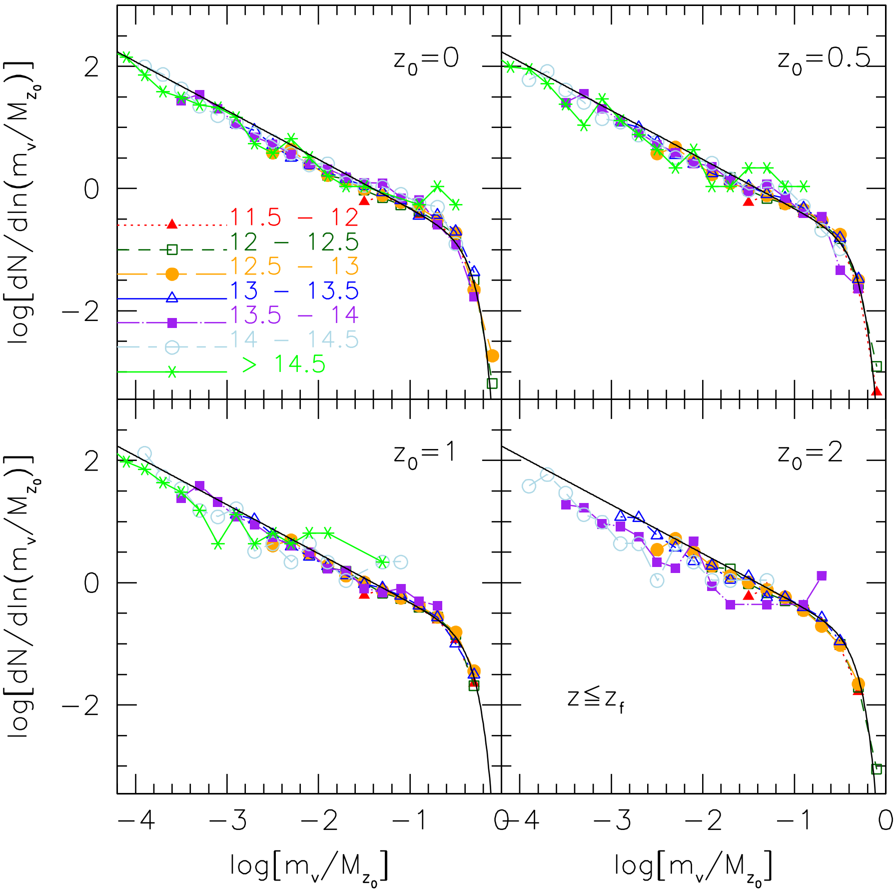

Figure 7.7: As Figure 7.5 but considering the satellites accreted after the formation of the host halo. The solid line is the equation (7.3) with the normalization factor equal to $N_{0,a}$.

With these data in hand, we can follow the time evolution of the self bound mass of each subhalo, snapshot by snapshot, from the merging redshift z_m to the present time $z = 0$. In the following section we will use this information - gathered from the resimulated haloes - to estimate the subhalo mass-loss rates at all redshifts.

In Figure 7.9 we show a schematic representation of the merging-history-tree of a halo. Time runs upward, and the final halo is on top. Light gray circles indicate the main progenitor at each time, and so define the tree "‘main branch"’. Dark gray circles indicate satellite haloes, i.e. progenitor haloes accreted directly by the main branch of the tree. Black circles are "‘leaves"’ progenitors, that is, progenitor with mass of the order of the resolution of the tree, with no progenitor haloes themselves. Leaves may also be satellites (as in the figure). On the other hand, progenitors which are not leaves may host themselves subhaloes. While a study of the evolution of subhaloes within subhaloes is beyond the purpose of this chapter, we will address this issue in the next chapter.

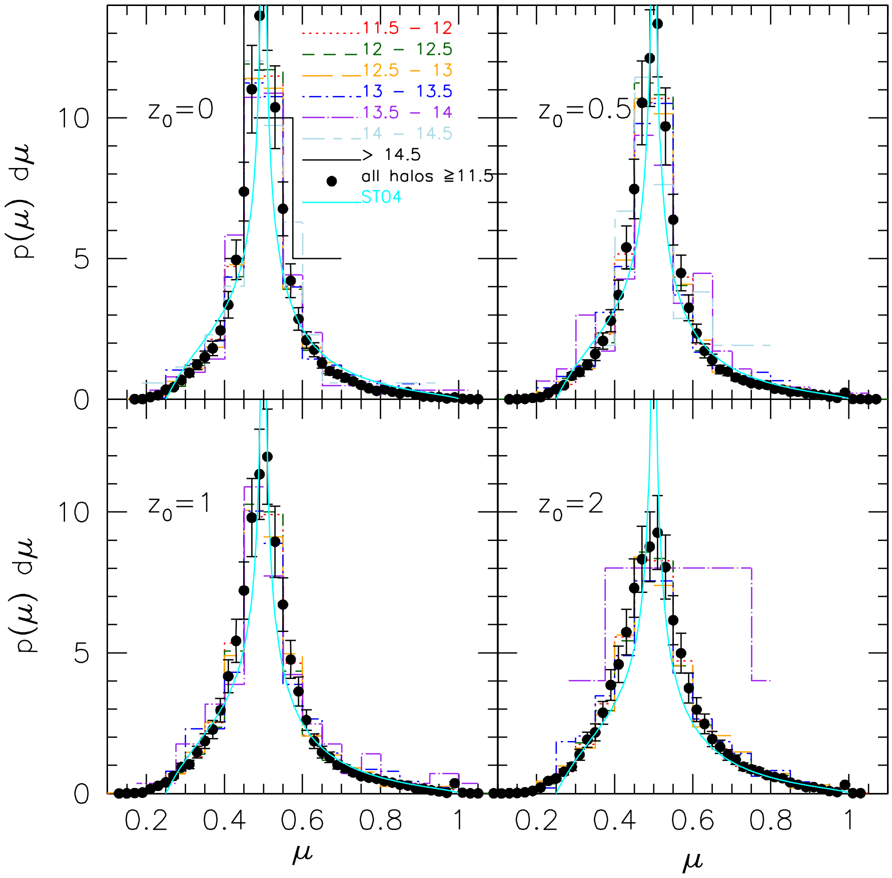

Figure 7.8: As Figure 7.3 but considering different observation redshifts z_0 as shown in the four panels.

As an example, in Figure 7.10 we show the subhalo population of the most massive halo found at $z = 0$ in the GIF2 cosmological run. In the top panel we show all particles inside the halo virial radius R_v. In the bottom left panel particles bound to subhaloes found inside R_v at $z = 0$. In the bottom right panel field particles, i.e. particles bound to the main halo but not to any subhalo.

In Figure 7.11 we plot the subhalo mass function for GIF2 haloes at redshift $z = 0$, split according to the final halo mass. We considered all self-bound subhaloes with at least 10 particles, and removed all subhaloes found at distances $d > 0.05R_v$, where subhalo definition is harder, and where few if any subhaloes are supposed to survive.

Gao *et al.* (2004) show that the mass function of subhaloes is not universal, but depends on the host halo mass M_0. The Monte Carlo model presented in van den Bosch *et al.* (2005) was able to reproduce this trend, and explained it in terms of halo formation redshift as follows. Small systems on average form at higher redshift than massive systems. Therefore, they also accrete their satellites at higher redshifts, when the universe is more dense, and dynamical effects (in-

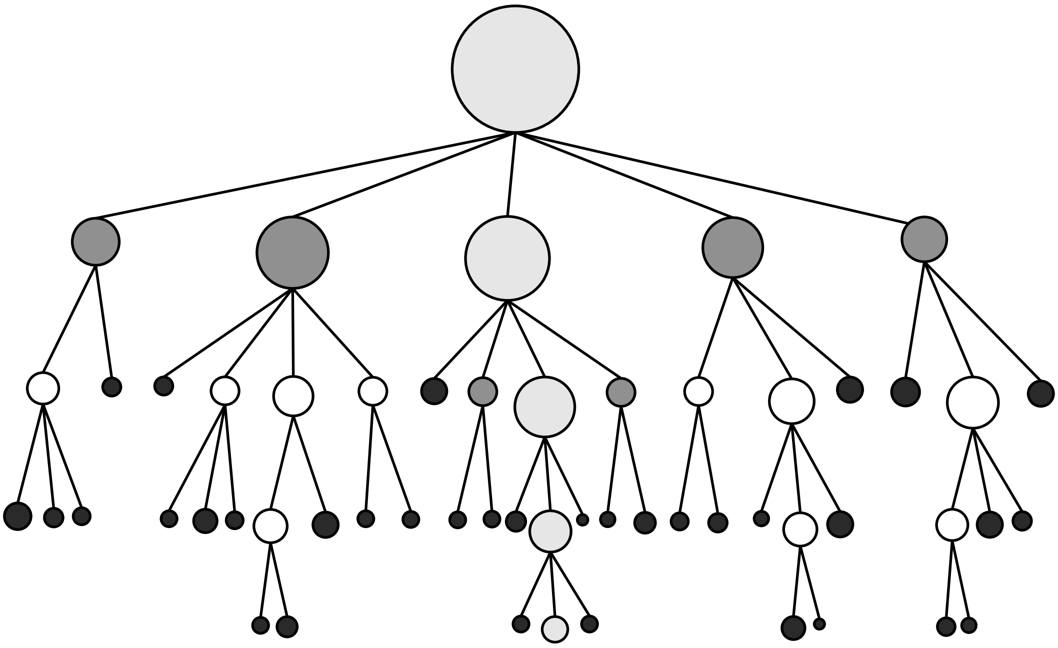

Figure 7.9: Schematic representation of the merging-history-tree of an halo. Solid light gray circles connected on the parent halo represent the main branch of the tree. Solid dark gray circles indicate satellites. Solid black circles indicate leaves progenitors. See the main text for explanation.

cluding tidal stripping, gravitational heating, close encounters etc.) have faster rates. Moreover, such satellites end up spending more time in the potential well of the host halo, lose more mass and are more likely to be completely destroyed.

The same idea is true if we observe an halo at redshift $z_0 > 0$ and, following the growth of its main progenitor halo compute, the self-bound particles in subhaloes. In Figure 7.12 we show the subhalo mass function at four different observation redshifts from which we started to follow the tree of the halo more massive than $10^{11.5}\, M_\odot/h$. As done previously, we consider only the haloes which main progenitor never exceed 10% of its final mass at any $z > z_0$.

In the next sections we will show that the subhalo population of our resimulated haloes agrees with this picture: global mass loss rates are higher at higher redshift. We will also find that mass loss rates turn out to be independent on the mass ratio $m_v(z)/M_v(z)$ between satellite and main progenitor. While the first result may be expected, and indeed is a dynamical prediction in van den Bosch *et al.* (2005), the second is less obvious, and in fact van den Bosch *et al.* (2005) left it as a free parameter.

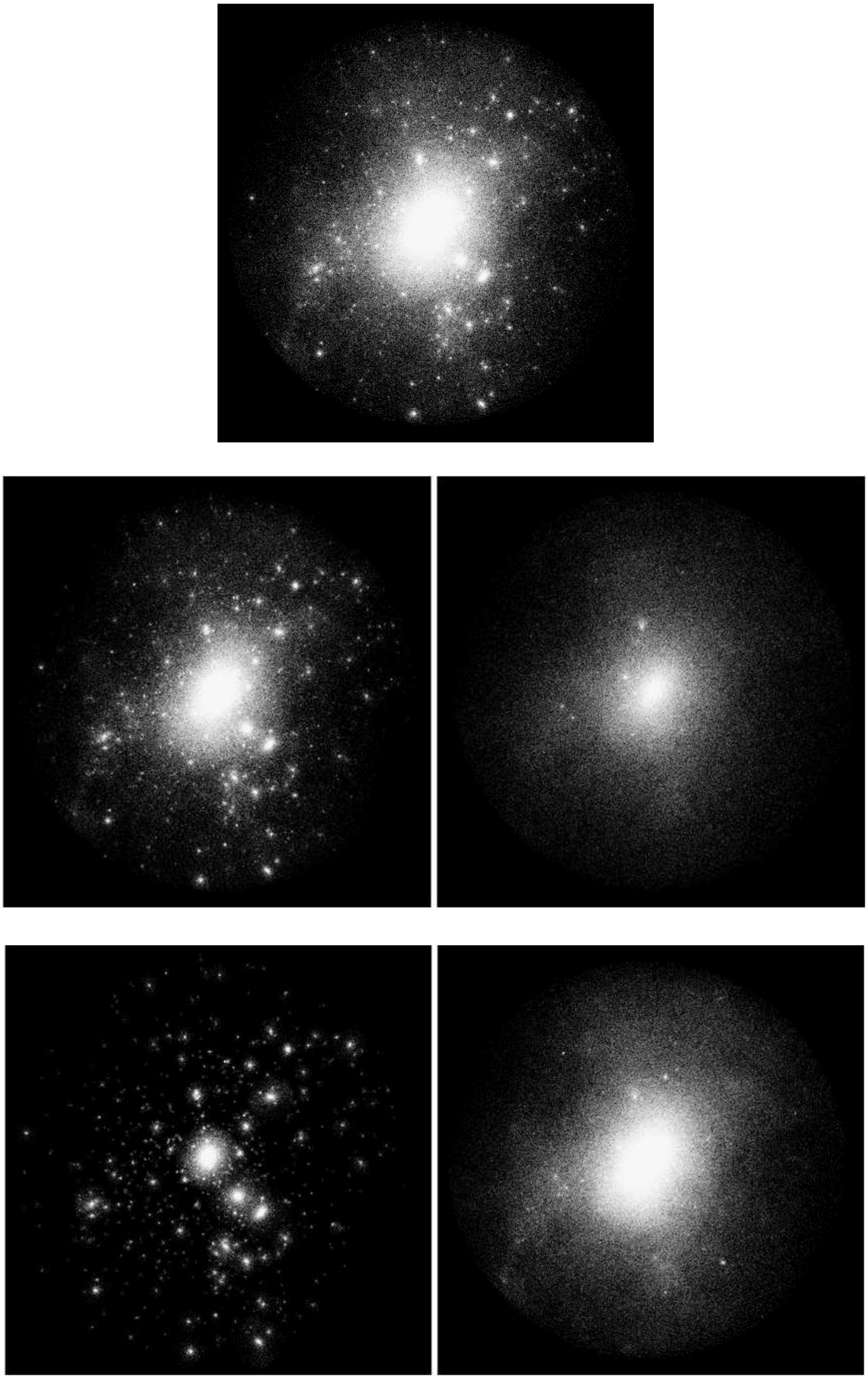

Figure 7.10: Subhalo population. **Top**: all particles composing the most massive halo found at $z = 0$ in the GIF2 simulation; the virial mass for this halo is $M_v = 1.8 \times 10^{15}\, M_\odot / h$, resolved by more than one million particles. **Middle left**: all particles in the present-day halo belonging to satellite progenitors, **middle right** corresponding dust particles. **Lower left**: particles bound to subhaloes at redshift $z = 0$. **Lower right**: particles bound to the main halo but not to subhaloes.

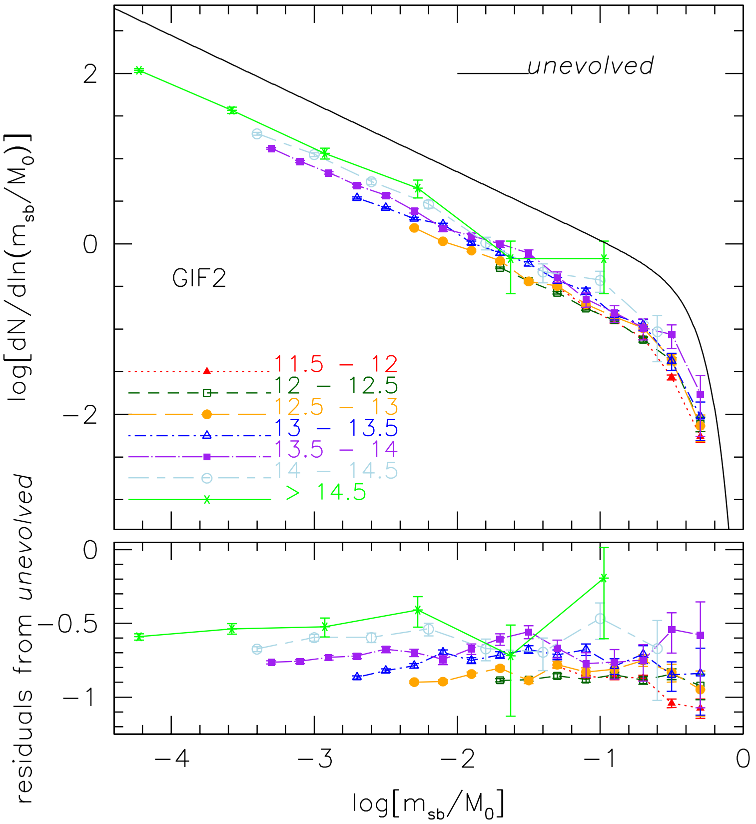

Figure 7.11: Subhaloes mass function of the self-bound particles of the haloes accreted by the main branch of the merger-history-tree of an halo,for GIF2 simulation. In the plot it has been considered all satellites with a distance from the center of the host halo less then the virial radius. We also plot the unevolved distribution: equation (7.3). In the bottom panel we show the residuals of the present day subhalo mass function respect to the unevolved fitting function.

7.4 Subhalo Mass-Loss Rates

In this section we estimate the subhalo mass loss rate, modeling it as a function of (i) the instantaneous satellite to host mass ratio: $m_{sb}(z)/M_v(z)$, (ii) the mass of the host halo at redshift zero: M_0, and (iii) the cosmic time through the redshift z. For this purpose we will use the subhalo population identified in the resimulations, as haloes in this sample have better force, mass and especially time resolution (88 snapshots between redshift ten and zero) than the cosmological GIF2 run. Since mass loss rates mostly depend on the local environment inside the host halo, the resimulated sample will provide correct rates even if the haloes themselves do not necessarily represent a fair sample for the given cosmological model.

In Figure 7.13 we show the unevolved subhalo mass function for satellites identified in the merger trees of the set of resimulated haloes; host haloes are

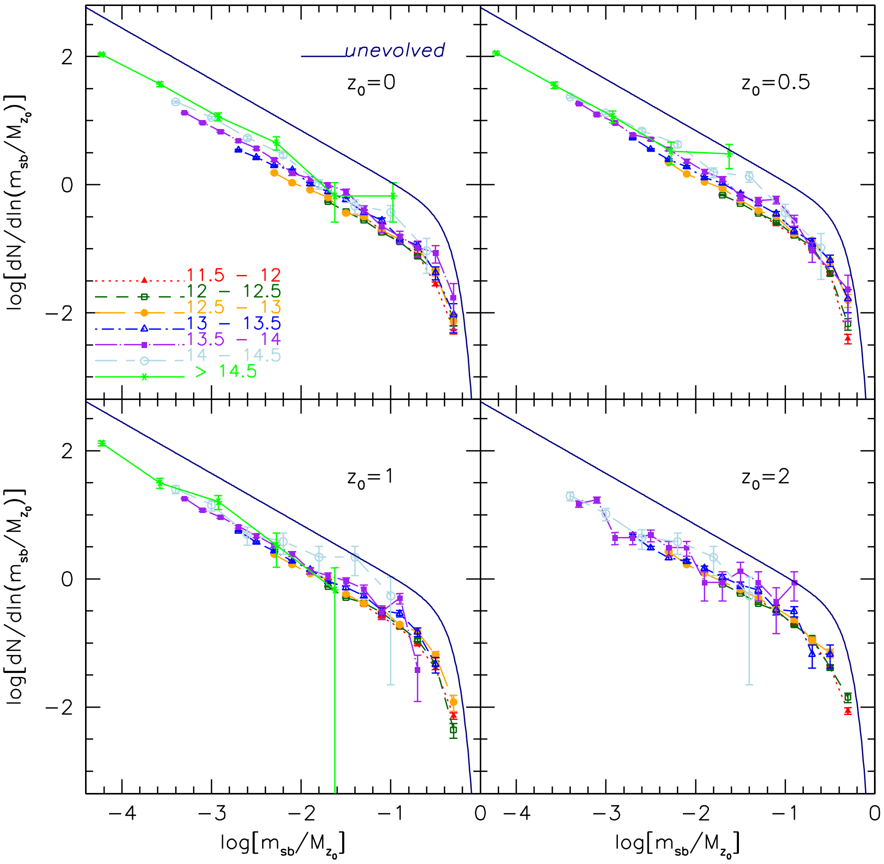

Figure 7.12: Subhalo mass function at four different observation redshifts, computed considering all satellites accreted at all redshift $z > z_0$. As did for the other plots, different final host mass progenitor haloes have been considered and correspond to different data points and line types. In each panel is also shown the unevolved subhalo mass function: equation (7.3).

split in three mass bins, according to Table 7.1. As for the GIF2 simulation, the unevolved subhalo mass function obtained from the resimulations is well fit by eq. 7.3.

After a satellite enters the virial radius of the host, various dynamical effects, including dynamical friction, tidal stripping, and close encounters with other subhaloes, cause the subhaloes to loose mass, and may eventually result in their complete disruption (e.g., Choi *et al.*, 2007). The (average) mass loss rate of dark matter subhaloes is the direct link between the unevolved and evolved subhalo mass functions, and also is a fundamental ingredient for semi-analytical models of galaxy formation, as it sets the rate at which satellite galaxies merge with the central galaxy in a halo, it determines the evolution of the mass-to-light ratios of satellite galaxies, and it regulates the importance of stellar streams in the haloes of central galaxies.

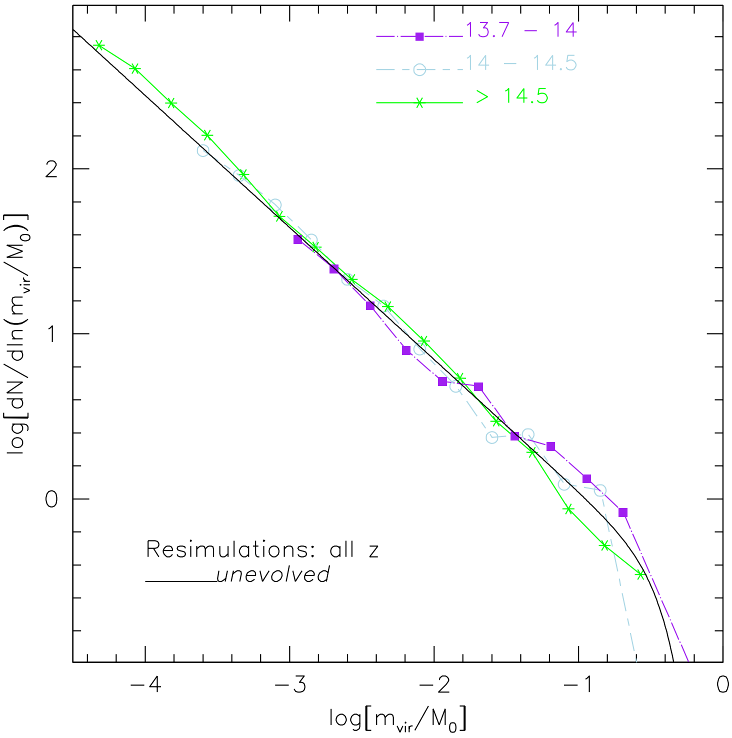

Figure 7.13: Unevolved subhalo mass function for the resimulated haloes. We notice that the function is independent on mass and well described by the same function fitting the GIF2 data (Figure 7.2). Haloes are split in three mass bins. In the figure the bounds of the bin are expressed in unit of $\log(M_\odot/h)$.

In this section we measure the mass loss rate experienced by each satellite. In addition, using statistical averaging, we determine the average mass loss rate of satellites as a function of the parameters listed at the beginning of this section. We define the average mass loss rate between two successive snapshots at redshift, z_1 and z_2, as

$$\frac{\mathrm{d}}{\mathrm{d}t}\left(\frac{m_{sb}}{M_v}\right)(z) = \frac{\dfrac{m_{sb}(z_2)}{M_v(z_2)} - \dfrac{m_{sb}(z_1)}{M_v(z_1)}}{t(z_2) - t(z_1)}, \quad z_1 < z < z_2 . \tag{7.13}$$

where the values of $m_{sb}(z)$ and $M_v(z)$ are obtained by linear interpolation of the values at z_1 and z_2. In Figure 7.14 we plot the subhalo mass loss rate as a function of the ratio $m_{sb}(z)/M_v(\mathrm{z})$; each panel refers to a different bin for the mass $M_v(z)$ of the host halo.

The green points and band in each panel indicate the median and quartiles of the distribution. The thick magenta line represents a least squares fit to the median values in each panel; the fit is limited to the region where the median exhibits a linear behavior: we excluded by hand median values for m_{sb}/M_v close to one, which correspond to major mergers and cannot be described by a simple

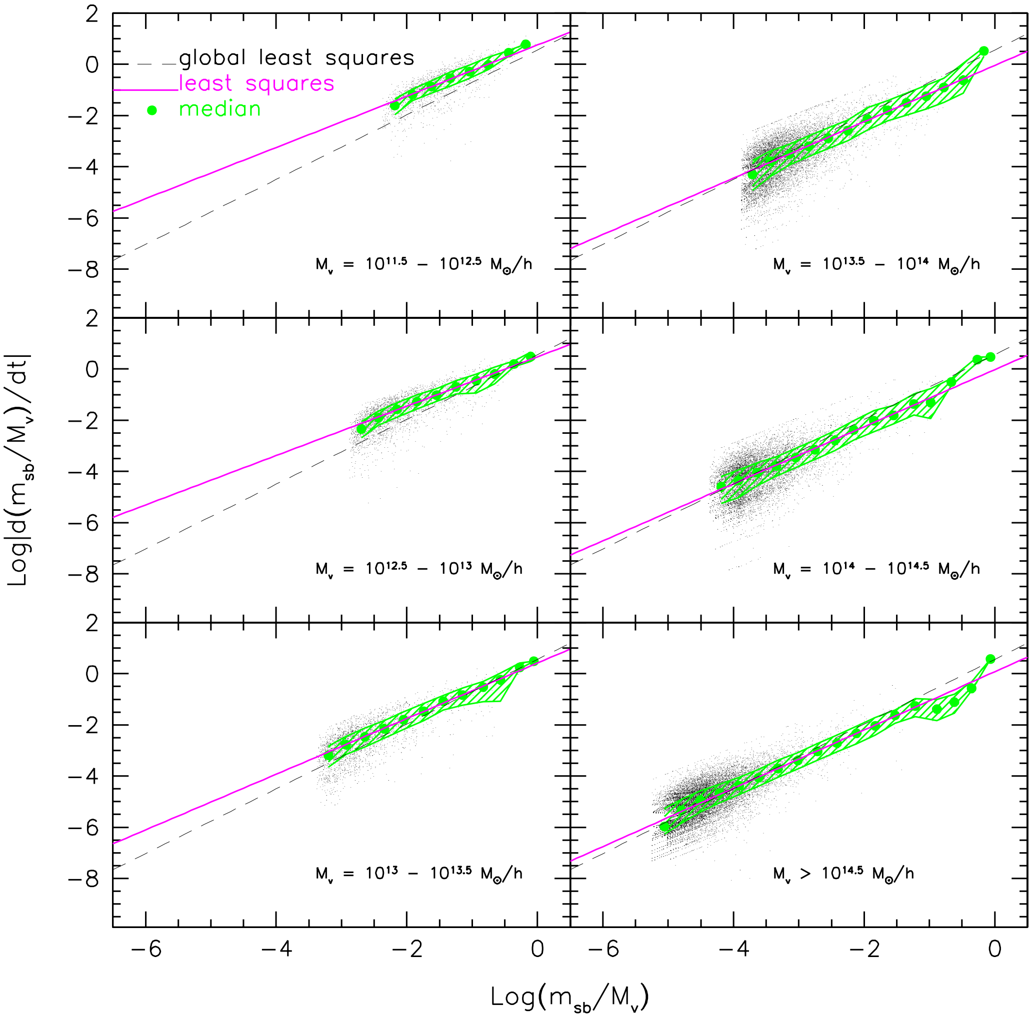

Figure 7.14: Subhalo mass loss rate. Each panel refers to a different bin in host halo virial mass at the redshift when the mass loss rate is computed. The filled circles represent the median of points and the hatched region the quartiles. The thick solid line is the least square fit to the median distribution for each panel. The thin dashed line is the average least squares for the different host halo masses.

mass loss model. The thin dashed black line, identical in all panels, shows the global least square fit obtained using the data from all panels.

The data show a clear linear relation between m_{sb}/M_v and its time derivative, so we can write our model as:

$$\log\left|\frac{\mathrm{d}(m_{sb}/M_v)}{\mathrm{d}t}\right| = a\log(m_{sb}/M_v) + b. \tag{7.14}$$

Exponentiating this relation, and expanding the derivative on the LHS, we obtain:

$$\left|\frac{\dot{m}_{sb}}{M_v} - \frac{\dot{M}_v}{M_v}\frac{m_{sb}}{M_v}\right| = 10^b\left(\frac{m_{sb}}{M_v}\right)^a . \tag{7.15}$$

Due to the large number of snapshots in the resimulations, the time separation between two subsequent snapshots is always short: $\mathrm{d}t \approx 0.1$ Gyr. This is small enough to assume a constant mass for the host halo: $\dot{M}_v = 0$. By doing so, we obtain an expression for the *specific* mass loss rate

$$\frac{\dot{m}_{sb}}{m_{sb}} = -\frac{1}{\tau}\left(\frac{m_{sb}}{M_v}\right)^{\zeta} , \tag{7.16}$$

where the free parameters $\tau(z, M_v) = 10^{-b}$ and $\zeta(z, M_v) = a-1$ might in principle depend both on cosmic time (or, equivalently, redshift z) and on the virial mass $M_v(z)$ of the host halo at that time. The negative sign arises from the mass loss of the satellites. Note that this specific mass loss rate is identical to that used by van den Bosch *et al.* (2005).

Figure 7.15 shows how the time scale of the mass loss rate, $\tau = 10^{-b}$, and $\zeta = a-1$, as measured from the data shown in Figure 7.14, depend on the virial mass, M_v, of the instantaneous host halo. Error bars reflect the usual uncertainty on the coefficients obtained from the least square fitting. The slope is found to be independent of the mass of the host halo, with a best fit value of $a = 1.07 \pm 0.03$ ($\zeta = 0.07 \pm 0.03$). This implies that the specific mass loss rate is almost independent of the instantaneous mass ratio m_{sb}/M_v. On the other hand, the zero point, b, is found to be larger for less massive haloes.

In order to show the typical spread of points in each panel of Fig. 7.14 around each median, in the bottom panel of Figure 7.15 we show the average (over the six panels of Figure 7.14) of the differences between each quartile and the median itself. We see that on average fifty percent of the points lay roughly within a distance $\log y = \pm 0.3$ from the median; that is, typical mass losses deviate from their median value by less than a factor of two.

In Figure 7.16 we plot the subhalo mass loss rate versus the ratio $m_{sb}(z)/M_v(z)$, now binned according to the redshift at which the mass loss rate is calculated. Medians, quartiles and lines are as in Figure 7.14. The time scale τ and ζ for the six panels are shown in Figure 7.17, plotted versus the mean redshift of each of the six bins; in the bottom panel the average quartile distribution for each fit (as explained above) is shown. The red solid curve superimposed to the trend in

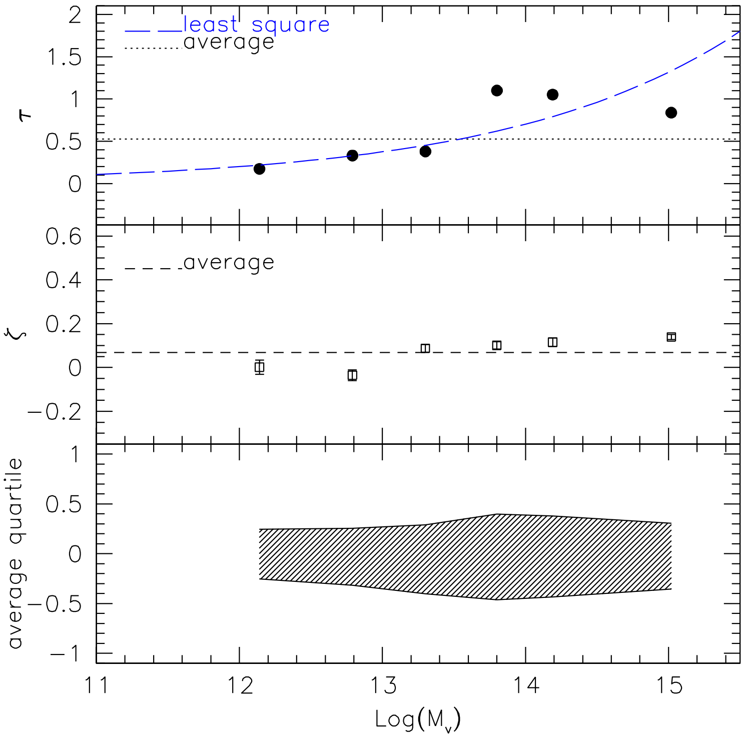

Figure 7.15: Dependence of the fit parameters of the Figure 7.14 on the host halo virial mass. The top panel shows the time scale of the mass loss rate $\tau = 10^{-b}$. The average and the least square fit of the data points have been computed on the plane (b, M_v). In the central panel we show the dependence of parameter $\zeta = a - 1$ on M_v. In the bottom panel we show the spread of the first and third quartiles around the median, averaged over the six panels of Figure 7.14 (see the main text for a detailed explanation).

zero point is the equation

$$\tau(z) = \tau_0 \left[\frac{\Delta_v(z)}{\Delta_0}\right]^{-1/2} \left[\frac{H(z)}{H_0}\right]^{-1}, \tag{7.17}$$

with $H(z)$ the Hubble constant at redshift z, and with $\tau_0 = 2.0\,\mathrm{Gyr}$.

This equation was proposed by van den Bosch *et al.* (2005) and describes the redshift dependence of mass loss rates obtained under the assumption that τ is proportional to the dynamical time $t_{\rm dyn} \propto \rho_v^{-1/2}(z)$, taking into account that, according to the spherical collapse model, the average density within the virial radius, ρ_v is independent of halo mass at fixed redshift. This means that we can write $\tau(M_v, z) = \tau(z)$. The red line in Figure 7.17 shows that indeed this provides a good description of the measured mass loss rates.

Note, though, that Figure 7.15 suggests that the average mass loss rates also depend on host halo mass. In order to reconcile this with the claim that the zero-point is independent of M_v, recall that, on average, more massive haloes assemble (and thus accrete their satellites) earlier than less massive haloes. Therefore,

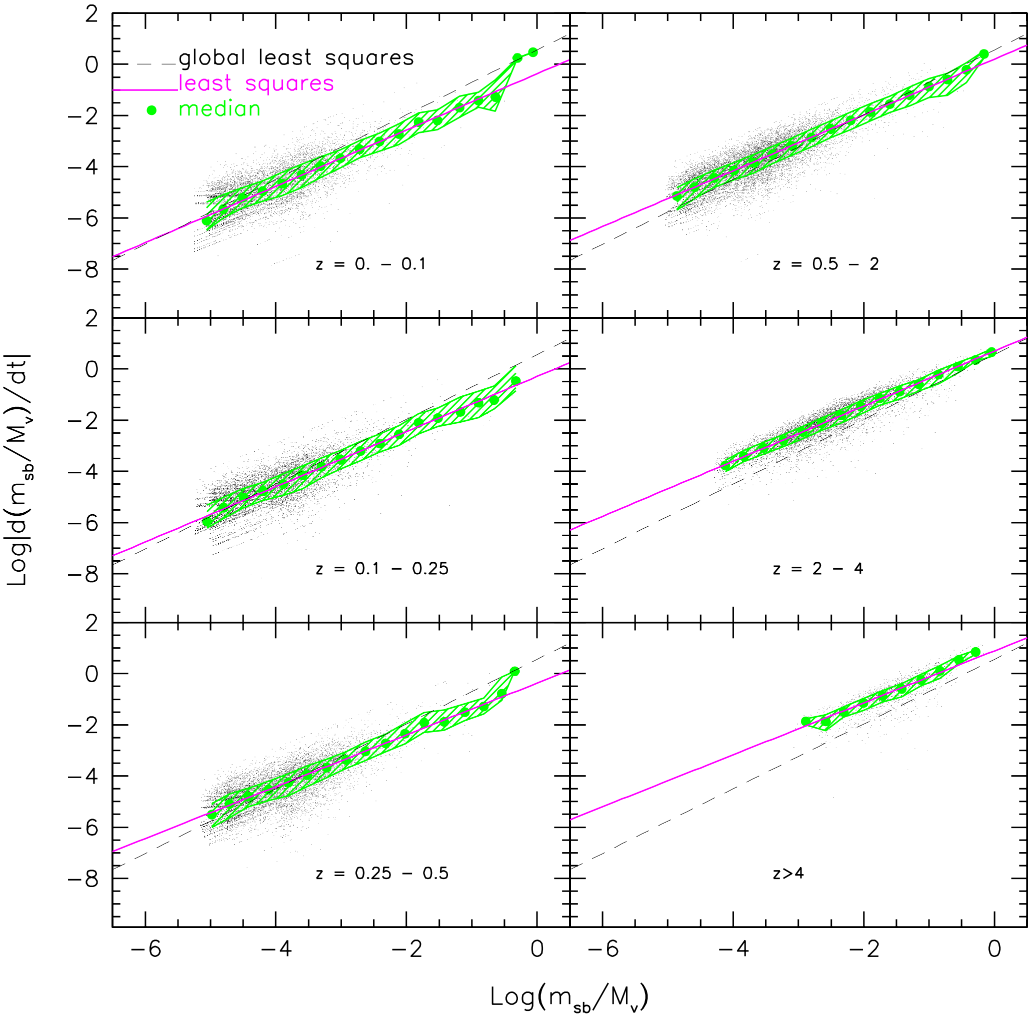

Figure 7.16: Subhalo mass loss rate. Each panel refers to a different bin in the redshift at which the mass loss rate is computed. Symbols and lines are as in Figure 7.14.

the different panels of Figure 7.14 actually refer to different average redshifts, with larger M_v corresponding to a lower average redshift. Consequently, the 'apparent' mass dependence evident in the upper panel of Figure 7.15 is merely a reflection of the redshift dependence described by equation (7.17). To demonstrate this we now split the data points of each panel of Figure 7.16 in different subsets, according to the mass of the host halo. Figure 7.18 shows the average slopes and zero points obtained for these subsets using least-squares fitting. This clearly shows that the characteristic time scale for mass loss (given by the zero point) is independent of the host mass $M_v(z)$ at fixed redshift, in accord with equation (7.17).

Thus, to good approximation, the average mass loss rate of dark matter subhaloes depends only on the density of the host halo, and thus on redshift (or cos-

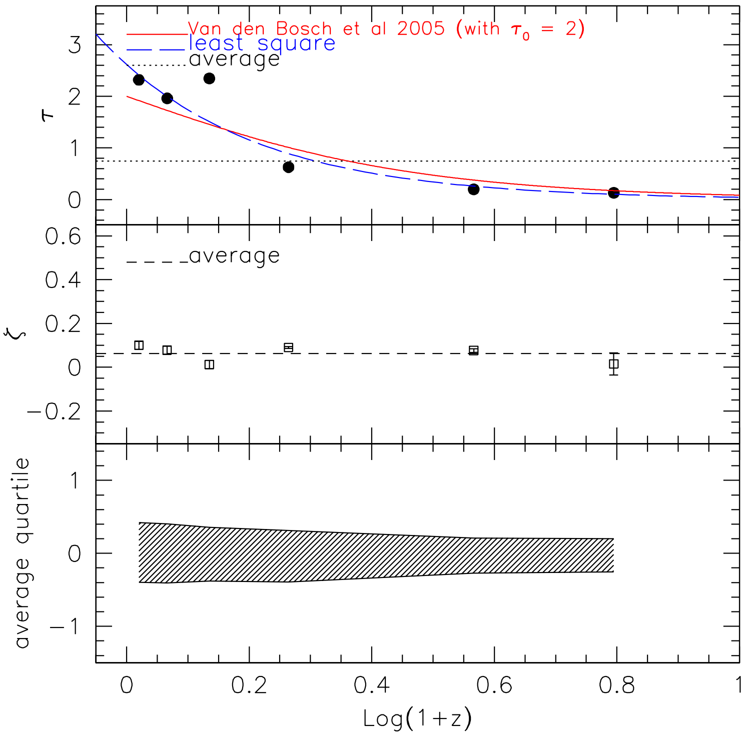

Figure 7.17: Time scale of the mass loss rate and ζ in term of the redshift at which the subhaloes are experiencing mass loss (Figure 7.16. The average and the least squares fit of the top panel were computed on the plane (b, z). The bottom panel shows the average first and third quartile for the median distribution in each panel of the Figure 7.16, constructed as previously described in the main text.

mic time), but not on the mass of the host halo. Furthermore, since the best-fit value of ζ is close to zero, to good approximation subhalo masses decay exponentially[2] according to

$$m_{sb}(t) = m_v \exp\left[-\frac{t-t_m}{\tau(z)}\right], \tag{7.18}$$

where m_v is the mass of the satellite at the time of accretion, t_m, and $\tau(z)$ is given by equation (7.17) with $\tau_0 = 2.0\,\mathrm{Gyr}$.

7.5 Monte Carlo Simulations

In this section we compare our results to those of van den Bosch *et al.* (2005), and we use their Monte Carlo method to check the self-consistency of the results presented above, i.e., we check whether the (universal) unevolved subhalo mass function, combined with the satellite accretion times and the average mass

---

[2] this follows from a simple integration of equation (7.16) with $\zeta = 0$

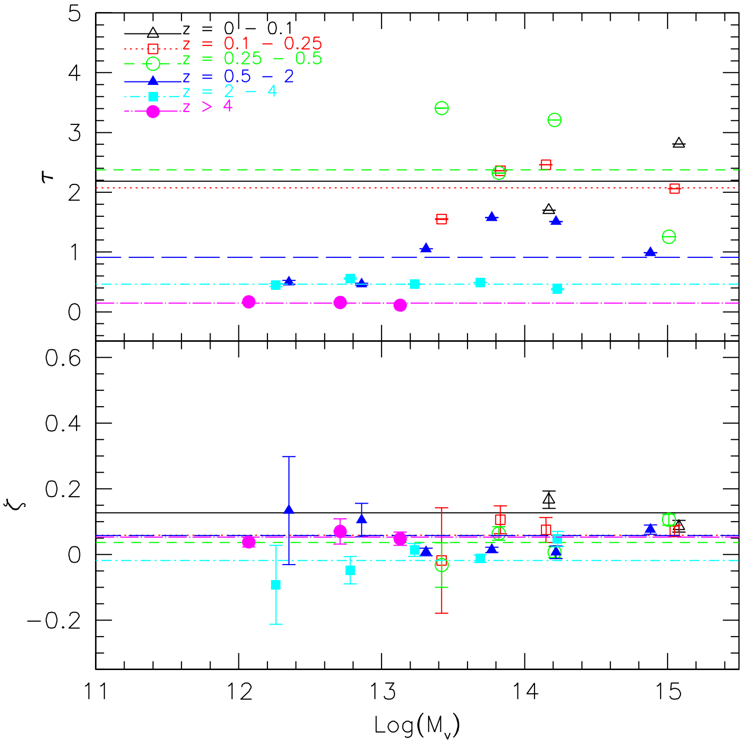

Figure 7.18: Time scale of the mass loss rate and ζ versus host mass, for six fixed redshift bins – represented by different data points. The horizontal lines, with various line type, show the average $b = -\log(\tau)$ and ζ for each redshift bin.

loss rates, can reproduce the evolved subhalo mass functions presented in Section 7.3.

The Monte-Carlo method of van den Bosch *et al.* (2005) starts by constructing EPS merger trees using the method described in van den Bosch (2002) (see also Somerville and Kolatt, 1999). These merger trees are then used to register the accretion times and masses of satellites merging onto the main progenitor. Starting from these inputs, van den Bosch *et al.* (2005) then proceeded as follows. In between two time-steps, they evolve the masses of the subhaloes using equations 7.16 and 7.17. The two free parameters, τ_0 and ζ were tuned to reproduce the subhalo mass function of massive, cluster sized haloes obtained from numerical simulations by Gao *et al.* (2004), De Lucia *et al.* (2004) and Tormen *et al.* (2004). This resulted in $\tau_0 = 0.13$ Gyr and $\zeta = 0.36$, which differs substantially from the results obtained here: $\tau_0 = 2.0$ Gyr and $\zeta = 0.06$. The reason for this discrepancy owes to the use of EPS merger trees, as opposed to merger trees extracted from numerical simulations. In fact, the unevolved subhalo mass function obtained by van den Bosch *et al.* (2005) differs significantly from that shown in Figures 7.2 and 7.13, in that it is significantly higher, and with a different slope

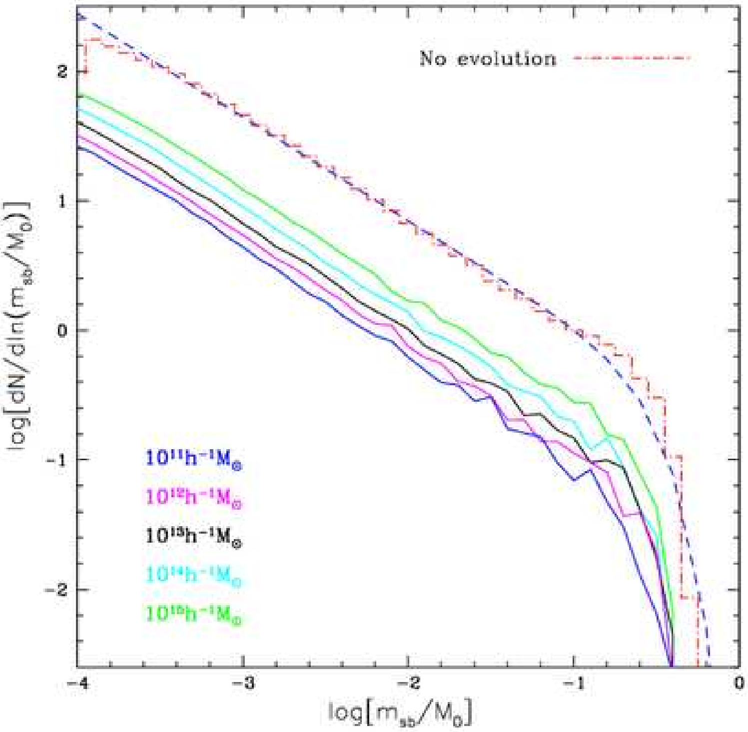

Figure 7.19: The dotted histogram show the mass accreted by the main branch in the Monte Carlo merger tree with the overplotted equation (7.3). The solid lines represent the subhaloes mass function obtained evolving the mass accreted by the main progenitors of different present day M_0-halo.

at the low mass end[3]. Consequently, in order to reproduce the subhalo mass functions obtained from numerical simulations, van den Bosch *et al.* (2005) had to adopt higher mass loss rates (i.e., a lower value for τ_0, and a different mass dependence (i.e., a different value for ζ).

The fact that EPS merger trees predict an unevolved subhalo mass function that differs significantly from that obtained in numerical simulations, should not come entirely as a surprise. After all, the construction of EPS merger trees relies on the spherical collapse model (see Lacey and Cole, 1993; Somerville and Kolatt, 1999). However, in reality, the collapse of dark matter haloes is influenced by the surrounding tidal force field, making the collapse ellipsoidal, rather than spherical (e.g., Sheth and Tormen, 1999; Sheth *et al.*, 2001; Sheth and Tormen, 2002). As shown by Sheth and Tormen (2002), the conditional and unconditional mass functions are different under ellipsoidal collapse conditions than under spherical collapse conditions, which has important consequences for the accuracy of the EPS merger trees. For instance, the halo formation times predicted by EPS are systematically offset from those obtained from numerical simulations (Lacey

---

[3] It is noteworthy, though, that the EPS formalism predicts that the unevolved subhalo mass function is universal, i.e., independent of the host mass, in good agreement with the simulation results presented here.

and Cole, 1993; Somerville *et al.*, 2000; van den Bosch, 2002; Wechsler *et al.*, 2002; Giocoli *et al.*, 2007), while the average mass of the main progenitor is typically overestimated (Somerville *et al.*, 2000).

To perform the self-consistency check mentioned above, we therefore use the same Monte-Carlo method as van den Bosch *et al.* (2005), but we randomly remove satellite-branches from the merger tree with a probability

$$P_{\rm reject} = \frac{n_{\rm sim}(m_v/M_0)}{n_{\rm EPS}(m_v/M_0)} \tag{7.19}$$

where $n_{\rm sim}$ and $n_{\rm EPS}$ are the unevolved subhalo mass functions obtained from the simulations and from the EPS merger trees, respectively. This ensures that the Monte Carlo method uses an effective, unevolved subhalo mass function that is identical to that of equation (7.3).

As in van den Bosch *et al.* (2005) we evolve the masses of the subhaloes using equations 7.16 and 7.17 with $\tau_0 = 2.0$ Gyr and $\zeta = 0.06$, which are the best-fit values obtained in Section 7.4. The resulting evolved subhalo mass functions, for five different masses of the present-day host halo, are shown in Figure 7.19, together with the unevolved subhalo mass function obtained using the rejection scheme outlined above (and which is independent of the host halo mass). Each evolved subhalo mass function is the average obtained from 2000 merger tree realizations (see van den Bosch *et al.*, 2005, for details). A comparison with the evolved subhalo mass functions obtained from our numerical simulations, and shown in Figure 7.19, shows good agreement. This indicates that the evolved subhalo mass functions are self-consistent with the (universal) unevolved subhalo mass function and the simple form for the average mass loss rate obtained in this work.

7.6 Discussion

In this work we have studied the mass loss rate of dark matter subhaloes using a set of high resolution N-body simulation of structure formation. Haloes were followed backward in time along the main branch of their merging history tree. At each snapshot the satellites accreted by the main branch were identified. We showed that the mass function of accreted satellites (unevolved subhalo mass function) is universal, that is, it does not depend on the present day host halo mass M_0, and we presented a fitting function for this distribution.

We then followed each accreted satellite forward in time, snapshot by snapshot, computing its self-bound mass and its mass loss rate. We found that the expression for the mass loss rate proposed by van den Bosch *et al.* (2005) is consistent with N-body simulations, and excellent agreement is obtained if the value with $\tau_0 = 2.0\,$Gyr is taken. In addition, we find that the average mass loss rate is virtually independent of the instantaneous mass ratio m_{sb}/M_v between the subhalo and its host halo. This differs substantially from the best-fit mass loss rate parameters obtained by van den Bosch *et al.* (2005) using EPS merger trees. In particular, van den Bosch *et al.* (2005) obtained $\tau_0 = 0.13\,\mathrm{Gyr}$, and a significant dependence on m_{sb}/M_v. The reason for this discrepancy is that the unevolved subhalo mass function of EPS merger trees is too high, so that a higher mass loss rate was inferred to be consistent with the evolved subhalo mass functions in numerical simulations.

With an unevolved subhalo mass function that is universal, and an average mass loss rate that is virtually independent of m_{sb}/M_v, it becomes straightforward to understand why less massive haloes have evolved subhalo mass functions with a lower normalization. This simply owes to the fact that less massive haloes assemble earlier, which implies that they accrete their satellites earlier. At earlier times the mass loss rate is higher, because the dynamical times of dark matter haloes are shorter. In addition, a subhalo that is accreted earlier is subjected to mass loss for a longer period. Both these effects contribute to the fact that less massive haloes have less substructure.

The present description does not consider the possible presence of subhaloes within subhaloes, accreted along the tree of each present day subhalo. In the following chapter we will investigate this issue in detail, comparing the populations of subhaloes found using different techniques.

CHAPTER

8

Subhaloes within Subhaloes

In this Chapter we describe an algorithm developed to identify the subhaloes within subhaloes in dark matter haloes extracted from numerical simulations. Code and results presented in the previous chapter take into account only the self-bound particles of satellite haloes. However we have to notice that a large fraction of satellites at merging time with the main progenitor, host subhaloes accreted when they where isolated systems. These satellites of satellites can still be isolated groups of self-bound particles in the host halo at $z = 0$ (Diemand *et al.*, 2007b; Li and Helmi, 2007). The idea beyond this algorithm is to follow all branches of the tree of a present-day host halo until the "leafs" satellites, and compute their self-bound particles at $z = 0$. We term "leaf" a satellite of a satellite which does not have progenitors surviving at the present time.

Hereafter the notation subhalo will be used referring to a clump identified by previous algorithm (Cap. 7) – self-bound particles of a satellite halo. To the other hand, we will term substructure, or survivor, a subhalo within subhalo – self-bound group of particles of a "leaf" satellite (see Section 8.1 for the description of the algorithm). Considering what are the ideas beyond galaxy formation models (Kauffmann *et al.*, 1999; De Lucia *et al.*, 2004), it is natural that, between the two algorithms, substructures can be more directly related to galaxies hosted in dark matter haloes. However the correlation between galaxies and substructures is still an open debate.

In the standard scenario of structure formations galaxies form at high redshift in dark matter haloes where baryons can shock, cool and eventually form stars. The gas condensation, through dissipative cooling, stabilized galaxies against the disruption caused by the merging of the dark haloes along the cosmic time. However additional processes, for example feedback, are needed to make small galaxies more diffuse so that they would be less successful at surviving the merging process, thus avoiding the production of more faint galaxies than are observed. However other mechanisms, as reionization of the universe, can play the role of preventing galaxy formation in small haloes. The reionization of cosmic hydrogen results in heating of the inter galactic medium (IGM) to $\sim 10^4$K, which drastically increases the minimum virial temperature of new galaxies to a value as high as $T_v \approx 10^5$K. In this way, star formation is prevented in haloes with virial mass smaller than $10^8\, M_\odot/h$. The WMAP measurement (Spergel *et al.*, 2007) and the observed drop of star formation rate indicate a reionization redshift $z \sim 6$ (Grebel and Gallagher, 2004).

The first small collapsed haloes, at high redshift, will merge together forming bigger and bigger systems at the present time. The galaxy clusters are at the top of this hierarchy and represent the biggest virialized structures in the universe. They typically host thousand of galaxies within their dark matter potential well. The evolution of individual dark matter haloes and the formation of galactic structure inside them is strongly dependent on the nonlinear dynamics of gravitational collapse, the stochastic process of merging, and the subsequent evolution of the merged substructures.

Recent N-Body simulations have opened a new debate in the ΛCDM cosmology predicting a number of substructures that is much larger than the observed number of satellite galaxies. For example, they compare results from numerical simulations of galaxy size haloes with the Milky-Way halo population, finding a mismatch in the number of satellites of more than one or two order of magnitude (Moore *et al.*, 1999; Ghigna *et al.*, 2000; Kravtsov *et al.*, 2004). This excess structure may be also implicated in several other problems, including the small disk size produced in hydrodynamic simulations (Navarro and Steinmetz, 2000), and the question of disk survival against heating in minor mergers (Toth and Ostriker, 1992; Kauffmann and White, 1993; Moore *et al.*, 1999). Different arguments have been proposed to solve this “missing satellites” problem: (i) low star formation efficiency in small haloes due to some feedback mechanisms, (ii) warm dark matter or also (iii) suppression of small scale fluctuation in the dark matter power spectrum.

To better understand the ΛCDM cosmological model we first need to establish a proper understanding of the build-up and evolution of the population of dark matter substructures. We will present a study about this in this chapter.

8.1 The Simulation and Substructure Finder Algorithm

The simulation used for this work is the GIF2 simulation (see Chapter 4 for more details about its numerical and cosmological parameters). This has a high mass and force resolution able to resolve systems down to the minimum mass of $1.73 \times 10^{10}\, M_\odot/h$ – corresponding to groups with at least 10 dark matter particles.

In the previous chapter we have shown how present-day subhalo population can be identified following the growth of the main progenitor halo along the main trunk of its merging history tree. From Figure 7.10 we notice that a large fraction of subhaloes host clumps of particles within them, and that some clumps, among the dust particles, have not been identified by the algorithm. All these missed clumps and the subhaloes within subhaloes are probably groups of particles belonging to satellite haloes of subhaloes accreted when the latter isolated. If we take a look to Figure 7.9, where we show a schematic representation of the merging history tree, we can see that satellites, before merge on the main progenitor halo have a hierarchical growth accreting mass in haloes. A fraction of these can survive at the present time in the host system as individual clumps. The unidentified clumps among the dust particles in Figure 7.10, probably represent situations in which a subhalo split in two or more pieces, belonging to its satellites.

At this point, some question spontaneously arise: (i) how will change the subhalo mass function considering also subhaloes within subhaloes? (ii) can we compare our algorithms with other substructure finders? (iii) the definition of substructure is universal or does it depend on the algorithm adopted? We will try to answer to these questions in the following pages of this chapter.

Description of the Algorithm

To work, the algorithm need the following input files, that come from the post-processing of the simulation:

- halo catalogue at each simulation snapshot;
- merger tree, density profile and subhalo catalogue of present-day haloes, or of haloes at the observation redshift z_0 where we want to compute the substructure catalogue.

In order to identify the substructures in a given host halo at $z = z_0$ (in this chapter we will consider only the case where $z_0 = 0$) we proceed in the following way:

1. for a given present-day halo, we read its subhalo catalogue;
2. for each subhalo in the catalogue, we read the informations about its progenitors at $z = z_i + \mathrm{d}z$ – where z_i represent the identification time of the satellite[1] and dz the redshift step in the simulation;
3. for each progenitor, we traced at redshift $z = z_0$ its particles, computing those that are self-bound in the tidal radius, the center is computed with the moving center method;
4. if at least two progenitors (the main and a satellite of it) have self-bound particles at redshift $z = 0$, we substitute the subhalo in the catalogue with the new ones; we compute also their orbital parameters and recall that the new systems will now have an identification redshift larger than the merging time: $z_i > z_m$,
5. we proceed in this way until all subhaloes for each host halo are scanned;
6. we call each subhalo not split in clumps "leaf" satellite of the tree.

---

[1] We recall that for subhaloes identification z_i and merging redshift with the main progenitor z_m correspond. However for substructures the two definitions do not coincide.

In this way we identified subhaloes within subhaloes at the first order, we call these subhaloes$^{1^{th}}$. However each subhalo$^{1^{th}}$ may also contain within itself other subhaloes accreted along its branch (see Figure 7.9). To identify subhaloes of order bigger than the first we repeat the previous items for each self-bound group in the catalogue, skipping the "leafs". For each subhalo$^{1^{th}}$ we go at its identification redshift z_i and read the informations about its progenitors at $z = z_i + \mathrm{d}z$. We then compute their self-bound particles, at the present time. If at least two of them (the main and a satellite) survive, we substitute the subahlo$^{1^{th}}$ with the new self-bound groups. We term these subhaloes$^{2^{th}}$. We proceed in this way repeating the items above until the n^{th} order. At the end we expect that all systems in the catalogue are "leaf" satellite haloes, i.e. no of them have more than one progenitor with self-bound particles at the present time. The mass resolution of the algorithm has been set equal to 10 self-bound particles – for GIF2 simulation this correspond to a self-bound mass of $1.73 \times 10^{10}\, M_{\odot}/h$.

In upper left panel of Figure 8.1 we show the particle distribution in the simulation box of the GIF2 at redshift $z = 0$. The upper right plot shows particle in the virial radius of the most massive halo and in the lower left the self-bound particles in survivors. The lower right show the correspondent dust particles, i.e. particles that do not belong to any survivor. Comparing the dust particles from subhaloes (lower right panel of Figure 7.10) and those from survivors (lower right panel of Figure 8.1) we see that in this last case the particle distribution is smoother and more free of clumps: it seems that all identifiable groups by eye have been captured by the algorithm.

In Figure 8.2 we plot the mass function of substructures in the dark matter haloes (that we will call also survivor mass function SuMF), at redshift $z = 0$. We considered substructures with at least 10 dark matter particles within the virial radius and more distant than $0.05 \times R_v$ where identify clump is harder. The various data points and line types refer to different host halo masses. As expected by the hierarchical clustering model, more massive systems host more substructures than small ones at fixed m_{sb}/M_0. This trend is a result of the fact that large haloes are still accreting mass in haloes at present times. Their substructures, spending less time in the potential well of the host, have more possibility to survive intacts until $z = 0$. To the other hand, in small systems satellite haloes have been accreted at high redshifts and spending long time in the potential well of the host loose a large fraction of their initial mass. In the figure, we consider all host haloes at $z = 0$ with at least $M_v = 10^{11.5}\, M_{\odot}/h$ whose main progenitor halo at any redshift never exceed $1.1 \times M_0$. Comparing this figure with the subhalo mass function (Figure 7.11) we notice that the survivor mass function, at least for the most massive haloes, is steeper. This trend is expected because more massive subhaloes have been split in smaller and smaller clumps. The survivor catalogue, for each halo, is so poor of large self-bound groups and rich of small ones, when compared to the subhalo mass function. However for host haloes in the two smallest mass bins, the SHMF and SuMF do not differ, this because for the mass resolution of the simulation, their subhaloes are already "leaf" satel-

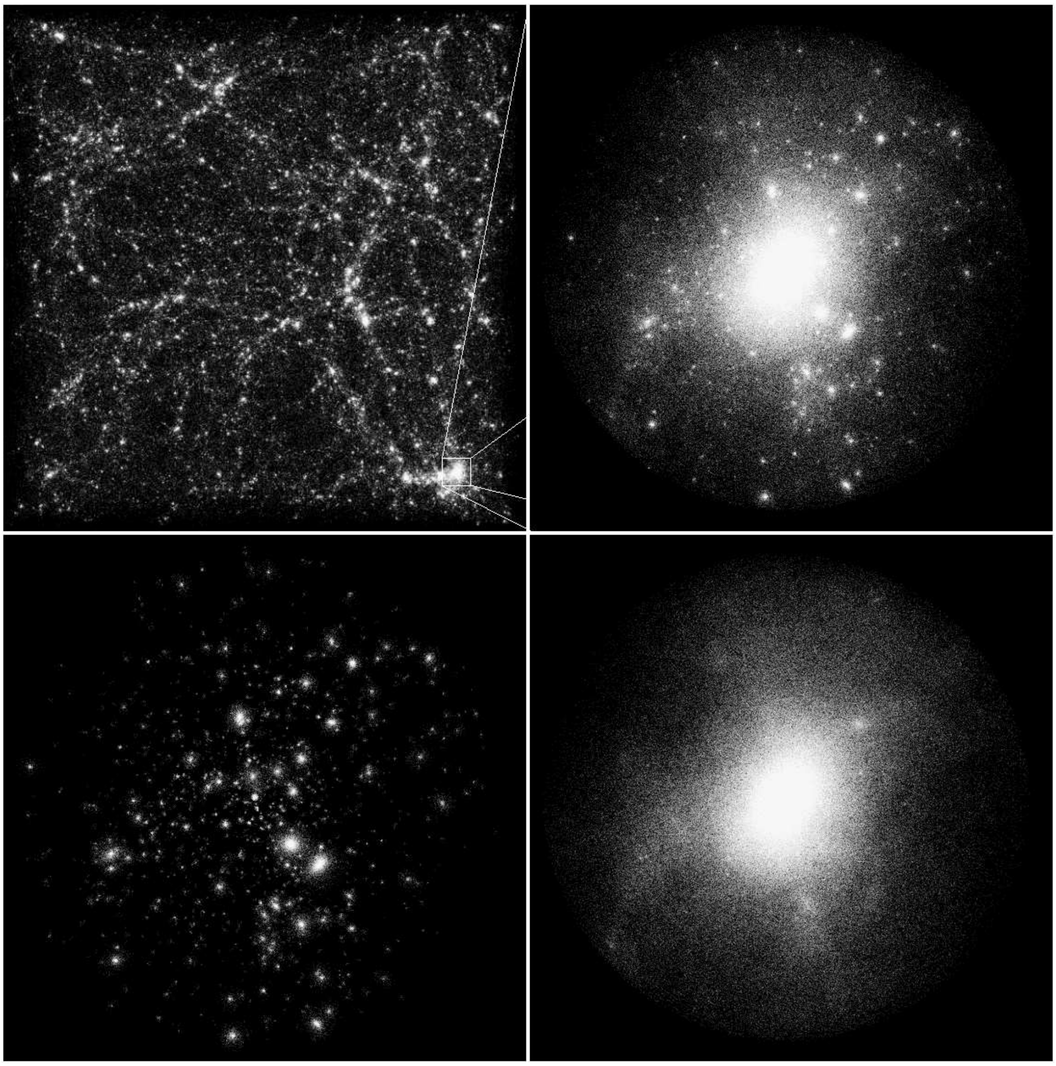

Figure 8.1: GIF2 Cosmological N-Body simulation. **Upper left**: particle distribution in the simulation box at $z = 0$, the side of the cube is $L = 110\,\mathrm{Mpc}/h$. **Upper right**: particles in the virial radius of the most massive halo. **Lower left**: particles in survivors within the virial radius of the host halo. **Lower left**: the dust particles in the halo.

lites.

Comparison Between Survivors and SUBFIND

The identification of substructures within dark matter haloes is a challenging technical problem, and several algorithms to find "haloes within haloes" have been proposed. Let us now describe some methods developed to identify substructures in numerical simulations.

In hierarchical friends-of-friends (HFOF) algorithms (Gottlöber *et al.*, 1999; Klypin *et al.*, 1999), the linking length of plain FOF is reduced in a sequence of discrete steps, thus selecting groups of higher and higher overdensity and even-

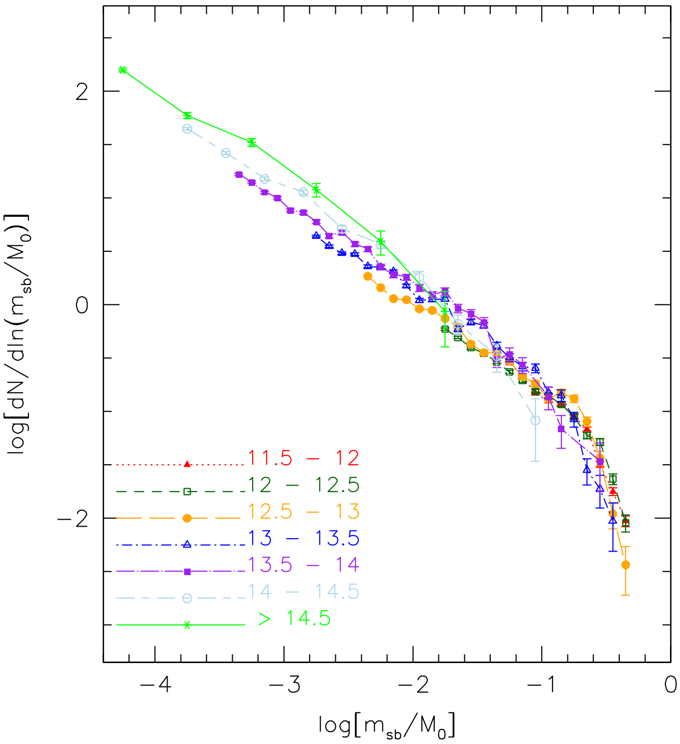

Figure 8.2: Survivor mass function of dark matter haloes at $z = 0$. We consider all the substructures with more than 10 self-bound particles, having also their center of mass inside the host halo.

tually capturing true substructures. However a more physical definition need to be adopted. Different authors have been required the substructures (or the subhaloes) to be locally overdense and self-bound.

Group-finding techniques, that use some criterion of selfboundedness, include the bound density maximum (BDM) algorithm (Klypin *et al.*, 1999), where the bound subset of particles is evaluated iteratively in spheres around a local density maximum. Another approach is followed in DENMAX (Gelb and Bertschinger, 1994) and SKID (Ghigna *et al.*, 1998), where particles are moved along the local gradient in density toward a local density maximum. Particles ending up in the 'same' maximum are then linked together as a group using FOF. Eisenstein and Hut (1998) developed HOP where group search is done in the set of original particle positions, just as FOF does. In HOP, one first obtains an estimate of the local density for each particle, and then attaches it to its densest neighbor. In this way a set of disjoint particle groups are formed.

Springel *et al.* (2001) developed another algorithm to identify substructures in dark matter haloes, its name is SUBFIND. Starting from a FoF group they computed, using an SPH-fashion technique, the density position of all particles. Any locally overdense region is considered within this field to be a substructure candidate. The region of isodensity contour that traverse a saddle point are computing imagining lowering a global density threshold slowly within the density field. SUBFIND tries to identify all locally overdense regions by imitating such a lowering of a global density threshold.

All these algorithms give a substructure mass function, in numerical simulations of ΛCDM universe, that have a power low trend $\mathrm{d}N/\mathrm{d}m_{sb} \propto m_{sb}^{\alpha}$ with the slope α ranging from -1.7 to -2 Moore *et al.* (1999); Ghigna *et al.* (1998); De Lucia *et al.* (2004); Gao *et al.* (2004).

Recently Gao *et al.* (2004) have studied the substructure populations of ΛCDM dark haloes in the GIF2 simulation. At each snapshot of the simulation they identified the haloes with a FoF algorithm, truncating their radius at 200 times the critical density of the universe (we will use M_{200} referring to this definition of mass), and identifying substructures in haloes using SUBFIND. At this point we have the possibility to compare our algorithms with SUBFIND. However we need to rescale the halo definition in order to reproduce the mass function of Gao *et al.* (2004) (upper left panel of their Figure 5). We recall that our haloes are 97 times denser than the critical density at $z = 0$. To compute M_{200} we read the density profile of each halo and interpolate it at $200 \times \rho_c$.

In Figure 8.3 we plot the survivor (open circles - dashed lines) and subhalo (filled triangles - dotted lines) mass function, considering different host halo masses. In this figure the mass of each clump has been rescaled respect to M_{200} and the systems considered are all these inside R_{200} (corresponding radius of M_{200}) and with at least 10 self-bound particles. The asterisks connected with solid lines represent the result of SUBFIND (Gao *et al.*, 2004). The dashed and the dotted-dashed straight lines are the best fit (by eye) to the SUBFIND mass function for haloes in the range $7 \times 10^{13}\, M_{\odot}/h \le M_{200} \le 1.8 \times 10^{15}\, M_{\odot}/h$, found by Gao *et al.* (2004); De Lucia *et al.* (2004) respectively. These are represented by the following equations:

$$\text{De Lucia et al. 2004} \quad \frac{\mathrm{d}n}{\mathrm{d}\ln(m_{sb}/M_{200})} = 0.016\left(\frac{m_{sb}}{M_{200}}\right)^{-0.94}; \tag{8.1}$$

$$\text{Gao et al. 2004} \quad \frac{\mathrm{d}n}{\mathrm{d}\ln(m_{sb}/M_{200})} = 0.017\left(\frac{m_{sb}}{M_{200}}\right)^{-0.91}. \tag{8.2}$$

In Figure 8.3 we notice that for the four mass bins considered, the survivor mass function reproduce the same trend of SUBFIND. We notice also, as said before, that survivors have few large mass clumps compared to the subhaloes, and the opposite is true for the small mass clumps. The survivor mass function is steeper than the subhalo distribution. At this point we can say that our definition of substructure is more similar to the definition of SUBFIND and that we need to have care when we refer to substructures in general: their definition depend on the algorithm used to identify them.

In the left panel of Figure 8.4 we plot the survivor mass function per unit of host halo mass (expressed in term of $10^{10}\, M_{\odot}/h$). The different data points and line types are the same of Figure 8.2 and refer to different host halo masses. The mean number of survivors for each mass bin has been normalized to the corre-

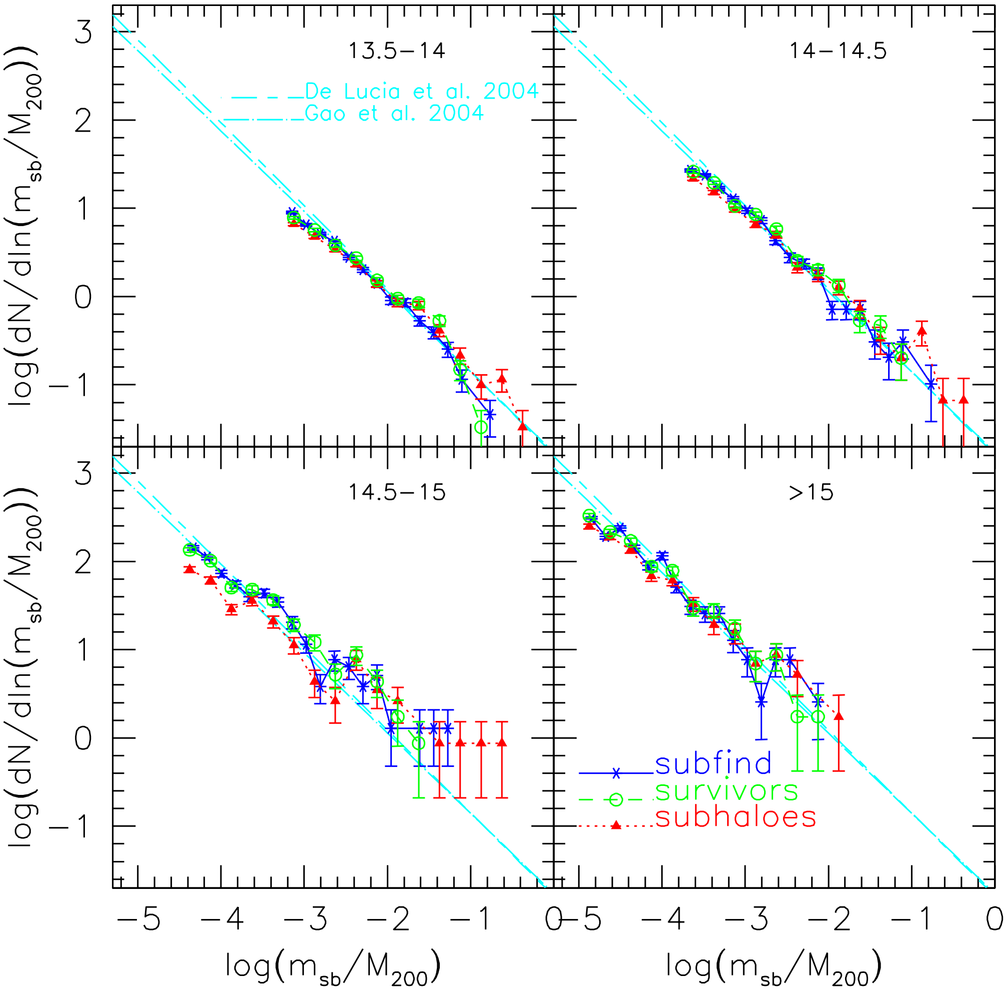

Figure 8.3: Comparison of three methods that identify clumps in dark matter haloes. To be consistent with Gao *et al.* (2004) we rescale the mass of dark matter haloes such that their enclosed density is 200 the critical one and considering all clumps within the corresponding radius R_{200}. The asterisks connected with solid lines represent the mass function obtained with SUBFIND. The open circles refer to the survivor mass function and the filled triangles to the subhalo mass function (Chapter 7). The dashed and the dotted-dashed lines are the best fit (by eye) to the SUBFIND mass function of the massive haloes for Gao *et al.* (2004) and De Lucia *et al.* (2004).

sponding host halo virial mass per unit of $10^{10}\ M_\odot/h$. In the right panel we plot the value of the distributions at the survivor mass resolution versus the mean host halo virial mass in each bin. From the figure we can see that, as argued by Gao *et al.* (2004), the substructure mass function per unit of host halo mass is universal down to $10^{13}\ M_\odot/h$ and well fitted, ignoring the high-mass cut off, by:

$$\frac{\mathrm{d}N}{\mathrm{d}m_{sb}} = 10^{\beta} m_{sb}^{\alpha}, \tag{8.3}$$

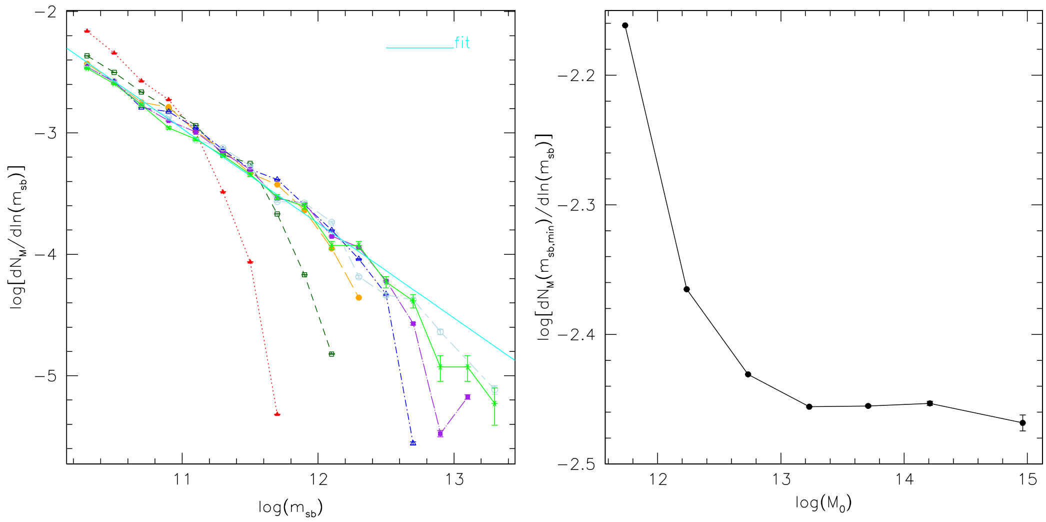

Figure 8.4: Survivor mass function per unit mass of the parent halo. **Left**: the differential substructure abundance normalized to the total mass of the parent haloes $\langle M_v \mathrm{d}n/\mathrm{d}m_{sb}\rangle$, in term of $10^{10}\,M_\odot/h$. The various data points and line types refer to different parent halo host masses. **Right**: the dependence on the host halo mass of the value of distributions corresponding to the minimum survivor mass plotted in the left panel.

with $\alpha = -1.8$ and $\beta = -4.4$. We recall that the value obtained by Gao *et al.* (2004) are $\alpha = -1.9$ and $\beta = -3.2$. The difference between the correspondent fit parameters obtained by us and by Gao *et al.* (2004) is due to the different definition of the host halo mass we adopted.

An immediate consequence of the universality of this relation, for large host halo masses, is a shift with parent halo mass in the abundance of substructures as a function of the corresponding scaled mass $m_n = m_{sb}/M_0$. For small masses this shift is

$$\Delta \log f(m_n : M_0) = 0.1 \Delta \log M_0\,, \tag{8.4}$$

where $f(m_n : M_0)$ is the mean abundance of substructures by normalized mass $\mathrm{d}N/\mathrm{d}m_n$ in host haloes of mass M_0. In Figure 8.4 we notice also that for mass smaller than $10^{13}\,M_\odot/h$ the survivor mass function per unit of host halo mass is not universal, the normalization factor β is larger for smaller host haloes.

8.2 Mass Fraction in Substructures and HOD

The total mass fraction in substructures is an interesting quantity but one for which there is little agreement in the numbers reported in literature. Most authors estimate a mass fraction between 5% and 20% (Gao *et al.*, 2004; De Lucia *et al.*, 2004; Stoehr *et al.*, 2002; Ghigna *et al.*, 1998), however Moore *et al.* (1999) argue that the true mass fraction might approach unity if substructures could be identified down to extremely small masses. Diemand *et al.* (2007a), performing the highest resolution simulation to data of Galactic CDM substructures, followed the formation of a Milky Way-size halo, using 243 million particles. They estimated a mass fraction equal to 5.3% but also argue that because of the significant contribution from the smallest resolved clumps, this fraction could not have converged yet.

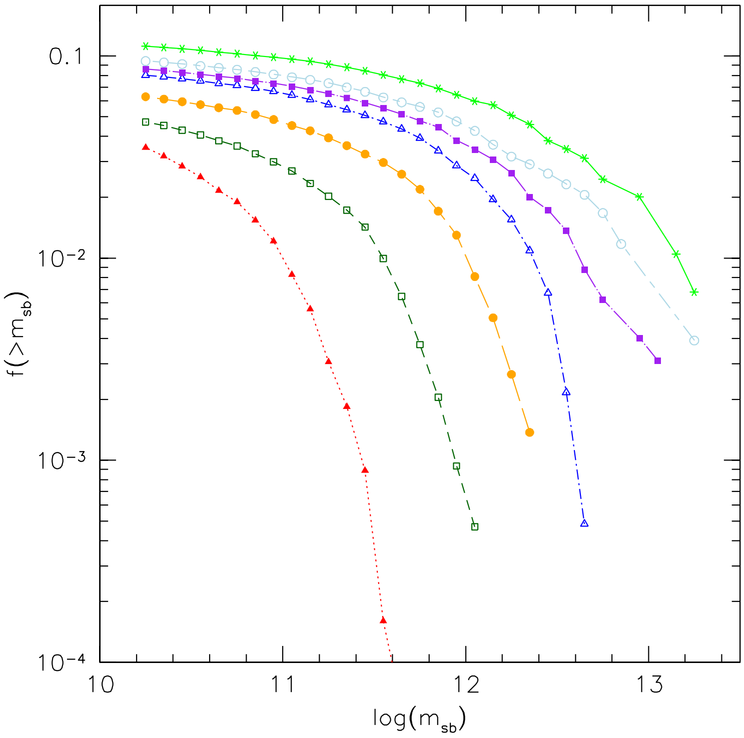

Figure 8.5: Cumulative virial mass fraction in substructures. The data points show the mass fraction of haloes, for the seven different mass bins considered, in survivors more massive than m_{sb}. We considered all substructures within the virial radius of the host halo and resolved with at least 10 dark matter particles.

In Figure 8.5 we show the cumulative mass fraction of the host halo in substructures more massive than m_{sb}, for haloes in the seven mass bins considered. These curves show a clear trend: the substructure mass fraction seems to converge to well defined value as the mass resolution is reduced. The asymptotic value is larger for more massive haloes, reflecting the trend in hierarchical clustering that once the ratio m_{sb}/M_0 is fixed, more massive haloes host more substructures than small ones.

In Figure 8.6 we show the average mass fraction in substructures in term of the host halo mass. The open circles show the result for haloes in GIF2 simulation more massive than $10^{11.5}\ M_{\odot}/h$. Clearly more massive haloes have a large mass fraction in substructures than the small ones. For a Milky Way-size halo, the mass fraction, in substructures more massive than $1.73 \times 10^{10}\ M_{\odot}/h$, is of the order of the 5%. For each of the seven mass bins we also divide the haloes in two sample: those with a formation redshift smaller than the median (open diamonds in the figure) and those with z_f larger (filled triangles), these two groups are also expected living in different environments. Those with $z_f > \bar{z}_f$ have been assembled before, accreted progenitors at early times and live, probably, now in an underdense region[2] of the universe. To the other hand, host haloes with $z_f \leq \bar{z}_f$ live in an overdense region and are still accreting progenitor haloes. In the first case substructures, spending more time in the potential well of the host halo, will retain at the present time only a small fraction of the original virial mass. In Figure 8.6 we can see that once the host halo mass is fixed, systems with a formation redshift larger than the median have a mass fraction in substructures that is smaller than the average relation. The opposite is true for parent haloes with $z_f \leq \bar{z}_f$. The three dashed lines in figure represent the least squares fit to the three different data points.

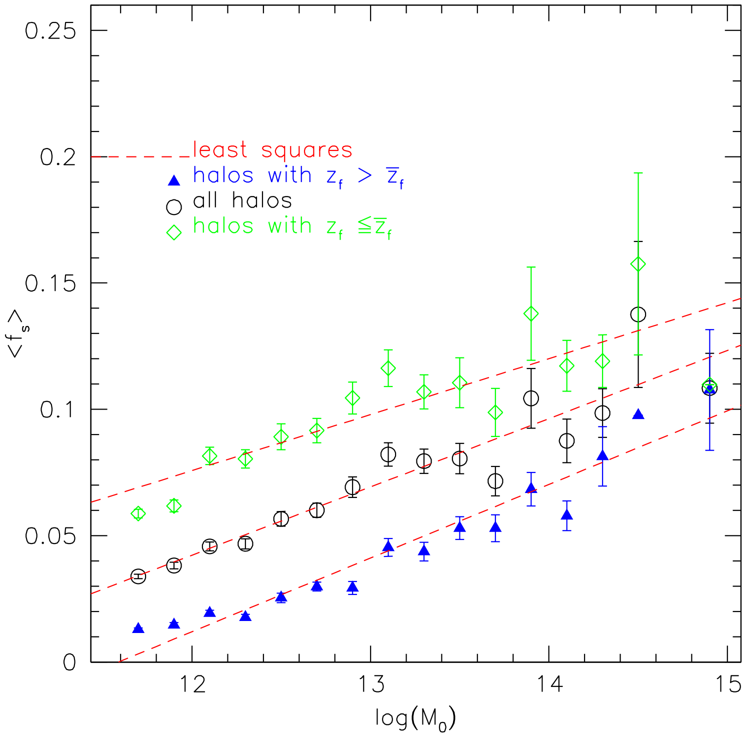

Figure 8.6: Average virial mass fraction in substructures in term of the host halo mass. Open circles show the results for haloes more massive than $10^{11.5}\,M_\odot/h$ in GIF2 simulation, error bars are the r.m.s. of the average of the distributions. The filled triangles refer to haloes with formation redshift larger than the median of the corresponding mass bin, while open diamonds to haloes with a formation redshift smaller than the median. The dashed lines represent the least squares fit to the three different data points.

These considerations are also very important to understand the properties of central galaxies and of the intergalactic light, that characterize dark matter

---

[2] The mean density of the region is smaller than the mean background density of the universe $\bar{\rho}$.

haloes. In the hierarchical picture, host galaxies are expected to form accreting new galaxies along the cosmic time. After entering in an host halo, the stars and gas in satellite galaxies can be deposited onto the central galaxy, stay bound as a satellite galaxy or be scattered into the intergalactic light (Conroy *et al.*, 2007). Hydrodynamical simulations have found that approximately 85% of the stars in the intergalactic light a $z = 0$ were deposited at $z < 1$ (Willman *et al.*, 2004; Murante *et al.*, 2007; Krick *et al.*, 2006) and less than 30% of the intergalactic light was built up by tidal stripping of satellite galaxies. The majority of the intergalactic light is thus built during violent merging events with the central galaxy and/or the complete disruption of satellites. In this picture we expect that two haloes of the same mass living in two different region of the universe will have different observables. The older halo will probably have a red central galaxy and more rich of intergalactic light. To the other hand, the younger, that is still accreting systems, is expected to be more poor of intergalactic light, because the satellites spent less time within its potential well.

Another interesting quantity that describes dark matter substructure clustering is the number of substructures that inhabit a halo of mass M_0: substructures Halo Occupation Distribution. This quantity can be predicted studying the clustering of dark matter, power spectrum, bispectrum, and higher order moments of the mass density field as showed by Scoccimarro *et al.* (2001). The mean number density of substructures can be written as:

$$\bar{n}_{surv} = \int n(M) \langle N_{surv}(M) \rangle \mathrm{d}M , \tag{8.5}$$

where $n(M)$ is the mass function of dark matter haloes and $\langle N_{surv}(M) \rangle$ indicates the mean number of substructures in an M-halo. Knowledge of the number of substructures per halo moments $\langle N^n_{surv}(M) \rangle$ as function of halo mass gives a complete description of the dark matter clustering within haloes. The number of substructures hosted by a dark matter halo represents an upper limit to the number of galaxies that can inhabit an halo.

Semi-analytical methods of galaxy formation (Kauffmann *et al.*, 1999; Sheth and Diaferio, 2001) predict an abundance of galaxy per dark matter halo mass that scale as a power-law. The slope of the distribution depends on the color of the galaxies as follow:

$$\begin{array}{rcl} \langle N_{gal} \rangle & = & \langle N_B \rangle + \langle N_R \rangle \\ \langle N_B \rangle = 0.7\,(M/M_B)^{\alpha_B} & & \langle N_R \rangle = (M/M_R)^{\alpha_R} , \end{array} \tag{8.6}$$

where $\alpha_B = 0$ for $10^{11}\,M_\odot/h \le M \le M_B$, $\alpha_B = 0.8$ for $M > M_B$, $M_B = 4 \times 10^{12}\,M_\odot/h$, $\alpha_R = 0.9$ and $M_R = 2.5 \times 10^{12}\,M_\odot/h$. The physical basis for this relation is that for large masses, the gas cooling time becomes larger than the Hubble time, so galaxy formation is suppressed in large-mass haloes; the number of galaxy per halo mass increases less rapidly than the mass. In small-mass haloes, however, effects such as supernova winds can blow away the gas from haloes, also suppressing galaxy formation producing also the cutoff at small masses.

In Figure 8.7 we show the substructure halo occupation statistic. In the upper left panel the average number of substructures per dark matter halo mass is represented (open circles). In the upper right we show the function $\alpha(M)$ that quantifies deviations from Poisson statistics of the distribution, and correlate the first and second moment obeying at the equation:

$$\alpha(M) \equiv \frac{\langle N_{surv}(N_{surv}-1)\rangle^{1/2}}{\langle N_{surv}\rangle}\,. \tag{8.7}$$

The two panels on the bottom shown the second and the third order factorial moment of the halo occupation statistic.

Hierarchical clustering model predict that galaxies form in dark matter haloes where gas can shock, cool and eventually form stars. The center of dark matter haloes is, in this contest, expected inhabited by a peculiar galaxy while substructure population could host the satellite galaxies. The upper limit to the number of galaxy that can be hosted by a dark matter halo is so represented by the total number of substructures + 1 (host central galaxy). In the four panels the filled circles refers to this statistic.

In the upper left panel of Figure 8.7 the solid line is the equation

$$\langle N_{surv}\rangle_f = 0.014\left(\frac{M_0}{M_{0,min}}\right)^{0.97}\,, \tag{8.8}$$

that represents the least squares fit to the survivors occupation distribution. In the equation $M_{0,min} = 1.73\times 10^{10}\, M_\odot/h$ is the minimum mass considered by the halo finder corresponding to systems with at least 10 particles. In the upper right the average value of the anisotropy parameter

$$\bar{\alpha}(M) = 1.07 \pm 0.01\,, \tag{8.9}$$

is represented by the solid horizontal line. The dotted lines in the lower panels show the least squares fit to the open circle data points. The solid line in the lower left panel is the equation:

$$\langle N_{surv}(N_{surv}-1)\rangle_f = \bar{\alpha}^2\langle N_{surv}\rangle_f^2 \tag{8.10}$$

where $\langle N_{surv}\rangle_f$ and $\bar{\alpha}$ are the fit to first moment and the average anisotropy parameter. Also the higher order factorial moments are completely determined once the first two moments have been specified, they obey to the equation:

$$\langle N_{surv}(N_{surv}-1)...(N_{surv}-j)\rangle = \alpha^2(2\alpha^2-1)...(j\alpha^2-j+1)\langle N_{surv}\rangle^{j+1}\,. \tag{8.11}$$

In the lower right panel of Figure 8.7 the solid line has been obtained from the previous equation considering $j = 2$ and using the fit to first order moment $\langle N_{surv}\rangle_f$ and $\alpha = \bar{\alpha}$. In the case of a Poissonian distribution the equations for the high order moment become:

$$\langle N_{surv}(N_{surv}-1)...(N_{surv}-j)\rangle = \langle N_{surv}\rangle^{j+1}$$

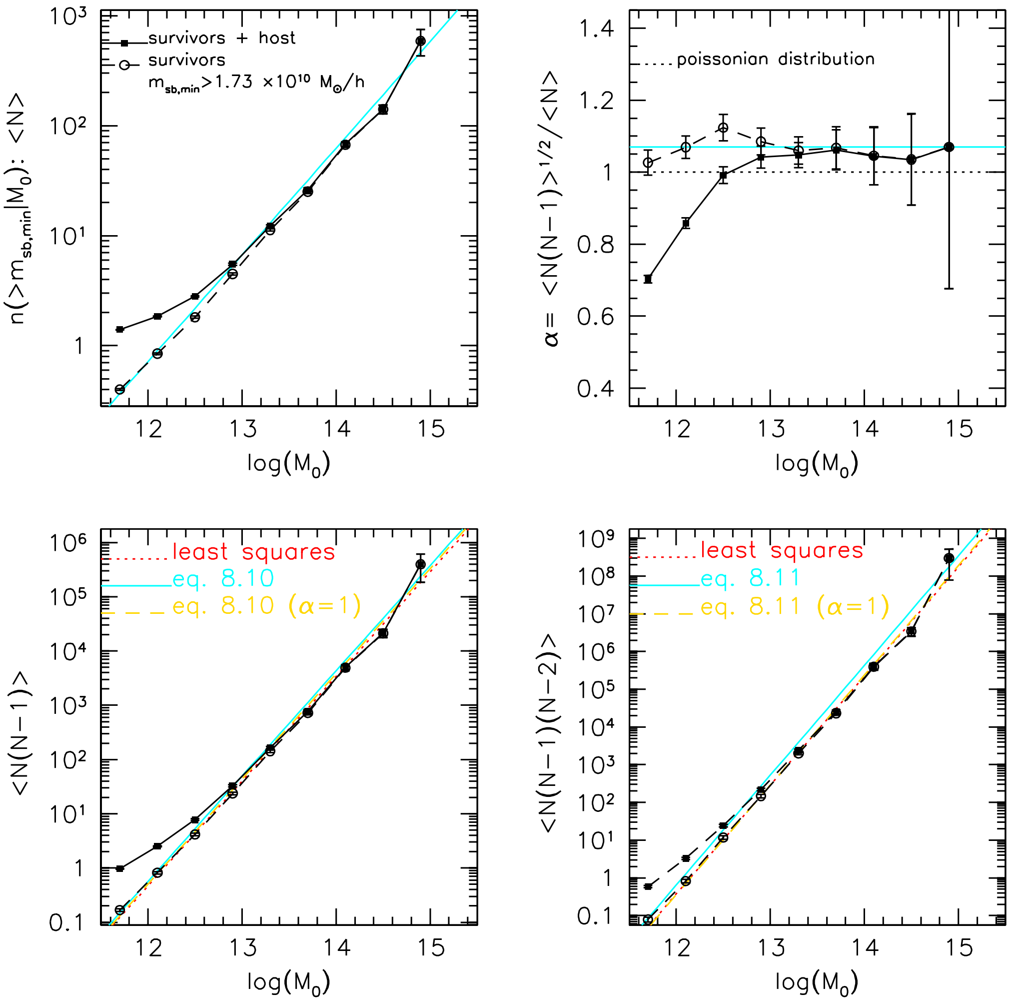

Figure 8.7: Halo occupation statistic of present day haloes in the GIF2 simulation. **Top left** panel show the first moment: average number of survivors inhabiting an M_0-halo. The solid line is the least squares fit to the open circles (eq. 8.8). **Top right** the deviation of the distribution from Poissonian statistic, equation (8.7). The horizontal solid line is the average value obtained mediating open circles along the y-axis. The two figures in the bottom show the second and the third order moments. Dotted lines represent the fit to the survivors distribution while the solid line are equations 8.10 and 8.11 for the second and third order moment expressed in therm of α and the first order moment. In the four panels, filled squares refer to the number of substructures + host. See the main text for more details.

The redshift evolution of the first order moment, of the halo occupation distribution, can be computed once the conditional mass function is known. Let us consider $\langle N_{surv}(m_v, z)\rangle$ as the number of survivors that populate and m_v-halo at redshift $z > 0$. The first moment of the halo occupation distribution at the present time will be:

$$\langle N_{surv}(M_0)\rangle = \int_0^{M_0} \langle N_{surv}(m_v, z)\rangle N(m_v, z|M_0)\mathrm{d}m_v\,, \tag{8.12}$$

where $N(m_v, z|M_0) = (M_0/m_v) f(m_v, z|M_0)$ and $f(m_v, z|M_0)$ the conditional mass function of a present day M_0-halo at redshift $z > 0$. In the case of $\langle N_{surv}(m_v, z)\rangle \propto m_v$ the equation become:

$$\langle N_{surv}(M_0)\rangle \propto \int_0^{M_0} m_v \frac{M_0}{m_v} f(m_v, z|M_0)\mathrm{d}m_v \propto M_0 \tag{8.13}$$

because for definition $\int_0^{M_0} f(m_v, z|M_0)\mathrm{d}m_v = 1$. This means that in the special case of $\langle N_{surv}(m_v, z)\rangle \propto m_v$ the mean number of substructures for a given host halo mass is constant with the redshift.

8.3 Discussion

In this chapter we have presented how subhaloes within subhaloes, in present-day dark matter haloes can be identified following all branches of the merging history tree. As showed by Gao *et al.* (2004), the substructures mass function is not universal but depends on the host halo mass M_0, more massive haloes at fixed m_{sb}/M_0 host more substructures that small ones. We have also shown that the mass fraction in survivors in large haloes is higher than in small systems. The scatter of this distribution at a fixed M_0 depends on the formation time of the host, the fraction is higher for smaller formation redshifts.

Comparing survivor catalogues with the SUBFIND ones, computed in the same numerical simulation, we showed that the agreement between the two algorithms is satisfying. However, we notice that the substructure mass function per unit volume is universal down to M^*, as found by Gao *et al.* (2004), but the normalization increase for small host masses.

In this chapter, we have also studied the halo occupation distribution and high order moments of the survivor population, finding the first moment with slope approximately equal to one. This theoretically predict no evolution with redshift for the average number of substructures that inhabit an halo of a given mass. The anisotropy parameter from a Gaussian distribution α is also approximately equal to one.

As future work, it will be very interesting test the evolution of the first moment of the HOD with redshift using the substructure catalogue at other snapshots of the numerical simulation. This will help us to better understand the redshift evolution of the HOD and see if its slope really does not depend on z.

CHAPTER

9

Monte Carlo Merger Tree with Micro-Solar Mass resolution

Along the different chapters of this dissertation we have enphasized that in the standard models of galaxy formation, including the Cold Dark Matter (CDM), haloes are assembled hierarchically through merging and accretion of many smaller objects, formed in a similar way at higher redshift. These structures provide the environment in which galaxies build up and evolve. Thus understanding the assembly histories of dark matter haloes is the first step towards the knowledge of the more complex process of galaxy formations.

In order to study the framework of structure formations two different approaches are feasible. The first one is with the use of N-body simulations, which are known to have some drawbacks. First of all they are computationally expensive and not possible to implement on standard computers. Moreover they have a limited mass resolution which is given by thr particle mass. The second way is the analytic approach which allows a detailed study of the merging history of haloes over a range of masses that is in principle unlimited (see Chapter 6). This method has its roots in the Press-Schecter formalism (Press and Schechter, 1974). We have shown that, in the spherical collapse model, haloes collapse on a certain scale once the smoothed density contrast on this scale exceeds the critical value $\delta_{sc}(z)$. The nonlinearities introduced by these virialized objects do not affect the collapse of overdense regions on larger scales. This simple assumption leads to the derivation of the global mass function of dark matter haloes (as discussed in Section 3.2) that is more or less in agreement whith that found in N-body simulation (Lacey and Cole, 1993; Somerville *et al.*, 2000; Sheth and Tormen, 1999, 2002).

An extension of this theory was made by several authors (Lacey and Cole, 1993; Bond *et al.*, 1991; Bower, 1991) with the aim of computing the conditional mass function, i.e. the probability that given a halo of mass M_0 at redshift z_0 it belongs to a halo of mass M_1 at an earlier redshift z_1. This extended Press-Schechter formalism can be also exploited to derive merger rates, halo formation times, mass growth histories, as we have shown in Section 4.4.

In this chapter we will discuss how it is possibile to construct a Monte Carlo merger tree with micro-solar mass resolution, using the extended Press & Schechter formalism. We will show that the algorithm generate a conditional mass function that is in perfect agreement with the spherical collapse model at any redshift and considering any present-day mass we want.

The simplest algorithm for a merger tree is through a binary tree. In this scene each halo is splitted in two haloes at an earlier epoch. Subsequently each halo is divided in other two pieces until all halo masses fall below an arbitrary chosen and desired mass resolution R (Lacey and Cole, 1993; Cole and Kaiser, 1988; Cole, 1991; Kauffmann and White, 1993). However, Somerville and Kolatt (1999) showed the failure of using a binary merger tree. In this way the first halo which is chosen from the Press & Schetchter distribution follow the correct probability, but the second one is chosen only in order to conserve mass and does not follow the theoretical model as expected. This leads to conditional mass function and formation redshift distribution in disagreement with the extended Press & Schechter predictions. To solve this problem they developed an new algorithm able to reproduce quite good the conditional mass function, however using a grid of time-step fine tuned.

To the other hand, Sheth and Lemson (1999) using the results found by Sheth (1996), realised that, for white-noise initial conditions, mutually disconnected regions are mutually independent. In this case it is possibile to split an halo, in a very elegant way, in progenitors whose mass function is in perfect agreement with the theoretical model of the spherical collapse. The great advantage of their method is that they are able to obtain arbitrary high mass resolution for any given time-step, generating progenitors in a very fast way.

In this chapter we describe as Sheth and Lemson (1999) method can be generalized to a ΛCDM power spectrum. The tree will be extended down to micro-solar mass resolution in order to study the subhalo population of a present-day halo, until the typical neutralino Jeans' mass.

Using random walks, instead of extracting number from a given distribution (that is Gaussian for the spherical collapse model), it is possible to extend the shperical collapse procedure to the ellipsoidal collapse (Giocoli, Sheth & Tormen, in preparation) considering a moving barrier as in equation 3.26.

9.1 Poissonian Initial Conditions: Partition Algorithm

Let us consider a discrete Possonian distribution of identical particles. Epstein (1983); Sheth (1995) showed that the probability that a clump has N particles is given by the following equation:

$$\eta(N,b) = \frac{(Nb)^{N-1}\mathrm{e}^{-Nb}}{N!}, \tag{9.1}$$

knwon as Borel distribution (Borel 1942), where $N \geq 1$ and $0 \leq b < 1$. We will see, along the different equations of this chapter, that the variable b can related to the Press & Schetchter overdensity threshold δ_{sc} in the continuous case by the relation:

$$b = 1/(1+\delta_{sc})\,.$$

We know that the average number of particles in a Borel clump is given by $\langle N\rangle = 1/(1-b)$, while the probability that a randomly chosen particle is in a such a clump by $(1-b)N\eta(N,b)$. In the limit of a large number of particles and small δ_{sc}, the Stirling's approximation for the factorial term implies that

$$\begin{aligned}(1-b)N\eta(N,b) &= \frac{\delta_{sc}}{(1+\delta_{sc})}\left(\frac{N}{1+\delta_{sc}}\right)^{N-1}\frac{\mathrm{e}^{-N/(1+\delta_{sc})}}{(N-1)!}\\ &\to \frac{\delta_{sc}}{\sqrt{2\pi N}}\exp\left(-\frac{N\delta_{sc}^2}{2}\right).\end{aligned} \tag{9.2}$$

This equation is precisely that wich obtains for a Gaussian density field considering white noise initial condition. In this contest the Poissonian distribution can be thought as the discrete analogue of the white noise Gaussian power spectrum as studied by Bond *et al.* (1991); Lacey and Cole (1993, 1994).

Starting from the same initial condition and considerations, it is possibile to write the conditional probability that a particle, belonging at the time b_0 to a clump made of N particles, is in an n-clump at $b_1 < b_0$, that is:

$$f(n,b_1|N,b_0) = N\left(1-\frac{b_1}{b_0}\right)\binom{N}{n}\frac{n^n}{N^N}\left(\frac{b_1}{b_0}\right)^{n-1}\left[N-n\frac{b_1}{b_0}\right]^{N-n-1} \tag{9.3}$$

where $1 \le n \le N$ and $0 \le b_1/b_0 \le 1$.

However, for a complete description of the merging history tree of an N-clump at b_0 we need to know what is the probability that at b_1 this is divided in a sample of n_j j-clumps with k subfamilies (so $n_1+...+n_N = k$). We recall that conserving the number of particles it holds $\sum_{j=1}^{k} j n_j = N$. The Poissinian Galton-Watson branching process gives for this probability the following equation:

$$p(n_1,...,n_k,b_1|N,b_0) = \frac{[N(b_1-b_0)]^{n-1}\mathrm{e}^{-N(b_1-b_0)}}{\eta(N,b_0)}\prod_{j=1}^{k}\frac{\eta(j,b_1)^{n_j}}{n_j!}, \tag{9.4}$$

where $\eta(l,b)$ is the Borel distribution with time parameter b. Since b_0 can be related to a density, the volume of the N-clump can be written as:

$$V_{N,0} = \frac{N}{\bar{n}(1+\delta_{sc,0})}, \tag{9.5}$$

where $\bar{n}$ denotes the average density of the universe. In this contest equation (9.4) can be seen as the probability that a region with N particles, at average density $\bar{n}(1+\delta_{sc,0})$, has k subregions each with average density $\bar{n}(1+\delta_{sc,1})$, where $\delta_{sc,1} \ge \delta_{sc,0}$. Let consider now at the time b_1 an n-subclump of the N-clump, in the Appendix A of the paper of Sheth and Lemson (1999) it is shown that if

$V_{n,1} = n/\bar{n}(1+\delta_{sc,1})$ is its associated volume, the remaining group of particles $N-n$ will obey to the following equation:

$$\frac{N-n}{V_{N,0}-V_{n,1}} \equiv \bar{n}(1+\delta'_{sc}) = \frac{\bar{n}}{b'}, \tag{9.6}$$

where $b' = 1/(1+\delta'_{sc})$ is density of the remaining volume, that represents the unknown quantity.

In the continuous limit, when $N \to M$ (with S the corresponding mass variance) and $b \to \delta_{sc}$, the equations (9.1) and (9.4) give the equations (3.23) and (4.6).

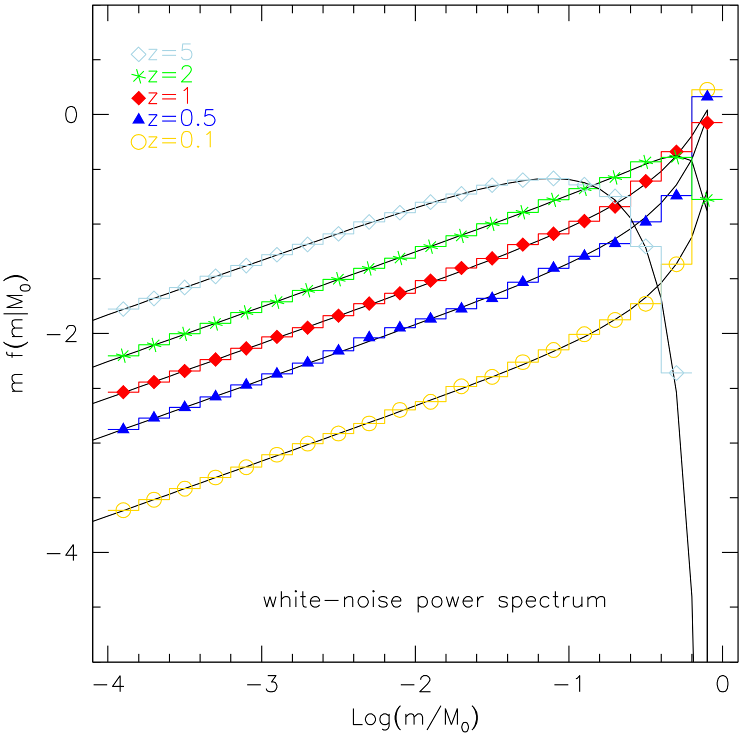

Figure 9.1: Conditional mass function of an M^*-present-day halo. The different data points correspond to five different redshifts at which the progenitors have been computed with a single time-step. The solid curves that fit the data points are the spherical collapse conditional mass function at each of the correspondent redshift (eq. 4.6).

Let us consider, as first case, a white-noise power spectrum, where $M \sim 1/S$, and suppose we want to split an M_0-halo, that lives at the present time $\delta_{sc,0}$, in progenitor haloes at time $\delta_{sc,1}$. We have seen in Chapter 4 that the spherical collapse conditional mass function written in term of $\nu = (\delta_{sc,1}-\delta_{sc,0})/\sqrt{s-S_0}$ is a Gaussian distribution with mean $\bar{\nu} = 0$ and $\sigma = 1$. To generate a progenitor, we draw a random number $\tilde{\nu}_1$ from this ditribution. The associated mass variance

$\tilde{s}_1$ of this first progenitor halo can be computed solving the equation:

$$\tilde{\nu}_1 = \frac{\delta_{sc,1} - \delta_{sc,R}}{\sqrt{\tilde{s}_1 - S_R}}, \tag{9.7}$$

where initially $R = M_0$ ($S_R \sim 1/R$) and $\delta_{sc,R} = \delta_{sc,0}$. The mass of the halo will thus be $\tilde{m}_1 \sim 1/\tilde{s}_1$. Considering that for white-noise power spectrum disconnected volume are mutually independent, the overdensity of the remaining mass $R = M_0 - \tilde{m}_1$ will be given by:

$$\delta_{sc,R} = \delta_{sc,1} - \frac{(\delta_{sc,1} - \delta_{sc,0})}{R/M_0}. \tag{9.8}$$

To generate the second halo we draw another number from the Gaussian distribution, we compute the mass variance from the equation (9.7), and after the corresponding mass. The remaining mass will new be $R = M_0 - \tilde{m}_1 - \tilde{m}_2$, with the corresponding overdensity given always by the equation (9.8). We can proceed in this way until the mass resolution R is as small as desired.

In Figure 9.1 we show the progenitor mass function at five different redshifts obtained using the algorith described above. For each final time-step we run 10^4 Monte Carlo realisations. The progenitors have been computed with a single time-step and it has been considered an M_0-present-day halo, with $M_0 = M^* = 10^{13}\, M_\odot/h$. The mass resolution has been set equal $R = 0.0001 \times M_0$. The solid curves, in perfect agreement with data points, are the spherical collpase predictions for the considered redshifts (eq. 4.6). Among the progenitor haloes we term main progenitor the most massive one.

To check the full consistency of the method we generate a merging-history-tree of a present-day halo until high redshift. However we followed only the main progenitor halo. In Figure 9.2 we show the formation redshift distribution, considering 10^3 realisation of the tree. The formation redshift has been rescaled in term of the universal formation time variable $w_f = (\delta_{sc,f} - \delta_{sc,0})/\sqrt{S_0}$. We know that for spherical collapse model the distribution in w_f is independent of the initial mass. In the figure the solid curve is the prediction of Lacey and Cole (1993), equation (5.9), which perfectly fits the distribution of the Monte Carlo tree.

9.2 Gaussian Initial Conditions for a ΛCDM Power Spectrum

In order to generate Monte Carlo realisations of the merging-history-tree of present-day haloes, considering a ΛCDM power spectrum, we need to do some modifications to the algorithm previously described. The assumption that disconnected volumes are mutually independet is wrong when the initial conditions differ from white-noise. Despite this, we notice that, when expressed as functions of the variance rather than the mass, all excursion set quantities are independent of power spectrum. Also, each chosen mass $\tilde{m}$, can be treated not as a progenitor having a mass $\tilde{m}$ but as region of volume $\tilde{v}$ containing a mass $\tilde{m}$, populated

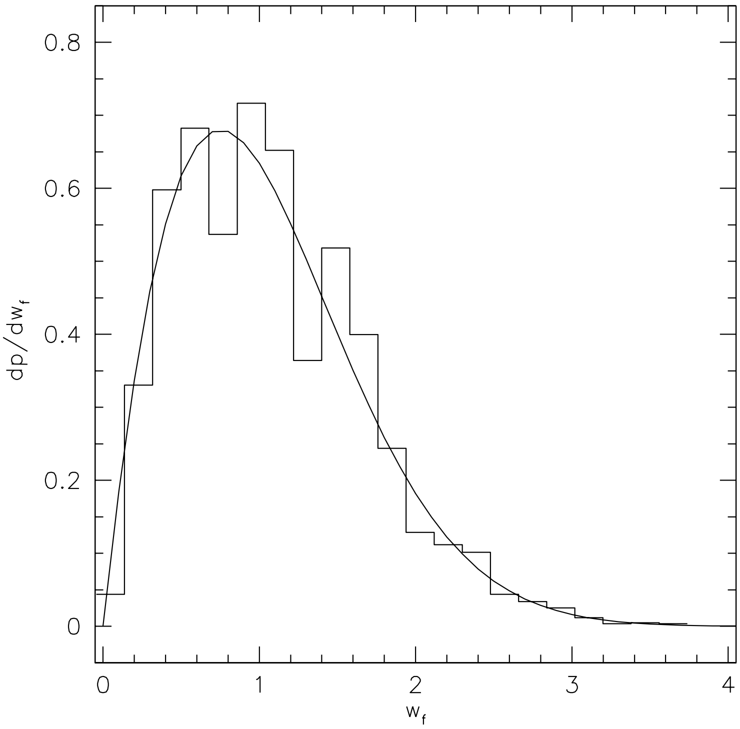

Figure 9.2: Formation redshift distribution for a present-day M^*-halo and white-noise power spectrum. The histogram is the realisation of 10^3 merger tree, the solid line is the spherical collapse prediction of Lacey and Cole (1993) (eq. 5.9).

by ζ objects having all the same mass μ. Thus with $\zeta = \tilde{m}/\mu$. The number of object is obtained by requiring that the objects have the same mass variance that is $s(\mu) = 1/\tilde{m}$. For a scale-free power spectrum $P \sim k^n$ ($\alpha = n + 3/3$) $\zeta = m^{(\alpha-1)/\alpha}$, and for $n = 0$ we have $\zeta = 1$, the region $\tilde{v}$ contains exactly one halo, as we want. For $n \neq 0$ and general power spectrum ζ is neither unity nor even integer. However, as we will see in the next section, this approach generates progenitor mass functions wich are in perfect agreement with the theoretical prediction for every power spectrum, redshift and initial mass. We recall that the general (or in our case the ΛCDM) and the white-noise power spectrum has to be such that:

$$S_{wn}(M_0) = S(M_0)\,, \tag{9.9}$$

where M_0 is the initial mass to be splitted.

Partition of a Milky-Way size halo with micro-solar mass resolution

In this section we will discuss how generate a sample of progenitors, for a present-day dark matter halo, at any redshift and with any mass resolution we want. We recall that if we consider the case of a ΛCDM power spectrum ($\Omega_\Lambda = 0.7, \Omega_m = 0.3$ and $\sigma_8 = 0.772$) the correspondent white-noise spectrum has to obey the

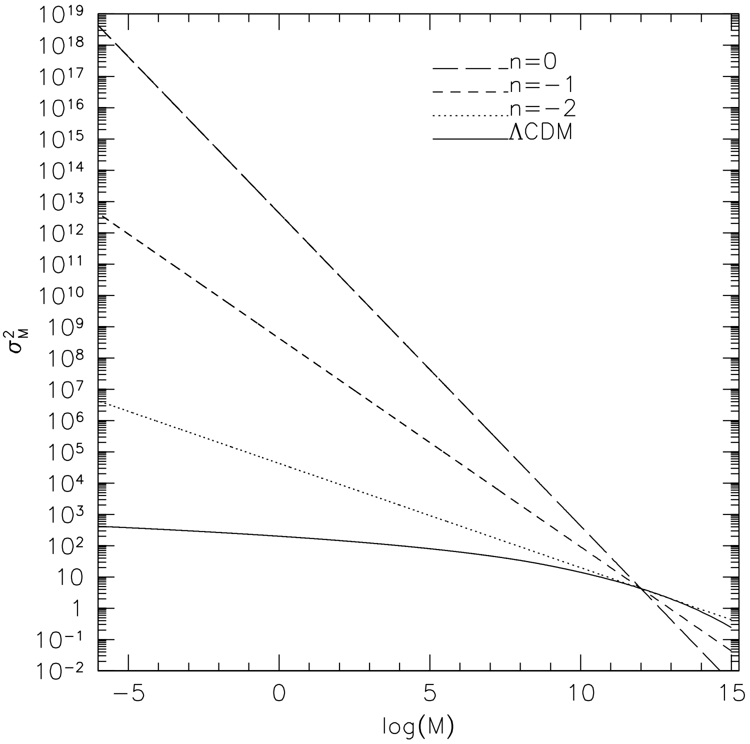

Figure 9.3: Mass variance for different power spectrum. For ΛCDM power spectrum the mass variance has been computed chosing a power spectrum with primordial spectral index $n = 1$, and a transfer function obtained from CMBFAST (Seljak and Zaldarriaga, 1996) for a concordance ΛCDM universe (Ω_m, Ω_Λ, $h = 0.3, 0.7, 0.7$) with $\sigma_8 = 0.772$, extended down to a mass $M = 10^6 M_\odot/h$. We have integrated this power spectrum using a top-hat filter in real space. To obtain the mass variance until the typical Jeans neutralino mass we linearly extrapolate the log(m)-s relation to $M = 10^{-6} M_\odot/h$. The three scale-free power spectrum as been normalized to have the same mass variance for an halo with mass $10^{12}\, M_\odot/h$.

equation (9.9). In this contest when we choose a mass resolution R, in the ΛCDM case, the correspondent mass resolution in the white-noise partition is such that $S_{wn}(R_{wn}) = S(R)$, with generally $R_{wn} > R$ (as can been seen in Figure 9.3).

Let us consider the case of a present-day Milky-Way size halo, $M_0 = 10^{12}\, M_\odot/h$, and suppose we want to generate a sample of progenitors at different redshifts until $R = 10^{-6}\, M_\odot$. This mass corresponds in the white-noise power spectrum to $R_{wn} = 2.15 \times 10^{10}\, M_\odot/h$ (see Figure 9.3). To generate progenitors at redshift z_1 (where $\delta_{sc,1}$ is the correspondent critical overdensity) we run the code considering a white-noise power spectrum. We extract a random number from the Gaussian distribution (zero mean and one variance) and compute the mass variance of the first halo using the equation (9.7). This mass variance will correspond to a mass $\tilde{m}$ for the case $n = 0$ and to a mass μ in the ΛCDM cosmology, where the number of μ-progenitors is $\zeta = \tilde{m}/\mu$. Generally this number is neither unity nor

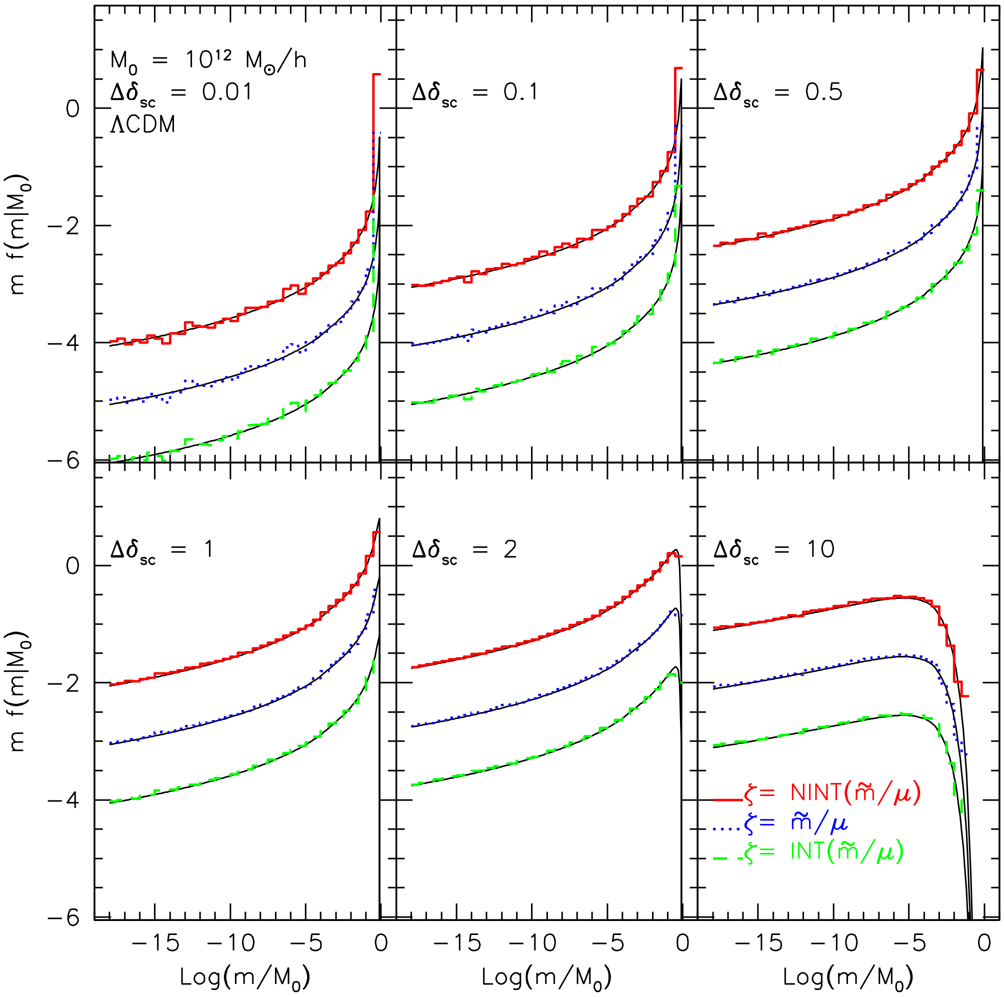

Figure 9.4: Single-step conditional mass function at six different redshifts for a present day Milky-Way size dark matter halo and considering a ΛCDM power spectrum. The mass resolution of the partition algorithm is $10^{-6}\,M_{\odot}$, corresponging to the typical neutralino Jeans-mass. For the cases $\zeta = \mathrm{NINT}(\tilde{m}/\mu)$ and $\zeta = \mathrm{INT}(\tilde{m}/\mu)$ the conditional mass function have been shifted respectively of a factor of ten up and down respect to the original distribution. The solid curves represent the corresponding spherical collapse conditional mass functions.

even integer, but we can consider two cases: the frist where $\zeta = \mathrm{NINT}(\tilde{m}/\mu)$ and the second where $\zeta = \mathrm{INT}(\tilde{m}/\mu)$. These cases not have any theoretical justification but prevent us to have a non-integer number of progenitors. To generate the second progenitor halo, we compute the overdensity of the remaining mass $M_0 - \tilde{m}$ from the equation (9.8), we draw a random number $\tilde{\nu}$ from the Gaussian distribution and from the (9.7) we estimate the mass variance. Finally, we compute the ΛCDM mass and the correpsonded number of progenitors. Thus the remaining mass will be $R = R - \tilde{m}$. We proceed in this way until the mass resolution is as small as desired. The most massive progenitor, in the poissonian tree at each redshift, is defined to be the main progenitor halo.

In Figure 9.4 we show the conditional mass function of a $M_0 = 10^{12}\,M_\odot/h$ halo at six different redshifts, considering a ΛCDM power spectrum. The conditional mass function in the cases $\zeta = \mathrm{NINT}(\tilde{m}/\mu)$ and $\zeta = \mathrm{INT}(\tilde{m}/\mu)$ has been shifted respectively of a factor of ten up and down respect to the original distribution. At all redshifts the progenitor haloes have been obtained with a single-step realization. In the figure the solid curves are the spherical collapse predictions, and as we can see, they are in perfect agreement with the partition code in all cases and final redshift considered.

Unevolved subhalo population

In Chapter 6 we have studied the substructure population of a present-day halo considering the progenitor mass functions at any redshift $z > 0$. We assumed that all progenitors will survive at the present in the host halo, without loose mass. The analytical distribution of the progenitor mass function has been extrapolated down to $10^{-6}\,M_\odot$ to study the γ-ray emission from micro-solar substructures that populate the Milky-Way halo. The γ-ray emission is due to dark matter particle and anti-particle annihilation. The rate of annihilation, and thus the γ-ray emission, depends on local density. Considering that substructures are dense clumps of dark matter, it is expected an enhancement of the γ-ray background signal in correspondence of these. Each considered progenitor has an associeted concentration parameter that, as shown by Diemand *et al.* (2005), is related to their $\nu = \delta_{sc}(z)/\sigma(m)$, where z is the correspondent redshift of the considered m-progenitor. However, in this discussion we did not consider that progenitor haloes merge with the host system, along the cosmic time. For this reason it would be more correct use for z and m the accretion redshift and mass before the satellite merges with the main progenitor halo. This kind of approach and modelling can not be done analycally and require a Monte Carlo merger history tree.

To compute the satellite mass function (that we termed also unevolved subhalo mass function), we run the Monte Carlo code, described above, generating merging history trees of a present-day M_0-halo always following the main trunk: (i) we generate a sample of progenitors at redshift $z_1 = z_0 + \mathrm{d}z$; (ii) among them we identify the main progenitor halo; (iii) starting from this we re-run the partition code computing its progentiros at redshift $z_2 = z_1 + \mathrm{d}z$. We go on in this way down to redshift $z_i = z_0 + i \times \mathrm{d}z$ until the mass of the main progenitor halo, in the ΛCDM tree, does not drop below the mass reslution $R = 10^{-6}\,M_\odot$. In Figure 9.5 we plot the satellite mass function, at all redshifts, computed with the algorithm described above, considering the case $\zeta = \mathrm{NINT}(\tilde{m}/\mu)$. As can be seen, the distribution has a power low trend $\mathrm{d}N/\mathrm{d}\ln(m) \propto m^{-\alpha}$, where the slope $\alpha = -0.93$, while at high satellite masses the distribution is truncated with an exponential cut off. The slope of the distribution is in agreement with the value obtained by van den Bosch *et al.* (2005) for the unevolved subhalo mass function. However, they used a different tecnique to generate the Monte Carlo merger tree (Somerville and Kolatt, 1999). This tecnique is time-step dependent and not able to reproduce the theoretical prediction of the conditional mass function down to micro-solar masses.

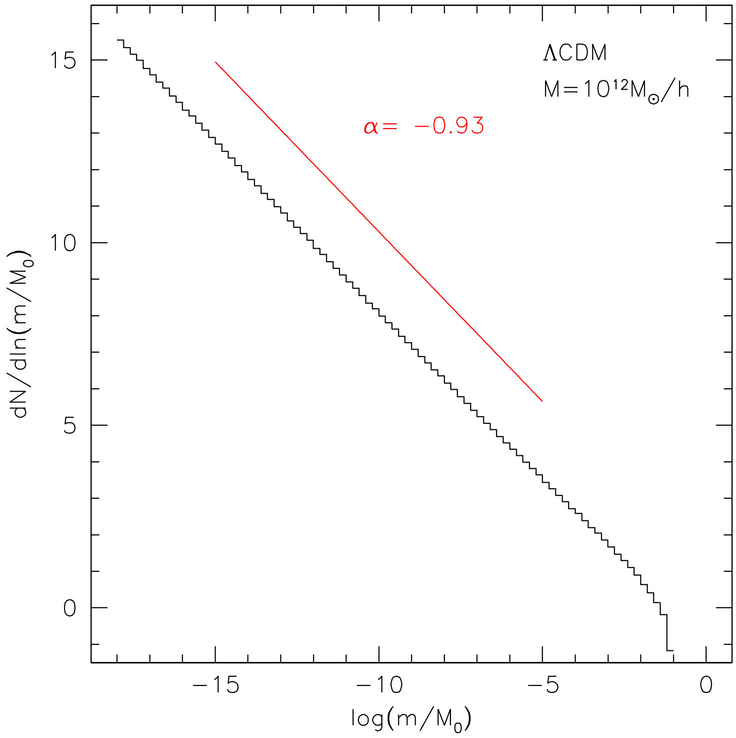

Figure 9.5: Mass function accreted by the Milky-Way halo. The merger history tree has been performed generating progenitor haloes until a mass resolution of $10^{-6}\,M_\odot$. The main progenitor halo has been followed in redshift until its mass does not drop below the mass resolution.

Using an N-Body simulation Diemand *et al.* (2005) showed that the present-day subhalo population preserves memory of the initial conditions. The high density peacks are found to be more centrally concentrated and move on more radial orbits than the overall mass distribution. This correlation has been interpreted and parametrized by the author using the variable $\nu = \delta_{sc}(z)/\sqrt{s}$. Thus, have a prediction for the satellites distribution in term of $\nu = \delta_{sc}(z)/\sqrt{s}$ is important both because ν is related to the own subhalo concentration, from which depends their γ-ray emission, and because the spatial distribution in the host halo can be parametrized in term of this variable (see eq. (1) in Diemand *et al.* (2005). In Figure 9.6 we plot the satellite mass function in term of the universal variable ν. In the figure the histogram is the result of 10^4 Monte Carlo realisations of the tree (as in Figure 9.5), while the dashed curve is a Gaussian distribution. From the figure we can see that the rescaled satellite mass function follow the

Gaussian distribution until $\nu \approx 2$ after which it has a cut-off.

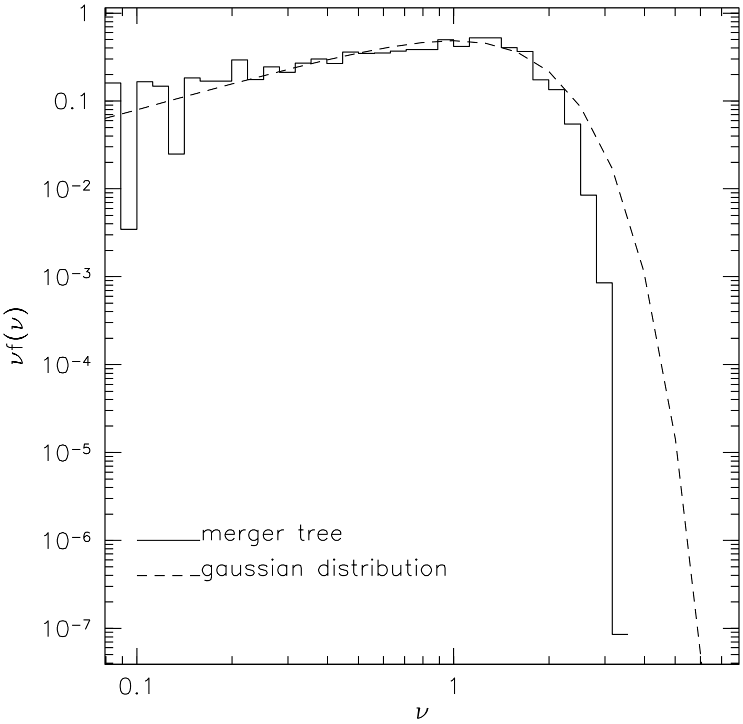

Figure 9.6: Satellite mass function in term of the universal variable $\nu = \delta_{sc}/\sigma(m)$. The histogram show the result of 10^4 realization of the Monte Carlo tree. The dotted line is a gaussian distribution with zero mean and one variance.

Draco accretion mass

The algorithm described above can be easly used to constrain and study some properties of the observed satellite galaxies. For example, let us consider the case of a satellite of the Milky-Way, Draco, and suppose that we what to compute its virial mass at merging time. This estimate is useful to construct a Monte Carlo merger tree of a Draco-size halo, starting from its accretion (or also merging) time on the Galaxy-halo, and estimate the subhaloes wihin the satellite galaxy.

To compute the original virial mass of the Draco we need to know its present-day mass and its accretion redshift on the Milky-Way. Using deep wide-field multicolor CCD photometry from the Sloan Digital Sky Survey, considering a King (1966) spherical model of equivalent size as a reference and adopting a line-of-sight velocity dispersion of either 10.7 km/s or 8.5 km/s (Armandroff *et al.*, 1995), Odenkirchen *et al.* (2001) derived estimates of the total mass of Draco within the tidal radius of $3.5 \pm 0.7 \times 10^7 M_\odot$ and $2.2 \pm 0.5 \times 10^7 M_\odot$, respectively. Considering all stars within R_{tid} they also determined the total luminosity of the Draco dwarf galaxy as a $(L/L_\odot)_i = 2.4 \pm 0.5 10^5$. This tell us that Draco is a dark matter-dominated galaxy with a very high mass-to-light ratio. To the other hand, Łokas *et al.* (2005) studing the distribution of dark matter in Draco, by modelling the moments of the line-of-sight velocity distribution of stars, from velocity data of Wilkinson *et al.* (2004), obtained a best-fitting total mass equal to $7\times10^7\,M_\odot$. The mass-to-light ratio (in V-band) found was $300\,M_\odot/L_\odot$ and almost constant with radius. For the merging time we do not have any direct observable that can be useful to estimate it. However, from its initial position and velocity the merging time of Draco on the Milky-Way can be estimate considering the one-to-one correspondence between virial radius and accretion time implied by the spherical secondary indall model. Hayashi *et al.* (2003) showed that an uperr limit for Draco merging redshift is $z_m \lesssim 2.8$.

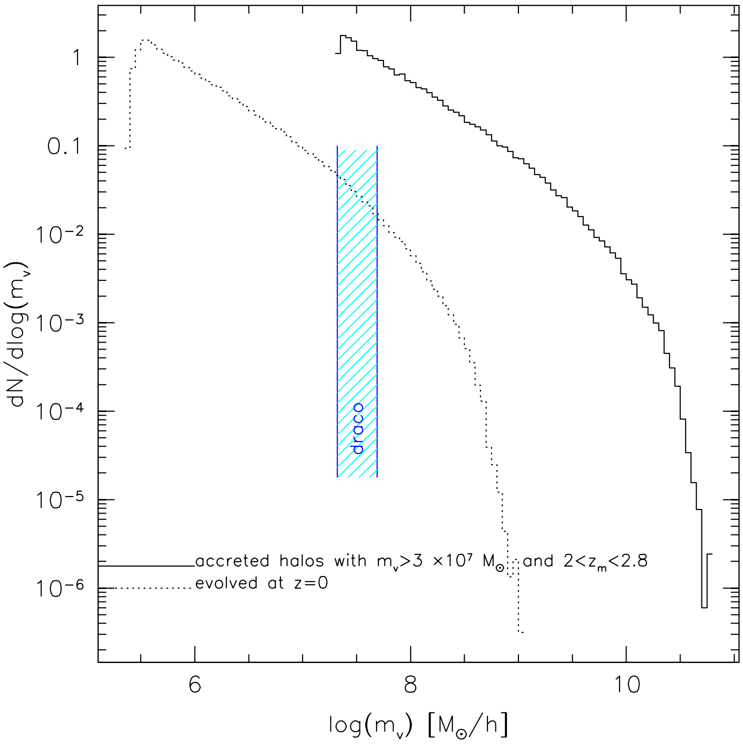

Figure 9.7: Unevolved and evolved subhalo mass function accreted by a present-day Milky-Way size halo between $z = 2$ and $z = 2.8$. The evolved distribution has been obtained from the accreted one using equation (7.18).

From these estimate, in order to compute Draco virial mass, we proceed in the followin way. We run our Monte Carlo merger tree considering a present-day Milky-Way size halo $M_0 = 10^{12}\,M_\odot/h$, and following the main progenitor halo. We noted down all masses larger than $3\times10^7\,M_\odot$ accreted from $z = 2$ to $z = 2.8$. This redshift interval correspong roughly to a time interval of 1Gyr from the upper limit of the accretion time. The solid histogram in Figure 9.7 show the mass function of these accreted systems. Each satellite halo once in the virial radius of the host loose mass due to gravitational heating and tidal stripping. In order to model this effect, we use the result from Section 7.4. Eeach accreted halo will retain at the present time a fraction of its original virial mass that depends on the time spend in the potential well of the host, given by equation (7.18). In Figure 9.7 the dotted histogram shows the evolved accreted mass function, which considering that the fractional mass loss rate is independent on the subhalo mass stays constat to the unevolved distribution. At this point to estimate the mass of Draco at merging time we compute the average of accreted masses that at present-time range between $3 \times 10^7\,M_\odot$ and $7 \times 10^7\,M_\odot$, that is: $m_{v,D} = 4.838 \pm 0.002 \times 10^9\,M_\odot$. This means that a satellite galaxy, that spent around 11Gyr in the potential well of the host halo retain roughly 0.01% of its initial mass.

9.3 Discussion

In this chapter we have discussed how to build up a Monte Carlo merger tree with micro-solar mass resolution, whose mass function perfectly reproduce the spherical collapse prediction for any power spectrum, initial mass and final redshift. We have showed that following the poissonian tree not only the conditional mass function is in agreement with the theoretical prediction, but also the formation redshift distribution agree with the model.

We generalized the Sheth and Lemson (1999) algorithm to the case of a ΛCDM power spectrum finding a conditional mass function in perfect agreement with the theoretical prediction of the spherical collapse model. We considered a present-day halo $M_0 = 10^{12}\,M_\odot/h$, corresponding to the Milky-Way halo. The tree has been run with a mass resolution $R = 10^{-6}\,M_\odot$, in order to estimate the subhalo population down to this mass. The idea of this tree is related to study the γ-ray emission from the subhalo population of the Milky-Way halo, extending the approach presented in Chapter 6 (Giocoli, Pieri, Sheth & Tormen in preparation).

Including the recipe of the mass loss rate in our Monte Carlo tree, we give an estimate of the Draco virial mass at merging time with Milky-Way. We notice that the satellite galaxy, spending more than 11Gyr in the virial radius of the host halo, loose roughly 99% of its mass until the present.

Appendix

APPENDIX

A

On Rescaling the Virial Radius of DM Haloes

In this first appendix we will present some fitting functions useful to rescale different definitions of the virial radius of dark matter haloes.

Following the spherical collapse model, a dark matter halo is assumed to virialize when its mean density reaches the predicted virial value (e.g. Eke *et al.* (1996)). For a concordance ΛCDM universe, with $\Omega_m = 0.3$ at the present time, the critical overdensity a $z = 0$ is $\rho_v = 324\bar{\rho}$, with $\bar{\rho}$ the mean background density of the universe. At higher redshifts Ω_m grows approaching unity, as can be seen in Figure 3.2, so that the virial overdensity approaches $178\,\bar{\rho}$, as in an Einstein-de Sitter universe.

However, in the literature other definitions have also been used. The Santa Cruz Theoretical Cosmological Group defines dark matter haloes in numerical simulations as groups of particles at 200 times the mean background density of the universe. On the other shore of the Atlantic Ocean, researchers of the Virgo Consortium use 200 times the critical density: $\rho_c = \bar{\rho}/\Omega_m$. Using different definitions often makes it hard to compare results obtained from different groups or simulations. It is interesting to notice that for an Einstein-de Sitter universe (or at high redshift in the case of a ΛCDM universe) the two definition are identical.

In order to compare these two definitions to that of the spherical collapse model, we considered haloes identified at different redshifts in the GIF2 simulation. These systems, as described in Section 4.3, have been identified using the SO criterion, and their virial radius and mass were defined according to the spherical collapse model (Eke *et al.*, 1996). For each redshift we consider all haloes with mass at least $M_v = 10^{11.5}\,M_\odot/h$, and compute their density profiles out to $3\,R_v$. Since $\rho_c = \bar{\rho}/\Omega_m$, all radii $R_{200,c}$, R_v and R_{200b} are always smaller than $3R_v$.

In Figure A.1 we plot the ratio $R_{200,b}/R_v$ versus $\nu = \delta_{sc}^2/S$, at four different redshifts. Open circles represent the median of the distribution, while gray bands enclose the second and third quartiles. Filled triangles show the average, error bars its r.m.s.. Similarly, in Figure A.2 we show the ratio $R_{200,c}/R_v$ versus ν. In all cases $R_{200,b}$ and $R_{200,c}$ were computed by appropriate interpolation of the density profile of each halo.

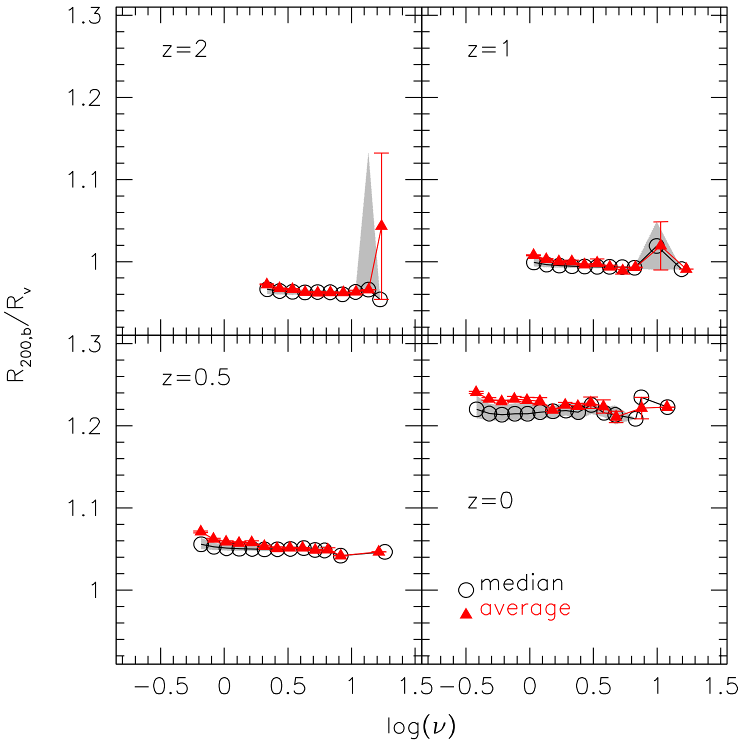

Figure A.1: Ratio between the virial radius and the radius enclosing 200 times the background density, versus the universal variable ν. In each panel the ratio refers to different simulation redshifts. The open circles represent the median of the distribution, while the shaded region encloses the second and the third quartile. The filled triangles instead represent the average of the distribution, and the error bars are the root mean squares.

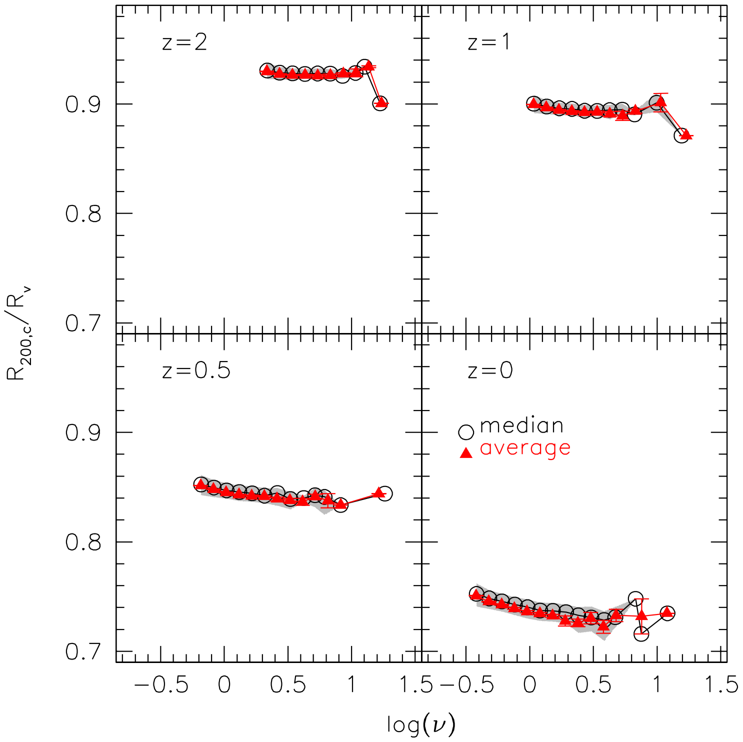

Figure A.2: Ratio between the virial radius and the radius enclosing 200 times the critical density, versus ν. In each panel the ratio refers to different redshift. The data points and error bars are the same as Figure A.1.

In Figure A.3 we plot the redshift dependence of the ratio $R_{200,b}/R_v$. Different data points refer to the GIF2 simulation for various value of $\nu = \delta_{sc}(z)^2/S$, where $\delta_{sc}(z)$ is the critical spherical collapse density for a halo collapsing at redshift z (see Eke *et al.* (1996)) and S the mass variance (eq. 3.9). In order to fit the data points we assume that the ratio between the two radii is independent of the halo mass at any given redshift, as can be seen in Figure A.1. The average value of the ratio $R_{200,b}/R_v$ is well fitted by the relation:

$$\frac{R_{200,b}}{R_v} = a\left[\frac{\Delta_v(z)}{\Delta_{v,0}}\right]^{-4/9}, \tag{A.1}$$

where $\Delta_v(z) = \rho_v(z)/\bar{\rho}$ represents the virial density contrast and $a = 1.23$.

We now proceeded in the same way as before, considering the ratio $R_{200,c}/R_v$. In Figure A.4 we plot the simulation data points and the best fit to the average ν at different redshifts. The solid line is the equation:

$$\frac{R_{200,c}}{R_v} = b\left[\frac{\Delta_v(z)}{\Delta_{v,0}}\right]^{2/5}, \tag{A.2}$$

where $b = 0.74$.

Doing the ratio of these two last equations we can write:

$$\frac{R_{200,b}}{R_{200,c}} = c\left(\frac{\Delta_v(z)}{\Delta_{v,0}}\right)^{-38/45}, \tag{A.3}$$

where $c = a/b$. We know that the two definitions $R_{200,c}$ and $R_{200,b}$ agree at high redshifts, where $\Omega_m(z \to \infty) \approx 1$ for ΛCDM universe, so we have:

$$1 = c\left(\frac{\Delta_v(z \to \infty)}{\Delta_{v,0}}\right)^{-38/45}, \tag{A.4}$$

that gives the relation between a and b considering that $\Delta_v(z \to \infty)/\Delta_{v,0} \approx 1.828$.

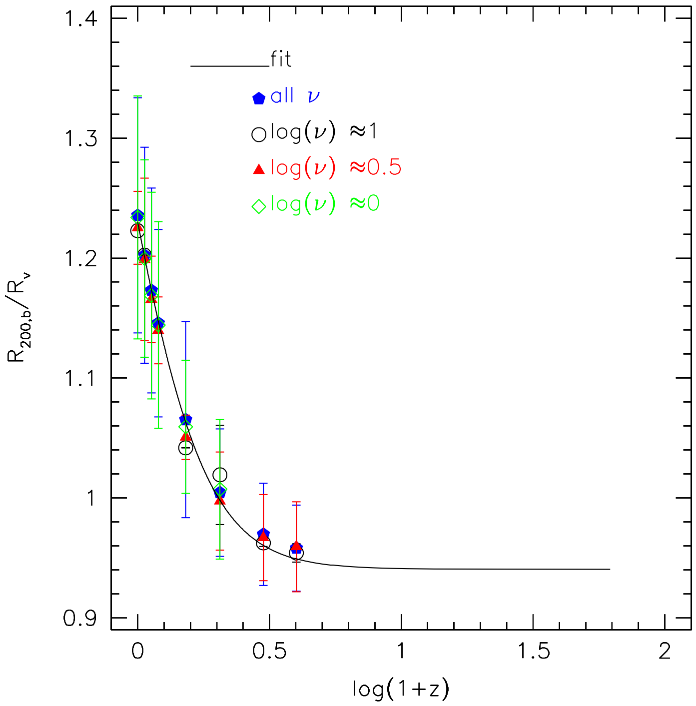

Figure A.3: Dependence on redshift of the ratio between $R_{200,b}$ and R_{ν}. The points refer to simulation data for different value of ν, while the solid line represents the best fit to the data point: equation (A.1).

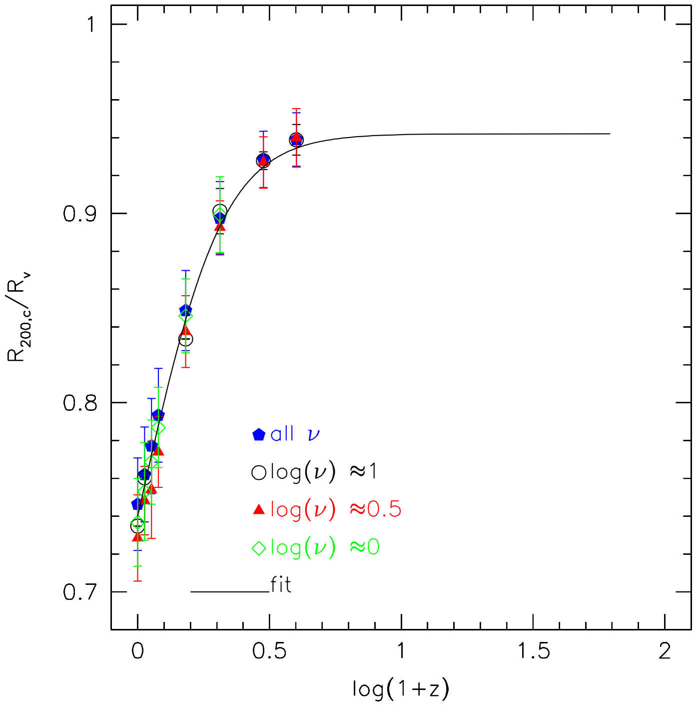

Figure A.4: As in the previous figure, but considering the radius that enclose 200 times the critical density of the universe. The solid line is equation (A.2).

APPENDIX

B

On the Difference Between Halo Formation and Creation

The main text deals with halo formation has defined by Lacey and Cole (1993). It is worth mentioning that there is another context in which the term 'halo formation' arises—this is when the halo population is modeled as arising from a binary coagulation process of the type first described by Smoluchowski (1916). In this description, the time derivative of the halo mass function is thought of as the difference of two terms: one represents an increase in the number of haloes of mass m from the merger of two less massive objects, and the other is the decrease in the number of m-haloes which results as m-haloes themselves merge with other haloes, creating more massive haloes as a result:

$$\frac{\mathrm{d}n(m,t)}{\mathrm{d}t} = C(m,t) - D(m,t) \tag{B.1}$$

The gain term, the first on the right hand side above, is sometimes called the halo formation (Sheth and Pitman, 1997) or creation (Percival and Miller, 1999; Sheth, 2003) term. In what follows, we will use the word 'creation' to mean this term, and 'formation' to mean the quantity studied by Lacey & Cole.

Halo formation and creation are *very* different quantities, as we show below. Nevertheless, they are sometimes used interchangeably in the literature (e.g. Verde *et al.* (2001)). Here we show explicitly how to compute the Lacey-Cole formation time distribution from the Smoluchowski-type creation and destruction terms, with the primary aim of insuring that the error of confusing one for the other is not repeated.

In the Lacey-Cole picture, the formation time distribution of M-haloes identified at T is given by equation (5.2). In this case, one first integrates over the conditional mass function, and then takes a time derivative. Here, we will instead take the time derivative inside the integral over mass and compute it before integrating over mass, as suggested by equation (5.3). In this case, the integrand has the form of a time derivative which plays a central role in the Smoluchowski picture. In particular, we can write

$$\frac{\mathrm{d}N(m,t|M,T)}{\mathrm{d}t} = C(m,t|M,T) - D(m,t|M,T), \tag{B.2}$$

where C and D are now the creation and destruction terms associated with the progenitor mass function, evaluated explicitly in Sheth (2003).

This simple step shows explicitly that $p(t|M,T)$ can be written in terms of Smoluchowski-like quantities:

$$p(t|M,T) = \int_{M/2}^{M} \mathrm{d}m\, C(m,t|M,T) - \int_{M/2}^{M} \mathrm{d}m\, D(m,t|M,T). \tag{B.3}$$

A little thought shows why this works out so easily. Simply integrating the halo creation rate $C(m,t|M,T)$ over the range $M/2 \leq m \leq M$ overestimates halo formation, since some of haloes created at t, with mass $3M/4 \leq m \leq M$ say, may actually have been may created by binary mergers in which one of the haloes had a mass in the range $M/2 \leq m \leq 3M/4$. Such creations should not be counted toward halo formation, since formation refers to the earliest time that m exceeds $M/2$. However, it is precisely this double-counting which the second term, the integral of $D(m,t|M,T)$ over the range $M/2 \leq m \leq M$, removes. Note in particular that, whereas the formation time distribution $p(t|M,T)$ is related to Smoluchowski-type quantities, it is *not* the same as $C(m,t)$. For completeness, note that

$$C(m,t) = \int_{m}^{\infty} \mathrm{d}M\, n(M,T)\, C(m,t|M,T), \tag{B.4}$$

where $n(M,T)$ denotes the number density of haloes of mass M at time T.

APPENDIX

C

On Different Definitions of Subhaloes

In this appendix we will show the results of different tests performed while developing our subhalo-finder code. The idea of the algorithm described in Chapter 7 is a further development of the method described in Tormen *et al.* (2004). In this paper the authors follow the growth of haloes through the repeated accretion of satellite haloes, defined as progenitors directly donating at least 50% of their particles to the main progenitor halo [1] In order to calculate the satellite properties after its merging time z_m, it is necessary to consider the subset of satellite particles which are still self bound at each $z < z_m$. The authors identify the satellite center using the so called moving-center method (Tormen *et al.*, 1997). Starting from it they make a list of all satellite particles inside the satellite virial radius, assuming that all particles outside this radius are physically unbound to the satellite. Next they remove from this list all unbound particles. These two steps are repeated until the self-bound mass converges to some value.

Our first step has been to test this code on the GIF2 simulation. In order to reduce computational time, we did not follow the satellites along all the simulation snapshots with $z < z_m$. Instead, we computed self-bound masses and orbital properties only at the desired redshift of observation z_0. As described in Section 7.1, we considered all haloes with final mass $M \geq 10^{11.5}\, M_\odot/h$, whose main progenitor at any redshift has virial mass not exceeding the final value by more than ten percent. Following the growth of each main progenitor halo we recorded all its satellites and noted down the index of the their particles. At the end, for each satellite we repeated the same procedures done by Tormen *et al.* (2004) at redshift z_0 by computing its self-bound mass.

In Figure C.1 we show the subhaloes identified in the most massive halo in GIF2 simulation using the algorithm described. In the top panel we show the distribution of particles within the corresponding host virial radius. The two panels on the bottom show the self-bound particles in subhaloes (left) and the halo particles not bound to any subhalo (right).

In Figure C.2 we show the subhalo mass function obtained using the Tormen

---

[1] However a check need to be done on the satellite particles: each accreted halo is considered as a "novel" satellite if it does not share more than 30% of its particles with any previous satellite.

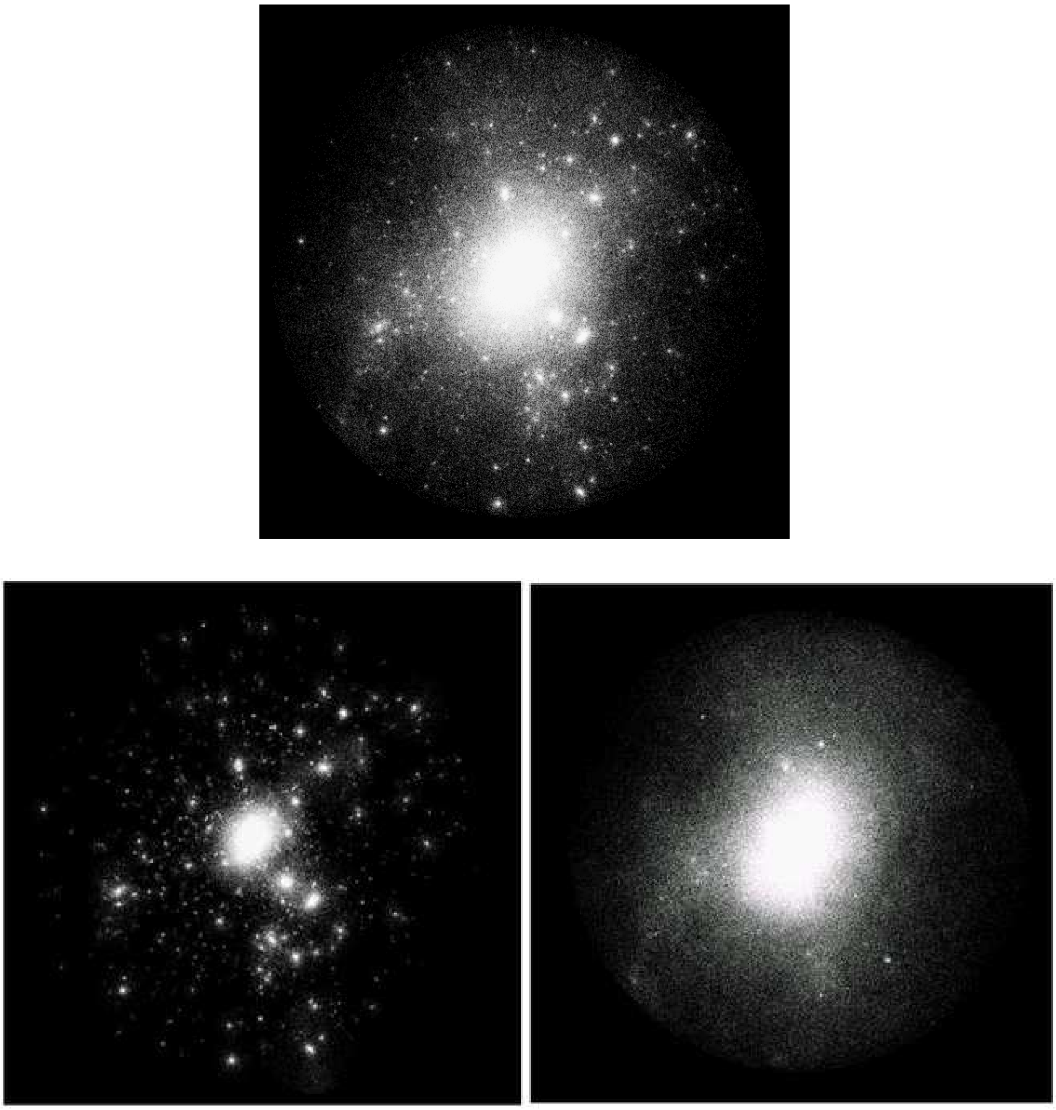

Figure C.1: **Top panel**: particle distributions in the most massive halo at redshift $z = 0$ in the GIF2 simulation. **Bottom left**: self-bound particles in subhaloes identified using the Tormen *et al.* (2004) algorithm. We recall that the halo has 1070564 particles within its virial radius ($M_v = 1.85 \times 10^{15}\ M_\odot/h$); 265607 of these are in self-bound groups. **Bottom right**: dust particles, i.e. particles that belong to the halo without being bound to any subhalo.

et al. (2004) algorithm. The various data points and line types refer to different present day host halo masses. The figure shows that, at fixed m_{sb}/M_0, more massive haloes have more subhaloes than less massive ones, as expected from the hierarchical clustering model. However, the differences in normalization are smaller than expected (Gao *et al.*, 2004; De Lucia *et al.*, 2004; van den Bosch *et al.*, 2005). Hereafter we will use the notation “mc - $R_{c,v}$” to refer to this algorithm, where “mc” stays for moving center.

We also notice that the mass fraction in subhaloes is rather high: for example, for cluster size haloes we found a mass fraction of the order of $0.3M_0$, while the value usually reported in the literature ranges between 5% and 20% (Gao *et al.*, 2004; De Lucia *et al.*, 2004; Ghigna *et al.*, 1998).

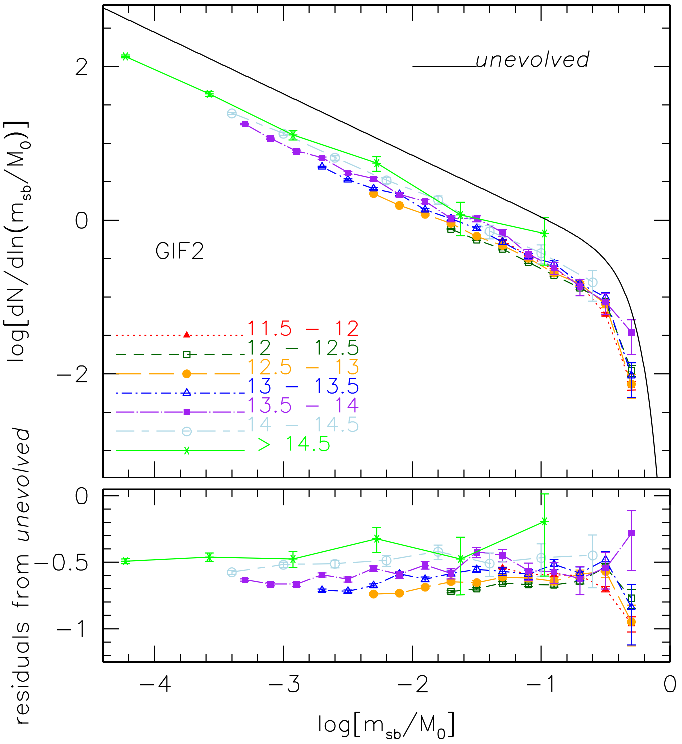

Figure C.2: Subhalo mass function in present-day haloes with $M \geq 10^{11.5}\, M_\odot/h$, from the GIF2 simulation. We only considered haloes with main progenitor mass $M_v(z) < 1.1M_v(z=0)$, (see Table 7.1 for the corresponding number of haloes in each considered mass bin). For each satellite the self-bound mass has been computed considering all its particles within the comoving virial radius $R_{c,v}$. The various data points and line types refer to different present day mass host halo masses. The solid curve indicates the unevolved subhalo mass function fit: equation (7.3).

A first possible explanation of the discrepancies between our results and those by Gao *et al.* (2004); De Lucia *et al.* (2004); Ghigna *et al.* (1998) is the fact that probably our algorithm includes too many particles in the self-bound mass of each satellite. Our method does not consider the fact that particles outside the tidal radius R_{tid} are likely to be unbound. In general, $R_{c,v} > R_{tid}$, so the self-bound mass computed considering particles within $R_{c,v}$ is an upper limit to the true subhalo mass. As we showed in Chapter 7, the algorithm we used computes the satellite mass using only the particles within R_{tid}.

Tidal radius

The tidal radius of a subhalo is defined as the distance from the center where the differential tidal force of the host equals the gravitational attraction of the subhalo, that is:

$$\mathrm{d}F_{tid}(R) = \frac{\partial F}{\partial R}\mathrm{d}R = \frac{Gm_{sb}}{R_t^2}. \tag{C.1}$$

Assuming the subhalo mass and tidal radius are much smaller than the host mass and orbital distance, respectively, i.e. $m_{sb} \ll M_0$, $R_{tid} = \mathrm{d}R \ll R$, we readily obtain:

$$R_{tid} = R\left[\frac{m_{sb}}{(2 - \partial M/\partial R)M(<R))}\right]^{1/3}. \tag{C.2}$$

Therefore the tidal radius is such that the mean density of the subhalo within R_{tid} is of the order of the mean density of the main halo within R. This definition captures the essence of the natural definition of R_{tid}, defined as the distance of the center of mass of the subhalo from the saddle point of the potential of the total system.

Satellite particles beyond the tidal radius will be stripped away and heated at the local virial temperature of the host. Tidal radii will become smaller and smaller as subhaloes move closer and closer to the host halo center, where density is higher.

Center defined by the most bound particle

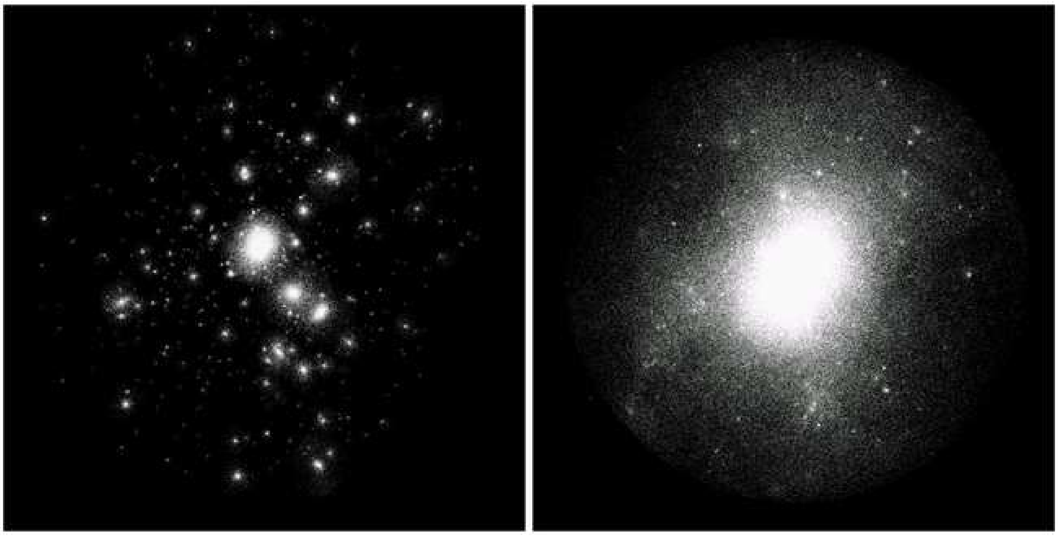

Figure C.3: **Left**: self-bound particles in subhaloes. The self-bound mass of each satellite was computed considering all the particles inside the subhalo tidal radius, and taking as center of the system the position of the most bound particle. **Right**: dust particles of the host halo.

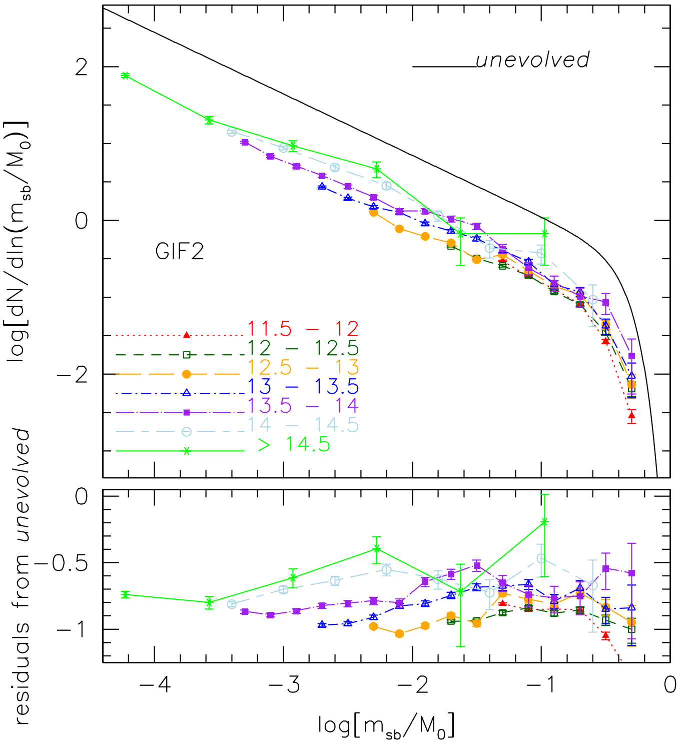

Figure C.4: Subhalo mass function in the GIF2 simulation. The self-bound mass of each subhalo has been computed considering all the satellite particles inside the subhalo tidal radius and taking as center the position of the most bound particle. The line and point types are as in Figure C.2.

The particle distribution of a subhalo may be very irregular, due to the dynamical effects just described. In particular, if the subhalo had itself substructures, we can easily observe a scatter of diffused particles, together with a few small knots. In such cases, the moving center may fail to define an appropriate center for the subhalo, meaning that it will not correctly identify the center of the largest knot of particles. When this is the case, the self-bound subhalo mass will be probably incorrectly computed.

It is thus interesting trying another common definition for the center of a bound structure, which uses the position of the most self-bound particle. We should stress the fact that, for most haloes, the moving center actually coincides with high accuracy with such position. It is only in special cases like those of subhaloes that the two algorithms may lead to different results. We will now construct the subhalo mass function using this new center definitions, and compare it to our previous results.

In order to construct the subhalo catalogues we proceeded in the following way: (i) we identify all particles composing a satellite at its merging redshift z_m; (ii) we track these particles down to redshift $z = 0$, and calculate the center of their distribution using the moving-center method; (iii) we compute the total

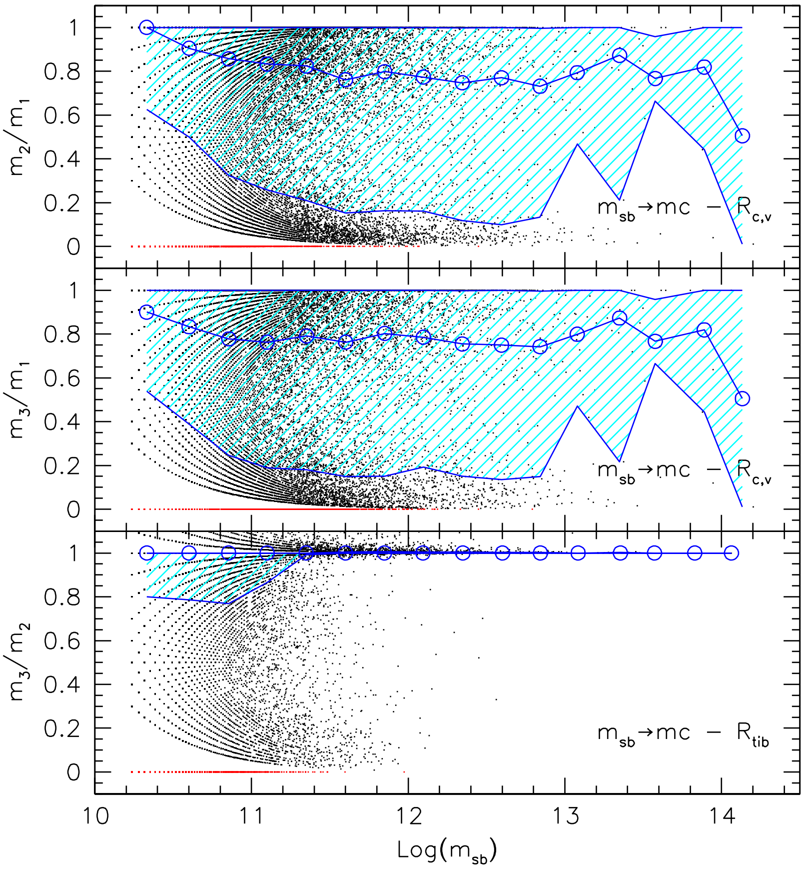

Figure C.5: Ratio between the self-bound masses assigned to subhaloes by the different algorithms. The **top** panel shows the ratio between mc $-$ R_{tid} and mc $-$ $R_{c,v}$ versus mc $-$ $R_{c,v}$, as shown in the label. The other two panels show the ratio of mbp $-$ R_{tid} over mc $-$ $R_{c,v}$ and mbp $-$ R_{tid} over mc $-$ R_{tid}, from top to bottom. The open circles represent the median of the distribution and the shaded region enclose the first and the third quartile.

energy E_i for each particle as the sum of its kinetic $E_{i,k}$ and potential $E_{i,p}$ energies, and select the most bound particle as that with most negative total energy; kinetic energies are calculated using the velocities in the reference frame defined by the center of mass; (iv) we estimate the tidal radius of the satellite picking as center the position of the most bound particle, and remove all particles with positive total energy residing within R_{tid}. Step (iv) is repeated until the self-bound mass converges to within 10%. Hereafter the notation “mbp - R_{tid}” will be used to refer to these subhaloes, where “mbp” stands "‘for most bound particle"’.

On the left panel of Figure C.3 we show the particle distribution in subhaloes identified using the method described above. On the right panel we show the dust particles of the host halo: the fact that we can observe a lot of small clumps means that the method is not really working as we would like. In order to understand what is happening, we now compare in more detail the self-bound sub-

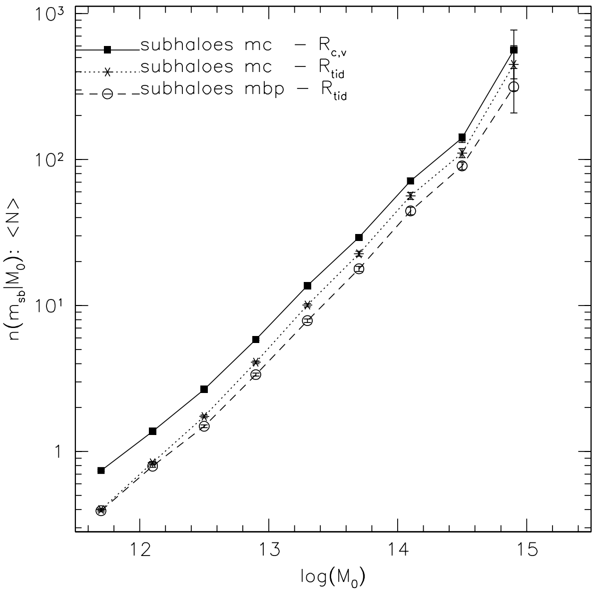

Figure C.6: Halo occupation distribution: average number of subhaloes versus host halo mass. The different data points and line types refer to the three definitions of subhaloes described in this Appendix and in Chapter 7. In the figure "‘mc"’ refers to subhaloes with centers computed using the moving center method, while "‘mbp"’ refers to centers defined using the position of the most bound particle. R_{tid} and $R_{c,v}$ denote the radius of the sphere initially used to identify candidate subhalo particles.

halo masses obtained using the different methods outlined so far. We will refer to these masses and methods as "‘one"’ (moving center and virial radius); "‘two"’ (moving center and tidal radius); and "‘three"’ (center on most bound particle, and tidal radius).

In Figure C.5 we show the ratio of the self-bound mass of each satellite (defined using all combination of definitions) versus the subhalo mass. In all panels in the figure, open circles show the median of the distribution (using only subhaloes with self-bound mass different from zero), and the shaded region encloses the first and third quartile. In the top and middle panel we show the ratios m_2/m_1 and m_3/m_1 versus m_1. In the bottom panel we plot the ratio m_3/m_2 versus m_2. We notice that, independently of the center definition, m_2 and m_3 are very similar, and both are on average 20% smaller than m_1. Besides the difference in mass, the figure shows that many subhaloes identified with method 1 are missed in the other two methods (red points in the lower-left part of the first two panels), and that some subhaloes are missed in method 3 which are present in method 2 (red points in the bottom panel). Therefore, the population of subhaloes in the three methods differ at small masses both in number and in mass. On the other hand, massive subhaloes are identified consistently in all methods (no red points on the right of the panels), but their mass is larger in method one.

Since method one and two only differ in terms of the searching radius, this

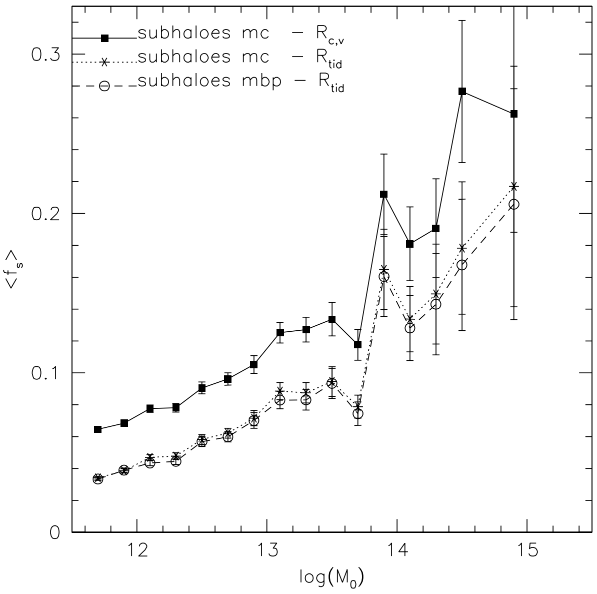

Figure C.7: Average mass fraction in subhaloes. The data points and line types are the same as in Figure C.6.

result tells us that in many cases the subhalo particles have been physically diluted and are outside the tidal radius, but their velocity has not yet increased to the virial value of the host halo, and so they are still bound to the substructure when included in the search. For small subhaloes this is so extreme that m_2 and m_3 may be zero, while m_1 is not.

In Figure C.6 we plot the first moment of the halo occupation distribution, that is the mean number of subhaloes for a given host halo mass. Various data points and line types refer to the three definitions as indicated in the label. As expected, since this statistics is dominated by small systems, method one identifies more subhaloes compared to the other two algorithms.

Finally, in Figure C.7 we show the mean mass fraction in subhaloes, for a given host halo mass. Since this is dominated by large systems, the trend is that expected from Figure C.5: on average, the total mass fraction in subhaloes is 5% larger for method one compared to the other two methods.

Bibliography

Abell, G. O. 1958. The Distribution of Rich Clusters of Galaxies. *ApJS* **3**, 211–+.

Abell, G. O., H. G. Corwin, Jr., and R. P. Olowin 1989. A catalog of rich clusters of galaxies. *ApJS* **70**, 1–138.

Aharonian, F. A., W. Hofmann, A. K. Konopelko, and H. J. Völk 1997. The potential of ground based arrays of imaging atmospheric Cherenkov telescopes. I. Determination of shower parameters. *Astroparticle Physics* **6**, 343–368.

Appelquist, T., H.-C. Cheng, and B. A. Dobrescu 2001. Bounds on universal extra dimensions. *Physical Review D 64*(3), 035002–+.

Applegate, J. H., C. J. Hogan, and R. J. Scherrer 1987. Cosmological baryon diffusion and nucleosynthesis. *Physical Review D* **35**, 1151–1160.

Armandroff, T. E., E. W. Olszewski, and C. Pryor 1995. The Mass-To-Light Ratios of the Draco and Ursa Minor Dwarf Spheroidal Galaxies.I. Radial Velocities from Multifiber Spectroscopy. *Aj* **110**, 2131–+.

Astier, P., J. Guy, N. Regnault, R. Pain, E. Aubourg, D. Balam, S. Basa, R. G. Carlberg, S. Fabbro, D. Fouchez, I. M. Hook, D. A. Howell, H. Lafoux, J. D. Neill, N. Palanque-Delabrouille, K. Perrett, C. J. Pritchet, J. Rich, M. Sullivan, R. Taillet, G. Aldering, P. Antilogus, V. Arsenijevic, C. Balland, S. Baumont, J. Bronder, H. Courtois, R. S. Ellis, M. Filiol, A. C. Gonçalves, A. Goobar, D. Guide, D. Hardin, V. Lusset, C. Lidman, R. McMahon, M. Mouchet, A. Mourao, S. Perlmutter, P. Ripoche, C. Tao, and N. Walton 2006. The Supernova Legacy Survey: measurement of Ω_M, Ω_Λ and w from the first year data set. *A&A* **447**, 31–48.

Avila-Reese, V., P. Colín, O. Valenzuela, E. D'Onghia, and C. Firmani 2001. Formation and Structure of Halos in a Warm Dark Matter Cosmology. *ApJ* **559**, 516–530.

Baer, H., and M. Brhlik 1998. Neutralino dark matter in minimal supergravity: Direct detection versus collider searches. *Physical Review D* **57**, 567–577.

Baixeras, C. 2003. The MAGIC telescope. *Nuclear Physics B Proceedings Supplements* **114**, 247–252.

Barrow, J. D., and J. Silk 1981. The growth of anisotropic structures in a Friedmann universe. *ApJ* **250**, 432–449.

Bartelmann, M., A. Huss, J. M. Colberg, A. Jenkins, and F. R. Pearce 1998. Arc statistics with realistic cluster potentials. IV. Clusters in different cosmologies. *A&A* **330**, 1–9.

Becciani, U., M. Comparato, A. Costa, C. Gheller, and B. Larsson 2006. VisiVO: an interoperable visualisation tool for VO data. *The Virtual Observatory in Action: New Science, New Technology, and Next Generation Facilities, 26th meeting of the IAU, Special Session 3, 17-18, 21-22 August, 2006 in Prague, Czech Republic, SPS3, #53* **3**, –.

Bennett, C. L., A. J. Banday, K. M. Gorski, G. Hinshaw, P. Jackson, P. Keegstra, A. Kogut, G. F. Smoot, D. T. Wilkinson, and E. L. Wright 1996. Four-Year COBE DMR Cosmic Microwave Background Observations: Maps and Basic Results. *ApJL* **464**, L1+.

Bennett, C. L., M. Halpern, G. Hinshaw, N. Jarosik, A. Kogut, M. Limon, S. S. Meyer, L. Page, D. N. Spergel, G. S. Tucker, E. Wollack, E. L. Wright, C. Barnes, M. R. Greason, R. S. Hill, E. Komatsu, M. R. Nolta, N. Odegard, H. V. Peiris, L. Verde, and J. L. Weiland 2003. First-Year Wilkinson Microwave Anisotropy Probe (WMAP) Observations: Preliminary Maps and Basic Results. *ApJS* **148**, 1–27.

Benson, A. J., C. G. Lacey, C. M. Baugh, S. Cole, and C. S. Frenk 2002. The effects of photoionization on galaxy formation - I. Model and results at z=0. *MNRAS* **333**, 156–176.

Benson, A. J., C. G. Lacey, C. S. Frenk, C. M. Baugh, and S. Cole 2004. Heating of galactic discs by infalling satellites. *MNRAS* **351**, 1215–1236.

Berezinsky, V., A. Bottino, J. Ellis, N. Fornengo, G. Mignola, and S. Scopel 1996. Neutralino dark matter in supersymmetric models with non-universal scalar mass terms. *Astroparticle Physics* **5**, 1–26.

Berezinsky, V., V. Dokuchaev, and Y. Eroshenko 2003. Small-scale clumps in the galactic halo and dark matter annihilation. *Physical Review D 68*(10), 103003–+.

Bergström, L. 2000. Non-baryonic dark matter: observational evidence and detection methods. *Reports of Progress in Physics* **63**, 793–841.

Bergström, L., P. Ullio, and J. H. Buckley 1998. Observability of gamma rays from dark matter neutralino annihilations in the Milky Way halo. *Astroparticle Physics* **9**, 137–162.

Bertone, G. 2006. Prospects for detecting dark matter with neutrino telescopes in intermediate mass black hole scenarios. *Physical Review D 73*(10), 103519–+.

Bertone, G., D. Hooper, and J. Silk 2005. Particle dark matter: evidence, candidates and constraints. *Physical Report* **405**, 279–390.

Bertone, G., and D. Merritt 2005. Time-dependent models for dark matter at the galactic center. *Physical Review D 72*(10), 103502–+.

Blasi, P., and R. K. Sheth 2000. Halo dark matter and ultra-high energy cosmic rays. *Physics Letters B* **486**, 233–238.

Bond, J. R., S. Cole, G. Efstathiou, and N. Kaiser 1991. Excursion set mass functions for hierarchical Gaussian fluctuations. *ApJ* **379**, 440–460.

Bond, J. R., and S. T. Myers 1996. The Peak-Patch Picture of Cosmic Catalogs. I. Algorithms. *ApJS* **103**, 1–+.

Bower, R. G. 1991. The evolution of groups of galaxies in the Press-Schechter formalism. *MNRAS* **248**, 332–352.

Bower, R. G., A. J. Benson, R. Malbon, J. C. Helly, C. S. Frenk, C. M. Baugh, S. Cole, and C. G. Lacey 2006. Breaking the hierarchy of galaxy formation. *MNRAS* **370**, 645–655.

Bullock, J. S., T. S. Kolatt, Y. Sigad, R. S. Somerville, A. V. Kravtsov, A. A. Klypin, J. R. Primack, and A. Dekel 2001. Profiles of dark haloes: evolution, scatter and environment. *MNRAS* **321**, 559–575.

Bullock, J. S., A. V. Kravtsov, and D. H. Weinberg 2000. Reionization and the Abundance of Galactic Satellites. *ApJ* **539**, 517–521.

Bullock, J. S., A. V. Kravtsov, and D. H. Weinberg 2001. Hierarchical Galaxy Formation and Substructure in the Galaxy's Stellar Halo. *ApJ* **548**, 33–46.

Carroll, S. M., W. H. Press, and E. L. Turner 1992. The cosmological constant. *ARA&A* **30**, 499–542.

Chandrasekhar, S. 1943. Stochastic Problems in Physics and Astronomy. *Reviews of Modern Physics* **15**, 1–89.

Choi, J.-H., M. D. Weinberg, and N. Katz 2007. The dynamics of tidal tails from massive satellites. *MNRAS* **381**, 987–1000.

Cole, S. 1991. Modeling galaxy formation in evolving dark matter halos. *ApJ* **367**, 45–53.

Cole, S., J. Helly, C. S. Frenk, and H. Parkinson 2008. The statistical properties of Λ cold dark matter halo formation. *MNRAS* **383**, 546–556.

Cole, S., and N. Kaiser 1988. Sunyaev-Zel'dovich fluctuations in the cold dark matter scenario. *MNRAS* **233**, 637–648.

Colín, P., V. Avila-Reese, and O. Valenzuela 2000. Substructure and Halo Density Profiles in a Warm Dark Matter Cosmology. *ApJ* **542**, 622–630.

Conroy, C., R. H. Wechsler, and A. V. Kravtsov 2007. The Hierarchical Build-Up of Massive Galaxies and the Intracluster Light since z = 1. *ApJ* **668**, 826–838.

Copi, C. J., D. N. Schramm, and M. S. Turner 1995. Big-Bang Nucleosynthesis and the Baryon Density of the Universe. *Science* **267**, 192–+.

Couchman, H. M. P. 1991. Mesh-refined P3M - A fast adaptive N-body algorithm. *ApJL* **368**, L23–L26.

Couchman, H. M. P., P. A. Thomas, and F. R. Pearce 1995. Hydra: an Adaptive-Mesh Implementation of P 3M-SPH. *ApJ* **452**, 797–+.

Croton, D. J., V. Springel, S. D. M. White, G. De Lucia, C. S. Frenk, L. Gao, A. Jenkins, G. Kauffmann, J. F. Navarro, and N. Yoshida 2006. The many lives of active galactic nuclei: cooling flows, black holes and the luminosities and colours of galaxies. *MNRAS* **365**, 11–28.

Dalal, N., and C. S. Kochanek 2002. Direct Detection of Cold Dark Matter Substructure. *ApJ* **572**, 25–33.

Davis, M., G. Efstathiou, C. S. Frenk, and S. D. M. White 1985. The evolution of large-scale structure in a universe dominated by cold dark matter. *ApJ* **292**, 371–394.

De Lucia, G., G. Kauffmann, V. Springel, S. D. M. White, B. Lanzoni, F. Stoehr, G. Tormen, and N. Yoshida 2004. Substructures in cold dark matter haloes. *MNRAS* **348**, 333–344.

De Lucia, G., V. Springel, S. D. M. White, D. Croton, and G. Kauffmann 2006. The formation history of elliptical galaxies. *MNRAS* **366**, 499–509.

Diemand, J., M. Kuhlen, and P. Madau 2006. Early Supersymmetric Cold Dark Matter Substructure. *ApJ* **649**, 1–13.

Diemand, J., M. Kuhlen, and P. Madau 2007a. Dark Matter Substructure and Gamma-Ray Annihilation in the Milky Way Halo. *ApJ* **657**, 262–270.

Diemand, J., M. Kuhlen, and P. Madau 2007b. Formation and Evolution of Galaxy Dark Matter Halos and Their Substructure. *ApJ* **667**, 859–877.

Diemand, J., P. Madau, and B. Moore 2005. The distribution and kinematics of early high-σ peaks in present-day haloes: implications for rare objects and old stellar populations. *MNRAS* **364**, 367–383.

Diemand, J., B. Moore, and J. Stadel 2004. Convergence and scatter of cluster density profiles. *MNRAS* **353**, 624–632.

Diemand, J., B. Moore, and J. Stadel 2005. Earth-mass dark-matter haloes as the first structures in the early Universe. *Nature* **433**, 389–391.

Dimopoulos, S. 1990. LHC, SSC and the universe. *Physics Letters B* **246**, 347–352.

Dressler, A. 1980. Galaxy morphology in rich clusters - Implications for the formation and evolution of galaxies. *ApJ* **236**, 351–365.

Efstathiou, G., M. Davis, S. D. M. White, and C. S. Frenk 1985. Numerical techniques for large cosmological N-body simulations. *ApJS* **57**, 241–260.

Efstathiou, G., C. S. Frenk, S. D. M. White, and M. Davis 1988. Gravitational clustering from scale-free initial conditions. *MNRAS* **235**, 715–748.

Eisenstein, D. J., and P. Hut 1998. HOP: A New Group-Finding Algorithm for N-Body Simulations. *ApJ* **498**, 137–+.

Eisenstein, D. J., and A. Loeb 1995. An analytical model for the triaxial collapse of cosmological perturbations. *ApJ* **439**, 520–541.

Eke, V. R., S. Cole, and C. S. Frenk 1996. Cluster evolution as a diagnostic for Omega. *MNRAS* **282**, 263–280.

Epstein, R. I. 1983. Proto-galactic perturbations. *MNRAS* **205**, 207–229.

Fornengo, N., L. Pieri, and S. Scopel 2004. Neutralino annihilation into γ rays in the Milky Way and in external galaxies. *Physical Review D 70*(10), 103529–+.

Frenk, C. S., A. E. Evrard, S. D. M. White, and F. J. Summers 1996. Galaxy Dynamics in Clusters. *ApJ* **472**, 460–+.

Frenk, C. S., S. D. M. White, M. Davis, and G. Efstathiou 1988. The formation of dark halos in a universe dominated by cold dark matter. *ApJ* **327**, 507–525.

Gao, L., V. Springel, and S. D. M. White 2005. The age dependence of halo clustering. *MNRAS* **363**, L66–L70.

Gao, L., S. D. M. White, A. Jenkins, F. Stoehr, and V. Springel 2004. The subhalo populations of ΛCDM dark haloes. *MNRAS* **355**, 819–834.

Gelb, J. M., and E. Bertschinger 1994. Cold dark matter. 1: The formation of dark halos. *ApJ* **436**, 467–490.

Ghigna, S., B. Moore, F. Governato, G. Lake, T. Quinn, and J. Stadel 1998. Dark matter haloes within clusters. *MNRAS* **300**, 146–162.

Ghigna, S., B. Moore, F. Governato, G. Lake, T. Quinn, and J. Stadel 2000. Density Profiles and Substructure of Dark Matter Halos: Converging Results at Ultra-High Numerical Resolution. *ApJ* **544**, 616–628.

Giocoli, C., J. Moreno, R. K. Sheth, and G. Tormen 2007. An improved model for the formation times of dark matter haloes. *MNRAS* **376**, 977–983.

Goerdt, T., O. Y. Gnedin, B. Moore, J. Diemand, and J. Stadel 2007. The survival and disruption of cold dark matter microhaloes: implications for direct and indirect detection experiments. *MNRAS* **375**, 191–198.

Gottlöber, S., A. Klypin, and A. V. Kravtsov 1999. Merging Rate of Dark Matter Halos: Evolution and Dependence on Environment. *Astrophysics and Space Science* **269**, 345–348.

Götz, M., and J. Sommer-Larsen 2002. Warm Dark Matter and the Missing Satellites Problem. *Astrophysics and Space Science* **281**, 415–416.

Grebel, E. K., and J. S. Gallagher, III 2004. The Impact of Reionization on the Stellar Populations of Nearby Dwarf Galaxies. *ApJL* **610**, L89–L92.

Green, A. M., S. Hofmann, and D. J. Schwarz 2005. The first WIMPy halos. *Journal of Cosmology and Astro-Particle Physics* **8**, 3–+.

Green, D. A., R. J. Tuffs, and C. C. Popescu 2004. Far-infrared and submillimetre observations of the Crab nebula. *MNRAS* **355**, 1315–1326.

Gunn, J. E., and J. R. I. Gott 1972. On the Infall of Matter Into Clusters of Galaxies and Some Effects on Their Evolution. *ApJ* **176**, 1–+.

Hahn, O., C. M. Carollo, C. Porciani, and A. Dekel 2007. The evolution of dark matter halo properties in clusters, filaments, sheets and voids. *MNRAS* **381**, 41–51.

Harker, G., S. Cole, J. Helly, C. Frenk, and A. Jenkins 2006. A marked correlation function analysis of halo formation times in the Millennium Simulation. *MNRAS* **367**, 1039–1049.

Hayashi, E., J. F. Navarro, J. E. Taylor, J. Stadel, and T. Quinn 2003. The Structural Evolution of Substructure. *ApJ* **584**, 541–558.

Hofmann, S., D. J. Schwarz, and H. Stöcker 2001. Damping scales of neutralino cold dark matter. *Physical Review D 64*(8), 083507–+.

Icke, V. 1973. Formation of Galaxies inside Clusters. *A&A* **27**, 1–+.

Jenkins, A., C. S. Frenk, S. D. M. White, J. M. Colberg, S. Cole, A. E. Evrard, H. M. P. Couchman, and N. Yoshida 2001. The mass function of dark matter haloes. *MNRAS* **321**, 372–384.

Jungman, G., M. Kamionkowski, and K. Griest 1996. Supersymmetric dark matter. *Physical Report* **267**, 195–373.

Kauffmann, G., J. M. Colberg, and S. D. M. Diaferio, A. White 1999. Clustering of galaxies in a hierarchical universe - I. Methods and results at z=0. *MNRAS* **303**, 188–206.

Kauffmann, G., and S. D. M. White 1993. The merging history of dark matter haloes in a hierarchical universe. *MNRAS* **261**, 921–928.

King, I. R. 1966. The structure of star clusters. III. Some simple dynamical models. *Aj* **71**, 64–+.

Klypin, A., A. V. Kravtsov, O. Valenzuela, and F. Prada 1999. Where Are the Missing Galactic Satellites? *ApJ* **522**, 82–92.

Koushiappas, S. M. 2006. Proper Motion of Gamma Rays from Microhalo Sources. *Physical Review Letters 97*(19), 191301–+.

Kravtsov, A. V., A. A. Berlind, R. H. Wechsler, A. A. Klypin, S. Gottlöber, B. Allgood, and J. R. Primack 2004. The Dark Side of the Halo Occupation Distribution. *ApJ* **609**, 35–49.

Kravtsov, A. V., O. Y. Gnedin, and A. A. Klypin 2004. The Tumultuous Lives of Galactic Dwarfs and the Missing Satellites Problem. *ApJ* **609**, 482–497.

Krick, J. E., R. A. Bernstein, and K. A. Pimbblet 2006. Diffuse Optical Light in Galaxy Clusters. I. Abell 3888. *Aj* **131**, 168–184.

Lacey, C., and S. Cole 1993. Merger rates in hierarchical models of galaxy formation. *MNRAS* **262**, 627–649.

Lacey, C., and S. Cole 1994. Merger Rates in Hierarchical Models of Galaxy Formation - Part Two - Comparison with N-Body Simulations. *MNRAS* **271**, 676–+.

Lemson, G. 1993. Dynamical Effects of the Cosmological Constant - the Evolution of Aspherical Structures. *MNRAS* **263**, 913–+.

Li, Y.-S., and A. Helmi 2007. Infall of Substructures onto a Milky Way-like Dark Halo. *ArXiv e-prints* **711**, –.

Lin, W. P., Y. P. Jing, and L. Lin 2003. Formation time-distribution of dark matter haloes: theories versus N-body simulations. *MNRAS* **344**, 1327–1333.

Łokas, E. L., G. A. Mamon, and F. Prada 2005. Dark matter distribution in the Draco dwarf from velocity moments. *MNRAS* **363**, 918–928.

Mahmood, A., and R. Rajesh 2005. Cosmological mass functions and moving barrier models. *ArXiv Astrophysics e-prints* **0**, –.

McKay, T. A., B. Koester, R. Wechsler, J. Annis, A. Evrard, E. Sheldon, D. Johnston, S. Hansen, R. Scranton, and SDSS Collaboration 2005. A MaxBCG Galaxy Cluster Catalog Selected from SDSS Imaging Data. In *Bulletin of the American Astronomical Society*, Volume 37 of *Bulletin of the American Astronomical Society*, pp. 445–+.

Merritt, D., M. Milosavljević, L. Verde, and R. Jimenez 2002. Dark Matter Spikes and Annihilation Radiation from the Galactic Center. *Physical Review Letters 88*(19), 191301–+.

Metcalf, R. B., and P. Madau 2001. Compound Gravitational Lensing as a Probe of Dark Matter Substructure within Galaxy Halos. *MNRAS* **563**, 9–20.

Miller, C. J., R. C. Nichol, D. Reichart, R. H. Wechsler, A. E. Evrard, J. Annis, T. A. McKay, N. A. Bahcall, M. Bernardi, H. Boehringer, A. J. Connolly, T. Goto, A. Kniazev, D. Lamb, M. Postman, D. P. Schneider, R. K. Sheth, and W. Voges 2005. The C4 Clustering Algorithm: Clusters of Galaxies in the Sloan Digital Sky Survey. *Aj* **130**, 968–1001.

Moore, B., S. Ghigna, F. Governato, G. Lake, T. Quinn, J. Stadel, and P. Tozzi 1999. Dark Matter Substructure within Galactic Halos. *ApJL* **524**, L19–L22.

Mori, M., M. M. Nojiri, K. S. Hirata, K. Kihara, Y. Oyama, A. Suzuki, K. Takahashi, M. Yamada, H. Takei, M. Koga, K. Miyano, H. Miyata, Y. Fukuda, T. Hayakawa, K. Inoue, T. Ishida, T. Kajita, Y. Koshio, M. Nakahata, K. Nakamura, A. Sakai, N. Sato, M. Shiozawa, J. Suzuki, Y. Suzuki, Y. Totsuka, M. Koshiba, K. Nishijima, T. Kajimura, T. Suda, A. T. Suzuki, T. Hara, Y. Nagashima, M. Takita, H. Yokoyama, A. Yoshimoto, K. Kaneyuki, Y. Takeuchi, T. Tanimori, S. Tasaka, and K. Nishikawa 1993. Search for neutralino dark matter heavier than the W boson at Kamiokande. *Physical Review D* **48**, 5505–5518.

Morselli, A. 1997. The Gamma-Ray Large Area Space Telescope (glast). In Y. Giraud-Heraud and J. Tran Thanh van (Eds.), *Very High Energy Phenomena in the Universe; Moriond Workshop*, pp. 123–+.

Murante, G., M. Giovalli, O. Gerhard, M. Arnaboldi, S. Borgani, and K. Dolag 2007. The importance of mergers for the origin of intracluster stars in cosmological simulations of galaxy clusters. *MNRAS* **377**, 2–16.

Navarro, J. F., C. S. Frenk, and S. D. M. White 1996. The Structure of Cold Dark Matter Halos. *ApJ* **462**, 563–+.

Navarro, J. F., C. S. Frenk, and S. D. M. White 1997. A Universal Density Profile from Hierarchical Clustering. *ApJ* **490**, 493–+.

Navarro, J. F., E. Hayashi, C. Power, A. R. Jenkins, C. S. Frenk, S. D. M. White, V. Springel, J. Stadel, and T. R. Quinn 2004. The inner structure of ΛCDM haloes - III. Universality and asymptotic slopes. *MNRAS* **349**, 1039–1051.

Navarro, J. F., and M. Steinmetz 2000. Dark Halo and Disk Galaxy Scaling Laws in Hierarchical Universes. *ApJ* **538**, 477–488.

Neto, A. F., L. Gao, P. Bett, S. Cole, J. F. Navarro, C. S. Frenk, S. D. M. White, V. Springel, and A. Jenkins 2007. The statistics of Λ CDM halo concentrations. *MNRAS* **381**, 1450–1462.

Netterfield, C. B., P. A. R. Ade, J. J. Bock, J. R. Bond, J. Borrill, A. Boscaleri, K. Coble, C. R. Contaldi, B. P. Crill, P. de Bernardis, P. Farese, K. Ganga, M. Giacometti, E. Hivon, V. V. Hristov, A. Iacoangeli, A. H. Jaffe, W. C. Jones, A. E. Lange, L. Martinis, S. Masi, P. Mason, P. D. Mauskopf, A. Melchiorri, T. Montroy, E. Pascale, F. Piacentini, D. Pogosyan, F. Pongetti, S. Prunet, G. Romeo, J. E. Ruhl, and F. Scaramuzzi 2002. A Measurement by BOOMERANG of Multiple Peaks in the Angular Power Spectrum of the Cosmic Microwave Background. *ApJ* **571**, 604–614.

Newman, J. A., and M. Davis 2002. Measuring the Cosmic Equation of State with Counts of Galaxies. II. Error Budget for the DEEP2 Redshift Survey. *ApJ* **564**, 567–575.

Odenkirchen, M., E. K. Grebel, D. Harbeck, W. Dehnen, H.-W. Rix, H. J. Newberg, B. Yanny, J. Holtzman, J. Brinkmann, B. Chen, I. Csabai, J. J. E. Hayes, G. Hennessy, R. B. Hindsley, Ž. Ivezić, E. K. Kinney, S. J. Kleinman, D. Long, R. H. Lupton, E. H. Neilsen, A. Nitta, S. A. Snedden, and D. G. York 2001. New Insights on the Draco Dwarf Spheroidal Galaxy from the Sloan Digital Sky Survey: A Larger Radius and No Tidal Tails. *Aj* **122**, 2538–2553.

Pearce, F. R., and H. M. P. Couchman 1997. Hydra: a parallel adaptive grid code. *New Astronomy* **2**, 411–427.

Percival, W., and L. Miller 1999. Cosmological evolution and hierarchical galaxy formation. *MNRAS* **309**, 823–832.

Pieri, L., G. Bertone, and E. Branchini 2007. Dark Matter Annihilation in Substructures Revised. *ArXiv e-prints* **706**, –.

Press, W. H., and P. Schechter 1974. Formation of Galaxies and Clusters of Galaxies by Self-Similar Gravitational Condensation. *ApJ* **187**, 425–438.

Quinn, P. J., and W. H. Zurek 1988. The angular momentum distribution in galactic halos. *ApJ* **331**, 1–18.

Refregier, A., J. Rhodes, and E. J. Groth 2002. Cosmic Shear and Power Spectrum Normalization with the Hubble Space Telescope. *ApJL* **572**, L131–L134.

Scoccimarro, R., R. K. Sheth, L. Hui, and B. Jain 2001. How Many Galaxies Fit in a Halo? Constraints on Galaxy Formation Efficiency from Spatial Clustering. *ApJ* **546**, 20–34.

Seljak, U., and M. Zaldarriaga 1996. A Line-of-Sight Integration Approach to Cosmic Microwave Background Anisotropies. *ApJ* **469**, 437–+.

Servant, G., and T. M. P. Tait 2003. Is the lightest Kaluza-Klein particle a viable dark matter candidate? *Nuclear Physics B* **650**, 391–419.

Shen, J., T. Abel, H. J. Mo, and R. K. Sheth 2006. An Excursion Set Model of the Cosmic Web: The Abundance of Sheets, Filaments, and Halos. *ApJ* **645**, 783–791.

Sheth, R. K. 1995. Merging and Hierarchical Clustering from an Initially Poisson Distribution. *MNRAS* **276**, 796–+.

Sheth, R. K. 1996. Galton-Watson branching processes and the growth of gravitational clustering. *MNRAS* **281**, 1277–+.

Sheth, R. K. 1998. An excursion set model for the distribution of dark matter and dark matter haloes. *MNRAS* **300**, 1057–1070.

Sheth, R. K. 2003. Substructure in dark matter haloes: towards a model of the abundance and spatial distribution of subclumps. *MNRAS* **345**, 1200–1204.

Sheth, R. K., M. Bernardi, P. L. Schechter, S. Burles, D. J. Eisenstein, D. P. Finkbeiner, J. Frieman, R. H. Lupton, D. J. Schlegel, M. Subbarao, K. Shimasaku, N. A. Bahcall, J. Brinkmann, and Ž. Ivezić 2003. The Velocity Dispersion Function of Early-Type Galaxies. *ApJ* **594**, 225–231.

Sheth, R. K., and A. Diaferio 2001. Peculiar velocities of galaxies and clusters. *MNRAS* **322**, 901–917.

Sheth, R. K., and G. Lemson 1999. The forest of merger history trees associated with the formation of dark matter haloes. *MNRAS* **305**, 946–956.

Sheth, R. K., H. J. Mo, and G. Tormen 2001. Ellipsoidal collapse and an improved model for the number and spatial distribution of dark matter haloes. *MNRAS* **323**, 1–12.

Sheth, R. K., and J. Pitman 1997. Coagulation and branching process models of gravitational clustering. *MNRAS* **289**, 66–82.

Sheth, R. K., and G. Tormen 1999. Large-scale bias and the peak background split. *MNRAS* **308**, 119–126.

Sheth, R. K., and G. Tormen 2002. An excursion set model of hierarchical clustering: ellipsoidal collapse and the moving barrier. *MNRAS* **329**, 61–75.

Sheth, R. K., and G. Tormen 2004. Formation times and masses of dark matter haloes. *MNRAS* **349**, 1464–1468.

Smoluchowski, M. V. 1916. Drei Vortrage uber Diffusion, Brownsche Bewegung und Koagulation von Kolloidteilchen. *Zeitschrift fur Physik* **17**, 557–585.

Smoot, G. F., C. L. Bennett, A. Kogut, E. L. Wright, J. Aymon, N. W. Boggess, E. S. Cheng, G. de Amici, S. Gulkis, M. G. Hauser, G. Hinshaw, P. D. Jackson, M. Janssen, E. Kaita, T. Kelsall, P. Keegstra, C. Lineweaver, K. Loewenstein, P. Lubin, J. Mather, S. S. Meyer, S. H. Moseley, T. Murdock, L. Rokke, R. F. Silverberg, L. Tenorio, R. Weiss, and D. T. Wilkinson 1992. Structure in the COBE differential microwave radiometer first-year maps. *ApJL* **396**, L1–L5.

Somerville, R. S. 2002. Can Photoionization Squelching Resolve the Substructure Crisis? *ApJL* **572**, L23–L26.

Somerville, R. S., and T. S. Kolatt 1999. How to plant a merger tree. *MNRAS* **305**, 1–14.

Somerville, R. S., G. Lemson, T. S. Kolatt, and A. Dekel 2000. Evaluating approximations for halo merging histories. *MNRAS* **316**, 479–490.

Songaila, A., L. L. Cowie, C. J. Hogan, and M. Rugers 1994. Deuterium Abundance and Background Radiation Temperature in High Redshift Primordial Clouds. *Nature* **368**, 599–+.

Spergel, D. N., R. Bean, O. Doré, M. R. Nolta, C. L. Bennett, J. Dunkley, G. Hinshaw, N. Jarosik, E. Komatsu, L. Page, H. V. Peiris, L. Verde, M. Halpern, R. S. Hill, A. Kogut, M. Limon, S. S. Meyer, N. Odegard, G. S. Tucker, J. L. Weiland, E. Wollack, and E. L. Wright 2007. Three-Year Wilkinson Microwave Anisotropy Probe (WMAP) Observations: Implications for Cosmology. *ApJS* **170**, 377–408.

Spergel, D. N., L. Verde, H. V. Peiris, E. Komatsu, M. R. Nolta, C. L. Bennett, M. Halpern, G. Hinshaw, N. Jarosik, A. Kogut, M. Limon, S. S. Meyer, L. Page, G. S. Tucker, J. L. Weiland, E. Wollack, and E. L. Wright 2003. First-Year Wilkinson Microwave Anisotropy Probe (WMAP) Observations: Determination of Cosmological Parameters. *ApJS* **148**, 175–194.

Springel, V. 2005. The cosmological simulation code GADGET-2. *MNRAS* **364**, 1105–1134.

Springel, V., S. D. M. White, A. Jenkins, C. S. Frenk, N. Yoshida, L. Gao, J. Navarro, R. Thacker, D. Croton, J. Helly, J. A. Peacock, S. Cole, P. Thomas, H. Couchman, A. Evrard, J. Colberg, and F. Pearce 2005. Simulations of the formation, evolution and clustering of galaxies and quasars. *Nature* **435**, 629–636.

Springel, V., S. D. M. White, G. Tormen, and G. Kauffmann 2001. Populating a cluster of galaxies - I. Results at [formmu2]z=0. *MNRAS* **328**, 726–750.

Springel, V., N. Yoshida, and S. D. M. White 2001. GADGET: a code for collisionless and gasdynamical cosmological simulations. *New Astronomy* **6**, 79–117.

Sreekumar, P., D. L. Bertsch, B. L. Dingus, J. A. Esposito, C. E. Fichtel, R. C. Hartman, S. D. Hunter, G. Kanbach, D. A. Kniffen, Y. C. Lin, H. A. Mayer-Hasselwander, P. F. Michelson, C. von Montigny, A. Muecke, R. Mukherjee, P. L. Nolan, M. Pohl, O. Reimer, E. Schneid, J. G. Stacy, F. W. Stecker, D. J. Thompson, and T. D. Willis 1998. EGRET Observations of the Extragalactic Gamma-Ray Emission. *ApJ* **494**, 523–+.

Stewart, K. R., J. S. Bullock, R. H. Wechsler, A. H. Maller, and A. R. Zentner 2007. Merger Histories of Galaxy Halos and Implications for Disk Survival. *ArXiv e-prints* **711**, –.

Stoehr, F., S. D. M. White, V. Springel, G. Tormen, and N. Yoshida 2003. Dark matter annihilation in the halo of the Milky Way. *MNRAS* **345**, 1313–1322.

Stoehr, F., S. D. M. White, G. Tormen, and V. Springel 2002. The satellite population of the Milky Way in a ΛCDM universe. *MNRAS* **335**, L84–L88.

Taruya, A., and Y. Suto 2000. Nonlinear Stochastic Biasing from the Formation Epoch Distribution of Dark Halos. *ApJ* **542**, 559–577.

Taylor, J. E., and A. Babul 2004. The evolution of substructure in galaxy, group and cluster haloes - I. Basic dynamics. *MNRAS* **348**, 811–830.

Tegmark, M., D. J. Eisenstein, M. A. Strauss, D. H. Weinberg, M. R. Blanton, J. A. Frieman, M. Fukugita, J. E. Gunn, A. J. S. Hamilton, G. R. Knapp, R. C. Nichol, J. P. Ostriker, N. Padmanabhan, W. J. Percival, D. J. Schlegel, D. P. Schneider, R. Scoccimarro, U. Seljak, H.-J. Seo, M. Swanson, A. S. Szalay, M. S. Vogeley, J. Yoo, I. Zehavi, K. Abazajian, S. F. Anderson, J. Annis, N. A. Bahcall, B. Bassett, A. Berlind, J. Brinkmann, T. Budavari, F. Castander, A. Connolly, I. Csabai, M. Doi, D. P. Finkbeiner, B. Gillespie, K. Glazebrook, G. S. Hennessy, D. W. Hogg, Ž. Ivezić, B. Jain, D. Johnston, S. Kent, D. Q. Lamb, B. C. Lee, H. Lin, J. Loveday, R. H. Lupton, J. A. Munn, K. Pan, C. Park, J. Peoples, J. R. Pier, A. Pope, M. Richmond, C. Rockosi, R. Scranton, R. K. Sheth, A. Stebbins, C. Stoughton, I. Szapudi, D. L. Tucker, D. E. V. Berk, B. Yanny, and D. G. York 2006. Cosmological constraints from the SDSS luminous red galaxies. *Physical Review D 74*(12), 123507–+.

Tormen, G. 1997. The rise and fall of satellites in galaxy clusters. *MNRAS* **290**, 411–421.

Tormen, G. 1998. The assembly of matter in galaxy clusters. *MNRAS* **297**, 648–656.

Tormen, G., F. R. Bouchet, and S. D. M. White 1997. The structure and dynamical evolution of dark matter haloes. *MNRAS* **286**, 865–884.

Tormen, G., A. Diaferio, and D. Syer 1998. Survival of substructure within dark matter haloes. *MNRAS* **299**, 728–742.

Tormen, G., L. Moscardini, and N. Yoshida 2004. Properties of cluster satellites in hydrodynamical simulations. *MNRAS* **350**, 1397–1408.

Toth, G., and J. P. Ostriker 1992. Galactic disks, infall, and the global value of Omega. *ApJ* **389**, 5–26.

Ullio, P., H. Zhao, and M. Kamionkowski 2001. Dark-matter spike at the galactic center? *Physical Review D 64*(4), 043504–+.

Vale, A., and J. P. Ostriker 2006. The non-parametric model for linking galaxy luminosity with halo/subhalo mass. *MNRAS* **371**, 1173–1187.

van den Bosch, F. C. 2002. The universal mass accretion history of cold dark matter haloes. *MNRAS* **331**, 98–110.

van den Bosch, F. C., G. Tormen, and C. Giocoli 2005. The mass function and average mass-loss rate of dark matter subhaloes. *MNRAS* **359**, 1029–1040.

Van Waerbeke, L., Y. Mellier, M. Radovich, E. Bertin, M. Dantel-Fort, H. J. McCracken, O. Le Fèvre, S. Foucaud, J.-C. Cuillandre, T. Erben, B. Jain, P. Schneider, F. Bernardeau, and B. Fort 2001. Cosmic shear statistics and cosmology. *A&A* **374**, 757–769.

Verde, L., M. Kamionkowski, J. J. Mohr, and A. J. Benson 2001. On galaxy cluster sizes and temperatures. *MNRAS* **321**, L7–L13.

Viel, M., J. Lesgourgues, M. G. Haehnelt, S. Matarrese, and A. Riotto 2005. Constraining warm dark matter candidates including sterile neutrinos and light gravitinos with WMAP and the Lyman-α forest. *Physical Review D 71*(6), 063534–+.

Wang, J., G. De Lucia, M. G. Kitzbichler, and S. D. M. White 2007. The Dependence of Galaxy Formation on Cosmological Parameters: Can we distinguish the WMAP1 and WMAP3 Parameter Sets? *ArXiv e-prints* **706**, –.

Wechsler, R. H., J. S. Bullock, J. R. Primack, A. V. Kravtsov, and A. Dekel 2002. Concentrations of Dark Halos from Their Assembly Histories. *ApJ* **568**, 52–70.

Wechsler, R. H., A. R. Zentner, J. S. Bullock, A. V. Kravtsov, and B. Allgood 2006. The Dependence of Halo Clustering on Halo Formation History, Concentration, and Occupation. *ApJ* **652**, 71–84.

Weekes, T. C., C. Akerlof, S. Biller, A. C. Breslin, M. Catanese, D. A. Carter-Lewis, M. F. Cawley, B. Dingus, G. G. Fazio, D. J. Fegan, J. Finley, G. Fishman, J. Gaidos, G. H. Gillanders, P. Gorham, J. E. Grindlay, A. M. Hillas, J. Huchra, P. Kaaret, M. Kertzman, D. Kieda, F. Krennrich, R. C. Lamb, M. J. Lang, A. P. Marscher, S. Matz, T. McKay, D. Muller, R. Ong, W. Purcell, H. J. Rose, G. Sembroski, F. D. Seward, P. Slane, S. Swordy, T. Tumer, M. Ulmer, M. Urban, and B. Wilkes 1997. VERITAS: The Very Energetic Radiation Imaging Telescope Array System. In

International Cosmic Ray Conference, Volume 25 of *International Cosmic Ray Conference*, pp. 173–+.

White, S. D. M. 1993. Large-scale structure. In R. J. Gleiser, C. N. Kozameh, and O. M. Moreschi (Eds.), *General Relativity and Gravitation 1992*, pp. 331–+.

White, S. D. M., and M. J. Rees 1978. Core condensation in heavy halos - A two-stage theory for galaxy formation and clustering. *MNRAS* **183**, 341–358.

White, S. D. M., and J. Silk 1979. The growth of aspherical structure in the universe - Is the Local Supercluster an unusual system. *ApJ* **231**, 1–9.

Wilkinson, M. I., J. T. Kleyna, N. W. Evans, G. F. Gilmore, M. J. Irwin, and E. K. Grebel 2004. Kinematically Cold Populations at Large Radii in the Draco and Ursa Minor Dwarf Spheroidal Galaxies. *ApJl* **611**, L21–L24.

Willman, B., F. Governato, J. Wadsley, and T. Quinn 2004. The origin and properties of intracluster stars in a rich cluster. *MNRAS* **355**, 159–168.

Yoshida, N., R. K. Sheth, and A. Diaferio 2001. Non-Gaussian cosmic microwave background temperature fluctuations from peculiar velocities of clusters. *MNRAS* **328**, 669–677.

Zaroubi, S., A. Naim, and Y. Hoffman 1996. Secondary Infall: Theory versus Simulations. *ApJ* **457**, 50–+.

Zel'Dovich, Y. B. 1970. Gravitational instability: An approximate theory for large density perturbations. *A&A* **5**, 84–89.

Zentner, A. R., and J. S. Bullock 2003. Halo Substructure and the Power Spectrum. *ApJ* **598**, 49–72.

Publication List and Work in Progress

- ⥁ The mass function and average mass-loss rate of dark matter subhaloes
  van den Bosch, Frank C.; Tormen, Giuseppe; **Giocoli, Carlo**
  (*Bibliographic Code*: 2005MNRAS.359.1029V)

- ⥁ An improved model for the formation times of dark matter haloes
  Giocoli, Carlo; Moreno, Jorge; Sheth, Ravi K.; Tormen, Giuseppe
  (*Bibliographic Code*: 2007MNRAS.376..977G)

- ↷ Analytical Approach to Subhaloes Population in Dark Matter Haloes
  Giocoli, Carlo; Pieri, Lidia; Tormen, Giuseppe
  (MNRAS submitted - *Bibliographic Code*: 2007arXiv0712.1476G)

- ↷ The Population of Dark Matter Subhaloes: Mass Functions and Average Mass Loss Rates
  Giocoli, Carlo; Tormen, Giuseppe; van den Bosch, Frank C.
  (MNRAS submitted - *Bibliographic Code*: 2007arXiv0712.1563G)

- ⇝ Creation times of Dark Matter Haloes in Moving Barrier Models
  Moreno, Jorge; **Giocoli, Carlo**; Sheth, Ravi K.;
  (MNRAS submitted - *Bibliographic Code*: 2007arXiv0712.4100M)

- ⇝ Merger History Trees of Dark Matter Haloes
  Moreno, Jorge; **Giocoli, Carlo**; Sheth, Ravi K.;
  (MNRAS submitted - *Bibliographic Code*: 2007arXiv0712.3800M)

- ⇝ Substructures Population in Dark Matter Haloes
  Giocoli, Carlo; Tormen, Giuseppe; Sheth, Ravi K.; van den Bosch, Frank C.

- ⇝ Draco Population with Microsolar Mass Resolution Merger Tree: gamma ray detectability Haloes
  Giocoli, Carlo; Pieri, Lidia; Sheth, Ravi K.; Tormen, Giuseppe